

University of Southampton Research Repository

Copyright © and Moral Rights for this thesis and, where applicable, any accompanying data are retained by the author and/or other copyright owners. A copy can be downloaded for personal non-commercial research or study, without prior permission or charge. This thesis and the accompanying data cannot be reproduced or quoted extensively from without first obtaining permission in writing from the copyright holder/s. The content of the thesis and accompanying research data (where applicable) must not be changed in any way or sold commercially in any format or medium without the formal permission of the copyright holder/s.

When referring to this thesis and any accompanying data, full bibliographic details must be given, e.g.

Thesis: Author (Year of Submission) "Full thesis title", University of Southampton, name of the University Faculty or School or Department, PhD Thesis, pagination.

Data: Author (Year) Title. URI [dataset]

UNIVERSITY OF SOUTHAMPTON

FACULTY OF ENGINEERING AND PHYSICAL SCIENCES

Physics and Astronomy

**Lanthanide-doped Upconversion Nanoparticles: Synthesis and
Applications**

by

Elena Ureña Horno

Thesis for the degree of Doctor of Philosophy

August 2019

UNIVERSITY OF SOUTHAMPTON

ABSTRACT

FACULTY OF ENGINEERING AND PHYSICAL SCIENCES

PHYSICS AND ASTRONOMY

Thesis for the degree of Doctor of Philosophy

Lanthanide-doped Upconversion Nanoparticles: Synthesis and Applications

Elena Ureña Horno

Lanthanide-ion-doped upconversion nanoparticles (UCNPs) have emerged as a new class of luminescent materials that offer excellent chemical stability, good biocompatibility, narrow bandwidth, long luminescence times, good resistance to photobleaching and photoblinking.^{1,2} Most importantly, UCNPs can up-convert two or more low energy photons into one high energy photon because of their intra-configurational 4f electron transitions.^{1,2} Therefore, UCNPs are of great interest in many fields including photocatalysis, biomedicine and sensing.³

In this project the main aim was to explore the UCNPs synthesis under different conditions and their functionalization with organic and inorganic materials. We observed that the synthesis played a critical role in determining the structure, phase, and upconversion (UC) luminescence of the resulting materials. Different parameters including the role of oleic acid (OA) and the effect of the host lattice and the fluoride source were studied. Furthermore, different coatings materials were formed around the surface of the core UCNPs and were fully characterized.

With a view of developing a universal protocol for the silanization of UCNPs, we investigated the silica coating around different sizes and morphologies of UCNPs. We created an approach based on a calibration curve. The employment of this approach proved to produce uniform and individual silica coating of the UCNPs, which were employed for further functionalization with oligonucleotides and gold.

The synthesis and the photocatalysis activity of the UCNPs coated by TiO₂ were studied. Results showed efficient photocatalytic activity under UV as well as IR irradiation, using redox dyes (DCPIP and Resazurin). Different effects on the photocatalytic activity such as annealing effect, loading effect, and recyclability were also studied.

Additionally, we functionalized the surface of the UCNPs with IR-806 dyes in order to enhance the UC luminescence properties and to provide new insights on the energy migration and surface effects of the UCNPs. Hence, the UC and downconversion (DC) luminescence properties were individually investigated in the dye-sensitized UCNPs in comparison to the non-sensitized UCNPs.

Encouraged by the principle of dye sensitizing in UCNPs, we additionally investigated whether new IR dyes could be used to cover different part of the IR spectrum. We proposed a new IR-dye molecule (IR-1076) in order to alleviate the well-known concentration quenching that exist in UCNPs. Although the work is still ongoing, we expect that the strategy could be used to produce UCNPs with higher dopant concentrations, hence enhancing the UC and DC luminescence properties.

Table of Contents

Table of Contents	i
Table of Tables.....	vii
Table of Figures.....	xi
Table of Schemes.....	xxxi
List of Accompanying Materials.....	xxxiii
Academic Thesis: Declaration Of Authorship.....	xxxv
Acknowledgements	xxxvii
Definitions and Abbreviations	xxxix
Chapter 1 Theoretical background	1
1.1 Nanotechnology	1
1.2 Lanthanide-doped upconversion nanoparticles	2
1.2.1 Upconversion processes.....	5
1.2.1.1 Excited state absorption (ESA)	5
1.2.1.2 Energy transfer upconversion (ETU).	5
1.2.1.3 Cross-relaxation (CR) upconversion	6
1.2.2 Upconversion composition	7
1.2.2.1 Activator and Sensitizer.....	7
1.2.2.2 Host matrix	9
1.2.3 Synthesis of upconversion nanoparticles.....	10
1.2.3.1 Co-precipitation.....	11
1.2.3.2 Thermal decomposition	12
1.2.3.3 Hydro(solvo)thermal synthesis	13
1.2.4 Surface modification on the upconversion nanoparticles	13
1.2.4.1 Ligand exchange	14
1.2.4.2 Ligand oxidation	15
1.2.4.3 Ligand free nanoparticles	16
1.2.4.4 Ligand attraction	17

Table of Contents

1.2.4.5	Layer-by-layer assembly	18
1.2.4.6	Creating a silica shell around nanoparticles	18
1.2.4.7	Bioconjugation	20
1.2.5	Strategies for enhancement of upconversion efficiency	21
1.2.5.1	Creating a core@shell structure	21
1.2.5.2	Plasmonic-enhanced upconversion luminescence	23
1.2.6	Applications	24
1.2.6.1	Thermal sensing	24
1.2.6.2	Bioimaging.....	26
1.2.6.3	Photodynamic therapy.....	27
1.2.6.4	UCNPs for drug delivery	28
1.2.6.5	Photocatalysis	30
Chapter 2	Experimental procedures	33
2.1	Synthesis of lanthanides doped upconversion nanoparticles	33
2.1.1	Synthesis of β -NaYF ₄	33
2.1.2	Synthesis of a shell of β -NaYF ₄	33
2.1.3	Synthesis of small β -NaYF ₄ doped with Gadolinium	34
2.1.4	Synthesis of large β -NaYF ₄ doped with Lutetium	35
2.1.5	Synthesis of Na _x ScF _{3+x}	35
2.2	Synthesis of other types of nanoparticles	36
2.2.1	Synthesis of AuNRs	36
2.2.2	Synthesis of high aspect ratio AuNRs	36
2.3	Surface modification on upconversion nanoparticles	37
2.3.1	Annealing treatment.....	37
2.3.2	Silica shell.....	37
2.3.3	Amine-functionalisation	38
2.3.4	Growth of Au shell	38
2.3.5	Carboxylic acid functionalization	39
2.3.6	Surface modification with oligonucleotides	39
2.3.6.1	Synthesis of oligonucleotides	39

Table of Contents

2.3.6.2	ssDNA-attachment	39
2.3.6.3	Incubation of with A549 cells	40
2.3.6.3.1	Preparation fixation and staining of cells on coverslips for confocal.....	40
2.3.7	Ligand free.....	40
2.3.8	Ligand-Exchange reaction from OA to OAm	40
2.3.9	Coating of TiO ₂	41
2.3.9.1	Ligand exchange from OA to CTAB.....	41
2.3.9.2	Synthesis of TiO ₂	41
2.3.9.3	Modification of TiO ₂ with Cobalt Oxide (CoOx) as co-catalyst	41
2.3.9.4	Indicator ink.....	42
2.4	Functionalization of upconversion nanoparticles with near-IR dyes.....	42
2.4.1	Chemical modification of a commercial IR-dye	42
2.4.2	Synthesis of the dye-sensitized β -UCNPs.....	42
2.5	Characterization Techniques.....	43
2.5.1	Transmission electron microscopy (TEM)	43
2.5.2	Fourier transforms Infrared (FT-IR)	43
2.5.3	X-ray diffraction (XRD).....	43
2.5.4	Jasco FT-IR 620 spectrometer	44
2.5.5	Ultraviolet/Visible spectrometer (UV-vis).....	44
2.5.6	Zeta-Potential.....	44
2.5.7	Confocal microscopy	44
2.5.8	EDX and elemental mapping	44
2.5.9	¹ H and ¹³ C NMR spectra	44
2.5.10	Mass spectra.....	45
2.6	Laser set-up	45
2.6.1	Set-up for photoluminescence characterization of β -UCNPs	45
2.6.2	Set-up used for UC emission of β -UCNPs incubated with A549 cells	47
2.6.3	Set-up used for spectrally-resolved measurements in dye-sensitized β -UCNPs.....	49
2.6.4	Set-up used for time-resolved and spectral measurements in dye-sensitized β -UCNPs.....	50

Table of Contents

2.7	Solar simulator	51
2.7.1	Solar simulator for β -UCNPs coated by TiO_2	51
Chapter 3	Results and discussion on the synthesis and characterization of upconversion nanoparticles.....	53
3.1	Synthesis of oleate coated β - NaYF_4 upconversion nanoparticles	53
3.1.1	Synthesis of β - NaYF_4 UCNPs with NH_4F as fluoride source	53
3.1.2	Influence of oleic acid ligands on the growth kinetics	60
3.1.3	Upconversion luminescence properties of nanoparticles β - NaYF_4 with different aspect ratio	63
3.2	Synthesis of oleate coated $\text{Na}_x\text{ScF}_{3+x}$. upconversion nanoparticles.....	70
3.2.1	Synthesis of the $\text{Na}_x\text{ScF}_{3+x}$ UCNPs with NH_4F as a fluoride source	71
3.2.2	Upconversion luminescence properties of $\text{Na}_x\text{ScF}_{3+x}$	74
3.2.3	Synthesis of $\text{Na}_x\text{ScF}_{3+x}$ UCNPs with NaF as a fluoride source.....	76
3.2.3.1	Effect of the NaF : Ln^{3+} molar ratio to the morphology of upconversion nanoparticles.....	76
3.2.3.2	Influence of reaction time upon the morphology of upconversion nanoparticles.....	79
3.2.3.3	Reaction temperature effect on the synthesis of upconversion nanoparticles.....	85
3.3	Fabrication of a shell around a core of upconversion nanoparticles.	89
3.3.1	Effect of Epitaxial shelling on UCNPs	89
3.3.2	Upconversion luminescence properties of UCNPs coated with an inorganic shell	94
Chapter 4	Results and discussion on inorganic functionalization of upconversion nanoparticles.....	96
4.1	Silica coating on upconversion nanoparticles	96
4.1.1	Synthesis of silica coated upconversion nanoparticles	97
4.1.1.1	Silica coating regulations	100
4.1.2	Control of the silica thickness on upconversion nanoparticles.	106

Table of Contents

4.1.3	Prevention of nanoparticle aggregation during silanization.....	109
4.1.4	Surface functionalization of Silica coating UCNPs	112
4.1.5	Quenching of the upconversion luminescence by water	113
4.1.6	Mechanism of silanization on UCNPs.....	116
4.2	Oligonucleotide functionalization of upconversion nanoparticles.....	118
4.2.1	Covalent construction of ssDNA-UCNPs structure.....	119
4.2.2	Incubation of upconversion nanoparticles with A549 cells.....	123
4.2.3	Preparation fixation and staining of cells on coverslips for microscope imaging	124
4.2.4	Confocal microscopy of upconversion nanoparticles with A549 cells.....	125
4.2.5	Luminescence of upconversion nanoparticles incubated with A549 cells	126
4.3	Functionalization of gold nanoparticle with upconversion nanoparticles	128
4.3.1	Au shell coated UCNPs	128
4.3.2	Synthesis of Gold nanorods.....	132
4.3.3	Synthesis of high aspect ratio gold nanorods	135
4.4	Photocatalysis of upconversion nanoparticles coated with a TiO ₂ shell	137
4.4.1	Synthesis and characterization of UCNPs coated with TiO ₂	138
4.4.2	Photodegradation of different dyes using UCNPs@TiO ₂	143
4.4.2.1	Dye stability in the presence of light irradiation.....	146
4.4.2.2	Dye adsorption/desorption equilibrium reactions	147
4.4.2.3	Photocatalytic degradation of DCPIP under full solar radiation, IR and UV radiation	149
4.4.2.4	Photocatalytic degradation of Resazurin under full, IR and UV radiation	155
4.4.2.5	Effect of β -UCNPs/TiO ₂ dosage on the photocatalytic activities	158
4.4.2.6	Recyclability of the samples	161
4.4.3	Effect of Cobalt as dopant on the photocatalytic activities of the samples ..	161
4.4.4	Effect of varying the annealing temperatures on the photocatalysts.....	164
Chapter 5	Result and discussion on Organic functionalization of upconversion nanoparticles	169

Table of Contents

5.1	Synthesis and characterization of Near Infrared IR-806 Dyes	170
5.2	Synthesis of core-only, core@inert shell and core@active shell	174
5.2.1	Surface modification of the OA coated UCNPs with BF_4^-	176
5.3	Synthesis of IR-806 dye-sensitized β -UCNPs	177
5.3.1	Optimization of the surface coverage of the β -UCNPs by IR-806 molecules	178
5.3.2	Estimation of dye molecules attached to the upconversion surface	181
5.4	Analysis of excitation dynamics in dye-sensitized upconversion core and core@active shell nanoparticles.....	185
5.4.1	Non-radiative energy transfer in dye-sensitized β -UCNPs	185
5.4.2	Upconversion luminescence enhancement	189
5.4.3	Excitation dynamics in non-sensitized and dye-sensitized β -UCNPs.....	191
5.4.3.1	Non-sensitized Core-Only and Core@Active Shell β -UCNPs.	191
5.4.3.2	Non-sensitized Core-Only and Dye-Sensitized Core-Only β -UCNPs ...	192
5.4.3.3	Non-sensitized Core@active shell and Dye-Sensitized Core@Active Shell β -UCNPs.	193
5.5	Downconversion luminescence properties	195
5.6	Alleviating concentration quenching through IR-1076 nm.	202
Chapter 6	Summary and outlook	208
6.1	Summary of Results	208
6.2	Outlook of future work	213
Appendix A	Schlenk line set-up	215
Appendix B	Equations for the surface area calculation in a hexagonal prism.	216
Appendix C	Lattice constant calculation.....	217
Appendix D	Propagation of uncertainties equations list	219
Appendix E	Error analysis in TEM measurements.....	220
Appendix F	Error analysis for calibration curve	221
Appendix G	Error analysis in photocatalysis	223
Appendix H	Calculation of errors in IR-806 dye molecules attached to UCNPs	224
Appendix I	Extra images of silica coating before and after annealing treatment	227
Bibliography	229

Table of Contents

Table of Tables

Table 1. Ground state electronic configurations and other properties of the lanthanide elements. Table created from Ref. ^{20,22}	3
Table 2. Phonon energy of the most common host materials for UCNPs. Adapted from Ref. ¹¹	9
Table 3. Summary of the most common upconversion synthetic strategies with some examples.	10
Table 4. Dimensions of the β -NaYF ₄ : Yb ³⁺ (20%), Er ³⁺ (2%) UCNPs obtained by using different amounts of OA in the reaction. Samples (1-4).....	55
Table 5. Crystallite sizes computed by the Debye-Scherrer equation, for samples (1-4).60	
Table 6. Summary of the V, SA _T , and S/V for each of the as-synthesised β -NaYF ₄ : Yb ³⁺ (20%), Er ³⁺ (2%) UCNPs.....	64
Table 7. Values of absorbances measured experimentally for β -NaYF ₄ : Yb ³⁺ (20%), Er ³⁺ (2%) UCNPs and calculated by equation (4). In all cases concentration was fixed to 1 mg/ml.....	66
Table 8. Summary of RGR, UC emission multicolour and crystallographic phases obtained for Na _x LnF _{3+x} (Ln =Sc ³⁺ , Y ³⁺) UCNPs synthesised under the same co-precipitation experimental route and same fluoride source (NH ₄ F) but different volume of OA.	75
Table 9. Dimensions of the Na _x ScF _{3+x} : Yb ³⁺ (20%), Er ³⁺ (2%) UCNPs synthesized at different molar ratio NaF: Ln ³⁺ . The measured sizes correspond to the nanobubes for the NaF: Ln ³⁺ = 1, to the nanorods for the NaF: Ln ³⁺ = 1.5, and to the nanospheres for the NaF: Ln ³⁺ = 2 and NaF: Ln ³⁺ = 2.5.....	77
Table 10. Huang and co-workers results ²¹⁴ (working at 300 °C and 1hour and 30 min) vs our results (when working at 308 °C and 1hour and 20 min).....	78

Table 11. Summary of dimensions of the $\text{Na}_x\text{ScF}_{3+x}$: Yb^{3+} (20%), Er^{3+} (2%) UCNPs synthesized at different reaction times of 1 hour, 1 hour and 20 min and 1 hour and 40 min and using molar ratios of NaF : $\text{Ln}^{3+} = 1$ and 1.5.....	82
Table 12. Dimensions of the $\text{Na}_x\text{ScF}_{3+x}$: Yb^{3+} (20%), Er^{3+} (2%) UCNPs synthesized at different temperatures of 288 °C, 298 °C, 303 °C, 308 °C and 318 °C. NaF : $\text{Ln}^{3+} = 1.5$	87
Table 13. SA_T and concentrations of $\beta\text{-NaYF}_4$: Yb^{3+} (20%), Er^{3+} (2%) UCNPs in samples (1-4).	101
Table 14. Comparison for the silica thickness with the decreasing SA_T of UCNPs.....	105
Table 15. Parameters for adjusting the thickness shell of the silica, using in all cases sample 12 as the core.	107
Table 16. Dimensions of the AuNRs obtained by using different AgNO_3 contents.....	134
Table 17. List of dyes used in our experiments, including name (IUPAC), max λ_{abs} and molecular structure of Methylene blue (MB), Rhodamine B (RB), Resazurin (Rz) and 2,6-dichlorophenolindophenol (DCPIP).....	146
Table 18. Kinetic parameters of photocatalytic degradation of DCPIP at varying the β -UCNPs/ TiO_2 concentration.	160
Table 19. Kinetic parameters of photocatalytic degradation of Rz at varying the β -UCNPs/ TiO_2 concentration.	160
Table 20. Experimentally obtained concentration of bound and unbound IR-dye to the surface of the core-only and core@active shell β -UCNPs, using in both cases 0.8 mg/ml: 3 μg /ml of β -UCNPs: IR-806.	183
Table 21. Summary of: calculated molecular weight, experimental and real concentration between β -UCNPs and dyes, weigh ratio and number of IR-dye antennas per single β -UCNP for the core-only and core@active shell β -UCNPs.	184
Table 22. Data of the XRD diffraction peaks of the Sample (1-4) made of NaYF_4 , with 0.2 s/degree scan rate and 0.02° step size from 10° to 80°.Values were obtained by fitting the peaks individually with a Lorentzian function.	217

Table of Tables

Table 23. Experimental values of d_{hkl} obtained for Samples (1-4) using the first three peaks from the XRD patterns.	217
Table 24. Experimental values of the lattice constants obtained for Samples (1-4)....	218
Table 25. Crystal lattice reported in the literature. Table adapted from Ref. ³⁸²	218

Table of Figures

- Figure 1.** Schematic representation of the excited state absorption process (ESA). G, E1 and E2 indicate ground state, first excited state and second excited state, respectively. 5
- Figure 2.** Schematic representation of the energy transfer upconversion (ETU) process. 6
- Figure 3.** Schematic representation of the cross-relaxation (CR) upconversion process. 6
- Figure 4.** Simplified energy level diagram for UCNPs co-doped with $\text{Yb}^{3+}/\text{Er}^{3+}$ and $\text{Yb}^{3+}/\text{Tm}^{3+}$. Reproduced from Ref.⁴⁵ The full, dotted, and curly arrows represent emission, energy transfer, and multiphonon relaxation processes, respectively. 8
- Figure 5.** A diagram of the subsequent ligand exchange of $\text{NOBF}_4/\text{UCNPs}$ with OA, OAm, tetradecylphosphonic acid (TDPA), hexylamine (HAM), or polyvinylpyrrolidone (PVP), respectively. Reproduced from Ref. ⁷²..... 15
- Figure 6.** Scheme showing the oxidation of OA on UCNP with Lemieux-von Rudloff reagent to produce carboxylic acid functionalized UCNPs. Reproduced from Ref. ⁷³ 16
- Figure 7.** A diagram showing the modification of hydrophobic UCNPs *via* the ligand attraction using (a) amphiphilic polymers with multiple hydrophobic chains and (b) surfactants with a single hydrophobic chain. Reproduced from Ref. ⁷⁶ 17
- Figure 8.** Schematic illustration of layer-by-layer assembly. Sequential deposition of oppositely charged PAH, PSS, and PAH to generate hydrophilic PAH–PSS–PAH-coated UCNPs with stable amino-rich shells. Reproduced from Ref. ⁸³ 18
- Figure 9.** Schematic illustration and TEM images of (a) $\text{UCNP}@d\text{SiO}_2$, (b) $\text{UCNP}@m\text{SiO}_2$, (c) $\text{UCNP}@d\text{SiO}_2@m\text{SiO}_2$, and (d) $\text{UCNP}@hm\text{SiO}_2$. Adapted from Ref. ^{91,95}20
- Figure 10.** (a) Illustration of the core@active-shell UCNPs showing the absorption of NIR light by the Yb^{3+} ions doped in the shell (represented in red) and

Table of Figures

subsequent energy transfer to the $\text{Er}^{3+}/\text{Yb}^{3+}$ co-doped in the core (represented in green), which leads to upconverted blue, green, and red emissions. (b) Digital photographs of colloidal solutions of $\text{NaGdF}_4:\text{Er}^{3+}/\text{Yb}^{3+}@\text{NaGdF}_4$ and $\text{NaGdF}_4:\text{Er}^{3+}/\text{Yb}^{3+}@\text{NaGdF}_4:\text{Yb}^{3+}$ UCNPs under excitation with 980 nm. Reproduced from Ref. ¹³⁸	22
Figure 11. (a) Intracellular temperature as a function of the applied voltage and (b) luminescence emission spectra under laser excitation at two different temperatures. Reproduced from Ref. ¹⁵¹	25
Figure 12. UCNPs-based multimode bioimaging. Adapted by Ref. ⁹⁷	27
Figure 13. Schematic representations of the UCNPs-based drug delivery systems: (a) mesoporous shells, (b) hollow spheres, and (c) PEG grafted amphiphilic polymer with hydrophobic pockets. Adapted from Ref. ¹⁷¹	29
Figure 14. Illustration of the energy transfer mechanism among $\text{Yb}^{3+}/\text{Tm}^{3+}$ and TiO_2 in a photocatalytic process and the generation of $\bullet\text{OH}$ radicals <i>via</i> the reaction of electron and hole with the surface species of TiO_2 . Reproduced by Ref. ¹⁸¹	31
Figure 15. Illustration of the (a) Au-UCNs–CdTe–ZnO system and (b) the mechanism of energy transfer. Reproduced by Ref. ²¹⁰	32
Figure 16. Laser setup for the analysis of UCNPs using a 980 nm laser.....	45
Figure 17. Schematic illustration for the transmission measurements.	46
Figure 18. Digital images of the set-up used for detection of UC emission in cells incubated with β -UCNPs@ SiO_2 -ssDNA.....	47
Figure 19. Schematic illustration of the microscopy setup used for fluorescence imaging using the UCNPs incubated with A549 cells.	48
Figure 20. Schematic illustration of the set-up used at the University of Southampton to characterize the β -UCNPs.....	49
Figure 21. Photograph of the set-up used at the University of Southampton for the characterization of the β -UCNPs to measure UC (green arrow) and DC (blue	

Table of Figures

arrow) luminescence using the incident light at an angle of 90° (red light).	50
Figure 22. Digital photography of the solar simulator. (a) shows the stirring plate where the sample was located on and followed by the radiation source tailored by a UV filter and (b) shows the light generator. 150 W Xe arc light.....	52
Figure 23. TEM images and size distribution of the different samples of β -NaYF ₄ : Yb ³⁺ (20%), Er ³⁺ (2%) UCNP obtained with (a) 6 ml (b) 12 ml (c) 17 ml and (d) 21 ml of OA. Scale bars are 50 nm. Black bars from the histograms indicate the size of core diameter meanwhile the red colour corresponds to the length. Samples (1-4).....	54
Figure 24. Illustration of TEM holder indicating in green line the ($\pm \alpha$) and ($\pm \beta$) tilting angles.	56
Figure 25. TEM images at different α tilting angles (a) 0°, (b) 20°, (c) 40° and (d) 60° of the synthesised β -NaYF ₄ : Yb ³⁺ (20%), Er ³⁺ (2%) UCNP using 17 ml of OA. Scale bars are 50 nm. Sample 3.....	56
Figure 26. TEM images at different α tilting angles (a) 0°, (b) 20°, (c) 40° and (d) 50° of the synthesised β -NaYF ₄ : Yb ³⁺ (20%), Er ³⁺ (2%) UCNP using 21 ml of OA. Scale bars are 50 nm. Sample 4.....	57
Figure 27. Graphic representation of the prism-shape β -NaYF ₄ : Yb ³⁺ (20%), Er ³⁺ (2%) UCNP from different perspectives. From right to left, the structures correspond to sample 1, 2, 3, and 4.....	57
Figure 28. FTIR spectrums of β -NaYF ₄ : Yb ³⁺ (20%), Er ³⁺ (2%) UCNP prepared with different OA concentrations. Samples (1-4).	58
Figure 29. XRD patterns of β -NaYF ₄ : Yb ³⁺ (20%), Er ³⁺ (2%) UCNP prepared with different OA concentrations. Samples (1-4). Measurements were acquired using a Cu K- α source (with $\lambda = 1.54059 \text{ \AA}$). β -NaYF ₄ (PDF card No.: 00-016-0334).	59
Figure 30. (a) Graphic representation of different families of plane for the β -NaYF ₄ with hexagonal prism shape. (b) Representation of the hexagonal unit cell (Na _{1.5} Y _{1.5} F ₆), showing the ions distribution and different set of planes.	

Green, yellow and light blue balls refer to Y^{3+} ions, Na^+ ions and F^- ions, respectively. Figure was created with the open-source software package VESTA. Crystal structures were drawn based on the structural data reported by Grzechnik et al.²⁴³ but adapted to our experimental lattices constant. $a=b=5.96 \text{ \AA}$, $c=3.51 \text{ \AA}$ and $\alpha=\beta=90^\circ$, $\gamma=120^\circ$. See **Appendix C** for the theoretical calculations of the lattice constant..... 60

Figure 31. Changes in the particle size for $\beta\text{-NaYF}_4\text{: Yb}^{3+}(20\%), \text{Er}^{3+}(2\%)$ UCNP (samples 1-4) synthesised with different concentrations of OA. The Y axis represents the size of the core diameter and the X-axis is the OA volume added for each synthesis. (The OA volume were measured with an uncertainty of $\pm 0.1 \text{ ml}$, and error bars are very small to be seen). 62

Figure 32. (a) UC emission spectra of $\beta\text{-NaYF}_4\text{: Yb}^{3+}(20\%), \text{Er}^{3+}(2\%)$ UCNP dispersed in hexane measured with a 980 nm CW laser excitation and 400 mW. (b) Energy transfer mechanism in $\text{NaYF}_4\text{: Yb}^{3+}(20\%), \text{Er}^{3+}(2\%)$ adapted by Ref. 252 63

Figure 33. (a) Integrated intensity in the range of 510-570 nm (green bars) and 640-680 nm (red bars) and (b) RGR of the as-prepared samples (1-4). 65

Figure 34. From left to right. Digital images for $\beta\text{-NaYF}_4\text{: Yb}^{3+}(20\%), \text{Er}^{3+}(2\%)$ UCNP from samples (1-4) dispersed in hexane, under excitation wavelength of 980 nm. 65

Figure 35. Emission spectra of $\beta\text{-NaYF}_4\text{: Yb}^{3+}(20\%), \text{Er}^{3+}(2\%)$ UCNP in hexane measured with a 980 nm CW laser before and after the rescaling in accordance with their relative absorbance. (a) corresponds to sample 1 and 2, and (b) corresponds to sample 3 and 4. The measurements were taken at 350 mW and 5 second of exposure time. The rescaling factors are printed aside the curves for sample 1 and 4 in black and green, respectively..... 67

Figure 36. Dependence of the integrated intensity in the range of 510 – 570 nm (green line) and 640- 680 nm (red line) on pump power for $\beta\text{-NaYF}_4\text{: Yb}^{3+}(20\%), \text{Er}^{3+}(2\%)$ UCNP from (a) sample 1, (b) sample 2, (c) sample 3, and (d) sample 4. The excitation wavelength was fixed to 980 nm, and the PL spectra was

recorded using different pump powers from 100 mW to 400 mW in steps of 25 mW. The acquisition time was fixed to 5 s.	68
Figure 37. TEM images and size distribution of the different samples of $\text{Na}_x\text{ScF}_{3+x}$: Yb^{3+} (20%), Er^{3+} (2%) UCNPs obtained using (a) 6 ml (b) 12 ml (c) 17 ml and (d) 21 ml of OA. Scale bars are 50 nm. Samples (5-8).....	72
Figure 38. XRD patterns of $\text{Na}_x\text{ScF}_{3+x}$: Yb^{3+} (20%), Er^{3+} (2%) UCNPs prepared with different OA concentrations. Samples (5-8). Measurements were acquired using a Cu K- α source. Black and red reference lines correspond to the hexagonal NaScF_4 (PDF card No.: 00-020-1152) and monoclinic Na_3ScF_4 phase (PDF card No.: 00-020-1153), respectively.....	73
Figure 39. (a) Emission spectra and (b) RGR for $\text{Na}_x\text{ScF}_{3+x}$: Yb^{3+} (20%), Er^{3+} (2%) UCNPs synthesised with different concentrations of OA under 980 nm excitation wavelength. Samples (5-8).....	74
Figure 40. From left to right. Digital images for $\text{Na}_x\text{ScF}_{3+x}$: Yb^{3+} (20%), Er^{3+} (2%) UCNPs from samples (5-8), under excitation wavelength of 980 nm.	74
Figure 41. TEM images and size distribution of the $\text{Na}_x\text{ScF}_{3+x}$: Yb^{3+} (20%), Er^{3+} (2%) UCNPs synthesized at different NaF: Ln^{3+} ratio of (a) 1.0, (b) 1.5, (c) 2.0 and (d) 2.5. Scale bars are 200 nm. Black bars from the histograms indicate the diameter and the red colour corresponds to the length of the rods. ..	76
Figure 42. TEM images of the $\text{Na}_x\text{ScF}_{3+x}$: Yb^{3+} (20%), Er^{3+} (2%) UCNPs synthesized at different reaction times of (a) 1 hour, (b) 1 hour and 20 min and (c) 1 hour and 40 min. NaF: Ln^{3+} = 1.5 molar ratio. Scale bars are 200 nm. Black bars from the histograms indicate the diameter size meanwhile the red colour corresponds to the length of the rods.	80
Figure 43. TEM images of the $\text{Na}_x\text{ScF}_{3+x}$: Yb^{3+} (20%), Er^{3+} (2%) UCNPs synthesized at different reaction times of (a) 1 hour, (b) 1 hour and 20 min and (c) 1 hour and 40 min. NaF: Ln^{3+} = 1 molar ratio. Scale bars are 200 nm. Black bars from the histograms indicate the size in edge length.....	81

- Figure 44.** XRD patterns of the $\text{Na}_x\text{ScF}_{3+x}$: Yb^{3+} (20%), Er^{3+} (2%) UCNPs synthesized at different reaction time of 1 hour, 1 hour and 20 min and 1 hour and 40 min. NaF: Ln^{3+} =1.5 molar ratio. Measurements were acquired using a Cu K- α source. Black and red reference lines correspond to the hexagonal NaScF_4 (PDF card No.: 00-020-1152) and monoclinic Na_3ScF_4 phase (PDF card No.: 00-020-1153), respectively. 83
- Figure 45.** XRD pattern of the $\text{Na}_x\text{ScF}_{3+x}$: Yb^{3+} (20%), Er^{3+} (2%) UCNPs synthesized for 1 hour and 40 min at NaF: Ln^{3+} =1. Measurements were acquired using a Cu K- α source. Black reference line is the hexagonal NaScF_4 phase (PDF card No.: 00-020-1152). 84
- Figure 46.** Illustration of the growth process of $\text{Na}_x\text{ScF}_{3+x}$: Yb^{3+} (20%), Er^{3+} (2%) UCNPs *via* Ostwald ripening mechanism. NaF: Ln^{3+} =1.5 molar ratio (top) and NaF: Ln^{3+} =1molar ratio (bottom)..... 85
- Figure 47.** TEM images of the $\text{Na}_x\text{ScF}_{3+x}$: Yb^{3+} (20%), Er^{3+} (2%) UCNPs synthesized at different temperatures of (a) 288 °C, (b) 298 °C, (c) 303 °C, (d) 308 °C and (e) 318 °C. NaF: Ln^{3+} = 1.5. Scale bar are 200 nm. Black bars from the histograms indicate the diameter size meanwhile the red colour corresponds to the length of the rods. 86
- Figure 48.** XRD patterns of the $\text{Na}_x\text{ScF}_{3+x}$: Yb^{3+} (20%), Er^{3+} (2%) UCNPs synthesized at different temperatures of 288 °C, 298 °C, 308 °C and 318 °C. NaF: Ln^{3+} = 1.5. Reaction time reaction was adjusted to 1 hour and 40 min. Black and red reference lines correspond to the hexagonal NaScF_4 (PDF card No.: 00-020-1152) and monoclinic Na_3ScF_4 phase (PDF card No.: 00-020-1153), respectively..... 88
- Figure 49.** Cartoon showing the geometry of the different core@shell nanostructures. The measurements that were carried out are represented by coloured arrows. 90
- Figure 50.** TEM images of the core (a) $\beta\text{-NaYF}_4$ and core@shell (b) $\beta\text{-NaYF}_4\text{@NaYF}_4$ (c) $\beta\text{-NaYF}_4\text{@NaGdF}_4$, and (d) $\beta\text{-NaYF}_4\text{@NaLuF}_4$. Scale bars are 50 nm. Black and red bars at the histograms indicate the diameter and the length of the

UCNPs, respectively. Additionally, the green bars refer to the end diameters of β -NaYF ₄ @NaGdF ₄ structures.	91
Figure 51. Schematic illustration of core@shells obtained through the same core. It reflects how the shape of β -UCNPs changes during compressive or tensile strains.	92
Figure 52. (a) XRD patterns of core (β -NaYF ₄) and core@shell (β -NaYF ₄ @NaYF ₄ , β -NaYF ₄ @NaGdF ₄ , and β -NaYF ₄ @NaLuF ₄). Measurements were acquired using a Cu K- α source. (b) Zoom into the (201) diffraction peak area. Black reference line in figure a corresponds to the β -NaYF ₄ (PDF card No: 00-016-0334). Black triangle, black star and empty circle in figure b are the references of the β -NaLuF ₄ , (PDF card No: 00-027-0726), β -NaGdF ₄ (PDF card No: 00-027-0699) and β -NaYF ₄ (PDF card No: 00-016-0334), respectively.	93
Figure 53. UC emission intensity of core (β -NaYF ₄) and core@shell (β -NaYF ₄ @NaYF ₄ , β -NaYF ₄ @NaGdF ₄ , and β -NaYF ₄ @NaLuF ₄) excited by a 980 nm CW laser. 300 mW and 500 ms integration time.	94
Figure 54. TEM image and size distribution of β -NaYF ₄ : Yb ³⁺ (20%), Er ³⁺ (2%) UCNPs. Scale bar is 50 nm.	97
Figure 55. TEM image of silica coated β -NaYF ₄ : Yb ³⁺ (20%), Er ³⁺ (2%) UCNPs (β -UCNPs@SiO ₂) using in the synthesis (a) 2 mg/ml, (b) 6 mg/ml, (c) 10 mg/ml and (d) 13 mg/ml of β -UCNPs. Scale bars are 50 nm.	98
Figure 56. FTIR spectra of β -NaYF ₄ : Yb ³⁺ (20%), Er ³⁺ (2%) UCNPs (black line) and β -NaYF ₄ : Yb ³⁺ (20%), Er ³⁺ (2%) UCNPs coated by SiO ₂ (red line).	99
Figure 57. TEM images and size distribution of β -UCNPs@SiO ₂ using as a core β -NaYF ₄ : Yb ³⁺ (20%), Er ³⁺ (2%) UCNPs from (a) sample 1, (b) sample 2, (c) sample 3 and (d) sample 4. Scale bars are 50 nm and black bars at the histograms indicate the diameter of the β -UCNPs@SiO ₂ structures.	102

Figure 58. General calibration curve to estimate the amount of UCNPs core material to be used for silanization regardless of the morphology of the initial particles and only in accordance to its SA_T	103
Figure 59. TEM images and size distribution of (a) β -NaYF ₄ : Yb ³⁺ (20%), Er ³⁺ (2%) UCNPs and (b) β -NaY(28%)/Lu(50%)F ₄ : Yb ³⁺ (20%), Er ³⁺ (2%) UCNPs. Scale bars are 50 nm. Black bars at the histograms indicate the diameter and the red colour corresponds to the length of β -UCNPs.....	104
Figure 60. TEM images and size distribution of β -UCNPs coated with silica using as a core β -NaYF ₄ : Yb ³⁺ (20%), Er ³⁺ (2%) UCNPs from (a) sample 10 and (b) sample 11. Scale bars are 50 nm and black bars at the histogram indicate the diameter of the resulting β -UCNPs@SiO ₂ structures.....	105
Figure 61. TEM image of the initial β -NaYF ₄ : Yb ³⁺ (20%), Er ³⁺ (2%) UCNPs with a size distribution of 33 nm \pm 2 nm.	106
Figure 62. TEM image and size distribution of the β -NaYF ₄ : Yb ³⁺ (20%), Er ³⁺ (2%) UCNPs@SiO ₂ for (a) sample 12.1s, (b) sample 12.2s and (c) sample 12.3s according to the experimental parameters from Table 15 . Scale bars are 50 nm.....	108
Figure 63. From left to right. Digital images of β -NaYF ₄ :Yb ³⁺ (20%), Er ³⁺ (2%) UCNPs dispersed in hexane under ambient light and under a 980 nm laser pointer before and after annealing at 240 °C for 1.5 hour.....	110
Figure 64. (a) Emission intensities of β -NaYF ₄ : Yb ³⁺ (20%), Er ³⁺ (2%) UCNPs before (black line) and after the annealing (red line) measured by a 980 nm CW laser (365 mW. 500 ms), and (b) UV spectra of the β -NaYF ₄ : Yb ³⁺ (20%), Er ³⁺ (2%) UCNPs before (black line) and after annealing (blue line).	111
Figure 65. TEM images of β -UCNPs@SiO ₂ (a) before and (b) after annealing at 240 °C for 1.5 hour. Scales bars are 50 nm.....	112
Figure 66. Z-potential measurements of the β -UCNPs@SiO ₂ (sample 12.1s) and β -UCNPs@SiO ₂ -NH ₂ (sample 12.1sAm) in Milli-Q water.	113
Figure 67. (a) Comparison between emission intensities for β -UCNPs@SiO ₂ -NH ₂ dispersed in Milli-Q water and OA-coated β -UCNPs in hexane. (b) Zoom to the	

Table of Figures

emission intensity of β -UCNPs@SiO ₂ -NH ₂ dispersed in Milli-Q water. All measurements were taken after laser irradiation at 980 nm CW laser and 465 mW.	114
Figure 68. Energy level diagrams of NaYF ₄ :Yb ³⁺ , Er ³⁺ UCNPs. Solid, dotted and wavy arrows indicate photon absorption or emission, energy transfer and relaxation processes, respectively. The blue wavy arrows represent the increased multiphonon relaxations caused by OH- vibrations. Picture adapted from Arppe et al. ²⁹⁷	115
Figure 69. (a) Emission intensities and (b) RGR of OA free β -NaYF ₄ : Yb ³⁺ (20%), Er ³⁺ (2%) UCNPs dispersed in Milli-Q water and OA-coated β -NaYF ₄ : Yb ³⁺ (20%), Er ³⁺ (2%) UCNPs in hexane under a 980 nm CW laser at 480 mW.	116
Figure 70. Proposed mechanism illustrating the synthetic route to produce hydrophilic β -UCNPs@SiO ₂	118
Figure 71. Schematic illustration of the synthetic route to produce β -UCNPs@SiO ₂ functionalized with -COOH group. (a) Amine functionalized UCNPs denoted as β -UCNPs@SiO ₂ -NH ₂ , reacted with (b) succinic anhydride, in dimethylformamide (DMF) at room temperature and overnight to produce (c) NPs denoted as β -UCNPs@SiO ₂ -COOH. Pink and green colour spheres are referred to the core and silane layer on the surface of the β -UCNPs.	119
Figure 72. ζ -potential measurements of the β -UCNPs@SiO ₂ , β -UCNPs@SiO ₂ -NH ₂ and β -UCNPs@SiO ₂ -COOH in Milli-Q water.	120
Figure 73. Schematic illustration of EDC/s-NHS coupling reaction between β -UCNPs@SiO ₂ -COOH and amine group containing oligonucleotide. For simplicity β -UCNPs@SiO ₂ -COOH cartoon only shows the terminal -COOH group.	122
Figure 74. FTIR from sample before and after the oligonucleotides attached. Black line corresponds to the original OA coated β -NaYF ₄ : Yb ³⁺ , Er ³⁺ UCNPs, red line shows the β -NaYF ₄ : Yb ³⁺ , Er ³⁺ @SiO ₂ and blue line indicates the β -NaYF ₄ : Yb ³⁺ , Er ³⁺ @SiO ₂ -ssDNA.	123

Table of Figures

Figure 75. Illustration showing the incubation procedure and a representation of the β -UCNPs@SiO ₂ -ssDNA nanocomposite with the A549 cell during the incubation process.....	124
Figure 76. Preparation fixation and staining of cells on coverslips for confocal.	125
Figure 77. Confocal laser microscopy images of A549 cells (a) without treatment and (b) after the incubation with the β -UCNPs@SiO ₂ -ssDNA nanocomposite for 24 hours. 405 nm excitation for DAPI. Scale bars are 40.04 μ m.....	126
Figure 78. Luminescence images of cells incubated with β -UCNPs@SiO ₂ -ssDNA (a) using the DAPI excitation at 405 nm and (b) under 980 nm excitation.	127
Figure 79. Luminescence image of the cell nuclei using the control sample, under the DAPI excitation wavelength of 405 nm. No observed image was obtained with the 980 nm excitation wavelength.....	127
Figure 80. Schematic illustration of the synthetic route to produce β -UCNPs@SiO ₂ @Au shell dispersible in water.	128
Figure 81. UV-vis spectra and corresponding digital image of THPC coated Au seeds. Black line from the spectra represents the smallest seeds (yellow solution), red line corresponds to the medium size (orange solution) and blue line to the largest seeds (brown solution).	130
Figure 82. UV-Vis spectra and corresponding digital image of β -UCNPs@SiO ₂ @Au shell nanostructures. Black line represents the thinner shell (blue-grey solution), red line the middle thickness (purple solution) and blue line represent the thickest shell (red solution).	131
Figure 83. TEM figure of (a) Au seeds, (b) β -UCNPs@SiO ₂ @Au seeds and (c) β -UCNP@SiO ₂ @Au shell. Scales bars are 50 nm.	131
Figure 84. Schematic illustration for the formation process of AuNRs.....	132
Figure 85. TEM of AuNRs synthesised with (a) 120 μ l, (b) 300 μ l, (c) 400 μ l, and (d) 500 μ l of AgNO ₃ . Scales bars are 50 nm.	133

Table of Figures

Figure 86. UV-Vis spectra and optical photography of AuNRs synthesised with 120 μl , 300 μl , 400 μl and 500 μl of AgNO_3	135
Figure 87. Schematic illustration for the formation process of high AR of AuNRs.	136
Figure 88. TEM images of long AuNRs. Scales bars are 500 nm.	136
Figure 89. UV-Vis spectra of long AuNRs containing a large number of spheres and triangles.	137
Figure 90. TEM images of the $\beta\text{-NaYF}_4\text{: Yb}^{3+}(20\%), \text{Tm}^{3+}(0.5\%)$ UCNP with a size distribution of $39 \text{ nm} \pm 2 \text{ nm}$. Scale bar is 50 nm.	138
Figure 91. Schematic representation of $\beta\text{-NaYF}_4\text{: Yb}^{3+}(20\%), \text{Tm}^{3+}(0.5\%)$ UCNP coated with TiO_2 . Red and green arrows indicate OA and CTAB respectively and A- TiO_2 means amorphous TiO_2	138
Figure 92. Two representative TEM images of β -UCNPs coated with TiO_2 before annealing. Scales bar are 50 nm.	139
Figure 93. XRD patterns of β -UCNPs before and after the epitaxial growth of TiO_2 shell. Measurements were acquired using a Cu K- α source. Reference lines in yellow and purple correspond to β -UCNPs (PDF Card No.:00-016-0334) and TiO_2 anatase (PDF Card No.:00-002-0387), respectively.	140
Figure 94. EDX of $\beta\text{-NaYF}_4\text{: Yb}^{3+}(20\%), \text{Tm}^{3+}(0.5\%)$ UCNP coated with TiO_2 on a carbon-film coated copper grid. The peaks labelled Na, Y, F, Yb and Tm originate from the core, while that of Ti and O come from the shell. The elements C and Cu are from the carbon-film coated copper grid used in the EDX characterizations.....	141
Figure 95. Elemental mapping of $\beta\text{-NaYF}_4\text{: Yb}^{3+}(20\%), \text{Tm}^{3+}(0.5\%)$ UCNP coated with TiO_2	141
Figure 96. UV-vis absorbance of β -UCNPs with and without titania coating. Black line from the spectra represents the β -UCNPs before any coating, and red line represents the spectra of the particles coated with titania (β -UCNPs/ TiO_2 -anatase).....	142

Figure 97. Emission spectra of β -UCNPs before and after coating the TiO_2 . Black line from the spectra represents the β -UCNPs before coating, and red line represents the spectra of the β -UCNPs after titania coating (980 nm laser excitation, 350 mW and 500 ms).....	142
Figure 98. Schematic illustration of the working mechanism for the hybrid β -UCNPs/ TiO_2 . The β -UCNPs nuclei (in pink) absorbs the 980 nm light (red wiggled arrows) where UC is realized. Subsequently the β -UCNPs transfer the energy to the outer layer of the TiO_2 . The blue arrow represents the visible energy emitted by the β -UCNPs.	144
Figure 99. (a) Comparison of the absorbance spectra and (b) changes in the concentration (C/C_0) as a function of the time of different dyes. Samples were irradiated with the full spectrum source of a Xenon lamp (300-2500 nm).	147
Figure 100. (a) Degradation of four different dyes in the presence of same initial concentration of β -UCNPs/ TiO_2 under dark conditions. (b) Digital photograph of glass tubes after treatment with β -UCNPs/ TiO_2 . From left to right glass tube of β -UCNPs/ TiO_2 with MB, RB, Rz and DCPIP.	148
Figure 101. Schematic illustration of the mechanism by which a typical photocatalyst indicator ink works.	150
Figure 102. The structures of the sodium salt of DCPIP (left) and its reduced product, Leuco-DCPIP.....	150
Figure 103. (a) Effect of glycerol on the photocatalytic activity of the β -UCNPs/ TiO_2 using DCPIP under unfiltered Xenon lamp radiation. (b) and (c) are the absorbance spectra of the DCPIP with and without glycerol, respectively as a function of the irradiation time.	151
Figure 104. Proposed photocatalytic degradation pathways of DCPIP dye under the UV irradiation with no glycerol. (a) dechlorination and (b) intermediate. Image taken from H.A. Hamad's work. ³⁴³	152

Table of Figures

Figure 105. Comparison of samples under different irradiation bands using DCPIP/glycerol and β -UCNPs/ TiO_2 as catalysts. (a) Full spectra of a Xenon lamp, (b) UV and (c) NIR.	154
Figure 106. Photo-reduction of resazurin (Rz) to resorufin (Rf) by TiO_2	155
Figure 107. (a) Effect of glycerol on the photocatalytic activity of the β -UCNPs/ TiO_2 using Rz under unfiltered Xenon lamp radiation. (b) and (c) are the absorbance spectra of the Rz with and without glycerol, respectively as a function of the irradiation time.	156
Figure 108. Comparison of samples under different irradiation bands using Rz/glycerol and β -UCNPs/ TiO_2 as catalysts. (a) Full spectra of a Xenon lamp, (b) UV and (c) NIR.	157
Figure 109. Effect of the β -UCNPs/ TiO_2 dosage on the (a) Rz and (b) DCPIP photodegradation tested under full spectrum of a Xenon lamp.	159
Figure 110. Comparison of photocatalytic activity for different β -UCNPs/ TiO_2 dosage treated with (a) Rz and (b) DCPIP after 10 min of photoirradiation with full spectrum of a Xenon lamp.	159
Figure 111. Recyclability of β -UCNPs/ TiO_2 with (a) DCPIP/glycerol and (b) Rz/glycerol under full radiation. Using an initial concentration of 1 mg/ml of material.	161
Figure 112. Schematic illustration of the process to obtain β -UCNPs/ TiO_2 nanohybrid load of cobalt species by an impregnation method.	162
Figure 113. Photocatalytic degradation of (a) DCPIP and (b) Rz in the presence of TiO_2 co-doped with cobalt under full irradiation of a Xenon lamp.	163
Figure 114. Photocatalytic degradation of DCPIP in the presence of β -UCNPs/ TiO_2 co-doped with different loadings of cobalt using the full spectra irradiation of a Xenon lamp.	163
Figure 115. XRD patterns of β -UCNPs and β -UCNPs/ TiO_2 annealed at 500 °C, 700 °C, 900 °C and 1000 °C. Measurements were acquired using a Cu K- α source. Yellow, purple, and pink reference lines from the top correspond to β -UCNPs (PDF	

Table of Figures

Card No.:00-016-0334), TiO ₂ anatase and Y ₂ Ti ₂ O ₇ (PDF Card No.:00-027-0982), respectively.....	164
Figure 116. XRD patterns of non-annealed β -UCNPs and β -UCNPs annealed at 500 °C, 700 °C, and 900 °C. Measurements were acquired using a Cu K- α . Reference cards are indicated with a yellow-ochre line for β -UCNPs (PDF Card No.:00-016-0334), orange line for cubic YOF (PDF Card No.: 01-071-2100), and green line for trigonal Y ₂ O ₃ (PDF Card No.: 00-043-0661).	165
Figure 117. Emission spectra of β -UCNPs (a) before coating the TiO ₂ and (b) after TiO ₂ coating and annealing at different temperatures.	166
Figure 118. (a) UV-Vis spectra and (b) photodegradation of Rz using β -UCNPs/TiO ₂ annealed at different temperatures under full irradiation of a Xenon lamp.....	167
Figure 119. Schematic illustration of the dye-sensitized β -UCNPs energy transfer: antenna dyes (in green) absorb the NIR light (red wiggled arrows) and transfer it to the β -UCNP core (in pink) where the UC process is realized. The blue arrow represents the visible energy emitted by the β -UCNPs.	169
Figure 120. Synthesis of the organic dye IR-806 using the commercial dye IR-780. 4-mercaptobenzoic acid was used as the nucleophile and DMF as solvent.	171
Figure 121. Red and black lines indicate the absorption spectra of IR-806 (2 μ g/ml) and IR-780 (2.5 μ g/ml), respectively. For the measurements, organic dyes were dissolved in CHCl ₃	171
Figure 122. Normalized absorption of β -NaYF ₄ : Yb ³⁺ (20%), Er ³⁺ (2%) (black line) and emission of spectra of IR-806 dye (blue line) in CHCl ₃	172
Figure 123. HRMS spectrum of IR-806. The analysis was done to a sample containing 50 μ g/ml of the dye dissolved in anhydrous methanol.....	173
Figure 124. ¹ H NMR (400 MHz, CDCl ₃) spectrum of IR-806. (20 mg/ml). Diethyl ether D(CH ₃) at 3.472 ppm/ D(CH ₂) at 1.206/ J(CH ₃ -CH ₂) = 7.00.	173
Figure 125. ¹³ C NMR (101 MHz, CDCl ₃) spectrum of IR-806 dye. (20 mg/ml).....	174

Figure 126. TEM images and size distributions of (a) core-only, (b) core used to create (c) core@active shell and (d) core to grow the (e) core@inert shell. Scale bars are 50 nm.	175
Figure 127. Ligand exchange strategy using nitrosonium tetrafluoroborate (NOBF_4) to replace OA ligands attached to the β -UCNPs surface. The red and blue arrow represent the OA and OAm ligand attached to the surface of β -UCNPs.....	176
Figure 128. (a) UC emission intensities of IR-806 – sensitized core@active shell β -UCNPs in function of different excitation wavelengths and (b) UC excitation spectra integrated in the 500-680 nm range for the IR-806 – sensitized core@active shell β -UCNPs (black line) and no sensitized core@active shell β -UCNPs (blue line), dissolved in CHCl_3 . The spectra were recorded using a 2 mW laser excitation.	177
Figure 129. Normalized emission intensities integrated in the range 500-685 nm for IR-806–sensitized core-only β -UCNPs as a function of IR-806 content in CHCl_3 . Measured by a 2 mW, 800 nm laser excitation.	178
Figure 130. Normalized emission intensities integrated in the range 500-685 nm for IR-806–sensitized core@active shell β -UCNPs as a function of IR-806 content in CHCl_3 . Measured by a 2 mW, 800 nm laser excitation.	179
Figure 131. Normalized emission intensities integrated in the range 500-685 nm for IR-806–sensitized core@inert shell β -UCNPs as a function of IR-806 content in CHCl_3 . Measured by a 2 mW, 800 nm laser excitation.	179
Figure 132. Comparison of the UC emission intensities of the non-sensitized (black line) and IR-806-sensitized (red line) (a) core-only, (b) core@active shell and (c) core@inert shell β -UCNPs in CHCl_3 . IR-sensitized β -UCNPs and non-sensitized β -UCNPs were excited under 800 nm and 980 nm laser, respectively. All the measurements were recorded using a 2 mW laser excitation.....	180
Figure 133. Illustration showing the basic principle of dye-sensitized UC applied to the cases of (a) core-only, (b) core@active shell and (c) core@inert shell structures.	

Excitation at 800 nm results in efficient absorption by the dye molecules and subsequent energy transfer to the Ln^{3+} ions in the core and in the active shell of the β -UCNPs. Core@inert shell results in an inefficient energy transfer from the dye molecules to the Ln^{3+} ions of the β -UCNPs. 181

Figure 134. (a) UV-vis spectra of IR-806 at different concentrations. (b) Calibration curve, with the maxima absorption observed at 806 nm against the IR dye concentration..... 182

Figure 135. Digital images of IR-806 dye sensitized β -UCNPs dispersed in CHCl_3 under ambient light and under a 980 nm laser pointer (a) before and (b) after particles removal. 182

Figure 136. (a) UC spectra of dye-sensitized core@active β -UCNPs as a function of the excitation power at 800 nm. (b) Power dependence of UC luminescence intensity of dye-sensitized core@active shell β -UCNPs, spectrally integrated in the range of 510–690 nm pumped at 800 nm..... 186

Figure 137. Fluorescence decay curves of the pure IR-806 dye molecules (black solid curve), the molecules bound to the core-only β -UCNPs (red solid curve), and the molecules bound to the core@active shell β -UCNPs (blue solid curve). Excitation wavelength was 800 nm and the laser repetition rate was 20 MHz. The non-radiative energy transfer from the IR-806 dye to the β -UCNPs is evidenced by the acceleration of the fluorescence decay from 1.29 to 0.49 ns. 187

Figure 138. The fluorescence decay curves of the dye IR-806 molecules (black solid curves) attached to the surface of β -UCNPs pumped at 800 nm ($1\ \mu\text{W}$, 20 MHz) for (a) core-only and (b) core@active shell structure. Red solid curves are the results of bi-exponential fitting of the decay curves..... 187

Figure 139. Comparison of the UC luminescence intensities of the non-sensitized and dye-sensitized β -UCNPs pumped with 50 μW at 980 nm and 800 nm. 189

Figure 140. Reproducibility of UC luminescence signal (at 800 nm photoexcitation) to demonstrate short-term photostability of dye-sensitized β -UCNPs. Black

solid curve shows PL of β -UCNPs when excitation power (here 50 μ W) was increased step by step from low value (8 μ W) to higher (75 μ W). Red curve shows PL of β -UCNPs when excitation power was decreased from 75 μ W to 50 μ W. Blue dashed curve shows results of repeated one more time PL measurement at 50 μ W excitation. 190

Figure 141. The UC kinetics of non-sensitized and dye-sensitized β -UCNPs pumped with 50 μ W at 980 nm and 800 nm, respectively for (a) core-only and (b) core@active shell β -UCNPs. The UC luminescence rise dynamics between non-sensitized (red curves) and dye-sensitized (black curves) β -UCNPs differ substantially. The rise dynamics of the UC luminescence of dye-sensitized β -UCNPs is characterised by two-components: the fast component (AB) is driven by direct radiative pumping of Er^{3+} ions from the dyes, while the slow component (BC) is due to non-radiative energy transfer from the dyes predominantly to Yb^{3+} ions, followed by non-radiative energy transfer from Yb^{3+} to Er^{3+} ions. 191

Figure 142. UC kinetics of non-sensitized core-only (black solid curve) and core@active shell (red solid curve) β -UCNPs pumped at 980 nm with frequency of 295 Hz, duty cycle 5%. 192

Figure 143. UC kinetics of dye-sensitized core@active shell (black solid curve) and dye-sensitized core-only (red solid curve) β -UCNPs pumped at 800 nm with frequency of 295 Hz, duty cycle 5%. 194

Figure 144. Principle of dye-sensitized UC for core@active shell β -UCNPs. Black arrows indicate possible radiative and non-radiative channels of the energy transfer in dye-sensitized β -UCNPs. Adapted from Ref. ²⁷⁵ 194

Figure 145. Energy level diagram of Er^{3+} showing the excitation (808 nm) and the downshifted emission (1550 nm) levels. Picture adapted by Ref. ³⁸¹ 195

Figure 146. (a) DC emission spectra of IR-806 – sensitized core-only in function of IR-806 dye and (b) normalized DC emission intensities integrated in the range 1450-1650 nm of β - $\text{NaYF}_4\text{:Yb}^{3+}(20\%), \text{Er}^{3+}(2\%)$ (0.8 mg/ml) as a function of

IR-806 content in CHCl_3 excited by 50 mW 800 nm laser and 10 seconds of exposure time.....	196
Figure 147. (a) DC emission spectra of IR-806 – sensitized core@active shell in function of IR-806 dye and (b) normalized DC emission intensities integrated in the range 1450-1650 nm of $\beta\text{-NaYF}_4\text{:Yb}^{3+}(20\%), \text{Er}^{3+}(2\%)@ \text{NaYF}_4\text{:Yb}^{3+}(10\%)$ (0.8 mg/ml) as a function of IR-806 content in CHCl_3 excited by 50 mW 800 nm laser and 10 seconds of exposure time.....	197
Figure 148. (a) DC emission intensities of IR-806-sensitized core-only $\beta\text{-UCNPs}$ in CHCl_3 (0.003 mg/ml: 0.8 mg/ml) under 800nm laser excitation (red line) and emission of the same particles with no dye under 980 nm laser excitation (black line). (b) Integrated intensity in the range of 1450-1650 nm of the DC emission for the core-only $\beta\text{-UCNPs}$ (0.003 mg/ml: 0.8 mg/ml) dissolved in CHCl_3 at different excitation wavelengths. All measurements were taken under a 57 mW laser excitation, and 10 seconds of exposure time. .	198
Figure 149. Power dependence of DC luminescence intensity of IR-806–sensitized core-only $\beta\text{-UCNPs}$, spectrally integrated in the range of 1450–1650 nm pumped at 800 nm (red line) and non-sensitized core-only excited at 980 nm (black line).....	199
Figure 150. (a) DC emission intensities of IR-806-sensitized core@active shell $\beta\text{-UCNPs}$ in CHCl_3 (0.003 mg/ml: 0.8 mg/ml) under 800 nm laser excitation (red line) and DC emission of the same particles with no dye under 980 nm laser excitation (black line). (b) Integrated intensity in the range of 1450-1650 nm of the DC emission for the core@active shell $\beta\text{-UCNPs}$ (0.003 mg/ml: 0.8 mg/ml) dissolved in CHCl_3 at different excitation wavelengths. All measurements were taken under a 50 mW laser excitation.....	199
Figure 151. Power dependence of DC luminescence intensity of IR-806–sensitized core@active shell $\beta\text{-UCNPs}$, spectrally integrated in the range of 1450–1650 nm pumped at 800 nm (red line) and non-sensitized core@active shell excited at 980 nm (black line).	200

- Figure 152.** (a) DC emission intensities of IR-806-sensitized core@inert shell β -UCNPs in CHCl_3 (0.003 mg/ml: 0.8 mg/ml) under 800 nm laser excitation (red line) and DC emission of the same particles with no dye under 980 nm laser excitation (black line). (b) Integrated intensity in the range of 1450-1650 nm of the DC emission for the core@inert shell β -UCNPs (0.003 mg/ml: 0.8 mg/ml) dissolved in CHCl_3 at different excitation wavelengths. All measurements were taken under a 50 mW laser excitation. 201
- Figure 153.** Power dependence of DC luminescence intensity of β - $\text{NaYF}_4\text{:Yb}^{3+}$ (20%), Er^{3+} (2%) @ NaYF_4 spectrally integrated in the range of 1450 – 1650 nm pumped at 980 nm..... 201
- Figure 154.** DC emission spectra of the different types of β -UCNPs. Measured by a 50 mW, 980 nm and 800 nm laser excitation (10 s)..... 202
- Figure 155.** Proposed synthesis to obtain the IR-1076 nm though the IR-1048 nm.... 203
- Figure 156.** HRMS spectrum of IR-1076. The analysis was done to a sample containing 50 $\mu\text{g/ml}$ of the dye dissolved in anhydrous methanol. 204
- Figure 157.** Possible mixture of different isomers synthesised through the commercial IR-1048 nm. 204
- Figure 158.** (a) Absorption spectra of IR-1048 nm (0.4 $\mu\text{g/ml}$) and IR-1076 nm (5 $\mu\text{g/ml}$) dispersed in CHCl_3 . (b) Absorption spectra of IR-806 vs IR-1076 (0.25 $\mu\text{g/ml}$) in CHCl_3 205
- Figure 159.** Emission intensities of IR-1076 dye in CHCl_3 under 77 mW, 1070 nm laser excitation (5s)..... 205
- Figure 160.** TEM images and size distribution of the β - $\text{NaYF}_4\text{:Tm}^{3+}$ (5%) UCNPs. Scale bars are 50 nm. 206
- Figure 161.** TEM images and size distribution of the β - $\text{NaYF}_4\text{:Ho}^{3+}$ (1%) UCNPs. Scale bars are 50 nm. 206
- Figure 162.** (a) UC emission intensities of β - $\text{NaYF}_4\text{:Ho}^{3+}$ (1%) in CHCl_3 in function of the laser excitation and (b) Integrated intensity in the range of 600-700 nm of the

Table of Figures

UC emission for the β -NaYF ₄ : Ho ³⁺ (1%) dissolved in CHCl ₃ at different excitation wavelengths. All measurements were taken with 77 mW and 70 ms.....	207
Figure 163. (a) UC emission intensities of β -NaYF ₄ : Tm ³⁺ (5%) in CHCl ₃ in function of the laser excitation and (b) integrated intensity in the range of 650-850 nm of the UC emission for the β -NaYF ₄ : Tm ³⁺ (5%) dissolved in CHCl ₃ at different excitation wavelengths. All measurements were taken with 77 mW and 70 ms.....	207
Figure 164. Schematic illustration of nanoflares used for live cell mRNA detection. Fluorophore tagged oligonucleotides (flare strand) are used which are initially quenched. When the target mRNA binds to the sense strand the release of the flare can be detected as an increase in its fluorescence signature. Blue and yellow arrows indicate sense strand and flare strand, respectively.....	214
Figure 165. Diagram showing a scheme of the Schlenk – line used to synthesise lanthanides doped UCNPs.	215
Figure 166. Additional TEM images of β -UCNPs@SiO ₂ (a) before and (b) after the annealing treatment showing the visual NPs distribution. Scales bars are 50 nm. Red circles have been drawn around multiple NP cores coated by the same silica shell to facilitate the comparison.	227

Table of Schemes

Scheme 1. Chemical structure of APTMS.	113
Scheme 2. Chemical structure of (a) Igepal CO-520 and (b) TEOS	116
Scheme 3. Chemical structure of THPC.	129
Scheme 4. Chemical structure of OEG.....	130
Scheme 5. Chemical structure of TDDA.....	139

List of Accompanying Materials

Sigma-Aldrich:

The lanthanide chloride (99%): yttrium (III) chloride hexahydrate, ytterbium (III) chloride hexahydrate, erbium (III) chloride hexahydrate, thulium (III) chloride hexahydrate, holmium (III) chloride hexahydrate, gadolinium (III) chloride hexahydrate, lutetium (III) chloride hexahydrate, oleic acid (OA, 90%), 1-octadecene (ODE, 90%), sodium hydroxide (NaOH, $\geq 98\%$), ammonium fluoride (NH_4F , $\geq 98\%$), sodium fluoride (NaF , $\geq 99\%$), sodium tetrachloroaurate (III) dihydrate (NaAuCl_4 , 99%), cetyltrimethyl ammonium bromide (CTAB, $\geq 99\%$), sodium borohydrate (NaBH_4 , $\geq 98\%$), silver nitrate (AgNO_3 , $\geq 99\%$), L-ascorbic acid (reagent grade), sodium citrate ($\geq 99\%$), tetrakis(hydroxymethyl)phosphonium chloride solution (THPC, $\geq 80\%$ in H_2O), polyoxyethylene (5) nonylphenylether (IGEPAL CO-520, average Mn 441), tetraethyl orthosilicate (TEOS, $\geq 99\%$), (3-Aminopropyl) trimethoxysilane (APTMS, 97%), potassium carbonate (K_2CO_3 , $\geq 99\%$), titanium diisopropoxide bis(acetylacetonate) (TDAA, 75 wt. % in IPA), cobalt(II) nitrate hexahydrate ($\text{Co}(\text{NO}_3)_2 \cdot 6\text{H}_2\text{O}$, $\geq 98\%$), resazurin sodium salt (Rz, $\sim 80\%$), 2-[2-[2-chloro-3-[(1,3-dihydro-3,3-dimethyl-1-propyl-2H-indol-2-ylidene)ethylidene]-1-cyclohexen-1-yl]ethenyl]-3,3-dimethyl-1-propylindolium iodide (IR-780 dye, $\geq 95\%$), 1-butyl-2-[2-[3-[(1-butyl-6-chlorobenz[cd]indol-2(1H)-ylidene)ethylidene]-2-chloro-1-cyclohexen-1-yl]ethenyl]-6-chlorobenz[cd]indolium tetrafluoroborate (IR-1048 dye, 97%), 4-mercaptobenzoic acid (90%), nitrosyl tetrafluoroborate (NOBF_4 , 95%), N,N-dimethylformamide (DMF anhydrous, 99.8%), borate-buffered solution, N-(3-(dimethylamino)propyl)-N'-ethylcarbodiimide hydrochloride (EDC, $\geq 99\%$), N-hydroxysulfosuccinimide sodium salt (s-NHS, $> 98\%$), 2-(N-Morpholino)ethanesulfonic acid (MES, $\geq 99\%$), phosphate buffered saline (PBS), 2-(4-Amidinophenyl)-6-indolecarbamidine dihydrochloride (DAPI), Mowiol (4-88, 31 kDa), paraformaldehyde (PFA, 4%).

Synthetic oligonucleotides used throughout this project were synthesised and supplied by Dr. Afaf El-Sagheer at the University of Oxford. Cell lines were provided by Dr. Peter Lackie (MRC 5, 16 HBE) at the Biomedical Imaging Unit (Southampton General Hospital). A 549 cells were provided by Dr. Alastair Watson and Dr. Mirella C. Spaluto based at Southampton General Hospital.

List of Accompanying Materials

Thermo-Fisher:

SnakeSkin Dialysis Tubing, 10K MWCO, ammonia Solution, (35%).

Alfa-Aesar:

Scandium (III) chloride hexahydrate ($\geq 99.9\%$), methylene blue trihydrate (MB), 2,6-dichloroindophenol sodium salt hydrate (DCPIP), rhodamine B, glycerol (99%), succinic anhydride (99%).

Thorlabs:

2" Square UG5 Colored Glass UV-Passing Filter, 240 - 395 nm, 2" Square RG780 Colored Glass Filter, 780 nm Longpass

Others solvent with technical grade:

Ethanol, hexane, chloroform (CHCl_3), nitric acid (HNO_3) (70%), hydrochloric acid (HCl) (37%), isopropanol (IPA), dimethylformamide (DMF), diethyl ether, dichloromethane (CH_2Cl_2).

Academic Thesis: Declaration Of Authorship

I, **Elena Ureña Horno**, declare that this thesis and the work presented in it are my own and has been generated by me as the result of my own original research.

Lanthanide-doped upconversion nanoparticles: Synthesis and Applications

I confirm that:

1. This work was done wholly or mainly while in candidature for a research degree at this University;
2. Where any part of this thesis has previously been submitted for a degree or any other qualification at this University or any other institution, this has been clearly stated;
3. Where I have consulted the published work of others, this is always clearly attributed;
4. Where I have quoted from the work of others, the source is always given. With the exception of such quotations, this thesis is entirely my own work;
5. I have acknowledged all main sources of help;
6. Where the thesis is based on work done by myself jointly with others, I have made clear exactly what was done by others and what I have contributed myself;
7. Parts of this work have been published as:

In-Depth Analysis of Excitation Dynamics in Dye-Sensitized Upconversion Core and Core/Active Shell Nanoparticles

Sergey Alyatkin, Elena Ureña-Horno, Bigeng Chen, Otto L. Muskens, Antonios G. Kanaras, and Pavlos G. Lagoudakis. J. Phys. Chem. C 2018, 122, 18177–18184.

Signed:

Date:

Acknowledgements

Foremost, I would like to thank my supervisors, Prof. Antonios Kanaras and Prof. Pavlos Lagoudakis, for continual guidance and assistance throughout the duration of my Ph.D. I thank them for their enthusiasm, advice and effort, which make this thesis a reality. Their attitude towards academic research has greatly motivated me to be a good researcher. I learned a lot from them.

I would like to extend my gratitude to Prof. Otto Muskens for his kind help, for offering me the opportunity to develop some of my experiments in his lab and important comments on my project research. Also, many thanks to the department of Physics and Astronomy for a Mayflower studentship.

I would be also grateful to all the group members from my lab for their help throughout the work. Thanks to have been part of such a supportive, hardworking, and inspiring group. These people include: Maria-Eleni Kyriazi, Angela de Fazio, Konstantina Alexaki, and Peter Shaw.

A toda mi familia, sobre todo a mis padres, por creer en mí siempre. Su apoyo durante toda mi formación ha sido fundamental para llegar hasta aquí. A mis amigas y amigos. Ellos son mi momento de desconexión favorito.

Primero agradecer a Juri Fiaschi, por estar ahí cada día, ser mi apoyo incondicional y saber sacarme la sonrisa, incluso en los momentos más difíciles.

También me gustaría agradecer a mis amigos, Toni Iborra Torres y Ane Gutierrez Aguirregabiria por prestarme sus oídos, aguantar mis estados de ánimo, ofrecerme sus consejos y apoyarme día a día, desde que nos conocimos en Southampton. Gracias por su comprensión y apoyo a través de este desafiante y gratificante viaje.

A todos ellos...MUCHAS GRACIAS!

Definitions and Abbreviations

AgNO ₃	Silver nitrate
APTMS	(3-Aminopropyl)trimethoxysilane
AR(s)	Aspect ratio(s)
Au	Gold
AuNP(s)	Gold nanoparticle(s)
BSPP	Bis(p-sulfonatophenyl)phenylphosphine
CUC	Cooperative upconversion
COOH	Carboxylic acid
CR	Cross relaxation
CTAB	Cetyltrimethylammonium bromide
CW laser	Continuous wave laser
DAPI	(4',6-diamidino-2-phenylindole)
DC	Downconversion
DCPIP	2,6-Dichloro-4-[(4-hydroxyphenyl)imino]cyclohexa-2,5-dien-1-one
DMF	N, N-Dimethylformamide
DNA	Deoxyribonucleic acid
DOX	Doxorubicin hydrochloride
dSiO ₂	Dense silica
E1	First energy level
E2	Second energy level
EDC	1-Ethyl-3-(3-dimethylaminopropyl)carbodiimide
EDTA	Ethylenediaminetetraacetic acid
EDX	Energy-dispersive X-ray spectroscopy
Er	Erbium

Definitions and Abbreviations

ESA	Excited stated absorption
ETU	Energy transfer upconversion
FCC	Face centered cubic
FWHM	Full width at half maximum intensity
FRET	Förster resonance energy transfer
GSA	Ground state absorption luminescence
HCl	Hydrochloric acid
hmSiO ₂	Hollow mesoporous silica
FTIR	Fourier transform infrared spectroscopy
Ho	Holmium
IGEPAL Co-520	Polyoxyethylene (5) nonylphenylether
IR	Infrared
KOH	Potassium hydroxide
Ln ³⁺	Lanthanides
LSPR	Localized surface plasmon resonance
MB	Methylene blue (3,7-Bis(dimethylamino)phenothiazin-5-ium chloride)
mSiO ₂	Mesoporous silica
NaAuCl ₄ ·2H ₂ O	Sodium tetrachloroaurate (III) dehydrate solution
NaBH ₄	Sodium borohydride
NaF	Sodium fluoride
NaGdF ₄	Gadolinium sodium fluoride
NH ₄ OH	Ammonium hydroxide
NaLnF ₄	Lanthanide sodium fluoride
NaLuF ₄	Lutetium sodium fluoride
NaYF ₄	Yttrium sodium fluoride

Definitions and Abbreviations

NH ₄ F	Ammonium fluoride
NP(s)	Nanoparticle(s)
Nd	Neodymium
NH ₂	Amine
NIR	Near Infrared
NOBF ₄	Nitrosonium tetrafluoroborate
OA	Oleic acid
OAm	Oleylamine
OEG	Monocarboxy (1-mercaptoundec-11-yl) hexaethylene glycol
OH	Hidroxide
PA	Photon avalanche
PBS	Phosphate buffered saline
PDT	Photodynamic therapy
PL	Photoluminescence
PS	Photosensitizer
	Rhodamine B
RB	[9-(2-carboxyphenyl)-6-diethylamino-3-xanthenylidene]- diethylammonium chloride
RE	Rare earth
RGR	Red to green ratio
ROS	Reactive oxygen species
rpm	rotation per minute
Rz	Resazurin (7-Hydroxy-3H-phenoxazin-3-one 10-oxide)
ScYF ₄	Scandium yttrium fluoride
Silica	Silicon dioxide (SiO ₂)
ssDNA	Single-stranded DNA

Definitions and Abbreviations

S-NHS	(N-hydroxysulfosuccinimide)
SP(s)	Surface plasmon(s)
SPR	Surface plasmon(s) surface
S/V	Surface area to volume ratio
TEM	Transmission electron microscopy
TPL	Two-photon luminescence
TEOS	Tetraethyl orthosilicate
Titania	Titanium dioxide (TiO ₂)
(SA) _T	Total surface area
UC	Upconversion
UCNP(s)	Upconversion nanoparticle(s)
UV	Ultraviolet
Vis	Visible
V	Volumen
Yb	Ytterbium
XRD	X-ray diffraction
α -NaYF ₄	Cubic sodium yttrium fluoride
β -NaYF ₄	Hexagonal sodium yttrium fluoride
β -UCNPs	Hexagonal upconversion nanoparticles
β -UCNPs@SiO ₂	Silica-coated upconversion nanoparticles (hexagonal phase)
β - UCNPs@SiO ₂ @Au seeds	Gold seeds attached to upconversion nanoparticles
β - UCNPs@SiO ₂ @Au shell	Gold shell coated on upconversion nanoparticles
β -UCNPs@SiO ₂ -NH ₂	Amine-functionalized of upconversion nanoparticles

Definitions and Abbreviations

β -UCNPs@SiO ₂ -COOH	Carboxylic acid functionalization of upconversion nanoparticles
β -UCNPs@SiO ₂ -ssDNA	Upconversion nanoparticles functionalized with single-stranded DNA
β -UCNPs/TiO ₂	Titania coated of upconversion nanoparticles
ζ - potential	Zeta potential
°C	Degrees Celsius

Chapter 1 Theoretical background

1.1 Nanotechnology

Nanotechnology can be defined as the science and engineering focused on describing the design, synthesis and applications of materials at the nanoscale ⁴ (generally in the range of 1-100 nm). The concept for nanotechnology was introduced for the first time in 1959 by Richard Feynman in his talk “There’s plenty of room at the bottom” ⁵, in which he envisioned a future where the engineering of materials at the nanoscale would bring a revolution in many fields of science.

It is expected that progress in nanotechnology will have a considerable impact in the twenty-first century with the utilization of new materials, which will improve our quality of life. Nanotechnology is expected to bring important breakthroughs in several research fields such as energy, health, devices, and sensors. ⁶

Nanoparticles (NPs) are defined as particles of any substance with at least one of their dimensions at the range 1-100 nm. ⁷ NPs have exceptional properties, which cannot be found in their bulk counterparts, including high surface-to-volume ratio (S/V), ⁸ high surface energy, unique mechanical, thermal, electrical, magnetic, and optical behaviours. An important characteristic is that NPs when confined with a reduction in their sizes, exhibit strong effects on their optical properties. ^{9,10}

In general, the optical properties of nanomaterials are due to their quantum size effect, which is caused by the confinement of electrons within the NPs of dimensions smaller than the bulk counterpart. ^{11,12} The optical property is due to change in the optical energy band gap, which increases with the decrease in NPs size, especially for the semiconductor nanomaterials. In the case of semiconductor NPs with small sizes (normally less than 10 nm), the electronic excitations “feel” the presence of the NP boundaries and respond to changes in the NP size by adjusting their energy spectra. ¹³ The phenomenon is known as the quantum size effect, and the NPs that exhibit this effect are often called quantum dots. ¹³

Contrary to quantum dots, the size-dependent luminescence of lanthanides doped NPs cannot be explained by the theory of quantum confinement of electrons, since the luminescence arises from the electronic transition between the 4f configurations of lanthanides Ln^{3+} ions, which are sufficiently localized. ¹⁴ However, other effects such as

surface quenching have been shown to have important consequences on emission spectra and efficiency of UCNPs with different sizes.^{15,16}

In general, NPs are composed of an inorganic core, which is stabilised by a layer of surfactants or ligands attached to their surface.¹⁷ The physical and optical properties of these NPs can be widely and easily tuned by adjusting the composition, size, and shape of the crystal.¹⁷ Also, the ligands' choice is crucial, because they do not only passivate crystal facets and determine the NPs growth rates and shapes; but also affect size and colloidal stability.¹⁸

1.2 Lanthanide-doped upconversion nanoparticles

Lanthanides are referred to the group of metallic chemical elements with atomic numbers 57 to 71 located at the sixth period in the periodic table, ranging from lanthanum to lutetium. These lanthanide elements, along with other similar elements such as scandium and yttrium, are well known as the rare earth (RE) elements.

The term “RE” was introduced for the first time by the chemist Johan Gadolin in 1794.¹⁹ The RE elements received their name because of their low concentration within minerals.¹⁹ Historically, lanthanides were first discovered in 1787 when a black mineral was found in a town called Ytterby in Sweden.²⁰ After some years, Professor Gadolin discovered a new element from the mineral, yttrium in 1794.¹⁹

The most common and stable lanthanide ions (Ln^{3+}) are the ones with +3 oxidation state.²¹ However, some of the lanthanides, such as cerium, praseodymium and terbium can be also stable at the oxidation state +4, while others such as europium and ytterbium are also stable at the oxidation state +2. This characteristic is due to the fact that the f orbital is full, half occupied or empty.

A summary of the electronic configurations of the lanthanides is shown in **Table 1**. After lanthanum, the electrons at the lanthanides start to occupy the sub-shell 4f before the sub-shell 5d. This is because the energy of the sub-shell 4f falls below that of the sub-shell 5d.

The lanthanide contraction when crossing the series from lanthanum (La) to lutetium (Lu) is caused by the poor screening of the 4f electrons.^{22,23} The screening effect is described as the phenomenon by which the inner-shell electrons screen the outer-shell electrons so they are not affected by nuclear charge. The f electrons are the poorest for shielding, while the s

Chapter 1

electrons are the best. The reduction in the entire 4f shell and the atomic radius is observed in **Table 1**.

Table 1. Ground state electronic configurations and other properties of the lanthanide elements. Table created from Ref. ^{22,24}

Z	Name	Symbol	Electronic configuration of Ln	Electronic configuration [Xe] Ln+3	Atomic radius (pm)	Ionic radius Ln ³⁺ (pm)	Colour of Ln ³⁺
57	Lanthanum	La	5d ¹ 6s ²	-	187	106	Colourless
58	Cerium	Ce	4f ¹ 5d ¹ 6s ²	4f ¹	183	103	Colourless
59	Praseodymium	Pr	4f ³ 6s ²	4f ²	182	101	Green
60	Neodymium	Nd	4f ⁴ 6s ²	4f ³	181	100	Lilac
61	Promethium	Pm	4f ⁵ 6s ²	4f ⁴	-	98	Yellow
62	Samarium	Sm	4f ⁶ 6s ²	4f ⁵	179	96	Yellow
63	Europium	Eu	4f ⁷ 6s ²	4f ⁶	204	95	Pale pink
64	Gadolinium	Gd	4f ⁷ 5d ¹ 6s ²	4f ⁷	180	94	Colourless
65	Terbium	Tb	4f ⁹ 6s ²	4f ⁸	178	92	Pale pink
66	Dysprosium	Dy	4f ¹⁰ 6s ²	4f ⁹	177	91	Yellow
67	Holmium	Ho	4f ¹¹ 6s ²	4f ¹⁰	176	89	Yellow
68	Erbium	Er	4f ¹² 6s ²	4f ¹¹	175	88	Pale pink
69	Thulium	Tm	4f ¹³ 6s ²	4f ¹²	174	87	Pale green
70	Ytterbium	Yb	4f ¹⁴ 6s ²	4f ¹³	194	86	Colourless
71	Lutetium	Lu	4f ¹⁴ 5d ¹ 6s ²	4f ¹⁴	174	85	Colourless

The narrow emission bands of the Ln³⁺ ions arise from the 4f-4f transitions that, being Laporte-forbidden, are also characterised by low absorption coefficients and relatively long lifetimes. ^{25,26}

It is well known that transitions between levels inside the 4f electronic shell are forbidden by the Laporte selection rule. ²⁷ Briefly, the Laporte (or parity) selection rule states that electric dipole transitions that maintain parity cannot occur. Then, states with even parity can be connected by electric dipole transitions only with states of odd parity and odd states only with even ones. ^{28,29} However, the original parity forbidden intra 4f -4f electronic transitions can become partially allowed by altering the symmetry of the electronic states. By manipulating the geometry of the host lattice, RE³⁺ ions can intermix their f states with higher electronic configurations. ^{30,31}

The energies of the 4f states are split under crystal field, generating a series of states with many closely spaced energies. The narrow emission of Ln³⁺ ions is attributed to their unique electronic configurations in which 5s and 5p electrons (which are lower in energy, but spatially located outside the 4f orbitals) provide strong shielding from the exterior crystal field. As a consequence, they effectively screen the 4f electrons from environmental effects and ligand perturbation and therefore, the coupling of electronic excited states to the surrounding lattice is weak, leading to long excited state lifetimes and sharp optical line

Chapter 1

shapes. Ln^{3+} ions retain therefore, to a great extent the spectroscopic and magnetic properties of the free ions.³²

In general, the emission occurs by direct excitation into an excited state followed by emission and return to the ground state. An adequate source of excitation is required, with a wavelength resonant with the energy gap separating the ground and excited states. A typical method to achieve the emission of lanthanides is through a process known as upconversion (UC).^{1,2}

Briefly, UC is a process in which low-energy near-infrared (NIR) excitation light is converted into higher energies, such as ultraviolet (UV) and visible (Vis) light.^{1,2} It is a process characterized by the emission of light at shorter wavelengths than the excitation wavelength, where the UC is generated by the absorption of energy through two or more excitation photons to finally generate an emission photon.^{1,2}

The absorption of photons is sequential and not simultaneous. UC process benefits from long-lived intermediate excited states, typically in the range of μs to ms . This allows for a sequential absorption of the NIR photons to achieve the excitation of the final energy state followed by the generation of a higher energy photon.^{2,33}

The fact that f-f transitions have low probability to occur due to the Laporte rule turns out to be an advantage for UC. Low probability of f-f transitions imply that energy states have long lifetimes which favour UC processes.

The UC procedure can occur through three main mechanisms known as: excited state absorption (ESA), energy transfer upconversion (ETU), and cross-relaxation (CR). These 3 mechanisms are briefly described below. There exist other mechanisms more complex such as photon avalanche (PA), cooperative upconversion (CUC), however, these processes are unlikely and therefore are less implemented in the design of UC materials.

1.2.1 Upconversion processes

1.2.1.1 Excited state absorption (ESA)

ESA is an UC process, which involves only a single RE ion. As shown in the **Figure 1**, if an incoming photon of energy ($h\nu$) resonates with the energy gap separating ground state G and excited state E1, it will take the ion to an intermediate excited level E1 from the ground state G. The phenomenon is referred to ground state absorption (GSA).^{2,26,33,34}

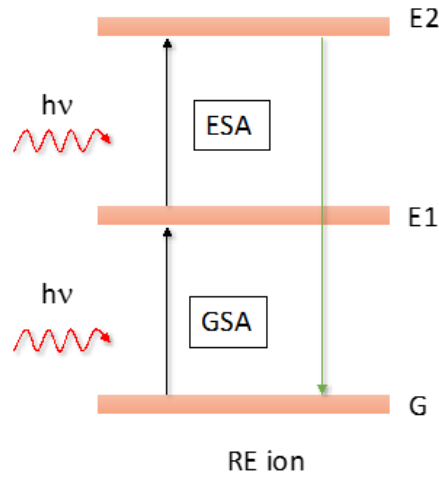


Figure 1. Schematic representation of the excited state absorption process (ESA). G, E1 and E2 indicate ground state, first excited state and second excited state, respectively.

Due to the long lifetime of E1, the RE ion can then absorb an additional second photon which excites the ion from the metastable state E1 to the higher excited state E2. This phenomenon is known as excited state absorption (ESA). UC emission is generated when ions in the E2 state fall to the ground state G and release a photon with higher energy than either of the photons absorbed. This is the least efficient UC mechanism, and occurs in materials having low lanthanide dopant concentrations since the distance separating them is too large for any effective interaction.^{2,26,33,34} The ESA and GSA transitions are illustrated in **Figure 1**.

1.2.1.2 Energy transfer upconversion (ETU).

The ETU mechanism implies energy transfer between two neighbouring RE ions, where one ion acts as a donor of energy, and the second acts as an acceptor of energy.^{2,26,33,34} The ETU mechanism is produced in co-doped materials, which involves the successive energy transfer from a “donor sensitizer ion” to an “acceptor activator ion”. During the process (**Figure 2**), sensitizer ions first get excited to their intermediate states E1 through GSA. As long as the

sensitizer and activator ions are in close vicinity, a non-radiative energy transfer (ETU1) can occur between them, resulting in the promotion of the activator ion to its intermediate state E1. A second transfer (ETU2) can occur, which promotes the activator ions to the emitting state E2. ^{2,26,33,34} The UC luminescence is generated from the E2 → G transition of the activator ion releasing a photon with higher energy than either of the photons absorbed.

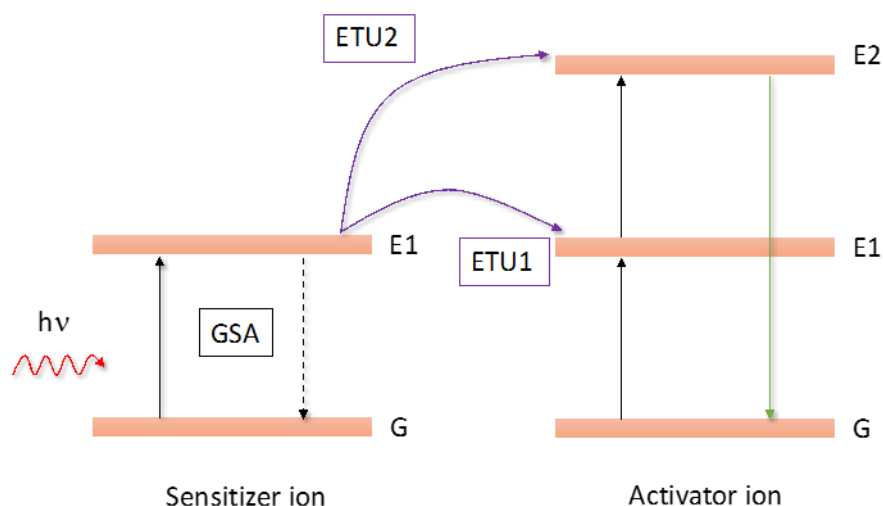


Figure 2. Schematic representation of the energy transfer upconversion (ETU) process.

1.2.1.3 Cross-relaxation (CR) upconversion

The CR mechanism occurs usually between two identical ions in close proximity. ^{26,34} See **Figure 3**. The process arises when the first ion (donor ion) in the excited energy state E2, instead of decaying radiatively, transfers part of its energy to a neighbouring ion (acceptor ion) which is in the ground state. This results in the emission of two photons of low energy ^{26,34–36} denoted by green dashed lines from both ions.

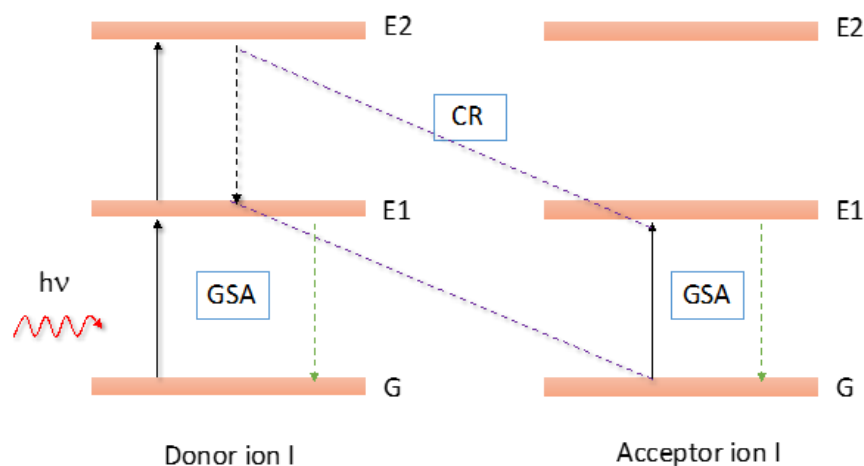


Figure 3. Schematic representation of the cross-relaxation (CR) upconversion process.

1.2.2 Upconversion composition

The development of upconversion nanoparticles (UCNPs) requires a sophisticated and thorough tuning of the inorganic material (so-called host matrix), the doped ions, and the dopant concentration to obtain a strong UC luminescence. Generally, the inorganic host matrix is doped with low concentrations of Ln^{3+} ions, in which the distance between Ln^{3+} ions should be below $\sim 10 \text{ \AA}$ to allow energy transfer, which constitutes the most efficient mechanism of UC. The amount and type of dopants, size and phase of NPs can be tuned to achieve multiple emissions over a wide spectral range.

1.2.2.1 Activator and Sensitizer

Regarding the ETU process, the sensitizer ions should possess a high absorption cross-section for the excitation wavelength. In addition, it is imperative that the sensitizer ions have energy levels matching those of the activator ions.

Yb^{3+} has a 10 times larger absorption cross section ($11.7 \cdot 10^{-21} \text{ cm}^2$) than Er^{3+} ($1.7 \cdot 10^{-21} \text{ cm}^2$).³⁷ The energy level of Yb^{3+} is quite simple, with only one excited state ($^2\text{F}_{5/2}$) and the 980 nm wavelength light matches the $^2\text{F}_{7/2} \rightarrow ^2\text{F}_{5/2}$ transition of Yb^{3+} . From **Figure 4**, we can observe that this energy gap between $^2\text{F}_{7/2}$ and $^2\text{F}_{5/2}$ is resonant with the energy gaps between several excited states of commonly used activator ions, such as Er^{3+} and Tm^{3+} .^{26,34,38} For these reasons, Yb^{3+} is considered the best sensitizer choice to donate energy to other ions.^{39,40}

According to the ETU process, the acceptors should be characterized by energy levels with energy separations equivalent to the sensitizer emission.³⁴ Er^{3+} and Tm^{3+} are the best activators for ETU owing to the unique ladder-like arrangement of their energy levels, long-lived intermediate excited states and excellent resonance with the band gap $^2\text{F}_{7/2} \rightarrow ^2\text{F}_{5/2}$ transition of Yb^{3+} .^{2,38}

Activator ions can promote to a higher energy level once nearby excited sensitizers (with matching energy) transfer their energy to them. It is important to establish a correct ion-to-ion distance between the dopants to minimize quenching effects by cross-relaxation events.^{2,34} In general the level of activators shall be kept low, typically less than 3% for Er^{3+} , and 0.5% for Tm^{3+} .³⁴ However, the number of sensitizers Yb^{3+} must be high enough (usually 20%) to allow an appropriate distance between sensitizers and activators to enable the energy transfer, but not so high to provoke the so-called “concentration quenching” effect due to cross-relaxation events.³⁴

Among the commonly used activators, Er^{3+} shows the highest UC efficiency, due to similar energy gaps from $^4\text{I}_{15/2}$ to $^4\text{I}_{11/2}$ and $^4\text{I}_{11/2}$ to $^4\text{F}_{7/2}$. In $\text{Yb}^{3+}/\text{Er}^{3+}$ co-doped UCNPs, the green (525 nm and 545 nm) and red emissions (655 nm) are the most observed under 980 nm excitation, however emission at 415 nm can also appear. Green and red emissions are both generated from two-photon processes, while the violet emission at 415 nm derives from a three-photon process. The mechanism of $\text{Yb}^{3+}/\text{Er}^{3+}$ co-doped UCNPS is shown in the right side panel from **Figure 4**, where the $^2\text{H}_{11/2}$, $^4\text{S}_{3/2} \rightarrow ^4\text{I}_{15/2}$ and $^4\text{F}_{9/2} \rightarrow ^4\text{I}_{15/2}$ transitions are responsible for the green and red emissions, respectively.^{41–45}

Under 980 nm laser irradiation, Yb^{3+} ions absorb NIR photons and the $^2\text{F}_{7/2} \rightarrow ^2\text{F}_{5/2}$ transition takes place. The $^4\text{I}_{11/2}$ energy level of Er^{3+} is resonant with the $^2\text{F}_{5/2}$ energy level of Yb^{3+} resulting in a very efficient energy transfer process from Yb^{3+} to Er^{3+} , while Yb^{3+} drops back to its $^2\text{F}_{7/2}$ ground state. Due to the energy level match, the Er^{3+} can be populated to the higher excited states ($^4\text{F}_{7/2}$, $^4\text{F}_{9/2}$) through similar resonant energy transfer from the sensitizer. After relaxation to $^2\text{H}_{11/2}$ and $^4\text{S}_{3/2}$, green emissions corresponding to 525 and 545 nm are observed when radiative decay to the $^4\text{I}_{15/2}$ ground state. The red emission at 655 nm arises from the $^4\text{F}_{9/2}$ state, which is attributed to either relaxation from the higher $^4\text{S}_{3/2}$ state or exciting Er^{3+} ions from the $^4\text{I}_{13/2}$ state to the $^4\text{F}_{9/2}$ state *via* energy transferring from the $^2\text{F}_{5/2}$ of Yb^{3+} .^{2,26,33,34}

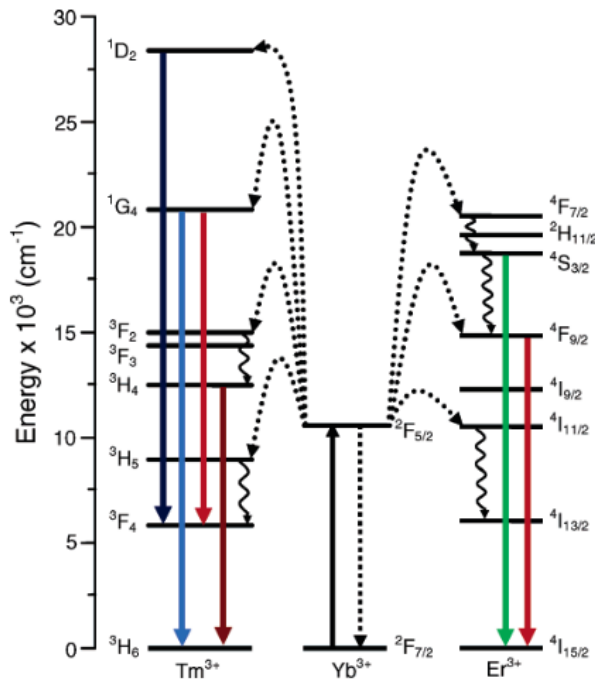


Figure 4. Simplified energy level diagram for UCNPs co-doped with $\text{Yb}^{3+}/\text{Er}^{3+}$ and $\text{Yb}^{3+}/\text{Tm}^{3+}$. Reproduced from Ref.⁴⁵ The full, dotted, and curly arrows represent emission, energy transfer, and multiphonon relaxation processes, respectively.

With respect to $\text{Yb}^{3+}/\text{Tm}^{3+}$ co-doped UCNPs, a similar mechanism occurs and the UV emissions (290 nm, 350, 362 nm), visible emissions (450, 475, 646, 696 nm) as well as the 800 nm NIR emission can all be obtained simultaneously under 980 nm irradiation.

Under 980 nm laser irradiation, Yb^{3+} ions absorb NIR photons and the $^2\text{F}_{7/2} \rightarrow ^2\text{F}_{5/2}$ transition takes place. Then, Yb^{3+} transfers energy to a Tm^{3+} ion resulting in the aforementioned UC emissions (see left side panel from **Figure 4**). The emissions at 290 nm and 345 nm result from five-photon processes, and emissions at 362 nm and 450 nm, 475 and 646 nm, 696 nm and 800 nm come from four-photon, three-photon and two-photon processes respectively. The blue emissions at 450 and 475 nm correspond to the $^1\text{D}_2 \rightarrow ^3\text{F}_4$ and the $^1\text{G}_4 \rightarrow ^3\text{H}_6$ transitions, respectively. The emissions at 646 nm, 696 nm, and 800 nm correspond to the $^1\text{G}_4 \rightarrow ^3\text{F}_4$, $^3\text{F}_3 \rightarrow ^3\text{H}_6$, and $^3\text{H}_4 \rightarrow ^3\text{H}_6$ transitions and are the responsible for the red and NIR emissions.^{41–46} Interestingly, it has been reported that the UC emission at the different wavelengths strongly differs between them. The near infrared (NIR) emission at 800 nm is the strongest and the red emissions at 646 nm and 696 nm is the weakest.^{36,47}

1.2.2.2 Host matrix

The primary requirement for the host matrix is that they should be optimally transparent in the visible and NIR regions. A suitable host material should be as well characterised by low energy phonons (see **Table 2**), to avoid undesired non-radiative multiphonon relaxation of the excited states of the dopants,⁴⁸ and with high chemical stability to avoid degradation.

Table 2. Phonon energy of the most common host materials for UCNPs. Adapted from Ref.¹³

Material	Phonon energy (cm^{-1})
Phosphate glass	1,200
Silica glass	1,100
Fluoride glass	550
Chalcogenide glass	400
Y_2O_3	550
ZrO_2	500
NaYF_4	350
LaF_3	300
LaCl_3	240
YVO_4	890
$\text{Y}_2\text{O}_2\text{S}$	520
GdOCl	500
LaPO_4	1,050

In addition, a good host matrix should present low crystal symmetry to enhance transition probabilities during the UC process.^{26,34} The best materials known to date belong to the family of fluorides. Fluorides usually exhibit low phonon energies ($<500\text{ cm}^{-1}$), high chemical stability and, therefore, are considered good host materials for UCNPs.^{26,34}

Sodium yttrium fluoride (NaYF_4) is currently one of the most suitable material for UCNPs, and there are two different types of it, cubic ($\alpha\text{-NaYF}_4$) and hexagonal ($\beta\text{-NaYF}_4$). The hexagonal phase is the most efficient phase exhibiting a UC efficiency that is one order of magnitude greater than the analogous cubic phase.³⁴ This is due to the highly ordered cation distribution in the $\beta\text{-NaYF}_4$ lattice compared to the random substitution of Na^+ and Y^{3+} in the $\alpha\text{-NaYF}_4$ phase.⁴⁹ The host material phase therefore, affects the UC emission; effectively low phase symmetry contains more uneven components which allow a stronger coupling between the 4f energy levels and give higher UC emission efficiency.³⁸

1.2.3 Synthesis of upconversion nanoparticles

One of the major challenges in the preparation of UCNPs is the reproducibility of fabrication of monodispersed NPs, which should also exhibit narrow size distribution and a pure phase. The most widely used methods for the preparation of UCNPs doped with Ln^{3+} are co-precipitation, thermal decomposition, and hydro(solvo)thermal.

Table 3. Summary of the most common upconversion synthetic strategies with some examples.

Method	Examples	Advantages	Disadvantages
Co-precipitation	$\text{LaF}_3\text{:Ln}^{3+}$ ⁽⁵⁰⁾ $\text{LaF}_3\text{:Yb}^{3+}, \text{Ln}^{3+}$ ⁽⁵¹⁾ where ($\text{Ln}^{3+} = \text{Eu}^{3+}, \text{Er}^{3+}, \text{Nd}^{3+}, \text{and Ho}^{3+}$) $\text{NaYF}_4\text{:Yb}^{3+}, \text{Er/Tm}^{3+}$ ^(52–55)	Convenient.	Post treatment usually required
Thermal decomposition	$\text{NaLnF}_4\text{:Yb}^{3+}, \text{Er/Tm}^{3+}$ ^(41,56–58) where ($\text{Ln}^{3+} = \text{Pr}^{3+} \text{ to } \text{Lu}^{3+}, \text{Y}^{3+}$) LaF_3 ⁽⁵⁹⁾ Y_2O_3 ⁽⁶⁰⁾	High uniformity and monodisperse.	Rigorous experimental conditions. Toxic precursors
Hydro(solvo)thermal synthesis	$\text{NaYF}_4\text{:Yb}^{3+}, \text{Er}^{3+}$ ^(61,62) NaYbF_4 ⁽⁶³⁾ NaGdF_4 ⁽⁶⁴⁾ LaF_3 ⁽⁶⁵⁾	Excellent control on morphology and size.	Specialized reaction vessels required

1.2.3.1 Co-precipitation

Currently, most high-quality UCNPs, and more specifically NaYF₄, are prepared *via* the co-precipitation method in solvents with high-boiling point, which uses oleic acid (OA) or oleylamine (OAm) as the surface ligand.⁵⁸ The surfactants usually contain a functional group to cap the surface of UCNPs for controlling their growth and a long hydrocarbon chain to assist their dispersion in organic solvents.²⁶ Since it does not require expensive equipment, complex procedures or extreme reaction conditions in the synthesis, co-precipitation is currently considered as the most convenient and simple way to prepare NaYF₄.⁴¹

One of the first reported usages of the co-precipitation method was by van Veggel's group in 2002,⁵⁰ who employed the technique to synthesise lanthanum trifluoride (LaF₃) NPs doped with Eu³⁺, Er³⁺, Nd³⁺, and Ho³⁺. In this technique, diethyl dithiophosphate ammonium was employed as the ligand agent to impart stabilization and subsequent growth of the NPs. The synthesis was further refined by Chow,⁵¹ who synthesised hexagonal LaF₃ co-doped with Yb³⁺ and Ln³⁺ (Ln = Er³⁺, Tm³⁺, and Ho³⁺) and obtained UCNPs with an average size of 5.4 nm and very narrow size distribution (± 0.9 nm).

NaYF₄ based UCNPs were first synthesised in 2004 using the co-precipitation method by Haase's group.⁵² NaYF₄ co-doped with Yb³⁺ and Ln³⁺ (Ln³⁺ = Er³⁺ and Tm³⁺) were successfully fabricated in high boiling organic solvent, using N-2-(hydroxyethyl)ethylenediamine (HEEDA) as a capping ligand. Unfortunately, this method produced UCNPs of a wide size distribution, and only the cubic phase (α -NaYF₄) was obtained.

In 2004, the synthesis of NaYF₄ co-doped with Yb³⁺ and Ln³⁺ (Ln³⁺ = Er³⁺ and Tm³⁺) with narrow size distributions using co-precipitation was reported by Guo's group.⁵³ Ethylenediaminetetraacetic acid (EDTA) was used as a chelating agent to form a Ln³⁺-EDTA complex, followed by a rapid injection of this complex into a vigorously stirred NaF solution. The lanthanide precursors used in this method were chlorides. The process was helpful in forming a homogenous nucleus for subsequent growth of the UCNPs. With this strategy, the particle size was effectively controlled between 37 nm and 166 nm by adjusting the molar ratio of EDTA to the Ln³⁺. The cubic phase of NaYF₄ UCNPs was obtained using the described method, which unfortunately suffered from a low photoluminescence yield. In view of that, a post-treatment by annealing was employed to drive transition of the UCNPs from cubic to hexagonal phase, which resulted in brighter UCNPs.⁵³

In an attempt to generate crystalline, highly uniform, purely hexagonal phase NaYF₄ UCNP with narrower size distributions and higher luminescence efficiencies than those produced by conventional co-precipitation methods, Zhang's group^{54,55} developed the so-called "user friendly" high-temperature co-precipitation method using 1-octadecane (ODE) as the solvent and OA as a capping ligand.⁵⁴ In their research, nanospheres, nanoellipses, and hexagonal-phase nanoplates with narrow size distributions were obtained by altering the OA:ODE ratio used in the reaction.⁵⁴ The method was demonstrated to be user-friendly in minimizing the use of fluoride reactions and decreasing the content of toxic by-products generated at high temperature.⁵⁴ The described strategy was adopted to prepare UCNP for the studies reported in this thesis.

1.2.3.2 Thermal decomposition

Thermal decomposition is a well-established method for the synthesis of monodispersed UCNP with uniform shape, tailored size, and single crystal structure. The strategy is almost exclusively implemented in the fabrication of lanthanide sodium fluoride (NaLnF₄) where Ln³⁺ can be Y³⁺, Gd³⁺, Lu³⁺, Li³⁺ or Gd³⁺.³⁴ The strategy is based on the decomposition of organometallic precursors in the presence of organic solvents such as ODE and surfactants such as OA and OAm. The commonly used precursors include metallic or lanthanide trifluoroacetate, lanthanide oleates, lanthanide acetates, and lanthanide chlorides.⁶⁶ Usually, the lanthanide trifluoroacetate precursors are prepared from the corresponding lanthanide oxides and trifluoroacetic acid (TFA).⁶⁶

The major drawback of the thermal decomposition relies on the expensive use of air sensitive metallic precursors, and the generation of toxic volatile by-products, which are generated from the reaction.^{34,57} In general, the synthetic process is conducted at elevated temperatures of ~300 °C in an oxygen-free and anhydrous environment, where the precursors decompose in the presence of the ligands to form the nucleus for a particle to grow on.³⁴

The thermal decomposition method was first introduced in 2006 by Yan's group⁵⁶ on the preparation of the cubic and hexagonal phase of UCNP. High quality and narrow size distribution of UCNP (Ln³⁺ = Pr³⁺ to Lu³⁺, Y³⁺) co-doped with Yb³⁺/Er³⁺ and Yb³⁺/Tm³⁺ were obtained in their research. In addition, various sizes and shapes of UCNP were produced by adjusting different experimental parameters, such as the reaction temperature, the reaction time, the nature and the concentration of solvents, and the concentration of precursors.^{56,57} Another approach was reported in 2009 by Liu's group,³⁸ where ethylene glycol (EG) was used as solvent and polyethyleneimine (PEI) as capping ligand. This

method produced UCNPs that were easily dispersed in aqueous media, however, only the cubic α -NaYF₄ phase was produced.

Although it has been shown that thermal decomposition is an effective strategy, the UCNPs manufactured with this method show usually low UC efficiency. The reason why this occurs is that the thermal decomposition favours a rapid nucleation and growth, which can cause defects on the surface of the UCNPs and, therefore, produce a relatively low UC efficiency.

1.2.3.3 Hydro(solvo)thermal synthesis

Hydro(solvo)thermal method is another strategy to produce monodispersed NaYF₄ UCNPs with controllable shape, phase and size. The possible advantages of this technique are the relatively lower reaction temperature, high-quality crystalline phase of the obtained UCNPs, and excellent control over the particle size and shape.

The hydro(solvo)thermal technique employs pressures and temperatures that are above the critical point of the solvent. The main disadvantage is the use of a reaction vessel (Teflon-lined autoclave) which leads to the inability to monitor the particle growth.⁶⁷

This technique was firstly reported by Li's group on the synthesis of NaYF₄.^{61,62} They fabricated hexagonal NaYF₄: Yb³⁺, Er³⁺ UCNPs in different solvents such as distilled water, acetic acid, and ethanol; and using cetyltrimethylammonium bromide (CTAB) and EDTA as capping ligands to tune the morphology and size of the UCNPs.

In a typical hydro(solvo)thermal process, lanthanide and fluoride precursors are mixed with the surfactant in aqueous solution and placed in an autoclave. The lanthanide precursors used in this method can be nitrites, chlorides or oxides while the fluoride precursors reported in the literature include HF, NH₄F, NH₄HF₂, NaF, and KF. After mixing the precursors, the solution is heated at 160 °C - 220 °C. It has been demonstrated that the morphologies of the resulting UCNPs can be easily tuned by varying the precursors concentration, reaction temperature, reaction time, and pH of the solution.³⁴

1.2.4 Surface modification on the upconversion nanoparticles

The hydrophilicity of UCNPs is a requirement for them to be used in biological applications. However, UCNPs prepared by the methods described above are generally hydrophobic due to the hydrophobic nature of the capping ligands, which greatly limits their application in biology. In order to transfer these hydrophobic UCNPs into water, a number of surface modification methods have been developed including ligand exchange, ligand oxidation,

ligand removal, ligand attraction, layer-by-layer assembly, and surface silanization.^{38,68,69} These surface modification not only renders UCNPs hydrophilic and thus water-dispersible but also provides reactive groups for their subsequent participation in bioconjugation reactions.

1.2.4.1 Ligand exchange

The ligand exchange is a physical process in which the original hydrophobic coating ligands, such as OA or OAm on UCNPs are replaced with new binding molecules.⁶⁹ It is imperative that the new binding molecules have functional groups that allow them to interact with the surface either through physisorption or through chemical binding.

Zhang et al. reported in 2007 a ligand exchange method to replace OA on iron oxide NPs as a model system under elevated temperature (240 °C).⁷⁰ A variety of molecules were used in their experiments including poly (acrylic acid) (PAA), poly(allylamine) (PAAm), and poly(sodium styrene sulfonate) (PSS). The ligand exchange with hydrophobic molecules resulted in NPs highly dispersible in water. In addition, the introduction of functional groups such as -COOH and -NH₂ allowed further functionalization of the NPs with biomolecules of interest.⁷⁰

Van Veggel's group reported in 2010 a ligand exchange method to produce water-dispersible NaYF₄ UCNPs.⁷¹ OA ligands were exchanged for PEG-phosphate ligands in a hexane–ethanol solution at 70 °C over the course of 24 h.⁷¹ In general, replacement of the original OA or OAm capping ligands with a ligand exhibiting polydentcity is desirable, because they bind to the particle at more sites by reducing desorption rates and can improve the colloidal stability of NPs in solution.³⁴

A more versatile strategy was developed in 2011 by Dong and co-workers,⁷² who reported the use of nitrosonium tetrafluoroborate (NOBF₄) to replace the original surface ligands (OA or OM) at room temperature. It was observed that the intermediate (NOBF₄/UCNP) was highly stable in solution and could be further modified by replacing the NOBF₄ with a new capping molecule for subsequent bioconjugation. See **Figure 5**.

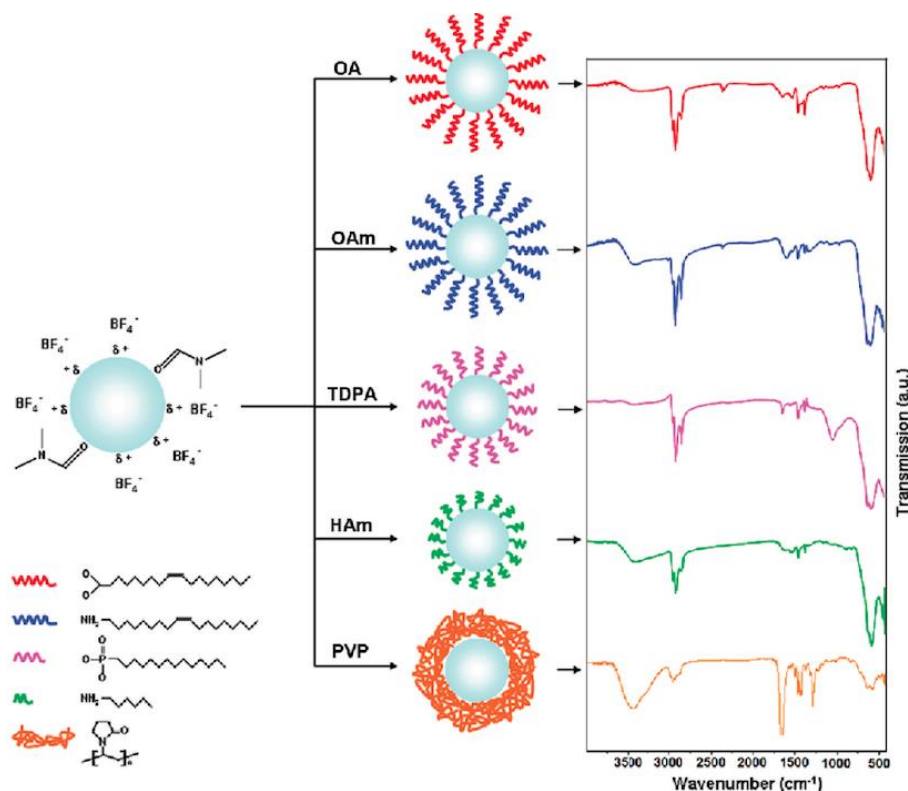


Figure 5. A diagram of the subsequent ligand exchange of $\text{NOBF}_4/\text{UCNPs}$ with OA, OAm, tetradecylphosphosphonic acid (TDPA), hexylamine (HAm), or polyvinylpyrrolidone (PVP), respectively. Reproduced from Ref. ⁷²

1.2.4.2 Ligand oxidation

Ligand oxidation refers to the direct oxidation of the unsaturated carbon-carbon double bond ($-\text{C}=\text{C}-$) of OA to carboxylic acid groups, rendering UCNPs water soluble.

The strategy was reported by Huang's group using as a model NaYF_4 . They employed the Lemieux-von Rudloff reagent, which is a mixture of sodium periodate (NaIO_4) and potassium permanganate (KMnO_4), to oxidize selectively the ($-\text{C}=\text{C}-$) from OA into azelaic acids, and thus producing two terminal carboxylic acids. ⁷³ A representative scheme of the synthesis can be seen in **Figure 6**. The carboxylic groups of the resulting azelaic acid not only provided high solubility to the NPs but also enabled them to conjugate to biomolecules. Unfortunately, oxidation using the Lemieux-von Rudloff reagent resulted in the formation of undesired MnO_2 , luminescence-quenching, and others by-products which are difficult to eliminate. ⁷³

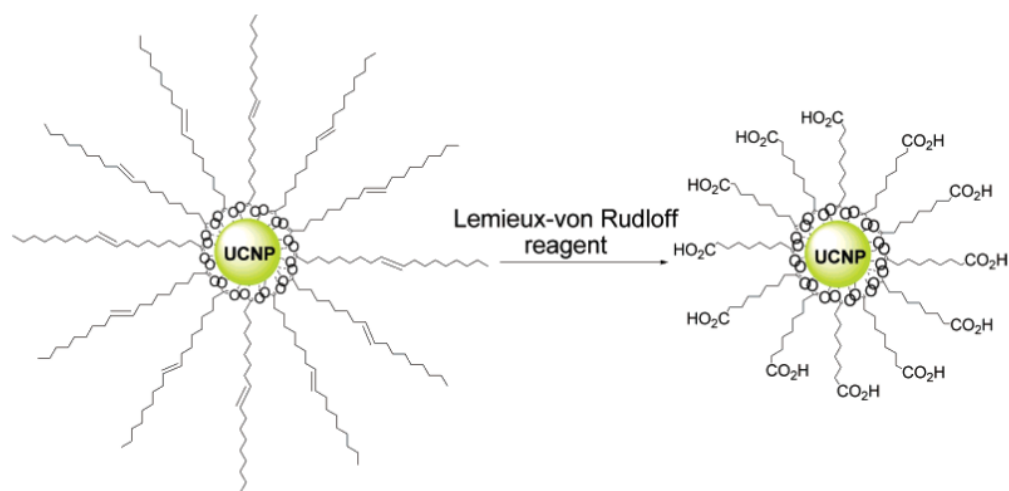


Figure 6. Scheme showing the oxidation of OA on UCNPs with Lemieux-von Rudloff reagent to produce carboxylic acid functionalized UCNPs. Reproduced from Ref. ⁷³

In order to minimize the production of undesired by-products, Yan's research group used a new synthetic strategy with ozone to oxidize OA into terminal carboxylic acid or aldehyde.⁷⁴ The new strategy proved to have no influence on the morphology, crystalline phase, composition and optical properties of UCNPs. This method of ligand oxidation is very easy to implement, nonetheless, it is only applicable to limited types of hydrophobic surface ligands that contain unsaturated carbon-carbon double bonds.

1.2.4.3 Ligand free nanoparticles

The transformation of hydrophobic UCNPs to hydrophilic ones can be achieved by removing the OA ligands coated on UCNPs. It has been reported that the OA can be removed by treating the UCNPs by excess of ethanol under sonication⁷⁵ or simply with incubation with an acid.⁴⁴

Capobianco's group mixed OA-coated UCNPs with HCl at pH 4 to remove OA and obtain hydrophilic UCNPs.⁴⁴ At low pH, OA was protonated gradually and dissociates from the particle, leaving the UCNPs naked with Ln^{3+} ions being exposed on their surfaces. Because of the high surface charge of these positive Ln^{3+} , the obtained UCNPs could coordinate to water molecules forming a stable dispersion in aqueous solutions for a long time. The surface of the Ln^{3+} ions were readily used to bind biomolecules that contained functional groups such as $-\text{COOH}$, $-\text{OH}$, $-\text{NH}_2$.⁴⁴

1.2.4.4 Ligand attraction

Another strategy to acquire water-dispersible UCNPs is based on the introduction of an additional molecular layer of amphiphilic polymers, which interacts with the original ligand molecules and changes the surface properties accordingly.⁶⁹ The method is based on Van-der-Waals interactions between hydrophobic amphiphilic molecules and hydrophobic capping ligands on the UCNP surface.

A schematic illustration of the strategy is shown in **Figure 7**, where the hydrophobic parts of the amphiphilic compounds (typically, modified polymers or detergents) interact with the organic capping molecules on the UCNP surface to form an inner layer, while the hydrophilic parts facing outwards form the external layer and facilitate dispersion of NPs in aqueous solution. In addition, the additional layer provides functional groups for the subsequent bioconjugation.⁶⁹

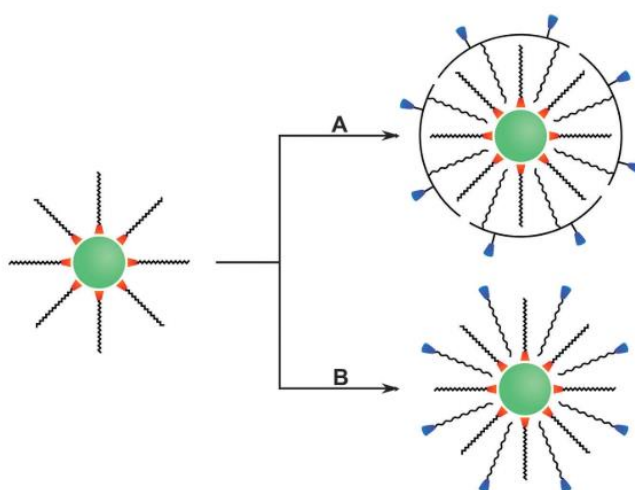


Figure 7. A diagram showing the modification of hydrophobic UCNPs *via* the ligand attraction using (a) amphiphilic polymers with multiple hydrophobic chains and (b) surfactants with a single hydrophobic chain. Reproduced from Ref.⁷⁶

In the literature, different amphiphilic molecules have been employed to render the UCNPs water-dispersible. Examples include poly(maleic anhydride-alt-1-octadecene) (PMAO),⁷⁷ PMAO with PEG (PMAO-PEG),⁷⁸ octylamine-poly(acrylic acid)-poly(ethylene glycol) (OA-PAA-PEG),⁷⁹ poly(ethylene glycol)-block-poly(caprolactone) (PEG-b-PCL),⁸⁰ poly((ethylene glycol)-block-lactic acid) (PEG-b-PLA),⁸⁰ poly(ethylene glycol)-block-poly(lactic-co-glycolic acid) (PEG-b-PLGA),⁸⁰ sodium dodecyl sulphate (SDS),⁸¹ CTAB,⁸¹ poly(ethylene glycol tert-octylphenyl ether) (C₈PhE₁₀)⁸¹, and phospholipids.⁸²

1.2.4.5 Layer-by-layer assembly

Unlike the above ligand attraction method, the layer-by-layer assembly employs the electrostatic interaction between opposite charged ligands to construct ligands layers.

In 2005, Li and co-workers reported the first ligand capping of β -NaYF₄: Yb³⁺, Er³⁺ UCNPs using this method. They deposited the positive charged ligand poly(allylamine hydrochloride) (PAH) and the negative charged polymer, poly(styrene sulfonate) (PSS), sequentially to generate PAH/PSS/PAH UCNP nanocomposites.⁸³ The outlayer of PAH provided abundant amine groups that enabled the conjugation with biotin.⁸³ The primary disadvantage of this technique is the amount of time required to undergo the laborious layer-by-layer fabrication along with the significant increase in the hydrodynamic size of the NPs. In addition, hydrophilic initial NPs must be used to start the layer assembly.

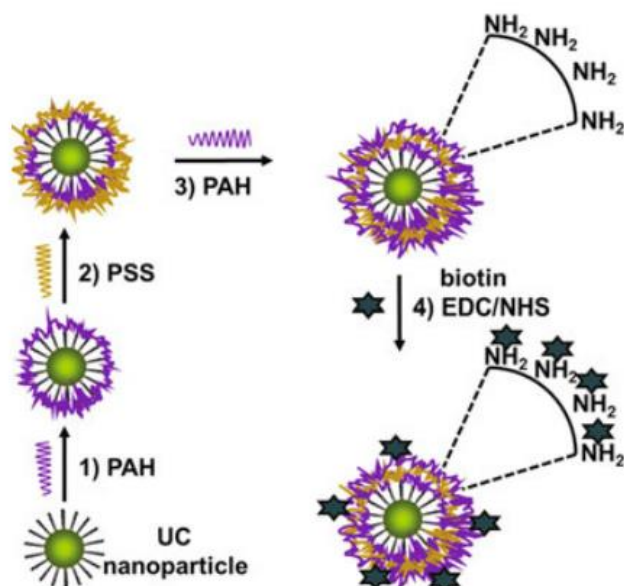


Figure 8. Schematic illustration of layer-by-layer assembly. Sequential deposition of oppositely charged PAH, PSS, and PAH to generate hydrophilic PAH–PSS–PAH-coated UCNPs with stable amino-rich shells. Reproduced from Ref.⁸³

1.2.4.6 Creating a silica shell around nanoparticles

Silica coating is another popular method to modify UCNPs owing to silica being a water-dispersible material with many known merits, such as optical transparency, biocompatibility, non-toxicity, and chemical stability.⁸⁴ The major drawback of this technique is the slight decrease in the photoluminescence (PL) properties of the UCNPs after silica growth, which can be attributed to scattering of the excitation light and emission light by silica.^{85,86}

Silica coating utilizes covalently attached polymers and is applicable to both hydrophobic and hydrophilic UCNPs. Hydrophobic UCNPs can be coated with silica by employing a reverse microemulsion method. The strategy makes use of a detergent (such as Igepal CO-520) to form reverse micelles in a nonpolar solvent, wherein tetraethyl orthosilicate (TEOS) undergoes hydrolysis in the presence of ammonia to grow a silica shell on the NPs. The first reported use of microemulsion method was in 2005, with the silica functionalization of YF_3 ⁸⁷ and extended to NaYF_4 in 2006 by Li and Zhang, where a thin layer of silica (1-3 nm) on PVP-stabilized NaYF_4 was obtained.⁸⁸

Hydrophilic UCNPs, on the other hand, can be functionalized with silica employing the Stöber method, which was first described in 1968.⁸⁹ Instead of using a nonpolar solvent, hydrophilic UCNPs are dispersed in ethanol, or a mixture of water and ethanol, where the hydrolysis reaction of TEOS occurs to form the silica shell on UCNPs. Based on this last approach, Shi and co-workers reported the coating of silica on $\text{NaYF}_4:\text{Yb}^{3+}, \text{Er}^{3+}, \text{Tm}^{3+}, \text{Gd}^{3+}$ UCNPs with a controllable shell thickness of 5 nm, 10 nm, 15 nm, and 20 nm by adding different amounts of TEOS.⁹⁰ In their work, silica shells of different thicknesses were coated and presented excellent water solubility and good biocompatibility.⁹⁰

The two above syntheses produce a silica layer on the UCNPs that is generally referred to as dense silica layer (dSiO_2). Many groups also have dedicated efforts to grow a mesoporous silica (mSiO_2) or hollow mesoporous silica (hmSiO_2) shell on the UCNPs, in an attempt to use the resulting NPs as drug delivery vehicles (**Figure 9**).⁹¹

Briefly, there are two routes to synthesise the mSiO_2 structure. The first one is to coat a mSiO_2 layer directly on the surface of UCNPs in one step; while the second is to coat the mSiO_2 layer on the surface of UCNP@SiO_2 to form a $\text{UCNP@SiO}_2@\text{mSiO}_2$ structure. The incorporation of this SiO_2 interlayer results in improved chemical stability.⁹¹

The mSiO_2 layer can be achieved by adding a micelle-forming reagent (such as CTAB) during the formation of a silica shell. The micelles are then removed by washing the colloid with a solvent of suitable pH.^{92,93}

The hollow mesoporous silica also known as rattle-structured UCNP@hmSiO_2 provides the larger accommodation volume for drugs due to the presence of hallowes between the UCNP core and mesoporous shell. They are attractive materials for many potential applications because of their high surface to volume ratio and large pore volume. The hmSiO_2 coating method was developed in 2014 by Shi and co-workers. In their experiments, they coated two layers of dSiO_2 on a hydrophobic UCNP followed by etching the first dSiO_2 shell, breaking

the internal Si–O–Si bonds along with generating mesoporous in the second silica shell. By adjustment of the etching duration, they obtained rattle structures with different cavity sizes.

94

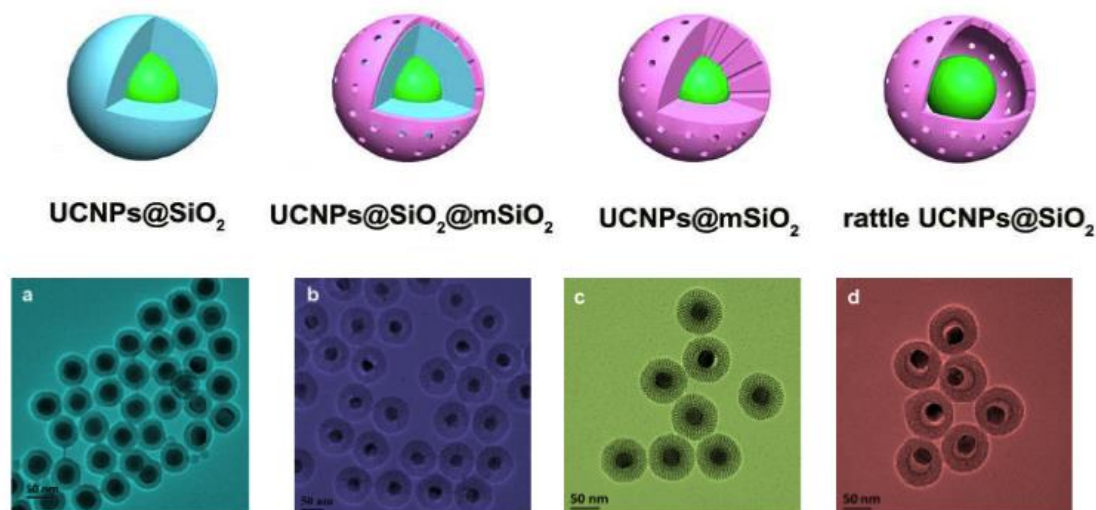


Figure 9. Schematic illustration and TEM images of (a) UCNP@dSiO₂, (b) UCNP@mSiO₂, (c) UCNP@dSiO₂@mSiO₂, and (d) UCNP@hmSiO₂. Adapted from Ref. ^{91,95}

1.2.4.7 Bioconjugation

In order to implement UCNPs in biological applications, it is crucial to couple them with molecules that possess biological functions, such as antibodies, peptides, and nucleic acid ligands. This biofunctionalization step, also referred to as bioconjugation, can be realized by attachment of biomolecules to the UCNP surface through covalent interactions, such as peptide couplings between amine and carboxylic functionalities, or through non-covalent interactions such as the adsorption of negatively charged nucleic acids to positively charged NP surfaces.⁴⁴

It was shown that a negatively-charged protein, streptavidin, adheres to the surfaces of positive UCNPs by means of electrostatic interaction.⁹⁶ Similarly, it has been proven that folic acid (FA), which is a widely used targeting ligand, can be coordinated to the surface of positive UCNPs through its carboxylic groups.⁹⁷ However, there is the risk that when nanocomposites are used in complex *in vivo* systems, physically adsorbed proteins might release from the surface of the UCNPs.

Conversely, the covalent bond formed between the reactive group of the UCNP and the group present in biomolecules is stronger and more robust, which provides a better

alternative for the bioconjugation of UCNPs. For this purpose, functional groups such as -COOH, -NH₂, and maleimide are generally introduced on the surface of the UCNP and are used for the binding of biomolecules.

The carboxyl-terminated UCNPs can create stable amide bonds with biological molecules containing NH₂ group. The COOH groups of the UCNPs are firstly activated by the use of 1-ethyl-3-(3-dimethylaminopropyl) carbodiimide hydrochloride (EDC) and N-hydroxysulfosuccinimide sodium salt (s-NHS) in buffers. This reaction generates the O-acylisourea intermediate product, which can afterwards react with the NH₂ group of the biomolecules to complete the chemical bonding. Carboxylic groups can be provided by a variety of surface ligands, such as azelaic acid,^{98,99} hexanedioic acid, citrate,^{97,100} thioglycolic acid,^{101,102} 3-mercaptopropionic acid,^{103,104} 5-mercaptosuccinic acid,¹⁰⁵ dimecaptosuccinic acid,¹⁰⁶ 1,10-decanedicarboxylic acid,¹⁰⁷ 11-mercaptoundecanoic acid,¹⁰⁷ 3-mercaptopropionic,⁸² diacid PEG,¹⁰⁸ PAA.^{109,110}

Regarding the amine-terminated UCNPs, -NH₂ groups can create covalent bonds with groups such as -COOH, -CHO (aldehyde) and S = C = N (thiocyanate) contained in many biomolecules. The NH₂ groups can be provided by surface modifications with aminoundecanoic acid,¹⁰⁸ PEI,^{111–113} diamino-PEG,^{114,115} PAH,¹¹⁶ PAMAM,¹¹⁷ 2-aminoethyl dihydrogen phosphate (AEP),¹¹⁸ and (3-aminopropyl) triethoxysilane (APTES).^{113,119} As an interesting example, Xiong and co-worker reported the synthesis of UCNPs modified with 6-aminohexanoic acid, which contained a high amine content for subsequent conjugation with FA.¹²⁰ It was shown that the resulting nanocomposites were effective in targeting HeLa cells that overexpress folate receptors.¹²⁰

It is known that biomolecules such as cysteines and thiolated peptides have active -SH (thiol) groups that preferentially react with maleimide groups in the UCNPs. A strong carbon-sulphur bond can be formed between the carbon double bond in the maleimide group of the UCNPs and the thiol group. For this purpose, the maleimide groups can be introduced into the UCNPs using maleimide PEG or *via* the reaction between the N-hydroxysuccinimide ester (NHS) and the amine-terminated UCNP.³⁴

1.2.5 Strategies for enhancement of upconversion efficiency

1.2.5.1 Creating a core@shell structure

The first study of the core@shell UCNPs was reported in 2006 by Lezhnina and et al.¹²¹ They created different core@shell UCNPs including EuF₃@GdF₃, GdF₃@EuF₃, LaF₃: Yb,

Ho@LaF₃, and LaF₃: Nd@LaF₃. In 2007, Yi et al.¹²² synthesized NaYF₄: Yb, Er@NaYF₄ and NaYF₄: Yb, Tm@NaYF₄ and achieved 7 and 29 times luminescence enhancement for the UCNPs doped with Yb³⁺/Er³⁺ and Yb³⁺/Tm³⁺, respectively.¹²² Since then, many core@shell nanocomposites have been prepared to improve the efficiency, such as NaYF₄: Yb, Er@NaGdF₄ and NaYF₄: Yb, Tm@NaGdF₄,^{123–125} NaYF₄: Yb, Er @NaYF₄,¹²⁶ NaYF₄: Yb, Tm@NaYF₄,¹²⁷ NaGdF₄: Yb, Tm@NaGdF₄,¹²⁸ NaGdF₄: Yb, Er@NaGdF₄,¹²⁹ NaGdF₄: Nd@NaGdF₄,¹³⁰ NaGdF₄: Ce, Tb@NaYF₄,¹³¹ CeF₃: Tb@LaF₃,^{132–134} KYF₄: Yb, Er @KYF₄,¹³⁵ YOF: Yb, Er@YOF,¹³⁶ and so on.

The shells mentioned so far are all host shells without dopants and are called inert shells. The core@active shell strategy is similar and the difference is that instead of using an inert shell material, a reasonable concentration of Ln³⁺ ions is introduced to the shell layer.¹³⁷ In 2009, Capobianco's group¹³⁸ synthesized for the first time an active shell around UCNPs. They grew a NaGdF₄ shell doped with Yb³⁺ ions around the NaGdF₄: Yb, Er UCNPs (see **Figure 10**). The nanocomposite showed a strong enhancement of the green and red emission bands. The UC emission of the core@active shell UCNPs showed greater intensities by a factor of about 3 (green) and 10 (red) compared to the standard core@shell UCNPs with a doped core and an inert shell.¹³⁸ In general, this new concept of core@active shell has important implications for the design of UCNPs, where the cross-relaxation effect between different Ln³⁺ dopants can be eliminated by the spatial confinement of the Ln³⁺ into different layers.¹³⁷

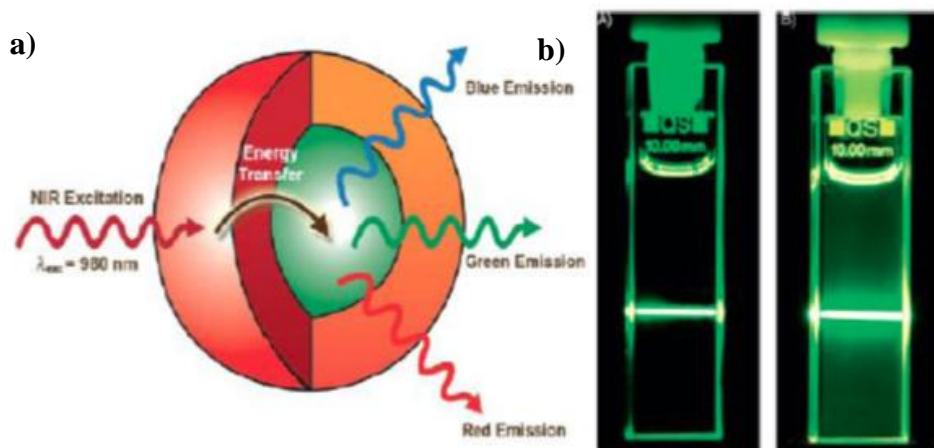


Figure 10. (a) Illustration of the core@active-shell UCNPs showing the absorption of NIR light by the Yb³⁺ ions doped in the shell (represented in red) and subsequent energy transfer to the Er³⁺/Yb³⁺ co-doped in the core (represented in green), which leads to upconverted blue, green, and red emissions. (b) Digital photographs of colloidal solutions of

NaGdF₄:Er³⁺/Yb³⁺@NaGdF₄ and NaGdF₄:Er³⁺/Yb³⁺@NaGdF₄:Yb³⁺ UCNPs under excitation with 980 nm. Reproduced from Ref. ¹³⁸

1.2.5.2 Plasmonic-enhanced upconversion luminescence

It is well known that metal nanostructures can efficiently collect light and enhance the intensity of the re-emitting light due to surface plasmon resonances (SPR). For the case of UCNPs, the principle is that the UC luminescence efficiency can be enhanced by tuning the SPR peak to the excitation/emission wavelength. ^{13,139} It is well known that the distance between the UCNPs and metal surface is crucial for plasmonic modulation of luminescence. Quenching would occur when the UCNPs are in direct contact with metallic surface and enhancement of the luminescence would occur on moving the UCNPs away from the metal surface at some critical distance. ^{13,139}

In 2010, Stucky's group ¹⁴⁰ reported the synthesis of Ag@SiO₂@Y₂O₃: Er structure using different SiO₂ thicknesses as spacers and they found that the optimal spacer thickness was 30 nm. Duan's group reported the modulation of UC luminescence through plasmonic interactions between AuNPs and NaYF₄: Yb, Tm. ¹⁴¹ They observed that the AuNPs enhanced the UC luminescence intensity by a factor of 2.6. From their experiments, they also observed that the formation of an Au shell suppressed the emission due to the strong scattering of the excitation irradiation. Indeed, it is well known that the SPR peaks of the AuNPs are confined around 500–550 nm and a selective enhancement occurs for this emission peak only. It is predicted "however" that enhancement for the UC emission peaks can be achieved if the SPR peak is tuned to NIR region and resonates with the absorption of UCNPs at 980 nm. In 2012, Priyam et al. ¹⁴² reported a poly-(amino acid)-templated Au shell encapsulation of the silica coated NaYF₄:Yb,Er UCNPs. They tuned the SPR peaks from the visible to the NIR region and they observed how the UC luminescence transformed from a quenching effect into an enhancement effect. ¹⁴²

In 2015, Liu and Lei ¹⁴³ carried out a theoretical study to investigate the luminescence enhancement of UCNPs in the vicinity of AuNRs. Their results demonstrated that when the localized surface plasmon resonance (LSPR) of AuNR is tailored to match both the excitation and emission wavelength of UCNPs, the total luminescence enhancement factor of the UCNPs has a strong dependence on the emitter-nanorod separation distance. The results demonstrated a maximum enhancement factor of ~120 fold and ~160 fold at emission wavelengths 650 and 540 nm, respectively.

More recently, in 2016, Luoshan¹⁴⁴ prepared a multi-shell of hexagonal NaYF₄:Yb,Er@SiO₂@Au@TiO₂ and incorporated into the photoanodes of a dye-sensitized solar cells (DSSCs). They investigated the influences of different coating layers and decorated Au-NPs on the performance of the DSSCs. Their studies indicated that the coated multi-shells had great influences on the UC and the properties of DSSCs.¹⁴⁴ Chen and co-worker prepared a nanocomposite of NaYF₄: Yb, Er@SiO₂ with Au nanorods (AuNRs) and use them for photodynamic therapy (PDT). They observed a plasmon enhanced PDT strategy by using the nanocomposites.¹⁴⁵

1.2.6 Applications

1.2.6.1 Thermal sensing

In recent years, luminescence nanothermometry has become a novel technique used to detect the local temperature of a living cell with sub-micrometer spatial resolution. It is well known that the luminescence generated from UCNPs doped with Ln³⁺ is produced by the emission of a photon of light when an electron relaxes from the excited state to the ground state. The properties of the emitted photons depend on the properties of the electronic states involved in the emission mechanism, which in turn depend on the local temperature. Therefore, when temperature changes, there is an overall change in emission intensity.¹³ Due to this, thermal sensing from the analysis of light can be achieved by exploiting the relationship between temperature and luminescence properties.¹³

The separation between the energetic levels of the Ln³⁺ ions has considerable effect upon the luminescence of the UC. When this separation is small, the electrons thermally populate and re-distribute in energy levels with similar energy, according to the Boltzmann distribution:¹³

$$N_i = C \times e^{\frac{-\varepsilon_i}{KT}} \quad (1)$$

where N_i is the population of a state i , ε_i is state energy, K is the Boltzmann constant and T is the temperature. Based on the Boltzmann distribution, small temperature changes would activate the population redistribution of the various energy states of Ln³⁺.

To date, there are several examples of luminescence nanothermometry applied to UCNPs, but among them, the thermometer based on UCNPs doped with the ion pair Yb³⁺/Er³⁺ is the most studied.^{146–150}

In a typical experiment, the $\text{Yb}^{3+}\text{-Er}^{3+}$ co-doped materials can be excited under laser irradiation at 980 nm, generating green and red emission. As we already mentioned, the green and red emission occur from the $^2\text{H}_{11/2}$, $^4\text{S}_{3/2} \rightarrow ^4\text{I}_{15/2}$ and $^4\text{F}_{9/2} \rightarrow ^4\text{I}_{15/2}$ transitions, respectively. Since the $^2\text{H}_{11/2}$ and $^4\text{S}_{3/2}$ states are very close in energy, the lower energy state ($^4\text{S}_{3/2}$) can thermally populate the higher energy state ($^2\text{H}_{11/2}$). As the temperature of the surroundings increase, the probability of the lower ($^4\text{S}_{3/2}$) state thermally populating the higher ($^2\text{H}_{11/2}$) state increases, causing a change in the relative intensities of the two emission bands ($^2\text{H}_{11/2} \rightarrow ^4\text{I}_{15/2}$ and $^4\text{S}_{3/2} \rightarrow ^4\text{I}_{15/2}$). Therefore, it is possible to use Er^{3+} -doped materials as thermal sensors by exploiting the intensity ratio of these two green emissions.

The use of $\text{NaYF}_4\text{:Er}^{3+}$, Yb^{3+} UCNP for single-cell thermal sensing was demonstrated by Capobianco's group.¹⁵¹ Intracellular thermal sensing was achieved by incubating UCNP in living HeLa cells after laser irradiation. Different voltages were applied to a metallic plate in physical contact with the cell, and representative transmission images of a single HeLa cell are shown in **Figure 11a**. The temperature of the HeLa cells was obtained from the changes of the relative intensities of luminescence bands, which is shown in **Figure 11b**. Intracellular temperature in the 25 – 45°C range with a sub-degree resolution as a function of the applied voltage could be monitored.¹⁵¹

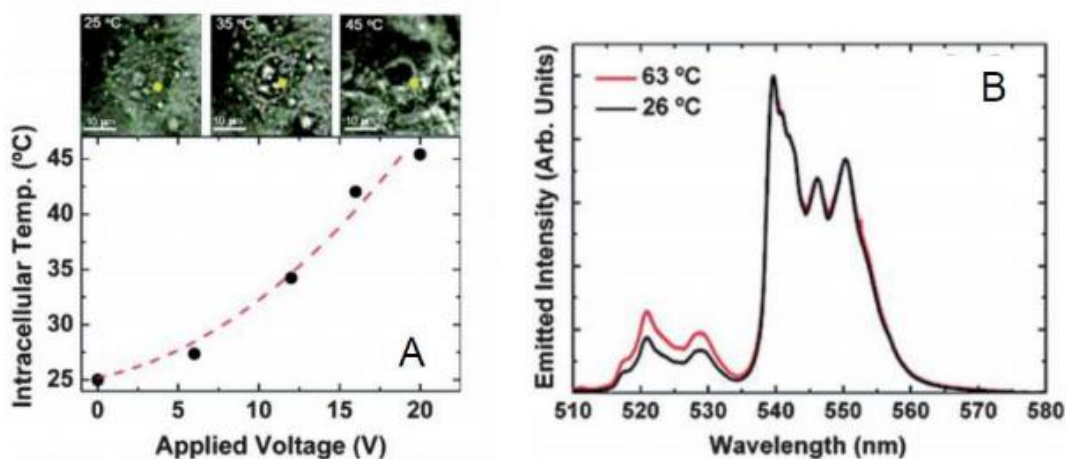


Figure 11. (a) Intracellular temperature as a function of the applied voltage and (b) luminescence emission spectra under laser excitation at two different temperatures. Reproduced from Ref.¹⁵¹

1.2.6.2 Bioimaging

Depending on the nature of the investigated biomaterial, the detection of biomolecules can be divided into *in vitro* and *in vivo* detection.

Regarding *in vitro* imaging, the first demonstration of the use of UC materials (Ln^{3+} doped yttrium oxysulfide) in diagnostics was reported about 20 years ago by Tanke's group^{152–154} and by Cooper's group.¹⁵⁵ Although at that time, the size of the UCNPs was in the range of hundreds of nanometers, the signal-to-noise ratio and the detection limit improved at least 100-fold compared to conventionally reported materials.¹⁵² By using 400 nm UCNPs, Cooper's group achieved a detection limit of 10 pg human chorionic gonadotropin in a 100 ml sample, a 10-fold improvement over conventional reporter systems like colloidal gold (Au).¹⁵⁵

However, smaller UCNPs with narrow size distribution and high luminescence efficiency were required by this time. In 2008, Ju's group prepared hydrophobic NaYF_4 UCNPs coated with amino and carboxyl groups in order to investigate their cellular cytotoxicity and cellular imaging.¹¹⁷ It was reported the cell imaging of these UCNPs, which were incubated with AB12 mouse mesothelioma cells. The results showed that the functionalized UCNPs had very low toxicity and high biocompatibility. Another example was studied by Capobianco's group in 2010. In their work they investigated the intracellular imaging of HeLa cells by using $\text{NaYF}_4:\text{Er}^{3+}$, Yb^{3+} UCNPs coated with PEI.¹⁵¹ Their results showed a redistribution of UCNP within the cell as the incubation time increased, which could have promising applications for real-time imaging of cell dynamics.¹⁵¹

Regarding *in vivo* imaging, Austin's group reported in 2006 the application of the NPs to image the digestive system of the nematode worm *Caenorhabditis elegans*.¹⁵⁶ In their studies, it was observed that there was strong luminescence in the intestines of the worms, and no cytotoxicity was detected over a 24 h period. However, the UCNPs used in this study were relatively large and the UC emission was weak.

In 2008, Zhang's group selected rats as models and injected UCNPs subcutaneously.¹⁵⁷ They observed a strong UC luminescence and it was confirmed that NIR excitation provided a very high penetration depth and a higher signal-to-noise ratio because the excitation wavelength is located in the "biological window" of the biological tissues.¹⁵⁷

In addition to the bioimaging utilizing the UC emission, there are other imaging modalities, including magnetic resonance imaging (MRI), computed tomography (CT), positron

emission tomography (PET), and single- photon emission computed tomography (SPECT).^{90,97,158} These imaging modalities vary in many aspects, and each of them has its own unique benefits and intrinsic limitations. The high potential of UCNPs as candidates for multimodal bioimaging was demonstrated (**Figure 12**).

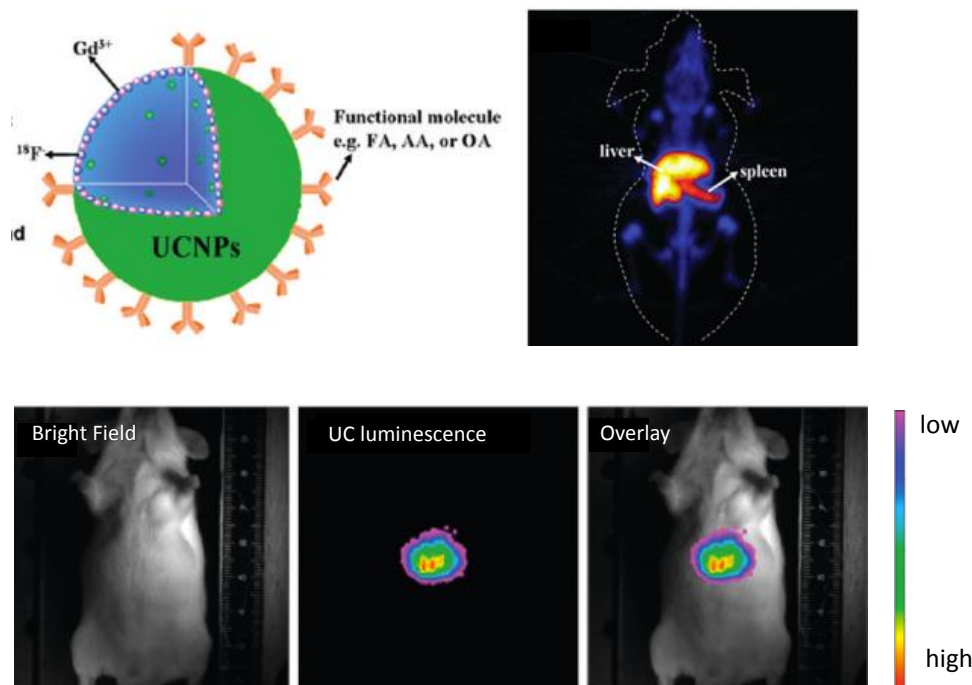


Figure 12. UCNPs-based multimode bioimaging. Adapted by Ref.⁹⁷

1.2.6.3 Photodynamic therapy

Photodynamic therapy (PDT) is a type of light-activated clinical treatment, which involves the use of a non-toxic and light sensitive drug, called photosensitizer (PS) to a tumour site. During the PDT, the PS is first introduced in the cells and upon light absorption, the PS is excited, generating reactive oxygen species (ROS), whose presence can trigger the death of the cells.^{159–161}

Although PDT is a promising therapeutic modality, already being used for numerous clinical cancer treatments,^{162 163 161} some limitations still persist, such as the need of UV or visible light to excite the photosensitizers. UV and visible light exhibit a limited penetration depth into and subsequently propagation out of biological samples and therefore limits application for deep-tissue imaging.

To overcome this limitation, the combination of UCNPs with PDT drugs has been introduced and gained great attention during the last years.¹⁶⁴ It is well known that NIR-excited UCNPs

can emit UV / visible photons, which in turn can be used to activate PS thereby generating ROS to kill the surrounding cancer cells. Therefore, the use of UCNP allows the use of NIR excitation wavelengths, increasing the penetration depth in the biological tissue of ~2 mm (in the case of standard PDT) to a few centimetres. Among other benefits, this would allow the treatment of deeper tumours and extend the versatility of this therapy.^{165,166}

In a typical experiment, NaYF₄:Yb³⁺, Er³⁺ UCNP as the upconverting material is combined with one or more PS, which absorption bands match perfectly the upconverted emissions from the UCNP. The first work combining UCNPs and PDT was published by Zhang et al. in 2007.¹⁶⁰ As a proof of concept, they coated UCNPs with a thin layer of silica where PS molecules were incorporated. In this manner, when the nanocomposite was irradiated by NIR light, emission from the UCNP resulted in the absorption by the PS molecules, which was coated on their surface, and the generation of free radicals.

However, depending on the PDT drug selected, other dopant ions could also be considered as good alternatives. Following this idea, in 2010, Zhang's group¹⁶⁷ prepared core@shell NaYF₄: Yb³⁺, Tm³⁺ @NaYF₄ Yb³⁺, Er³⁺ UCNPs, and attached covalently monomaleic fullerene (C60MA) by a crosslinking reaction between the amino group of the UCNPs and the carboxyl group of C60MA. Such molecules are particularly attractive because of their broad absorption spectra,¹⁶⁸ lack of dark toxicity, and high quantum yield to form reactive species.^{169,170} In this work, the efficiency of the resulting structure *in vitro* as well as the increased effect obtained thanks to the addition of Yb³⁺/Tm³⁺ dopants to the UCNPs was demonstrated.¹⁶⁶

1.2.6.4 UCNPs for drug delivery

UCNPs have emerged as an interesting element in drug delivery nanostructures, participating in monitoring drug location and studying the interaction with other cellular components. There are three approaches in literature to build up UCNP-based systems for drug delivery.¹⁷¹

Drug delivery systems consist of a porous shell in which the drug is loaded and slowly release in a rate normally regulated by diffusion. Owing to the biocompatibility of silica, silanization is to date one of the most popular techniques for NPs surface modification. In the case of UCNPs, a common strategy is to encapsulate them in a mesoporous silica shell, where the drug can be loaded through capillarity (**Figure 13a**). The UCNP core can act as a luminescence imaging probe, and the porous shell can load drugs for localized therapy.

For example, Lin's group added ibuprofen to mesoporous silica-coated β -NaYF₄:Yb³⁺/Er³⁺ and α -NaYF₄:Yb³⁺/Er³⁺ UCNPs, where the ibuprofen load was modulated by varying the thicknesses of mesoporous SiO₂ layers.^{137,172} The results demonstrated that the NPs could be used for controlled release of drugs. Moreover, it has been shown through intracellular analysis that mesoporous silica NPs were not toxic which motivates further research following this path.¹⁷³

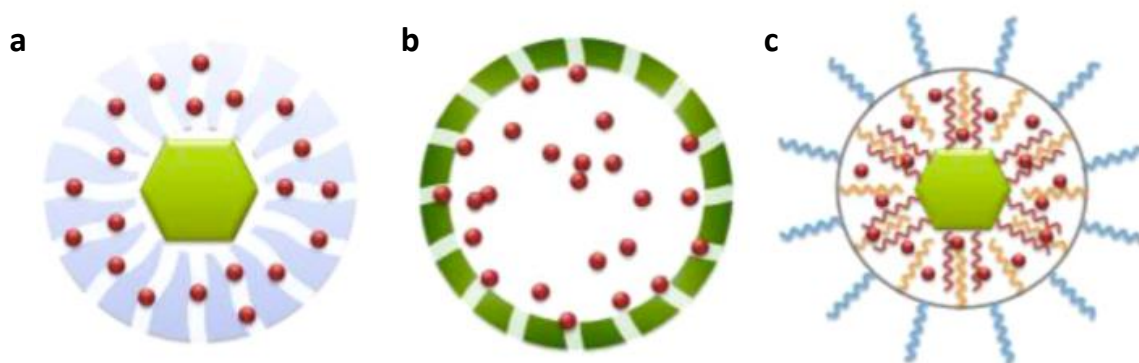


Figure 13. Schematic representations of the UCNPs-based drug delivery systems: (a) mesoporous shells, (b) hollow spheres, and (c) PEG grafted amphiphilic polymer with hydrophobic pockets. Adapted from Ref.¹⁷¹

A second strategy is to use hollow spheres with UCNPs encapsulating the drug (**Figure 13b**). In this regard, the group of J. Lin reported a self-sacrificing method to prepare UC hollow spheres.¹⁷⁴ They synthesized core-shell Yb(OH)CO₃@YbPO₄:Er³⁺ hollow spheres as drug carriers for the anticancer drug of doxorubicin (DOX), and showed that DOX loaded spheres released inside cells after endocytosis in 24 h.¹⁷⁴ Y₂O₃:Yb³⁺/Er³⁺ hollow nanospheres have been also synthesized by Yu's group for delivery of DOX into HeLa cells allowing high contrast cellular and tissue imaging with no damage from radiation.¹⁷⁵

The third strategy is to coat the UCNPs with an amphiphilic polymer (**Figure 13c**), which allows to transfer hydrophobic UCNPs into the biological environment. In this method, hydrophobic drugs are encapsulated into “hydrophobic pockets” on the UCNP surface utilizing the hydrophobic–hydrophobic interaction between the hydrophobic ligand on the particle surface and the drugs.

The group of Liu functionalized UCNPs with a polyethylene glycol (PEG) grafted amphiphilic polymer, modified the surface with folic acid to improve cancer targeting, and loaded DOX *via* physical adsorption.¹¹⁴ They observed that the loading and releasing of DOX from UCNPs was controlled by varying pH, with an increased drug dissociation rate

in acidic environment.¹¹⁴ Indeed, pH-sensitive polymers for controlled drug delivery have attracted the attention of many groups. The use of TWEEN 80¹⁷⁶ or poly(acrylic acid)-modified UCNP,¹⁷⁷ are some examples of pH-sensitive polymers showing optimal properties as carriers and pH dependent drug release.

1.2.6.5 Photocatalysis

Aside from the application in biology and nanomedicine, UCNP have also been studied for use in alternative energy applications such as photocatalysis.^{178–193}

Photocatalysis is an environmentally friendly solution for air and water contamination, and soil pollution.^{194–197} Generally, the materials used in photocatalysis are semiconductors which have band gaps that coincide with the wavelength of the light source. The most commonly used photocatalysts for the degradation of organic pollutants include TiO_2 ,^{198,199} ZnO ²⁰⁰, CdS ²⁰¹, and Bi_2WO_6 .²⁰² Although these are very efficient materials for photocatalysis, they are wide-band semiconductors and work only in the high-energy UV region, which comprises less than 6% of the solar spectrum. The NIR region covers however, about 46% of the solar energy spectrum. Therefore, the UCNP absorbing NIR and emitting UV-Vis can be utilized for enhancing the photocatalytic efficiency by integrating them with one of the aforementioned materials.

The first report for UC materials used for photocatalysis is from Xu's group in 2006. They developed a photocatalyst material, based on a physical mixture of $40\text{CdF}_2 \cdot 60\text{BaF}_2 \cdot 1.0\text{Er}_2\text{O}_3$ with TiO_2 .²⁰³ To date, there are several studies of hybridizing $\text{NaYF}_4: \text{Yb}^{3+}, \text{Tm}^{3+}$ UCNP with conventional oxides, such as TiO_2 , which showed excellent photocatalytic activity.^{181,183,204}

As previously mentioned, UCNP can convert lower energy NIR excitation light to higher energy photons. $\text{Yb}_{3+}/\text{Tm}_{3+}$ co-doped UCNP can be employed in combination with TiO_2 materials. Upon 980 nm of light excitation, this material emits two peaks in the UV range at 290 nm and 350 nm. They correspond to the $^1\text{I}_6 \rightarrow ^3\text{H}_6$ and $^1\text{I}_6 \rightarrow ^3\text{F}_4$ transition of Tm^{3+} ion, respectively.¹⁸² The converted UV or visible emission can be recaptured and reused by photon acceptors, such TiO_2 to generate free radicals (e.g. $\cdot\text{OH}$ and $\cdot\text{O}_2^-$). See **Figure 14**.

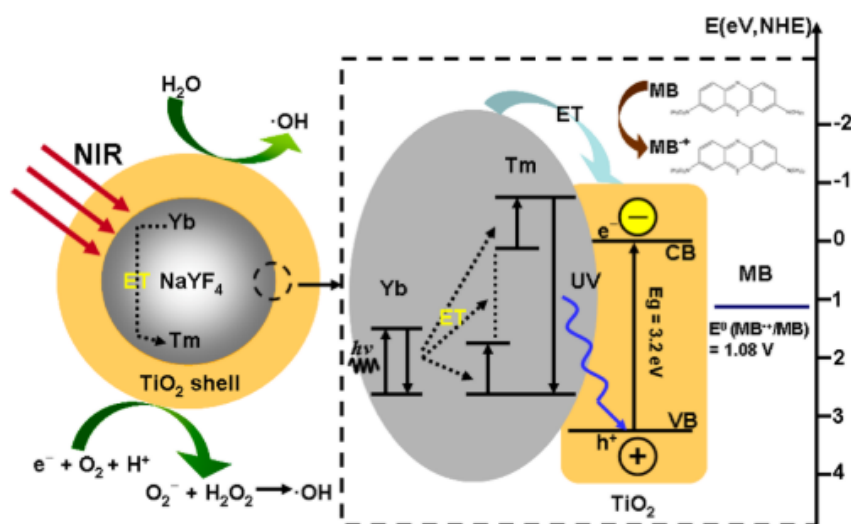


Figure 14. Illustration of the energy transfer mechanism among $\text{Yb}^{3+}/\text{Tm}^{3+}$ and TiO_2 in a photocatalytic process and the generation of $\bullet\text{OH}$ radicals *via* the reaction of electron and hole with the surface species of TiO_2 . Reproduced by Ref.¹⁸¹

Synthesizing a photocatalyst that is able to harvest all three regions of the solar spectrum, UV, visible, and NIR, to degrade organic pollutants has always been an active area of research. In 2017, the group of Claverie synthesized a core/shell nanohybrid photocatalyst with $\text{NaGdF}_4: \text{Yb}^{3+}/\text{Er}^{3+}$ as the core, and bismuth ferrite (BiFeO_3) as the shell.²⁰⁵ BiFeO_3 , with a bandgap of $\sim 2.0\text{--}2.6$ eV, exhibits excellent response both to UV, and visible light.^{206,207} In their experiments, they observed that the UC green emission from the Er^{3+} ion was partially absorbed by the BiFeO_3 . They demonstrated that the core/shell photocatalyst was able to photodegrade organic compounds such as methyl orange and 4-chlorophenol under visible and NIR irradiation illumination.²⁰⁵

In general, the preparation of photocatalytic systems with increased photocatalytic efficiency remains challenging. In most photocatalysts, photogenerated electrons and holes tend to quickly recombine to form electron-hole pairs, thus suppressing the catalytic reactivity of the photocatalysts.²⁰⁸ In order to solve this problem various alternatives have been proposed. For instance, the use of graphene sheets, which are excellent conductors capable of facilitating electron transfer and stabilizing the photogenerated electrons and holes upon NIR light irradiation.²⁰⁸ In 2012, Ren et al.²⁰⁹ fabricated a system composed of P25 with reduced graphene-oxide sheets and $\text{NaYF}_4: \text{Yb}/\text{Tm}$ UCNPs. They observed that after 10 min of irradiation with simulated sunlight (AM1.5 G), methylene orange molecules degraded in a 30%.

In another attempt to inhibit the recombination of the photogenerated charge carriers, Chen et al reported a highly efficient water-splitting system based on ZnO nanorod arrays, CdTe quantum dots, and gold plasmon-enhanced NaYF₄: Yb /Er UCNPs.²¹⁰ When irradiated at 980 nm, the visible photons emitted by the NaYF₄: Yb /Er UCNPs were absorbed by the CdTe quantum dots, resulting in the formation of electrons at the conduction band and holes at the valence band according to **Figure 15**. The electrons at the excited states were then transferred to the conduction band of the ZnO nanorod, effectively preventing the recombination of the electrons and the holes.

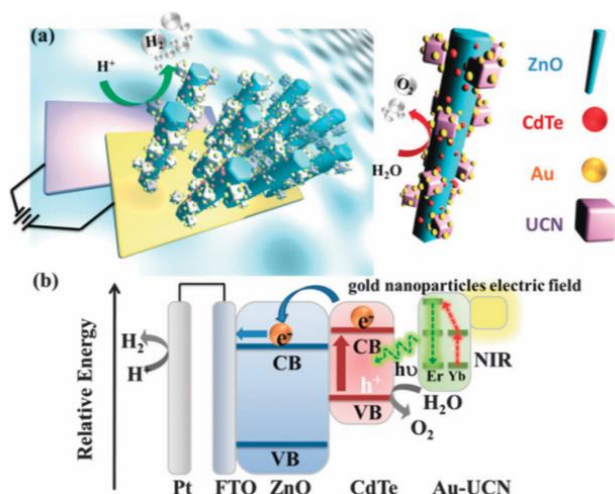


Figure 15. Illustration of the (a) Au-UCNs–CdTe–ZnO system and (b) the mechanism of energy transfer. Reproduced by Ref. ²¹⁰

Chapter 2 Experimental procedures

2.1 Synthesis of lanthanides doped upconversion nanoparticles

2.1.1 Synthesis of β -NaYF₄

β -NaYF₄: Yb³⁺(20%), Er³⁺(2%) UCNPs were synthesized following a previously reported protocol with slight modifications.⁵⁴ The synthesis was done using a Schlenk - line (see **Figure 165** in **Appendix A**). In a 100 mL three-neck round-bottomed flask, YCl₃·6H₂O (0.78 mmol, 236 mg), YbCl₃·6H₂O (0.20 mmol, 77.50 mg), and ErCl₃·6H₂O (0.02 mmol, 7.63 mg) were mixed together with 6 ml of OA (90%) and 15 mL of ODE (90%). The solution was then heated to 150 °C under the presence of Ar gas for 1 h and 30 min. After that, the solution was cooled down to room temperature, and a mixture of NaOH (2.5 mmol, 100 mg) and NH₄F (4 mmol, 148.16 mg) dissolved in 10 mL of methanol was added dropwise under vigorous stirring.

The mixture was stirred for 45 min at room temperature. After evaporating methanol, vacuum was applied for 30 min at 100 °C. Finally, the solution was heated up to 305 °C and maintained for 1 h and 20 min under an Ar atmosphere. The solution was cooled down naturally, and β -UCNPs were precipitated by centrifugation and washed with ethanol three times (8000 rpm, 15 min). The as-prepared β -UCNPs were dried and weighted. Then, they were re-dispersed in hexane or chloroform (CHCl₃) depending on further experiments, and stored for further use.

β -NaYF₄: Yb³⁺(20%), Tm³⁺(0.5%) UCNPs were synthesised with a similar protocol as above, by adding the corresponding YCl₃·6H₂O (0.795 mmol, 241.17 mg), YbCl₃·6H₂O (0.20 mmol, 77.50 mg), and TmCl₃·6H₂O (0.005 mmol, 1.92 mg) at the initial step of the reaction.

2.1.2 Synthesis of a shell of β -NaYF₄

The as synthesised β -UCNPs in **Section 2.1.1** served as core to grow an epitaxial shell of β -NaYF₄. The synthesis was again performed using a standard Schlenk-line following a method described in the literature with some modifications.^{77,211} In a 100 ml three-neck round bottom flask, YCl₃·6H₂O (0.5 mmol, 151.68 mg) was mixed with 6 ml of OA and 15 ml of ODE under Ar gas flow. The solution was heated to 150 °C to form a homogenous mixture. After that, the solution was cooled down to 80 °C under a steady flow of Ar, and the

previously prepared core β -UCNPs (125 mg) dispersed in CHCl_3 (20 mg/ml) were added. After removal of the CHCl_3 , the temperature of the solution was reduced to room temperature and a mixture of NaOH (1.25 mmol, 50 mg) and NH_4F (2 mmol, 74.08 mg) dissolved in 5 ml of methanol was added dropwise under vigorous stirring. The mixture was stirred for 45 min at room temperature. After evaporation of the methanol, the solution was heated up to 305 °C and maintained for 1 hour and 40 min under Ar atmosphere. The as-prepared β -UCNPs were cooled down naturally and were precipitated by centrifugation, and washed with ethanol three times (8000 rpm, 15 min). Finally, β -UCNPs were dried and weighted, and then re-dispersed in hexane, and stored for further use.

Various shells such as β -NaGdF₄, β -NaLuF₄, and β -NaYF₄: Yb³⁺(10%) were also created around the β -NaYF₄: Yb³⁺(20%), Er³⁺(2%) core structure by using a similar procedure. Essentially, the only difference between the different reactions was the addition of GdCl₃·6H₂O (0.5 mmol, 185.85 mg), LuCl₃·6H₂O (0.5 mmol, 194.71 mg), and YCl₃·6H₂O (0.45 mmol, 136.5 mg) and YbCl₃·6H₂O (0.05 mmol, 19.38 mg), respectively, at the first stage of the main reaction as reported above.

2.1.3 Synthesis of small β -NaYF₄ doped with Gadolinium

The synthesis of β -NaY(58%)/Gd(20%)F₄: Yb³⁺(20%), Er³⁺(2%) UCNPs was carried following a similar protocol to the one described in **Section 2.1.1** with some modifications in the RECl₃·6H₂O concentration and time reaction.^{212,213} Essentially, 1 mmol of RECl₃·6H₂O was mixed together with 6 ml of OA and 15 ml of ODE in a 100 mL three-neck round-bottomed flask. The salt concentrations were YCl₃·6H₂O (0.58 mmol, 175.95 mg), YbCl₃·6H₂O (0.20 mmol, 77.5 mg), ErCl₃·6H₂O (0.02 mmol, 7.63 mg), and GdCl₃·6H₂O (0.20 mmol, 74.34 mg). The solution was heated to 150 °C under the presence of Ar gas for 1 h and 30 min to form a homogenous solution and then, cooled to room temperature. A solution of 10 ml of methanol containing NaOH (2.5 mmol, 100 mg) and NH_4F (4 mmol, 148.16 mg) was slowly added to the flask. The solution was stirred for 45 min at room temperature and after evaporating methanol, vacuum was applied for 30 min at 100 °C. Then, the temperature of the solution was raised to 305 °C and maintained for 1 h under an Ar atmosphere. After the solution was cooled down, β -UCNPs were precipitated by centrifugation, and washed with ethanol three times (8000 rpm, 15 min). The as-prepared β -UCNPs were re-dispersed in hexane and stored for further use.

2.1.4 Synthesis of large β -NaYF₄ doped with Lutetium

The synthesis of β -NaY(28%)/Lu(50%)F₄: Yb³⁺(20%), Er³⁺(2%) UCNPs was carried following a similar protocol to the one described in **Section 2.1.1** and elsewhere.²¹⁴ In detail, 1 mmol of RECl₃·6H₂O was mixed together with 6 ml of OA and 15 ml of ODE in a 100 ml three-neck round-bottomed flask. The concentrations for each case were YCl₃·6H₂O (0.58 mmol, 175.95 mg), YbCl₃·6H₂O (0.20 mmol, 77.5 mg), ErCl₃·6H₂O (0.02 mmol, 7.63 mg) and LuCl₃·6H₂O (0.50 mmol, 194.71 mg). The solution was heated to 150 °C under the presence of Ar gas for 1 h and 30 min to achieve a complete solubilisation of salts. After that, the solution was cooled down to room temperature, and a mixture of NaOH (2.5 mmol, 100 mg) and NH₄F (4 mmol, 148.16 mg) in 10 ml of methanol was added. The mixture was stirred for 45 min at room temperature and after evaporating methanol, vacuum was applied for 30 min at 100 °C. Finally, the solution was heated up to 308 °C and maintained for 1 h and 35 min under an Ar atmosphere. The solution was cooled down naturally and β -UCNPs were precipitated by centrifugation and washed with ethanol -three times (8000 rpm, 15 min). The as-prepared β -UCNPs were re-dispersed in hexane and stored for further use.

2.1.5 Synthesis of Na_xScF_{3+x}

The Na_xScF_{3+x}: Yb³⁺(20%), Er³⁺(2%) UCNPs were synthesized following a previously reported protocol with slight modifications.^{215,216} In a typical experiment, ScCl₃·6H₂O (0.78 mmol, 196.19 mg), YbCl₃·6H₂O (0.20 mmol, 77.50 mg) and ErCl₃·6H₂O (0.02 mmol, 7.63 mg) were added to a 100 ml three-neck round bottom flask along with 15ml of OA and 15 ml of ODE. The solution was then heated to 160 °C under the presence of Ar gas for 1 h and 30 to form a homogenous solution. Subsequent, a certain amount of NaF (1.5 mmol, 62 mg) was added as powder directly into the reaction mixture. After 45 min of stirring, the temperature of the solution was raised to 308 °C and held for 1 hour and 40 min under an Ar atmosphere. Then, the solution was allowed to cool naturally and the product was collected by centrifugation and washed with ethanol (8000 rpm, 15 min). The obtained β -UCNPs were re-dispersed in hexane and stored for further use.

2.2 Synthesis of other types of nanoparticles

2.2.1 Synthesis of AuNRs

Gold nanorods (AuNRs) were synthesised following a seed-mediated protocol reported by El-Sayed ²¹⁷ with slight modifications where the aspect ratio (AR) was controlled by the amount of silver nitrate (AgNO_3) used.

Gold (Au) seeds were synthesised by mixing a CTAB solution (0.2 M, 1 ml) with a sodium tetrachloroaurate (III) dehydrate solution (NaAuCl_4) (5 mM, 1 ml) in a small glass tube. While stirring, an ice-cold solution of sodium borohydride (NaBH_4) (0.01 M, 0.5 ml) was added dropwise resulting in a sudden change of the reaction colour from colourless to dark brown, indicating the formation of the Au seeds. After two minutes, the stirring was stopped.

Alongside, in a 50 ml Erlenmeyer flask, the growth solution was prepared by heating a solution of CTAB (0.2 M, 14.24 ml) at 40 °C. Then, a NaAuCl_4 solution (5 mM, 2 ml) and an AgNO_3 solution (5 mM, x ml) were added successively, where the amount of the latter was varied from 0.15 ml to 0.4 ml in different experiments. Under stirring, a fresh L-ascorbic acid solution (78.8 mM, 0.16 ml) was added into the flask and the colour of the reaction changed to colourless. Immediately after 30 seconds, the as-prepared Au seeds solution (16 μl) was injected into the growth solution and the stirring was stopped. The flask was left overnight at 40 °C for completion of the reaction and then, the precipitate was collected by centrifugation (8000 rpm, 20 min). The resulting AuNRs were washed and re-dispersed in Milli-Q water and stored at 4°C for further use.

2.2.2 Synthesis of high aspect ratio AuNRs

The synthesis of long AuNRs was done following the work developed by Murphy et al ²¹⁸ with minor modifications.

Au seeds were prepared by mixing a sodium citrate solution (25 mM, 0.2 ml) with a NaAuCl_4 solution (0.25 mM, 19.8 ml) and stirred for 3 min. Simultaneously, a solution of NaBH_4 (0.01 M) was prepared in 10 ml of ice-cold sodium citrate solution (0.025 M). Then 0.6 ml of the NaBH_4 solution was injected into the NaAuCl_4 solution and the colour changed from orange to dark red, indicating the formation of Au seeds.

The growth solution was prepared by dissolving CTAB (0.01 mol) in 100 ml of a NaAuCl_4 solution (0.25 mM). The solution was then poured into three flasks (4.5 ml into flask A, 4.5

ml into flask B, and 45 ml into flask C). Subsequently, freshly prepared L-ascorbic acid (0.1 M) was added to each flask (25 μ l in flask A and B, and 250 μ l in flask C). Nitric acid (HNO_3) (200 μ l) was added additionally in flask C.

In a typical procedure, 400 μ l of an Au seeds solution was added to the solution in flask A and stirred for 5 seconds. Then, 400 μ l of solution in flask A was added promptly to flask B and stirred for 10 seconds. Immediately, 4 ml of solution in flask B was added to flask C and the solution was left to stand. Flask C was left overnight at 40 °C for the completion of the growth and then the precipitate was collected by centrifugation (8000 rpm, 20 min). AuNRs were washed and re-dispersed in Milli-Q water and stored at 4°C for further use.

2.3 Surface modification on upconversion nanoparticles

2.3.1 Annealing treatment

The β -UCNPs were annealed following a reported protocol with minor modifications.²¹⁹ In detail, OA coated β -UCNPs (100 mg) in hexane (10 ml) were added to a 100 ml three-neck round bottom flask together with OA (8 ml) and ODE (12 ml). The mixed solution was heated up gradually to 100 °C to evaporate the hexane. After 40 min, the temperature was increased to 240 °C and maintained for 1 hour and 30 min under Ar gas. The resulting annealed β -UCNPs were cooled down naturally, collected by centrifugation and washed with ethanol three times (8000 rpm, 15 min). The annealed β -UCNPs were re-dispersed in hexane and stored for further use.

2.3.2 Silica shell

Silica coated β -UCNPs were prepared by a modified published protocol.²²⁰ A solution containing an appropriate amount of the annealed β -UCNPs (prepared as described in **Section 2.3.1**) dispersed in 10 ml of hexane was mixed with Igepal Co-520 (0.5 g, average M_n 441) and sonicated for 15 min. Ammonium hydroxide (NH_4OH) (35%, 100 μ l) was then added and the solution was shaken and sonicated vigorously for 20 min. Finally, tetraethyl orthosilicate (TEOS) (75 μ l) was injected into the solution under continuous stirring. The mixture was left stirring overnight and the precipitate was collected by centrifugation (8000 rpm, 10 min) and washed with ethanol three times. The resulting β -UCNPs coated by silica (β -UCNPs@ SiO_2) were re-dispersed in 5 ml ethanol and stored for further use.

2.3.3 Amine-functionalisation

Amine-functionalized silica coated β -UCNPs (β -UCNPs@SiO₂-NH₂) were prepared following a reported procedure with minor modifications.²²¹ In detail, (3-Aminopropyl) trimethoxysilane (APTMS) (0.5 ml) was added to a solution containing β -UCNPs@SiO₂ (100 mg) suspended in 10 ml of ethanol. Then, the reaction mixture was left stirring overnight. The resulted β -UCNPs@SiO₂-NH₂ were collected by centrifugation, washed with ethanol (8000 rpm, 15 min) and re-dispersed in 10 ml of Milli-Q water.

2.3.4 Growth of Au shell

The synthesis to create an Au shell around the UCNPs^{142,222} was carried out by the reaction of β -UCNPs@SiO₂-NH₂ (see **Section 2.3.3**) with a Au seeds solution, followed by growth of the Au shell.

Au seeds were prepared following Duff's method^{223,224} and they were stabilised with tetrakis(hydroxymethyl)phosphonium chloride (THPC). In a 100 ml Erlenmeyer flask, Milli-Q water (45 ml) and a NaOH solution (2 M, 0.25 ml) were mixed under vigorous stirring. Then, THPC in H₂O (80% v/v, 12 μ l) was added and two minutes later, a NaAuCl₄ solution (1%, 2 ml) was injected into the mixture. The colour changed from colourless to light brown indicating the formation of small Au seeds. The seeds were purified overnight by dialysis with a semi-permeable film of 10,000 MWCO against 500 ml of Milli-Q water. After purification, the resulting Au seeds dispersed in Milli-Q water (5 ml) were mixed with the as-prepared β -UCNPs@SiO₂-NH₂ (10 ml) for 2 hours at room temperature in the dark. The obtained β -UCNPs@SiO₂@Au seeds were washed with Milli-Q water several times to remove the excess of Au seeds and finally re-dispersed in 10 ml of Milli-Q water.

In the meanwhile, potassium carbonate (K₂CO₃) (25 mg, MW = 138.2) was dissolved in Milli-Q water (100 ml) at room temperature in a separate flask. A NaAuCl₄ solution (1%, 1.5 ml) was added and the mixture was stirred for 30 min. Then, the mixture was cooled down to 4 °C. Subsequently, 200 μ l of the β -UCNPs@SiO₂@Au seeds solution was added to a 4 ml of the cold growth solution. While stirring, formaldehyde (0.36 mmol, 10 μ l) was injected and the mixture was allowed to react for 5 min, until colour change from colourless to blue. The growth was terminated by the addition of thiol containing molecule (100 μ l, 5 mg/ml) (MW = 526.7), which binds to the Au surface and prevents further growth of NP. β -UCNPs@SiO₂@Au shell were purified by three steps of centrifugation and decantation (8000 rpm, 10 min), re-dispersed in Milli-Q water and stored at 4°C for further use.

2.3.5 Carboxylic acid functionalization

In a typical experiment, amine-functionalized β -UCNPs@SiO₂-NH₂ were dissolved in anhydrous DMF at a final concentration of 2 mg/ml (10 mg in 5 ml) and transferred into a 25 ml two-neck round bottom flask. Next, a solution of succinic anhydride (1.49 mmol, 150 mg) dissolved in anhydrous DMF (3 ml) was added dropwise with a syringe and the mixture was left stirring overnight. The whole process was conducted under Ar atmosphere. The carboxylic acid functionalized (β -UCNPs@SiO₂-COOH) were collected by centrifugation and the DMF solvent traces were removed with ethanol (8000 rpm, 10 min). The resulting β -UCNPs@SiO₂-COOH were re-dispersed in Milli-Q water and used for further functionalization with ssDNA.

2.3.6 Surface modification with oligonucleotides

2.3.6.1 Synthesis of oligonucleotides

Synthetic oligonucleotides used throughout this project were synthesised and supplied by Dr. Afaf El-Sagheer at the University of Oxford. The ssDNA probe sequence that was used to covalently link to the surface of the β -UCNPs was:

5'-aminohexyl-2AAACGGGCTTTTTTTTTTTTTTTTTTTTTTTTTTTTTTTT-3'.

2.3.6.2 ssDNA-attachment

The ssDNA functionalized β -UCNPs were prepared following a previously reported protocol with minor modifications.²²⁵

DNA was attached to the β -UCNPs@SiO₂-COOH using an EDC coupling reaction. In detail, β -UCNPs@SiO₂-COOH were re-dispersed in a borate-buffered solution (pH=8.5) at a concentration of 1 mg/ml. 1 ml of the former solution was transferred to an Eppendorf tube and EDC (20 μ l, 0.3 M) and s-NHS (20 μ l, 98%) in MES buffer were added. The mixture was shaken for 1 hour, and then, the ssDNA was added (112 μ l, 86.23 μ M). The reaction was shaken overnight, and the obtained β -UCNPs functionalized with ssDNA (β -UCNPs@SiO₂-ssDNA) were collected, purified by centrifugation twice (16 400 rpm, 20 min) and re-dispersed in Milli-Q water. The obtained solution was stored at 4 °C for further experiments.

2.3.6.3 Incubation of with A549 cells

A549 cells were grown on cover slips in a 12 well plates. When a confluence of 90% was reached, cells were incubated with a sample of β -UCNPs@SiO₂-ssDNA in Milli-Q water (1 mg/ml, 250 μ l) for 24 h. One well of cells without particles, was used as a control. The incubation process was carried out by Konstantina Alexaki and Maria-Eleni Kyriazi.

2.3.6.3.1 Preparation fixation and staining of cells on coverslips for confocal

Following the 24 h incubation period, cell media was removed carefully and wells were washed with PBS three times for 5 min. Cells were then fixed for 60 min with paraformaldehyde (PFA) (4%) and then washed with PBS three times for 5 min each time. Finally, cell nuclei were stained with 4',6-diamidino-2-phenylindole dihydrochloride (DAPI) for 15 min and finally rinsed with PBS three times for 15 min. For imaging, coverslips were removed with tweezers from the wells and mounted onto glass microscope slides and set in place using a Mowiol solution of glycerol. Fixation and staining of cells were carried out by Konstantina Alexaki and Maria-Eleni Kyriazi.

2.3.7 Ligand free

The synthesis was carried out following a reported protocol.⁴⁴ In detail, a solution containing OA coated β -UCNPs in hexane (5 mg, 5 ml) was transferred to a 10 ml glass tube. Next, a solution of HCl (0.1 M, 5 ml) was added and the mixture was left stirring for 2 hours. The water layer was extracted and washed several times with diethyl ether and ethanol by centrifugation. Finally, the ligand free β -UCNPs were re-dispersed in Milli-Q water and stored for characterization.

2.3.8 Ligand-Exchange reaction from OA to OAm

The ligand exchange of β -UCNPs was performed following a reported method with minor alterations.⁷² In a typical experiment, a solution of 5 ml of OA coated β -UCNPs dispersed in hexane (5 mg/ml) was mixed with a dichloromethane solution of NOBF₄ (5 ml, 0.01 M) to create a two-phase solution. The mixture was stirred until the β -UCNPs migrated to the CH₂Cl₂ phase. Then, the CH₂Cl₂ phase was isolated, and the product was purified by slowly adding a mixture of toluene and hexane (1:1 ratio). The β -UCNPs were collected and re-dispersed in 5 ml of DMF to obtain a stable colloidal dispersion. This was combined with hexane to form a two-phase mixture where OAm was added in excess. The sediment was

Chapter 2

washed and purified by precipitation using ethanol, and the resultant OAm coated β -UCNPs were re-dispersed in CHCl_3 .

2.3.9 Coating of TiO_2

2.3.9.1 Ligand exchange from OA to CTAB

The synthesis of hydrophobic β -UCNPs coated with CTAB was carried following a reported method with minor modifications.^{187,189} In detail, a solution of OA coated β - NaYF_4 : Yb^{3+} (20%), Tm^{3+} (0.5%) UCNPs dispersed in hexane (20 mg, 1 ml) was added to a 50 ml three-neck round bottom flask along with CTAB (0.05 g, 364.45 MW) and Milli-Q water (20 ml). The solution was magnetically stirred for 5 min and then the flask was put into a water bath and slowly heated to 80 °C. The mixture was allowed to react for 30 min until the colour changed from milky to transparent indicating the evaporation of the hexane. Then, the flask was removed from the water bath and the solution was naturally cooled down to room temperature. The obtained CTAB coated β -UCNPs were collected by centrifugation (8000 rpm, 15 min), purified with Milli-Q water and re-dispersed in 10 ml of isopropanol (IPA).

2.3.9.2 Synthesis of TiO_2

The as-prepared CTAB coated β -UCNPs were used as cores to grow a TiO_2 shell.^{187,189} The solution containing CTAB coated β -UCNPs in IPA (10 ml) was transferred to a 25 mL three-neck round-bottomed flask. While stirring, Milli-Q water (2.5 ml) and NH_4OH (0.3 ml, 35%) were added to the flask. Then, titanium diisopropoxide bis(acetylacetonate) (TDAA) (36 μl in 10 ml of IPA) was slowly injected into the flask. The mixture was left stirring overnight, and the product was collected by centrifugation (6000 rpm, 10 min) and washed with ethanol twice. To achieve a crystalline anatase phase, the resulting β -UCNPs coated by TiO_2 (amorphous β -UCNPs/ TiO_2) were annealed at 500 °C for 3 hours in a furnace under air atmosphere.

2.3.9.3 Modification of TiO_2 with Cobalt Oxide (CoOx) as co-catalyst

NPs of cobalt oxide (CoOx) were loaded on the surface of the as-prepared β -UCNPs / TiO_2 using an impregnation method with several modifications.²²⁶ In a typical experiment, β -UCNPs/ TiO_2 -anatase (20 mg) and a calculated amount of $\text{Co}(\text{NO}_3)_2 \cdot 6\text{H}_2\text{O}$ dissolved in acetone were transferred into a glass tube and sonicated for 5 min. The cobalt loadings in

this research are expressed as %wt. Cobalt and were fixed to 0%, 0.3%, 0.7%, 1%, 2% and 3% wt. Cobalt.

The solution was slowly heated until the acetone was completely evaporated, resulting in a homogenous deposition of the Co-catalyst on the surface of the β -UCNPs/TiO₂. The resulting product was stored overnight in a dry environment. Finally, the loaded β -UCNPs/TiO₂ were collected, placed in an appropriate alumina boat and calcined under air atmosphere at 150 °C for 2 h (ramp 10 °C / min).

2.3.9.4 Indicator ink.

A stock solution of ink was prepared following the work of Mills,²²⁷ by mixing 10 mg of a redox dye (Resazurin and DCPIP) and 1 g of glycerol into 10 ml of Milli-Q water. The ink was stirred vigorously for 1 h to ensure uniform mixing of the dye throughout the solution. The resulting ink was stored in the dark and used during the following week to avoid degradation.

2.4 Functionalization of upconversion nanoparticles with near-IR dyes

2.4.1 Chemical modification of a commercial IR-dye

The chemical functionalization of the dye IR-806 was performed following a previously reported synthesis with a few alterations.²²⁸ A mixture of the dye IR-780 iodide (250 mg, 0.375 mmol) and 4-mercaptobenzoic acid (115.5 mg, 0.75 mmol) was dissolved in dimethylformamide (DMF) (10 ml) and stirred overnight.

DMF was removed using a rotary evaporator under vacuum at 40 °C, and the residue was dissolved in CH₂Cl₂ (5 ml). Diethyl ether (70 ml) was added to precipitate the product. The sediment was washed twice with diethyl ether and dried under vacuum to collect the chemically modified IR-806 dye.

The chemical functionalization of the dye IR-1048 was performed with a similar protocol as above, by adding the corresponding IR-1048 at the initial step of the reaction.

2.4.2 Synthesis of the dye-sensitized β -UCNPs

To obtain the optimal surface coverage of β -UCNPs with dye molecules, a series of samples were prepared under Ar atmosphere. Different amounts of the IR dye were mixed with a fixed concentration of OAm coated β -UCNPs (synthesised according to **Section 2.3.8**) in

CHCl₃ to a final volume of 2 ml. The IR dye concentrations in the resulting CHCl₃ mixture were 0.000, 0.001, 0.003, 0.005, 0.007, 0.010, and 0.015 mg/ml. The OAm coated β -UCNPs concentration was fixed to 0.8 mg/ml in CHCl₃, and was kept constant for all the samples. Then, the mixture was stirred for 2 h at room temperature in the dark. All measurements including UC luminescence spectra were carried out within 24 hours after this synthesis.

For the dye-sensitized core@shell β -UCNPs, the increased weight of the core@shell structure due to the shell formation was not considered in our experiments, which could lead to an underestimation in the number of particles. In that case, also the concentration was fixed to 0.8 mg/ml and based on the core β -UCNPs.

2.5 Characterization Techniques

2.5.1 Transmission electron microscopy (TEM)

The size and morphology of the synthesized NPs were obtained using a Hitachi HT7700 transmission electron microscope operating with an accelerating voltage of at 80 kV. All the samples were prepared by ultrasonic dispersion in different solvents according to experiments. The solutions were then added drop-wise onto a 200 mesh holey carbon copper grid for analysis. The nanoparticle size distribution was analysed with ImageJ (National Institutes of Health, USA) software considering over 100 NPs for each sample. See error analysis for the size distribution in **Appendix E**.

2.5.2 Fourier transforms Infrared (FT-IR)

Fourier transform infrared (FT-IR) spectra were recorded for all the experiments in the spectral range of 525 and 4000 cm⁻¹ on a Nicolet iS5 FT-IR spectrometer at room temperature. For the sample preparation, nanoparticles were dried and deposited directly on the glass.

2.5.3 X-ray diffraction (XRD)

The analysis of the crystal phase of the different samples was conducted via XRD at the X-ray diffraction facility using a 2D-phaser Bruker diffractometer. For all experiments, the diffracted intensities were measured at room temperature from 2θ angles of 10° to 80°, with a resolution of 0.02° and an acquisition time of 0.2 seconds.

2.5.4 Jasco FT-IR 620 spectrometer

The NIR absorption spectra of NPs were recorded on a Jasco FT-IR 620 spectrometer. For the sample preparation, the UCNPs were dispersed in different solvents according to the specific experiment and the mixtures were placed in a quartz cuvette with a path length of 10 mm.

2.5.5 Ultraviolet/Visible spectrometer (UV-vis)

Absorbance measurements were carried out using a Denovix DS-11+spectrophotometer, with a 1 nm resolution from 200 to 800 nm. The volume of solution used for each analysis was 1 ml contained in polystyrene cuvettes with a 10 mm window.

2.5.6 Zeta-Potential

The determination of the zeta potential of suspended nanoparticles in solution was recorded in a Malvern Instruments Nano-Zetasizer. NPs were dispersed in milli-Q water and sonicated vigorously before analysis. For a typical analysis, a folded capillary cell was filled with the sample at very low concentration and Zeta values were measured at 25°C.

2.5.7 Confocal microscopy

Confocal microscope images were recorded thanks to the collaboration of Maria-Eleni Kyriazi, using the Leica TCS -SP8 laser scanning confocal microscope at the University Hospital Southampton.

2.5.8 EDX and elemental mapping

EDX and elemental mapping of the β -UCNPs/TiO₂ catalyst were recorded and analysed thanks to the collaboration of P.Goggin, from University Hospital Southampton using a FEI Tecnai T12 transmission electron microscope operating with an accelerating voltage of at 80 kV.

2.5.9 ¹H and ¹³C NMR spectra

¹H and ¹³C NMR spectra were recorded on AVII400 with 400 MHz and 101 MHz, respectively. Chemical shifts (δ) are reported in parts per million (ppm) using the solvent peak as an internal reference. For sample preparation, the organic compounds were dried under vacuum for 24 h and then dispersed in the corresponding deuterated solvent, CDCl₃

in our case. The following abbreviations are used to describe the signals: s = singlet, d = doublet, dd = double doublet, t = triplet, and m = multiplet.

2.5.10 Mass spectra

The mass spectrum was recorded by an ACQUITY UPLC H-Class System.

2.6 Laser set-up

2.6.1 Set-up for photoluminescence characterization of β -UCNPs

The photoluminescence characterization from **Chapter 3** and **Chapter 4** was done in a set-up built by Prof. Otto Muskens (see **Figure 16**). Different lenses and mirrors were used to direct and focus the beam of the laser (980 nm) onto the sample. The luminescence was collected by a spectrophotometer detector (350-1000 nm USB4000 Ocean Optics). All samples were measured using a quartz cuvette with a path length of 10 mm. As can be seen from the set-up diagram, the emission was collected at an angle of 90° to avoid any interference

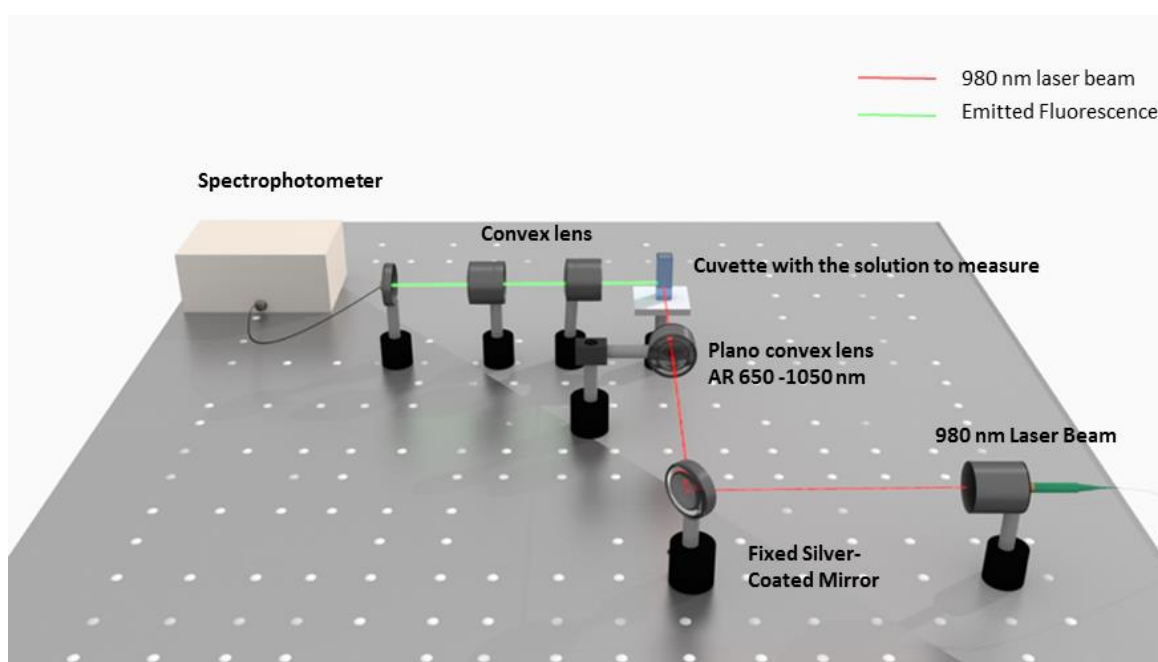


Figure 16. Laser setup for the analysis of UCNPs using a 980 nm laser.

Transmission measurements were taking using the same set-up but placing a power meter right after the cuvette to collect the power density after penetrating the samples as can be seen in **Figure 17**. A PDA100A-EC - Si Switchable Gain Detector, 340 - 1100 nm was used for the experiments.

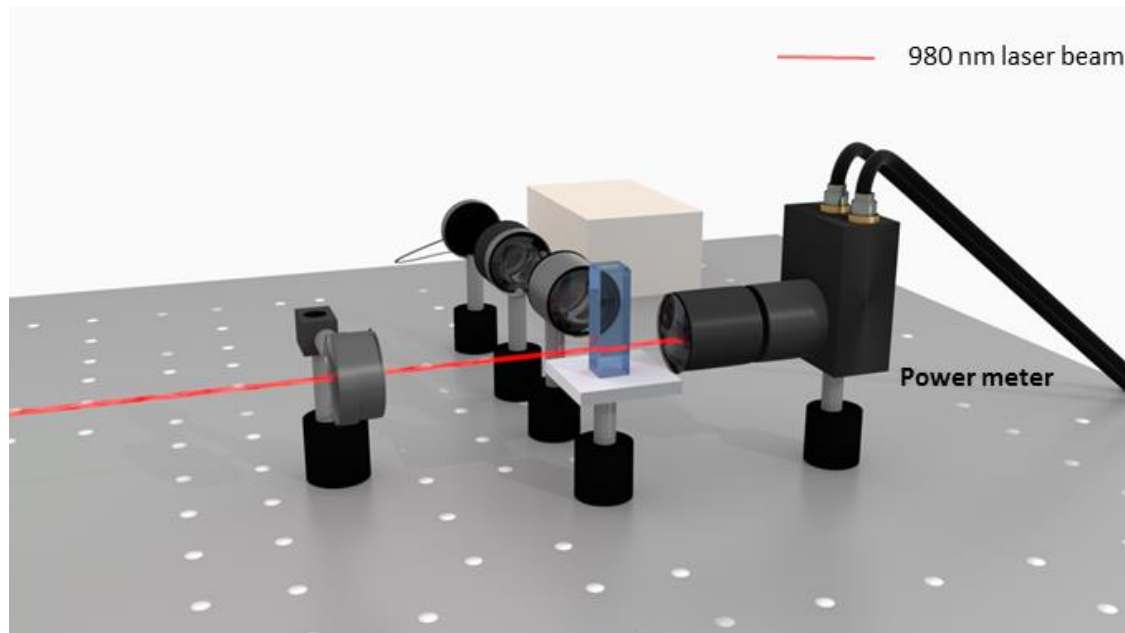


Figure 17. Schematic illustration for the transmission measurements.

2.6.2 Set-up used for UC emission of β -UCNPs incubated with A549 cells

The set-up consists of a set of mirrors and lenses, which conducts the laser beam to a $60\times$ objective lens. The emission signal is then guided back down through the objective and finally filtered by different filters depending on the experiment. Light excitation of 980 nm and 405 nm were used to track the emission of the β -UCNPs and DAPI, respectively. A photograph of the setup is shown in **Figure 18**.

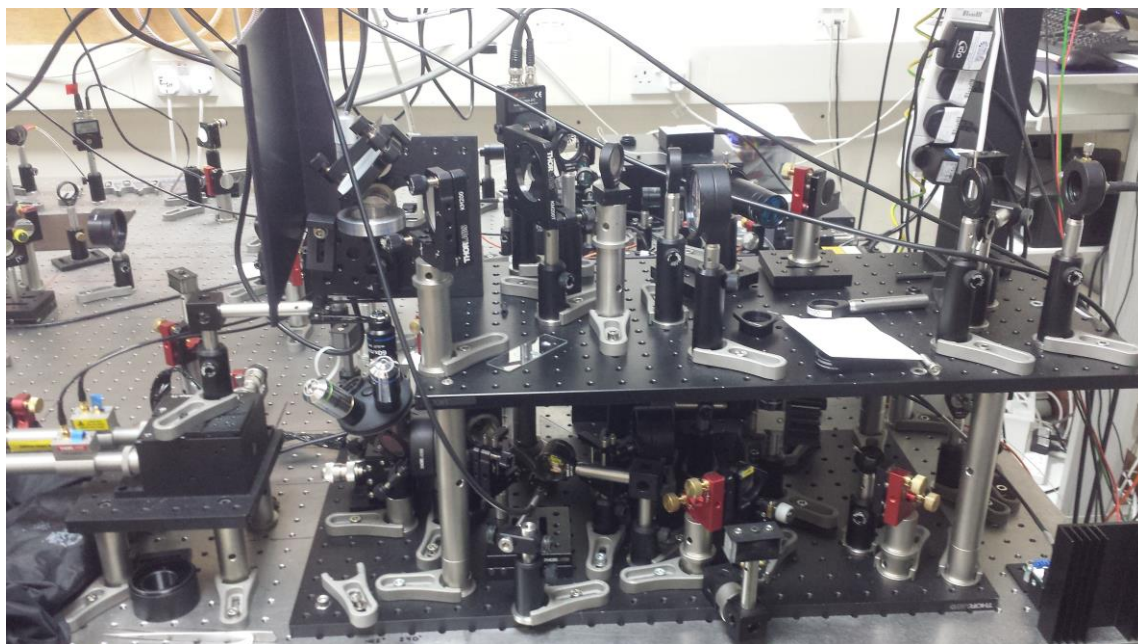


Figure 18. Digital images of the set-up used for detection of UC emission in cells incubated with β -UCNPs@SiO₂-ssDNA.

For clarity a schematic diagram of the set-up is shown in **Figure 19**.

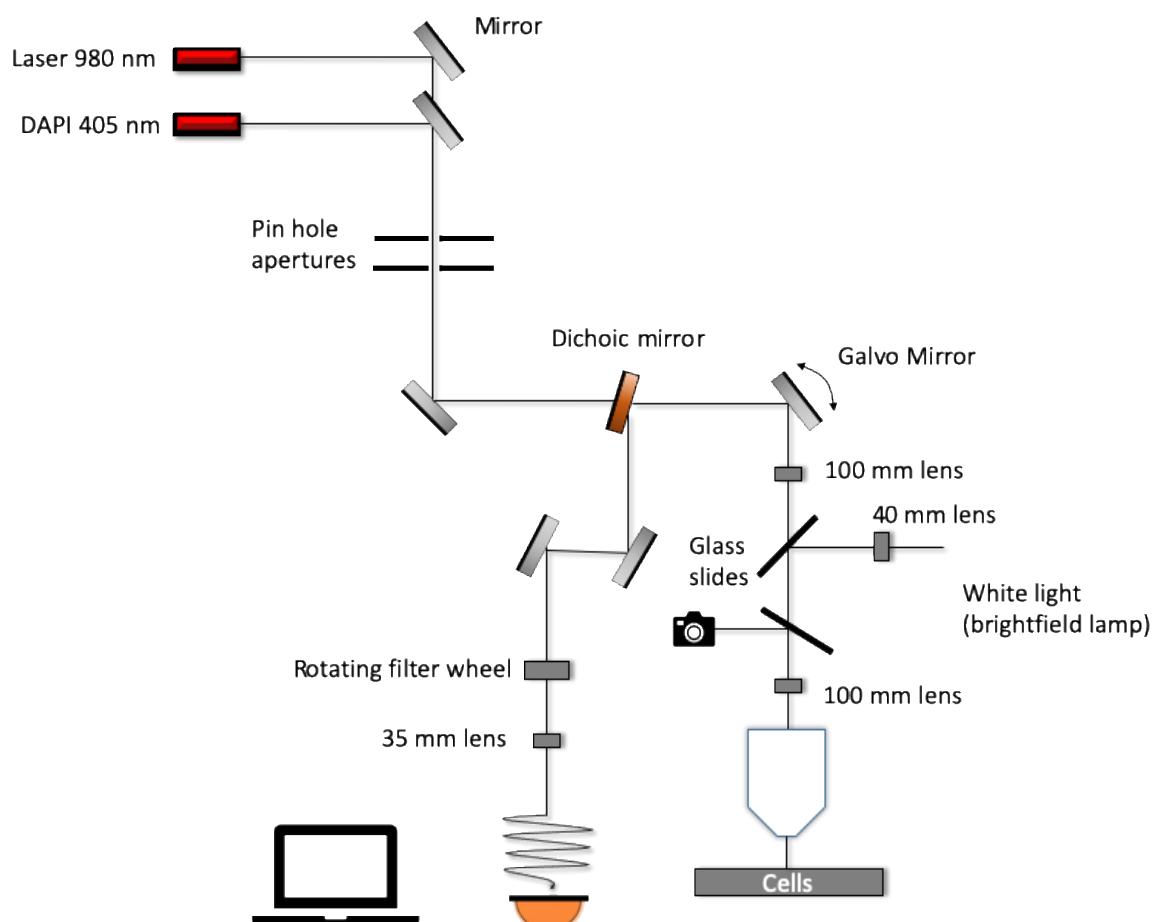


Figure 19. Schematic illustration of the microscopy setup used for fluorescence imaging using the UCNPs incubated with A549 cells.

2.6.3 Set-up used for spectrally-resolved measurements in dye-sensitized β -UCNPs

Spectroscopic characterization of the samples was carried out at the University of Southampton (see **Figure 20**). The luminescence characterization of the samples synthesised in **Chapter 5** was done in a set-up built by Prof. Otto Muskens. Integrated Intensity and luminescence spectra from different samples with varying IR-806 dye concentrations (in CHCl_3) were obtained using a Coherent Chameleon femtosecond laser, pulsed with 200 fs pulse duration and 80 MHz repetition rate, as the excitation source. The prepared dye-sensitized β -UCNPs in CHCl_3 were measured using a quartz cuvette with a path length of 10 mm. The excitation power was set to 2 mW, and the emission was collected at an angle of 90° using achromatic lenses and a dove prism for the projection of the pencil of luminescence onto the entrance slit of a spectrometer equipped with a cooled CCD array (Andor Shamrock/iDus). A short-pass IR-blocking filter (FGS900) and an optical bandpass filter from 515 to 710 nm (Semrock) were used to suppress the scattered excitation light and select only the luminescence emission.

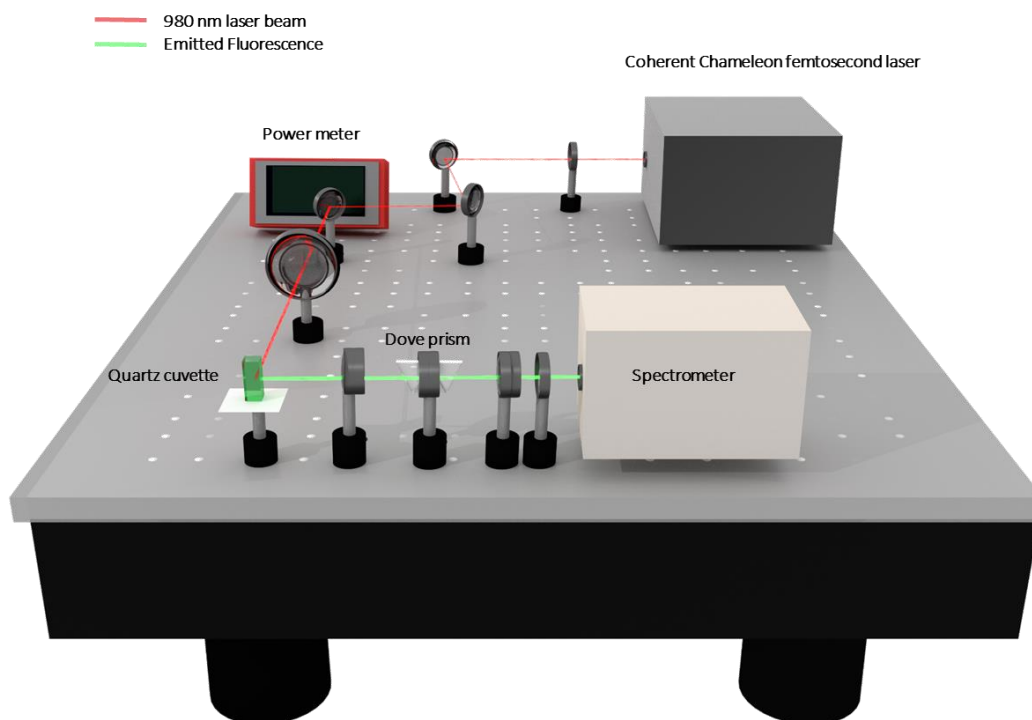


Figure 20. Schematic illustration of the set-up used at the University of Southampton to characterize the β -UCNPs.

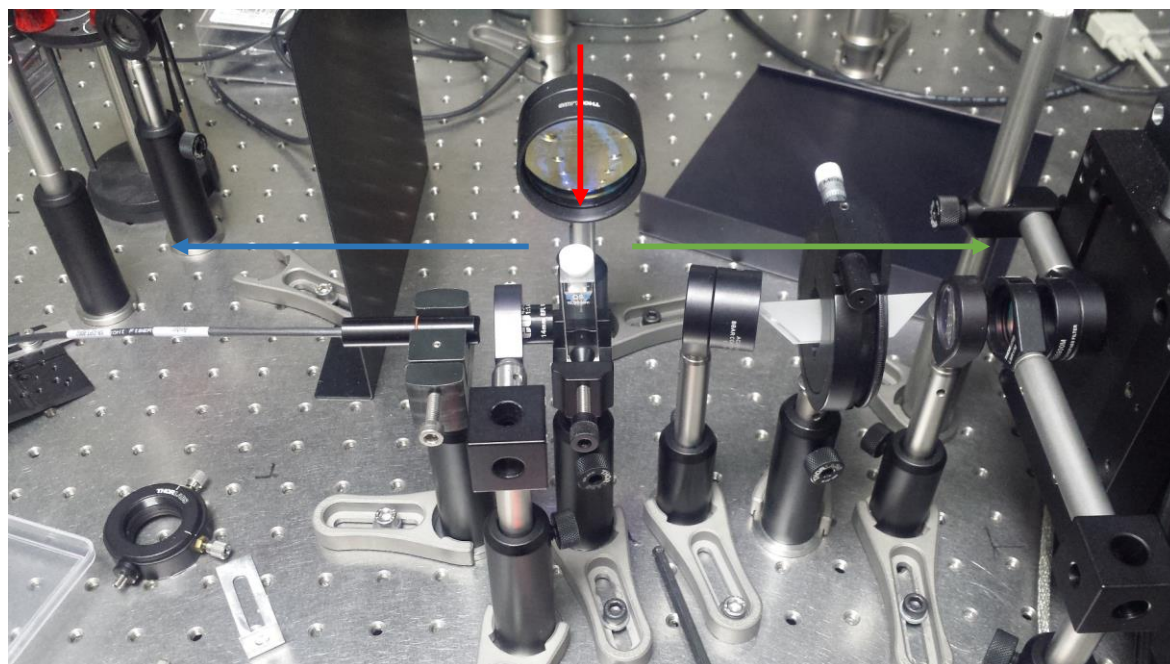


Figure 21. Photograph of the set-up used at the University of Southampton for the characterization of the β -UCNPs to measure UC (green arrow) and DC (blue arrow) luminescence using the incident light at an angle of 90° (red light).

2.6.4 Set-up used for time-resolved and spectral measurements in dye-sensitized β -UCNPs

Time-resolved and spectral measurements for the samples from **Chapter 5** were carried out in Russia. Skolkovo Institute of Science and Technology, Nobel Street, 3, Moscow 121205, Russia by Sergey Alyatkin and Pavlos G. Lagoudakis.

The UC spectra and kinetics of non-sensitized and dye-sensitized β -UCNPs were measured under the pulse train excitation with a wavelength of 980 and 800 nm, respectively. As an excitation source, we used an 80 MHz Ti: Sapphire laser system (Chameleon, Coherent), coupled with the pulse picker (Pulse Select, APE), which reduced the frequency to 20 MHz. Then, the excitation beam was modulated by an optical chopper with a 60-slot blade (MC1F60, Thorlabs) with each 10th slot opened. The chopper controller (MC2000B, Thorlabs) operated at the 10th harmonic of the reference frequency of 295 Hz, given externally by a waveform generator (33500B, Keysight). As a result, the β -UCNPs were excited at a frequency of 295 Hz with the duration of the pulse train of $\sim 170 \mu\text{s}$. The excitation frequency allows the excited states of Er^{3+} to decay completely before the next pulse train comes (see Figure S20). Each train consisted of multiple 150 fs pulses with 50 ns separation. The excitation beam with a diameter of 5 mm was reflected with a short pass

dichroic mirror (FF749-SDi01-25×36×3.0, Semrock) and focused with a 10× micro-objective (Plan Achromat, NA = 0.25, Olympus) in a thin quartz cuvette, filled with solution of the NPs in CHCl₃. The collected UC luminescence was filtered additionally with a short-pass filter (FF01-720/SP-25, Semrock) and a long-pass filter (LP02-488RU-25, Semrock) and coupled through a 50 μm fiber (Thorlabs) with either the spectrometer (QE Pro, Ocean Optics) or the avalanche photodiode (ID 100–50, ID Quantique). The output of the detector was connected with a TCSPC card (SPC-160, Becker & Hickl) to perform time-resolved characterization. The measurement of UC kinetics was performed in a triggered accumulation MCS mode of the TCSPC card that builds up the photons' distribution versus their macro times after the train of excitation pulses. The excitation power was measured by a calibrated power meter (S121C, Thorlabs) and fixed at 50 μW during the UC kinetics measurements of both dye-sensitized and non-sensitized β-UCNPs.

For the lifetime measurement of the IR-806 dye luminescence, 20 MHz excitation with a wavelength of 800 nm was used. The excitation power was fixed at 1 μW for the characterization of pure dyes and dyes, attached to the surface of β-UCNPs. The dye emission was filtered from the UC emission and laser excitation line by spectral filters: notch filter (NF808-34, Thorlabs), long-pass filter (LP02-808RU-25, Semrock), and short-pass filter (FF01-950/ SP-25, Semrock). All measurements with optimized dye concentration including UC luminescence spectra and fluorescence decay curves of pure dye and dye-sensitized β-UCNPs were carried out at room temperature after stirring (within 24 h after synthesis). Additionally, during all measurements, the quartz cuvette with the solution was continuously scanned in the focal plane of the focusing microscope objective using an automated stage, facilitating the effective mixing of the solution and allowing for highly reproducible results because of ensemble averaging and elimination of detrimental local heating.

2.7 Solar simulator

2.7.1 Solar simulator for β-UCNPs coated by TiO₂

The photocatalytic activity from **Section 4.4** was performed with a solar simulator at the University of Southampton. Samples were irradiated inside a chamber and the light source of the Xenon lamp was operated via a manual shutter located on the side of the unit as seen in **Figure 22**. The irradiation of samples under simulated sunlight was carried out using a

solar simulator fitted with a Xe OF arc lamp, with a collimated beam area of 50 mm x 50 mm. More specific details about the Xenon lamp are found below

Lamp type (150 W Xe OF), current= 7.5 A, voltage= 20 V, Approx. flux = 3000 Lumen, approx. brightness = 150 cd/mm², effective arc size = 0.5 x 2.2 mm², average life = 1200 h, bulb diameter = 20 mm.

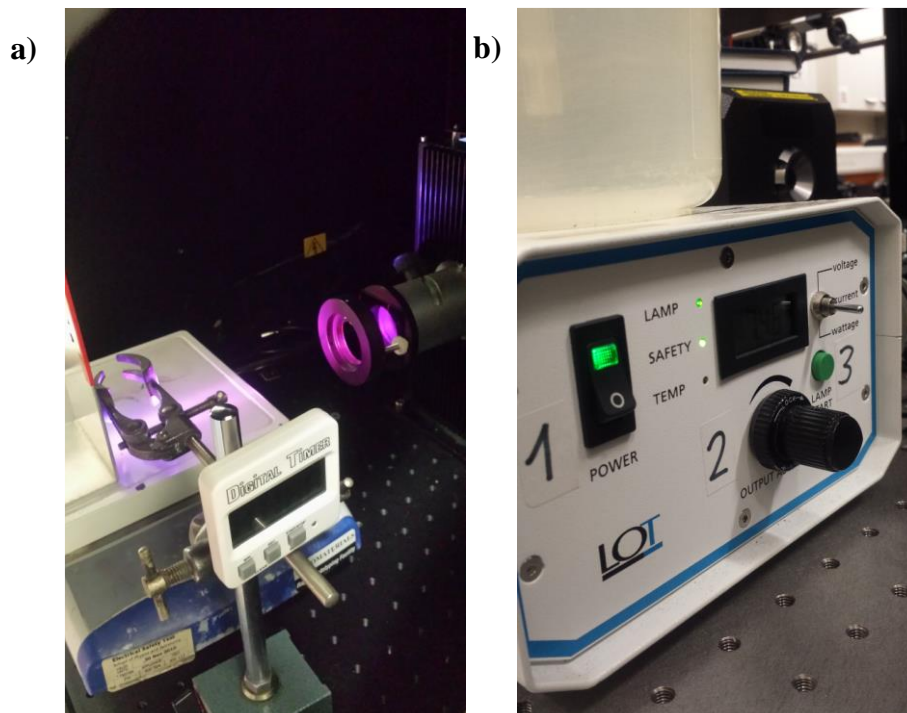


Figure 22. Digital photography of the solar simulator. (a) shows the stirring plate where the sample was located on and followed by the radiation source tailored by a UV filter and (b) shows the light generator. 150 W Xe arc light.

Chapter 3 Results and discussion on the synthesis and characterization of upconversion nanoparticles

3.1 Synthesis of oleate coated β -NaYF₄ upconversion nanoparticles

Ytterbium and erbium co-doped sodium yttrium fluoride (NaYF₄: Yb³⁺, Er³⁺) are amongst the most efficient UCNPs.^{53,229} It is well-known that a precise control in the structure, shape and size of the crystal is crucial to establish their interesting and unique properties and their future applications.²³⁰ In the literature, UCNPs based on hexagonal sodium yttrium fluoride (β -NaYF₄) have been synthesised with different shapes and controllable (length/diameter) AR by using different experimental routes such as hydrothermal and solvothermal methods.^{61,86,231–233} However, these synthetic protocols require a precise control on many parameters in order to optimize the size and crystal structure such as NaF concentrations, temperatures and reaction time, pH of solution along with others.^{234,235}

Section 3.1.1 will look into the synthesis and characterization of β -NaYF₄ UCNPs with a controllable size and AR, based on the co-precipitation procedure. The benefits of such method include mainly operational simplicity and lack of toxic by-products.^{54,236} In this section, the original strategy introduced by Zhang et al.⁵⁴ was adopted. In our work, the size and AR of β -UCNPs were controlled by only varying the amount of OA in the reaction mixture, using in all cases ODE as the solvent. The corresponding role of OA as capping ligand on the growth kinetics will be discussed in **Section 3.1.2**. Regarding the optical properties, the UC luminescence and absorbance of the β -UCNPs were studied and the results are discussed in detail in **Section 3.1.3**.

3.1.1 Synthesis of β -NaYF₄ UCNPs with NH₄F as fluoride source

β -UCNPs were synthesised following the experimental procedure detailed in **Section 2.1.1**. More precisely, four samples of β -NaYF₄: Yb³⁺(20%), Er³⁺(2%) were prepared using OA as capping ligand to control particle growth and to stabilise the particles against aggregation. The OA volume was gradually increased in the reaction mixture as following: 6 ml, 12 ml, 17 ml and 21 ml while the ODE volume was kept the same for all experiments (15 ml). The particle size and morphology were first evaluated using TEM and the images are showed in **Figure 23**. The size distribution was analysed with ImageJ software considering over 100 UCNPs for the statistical analysis.

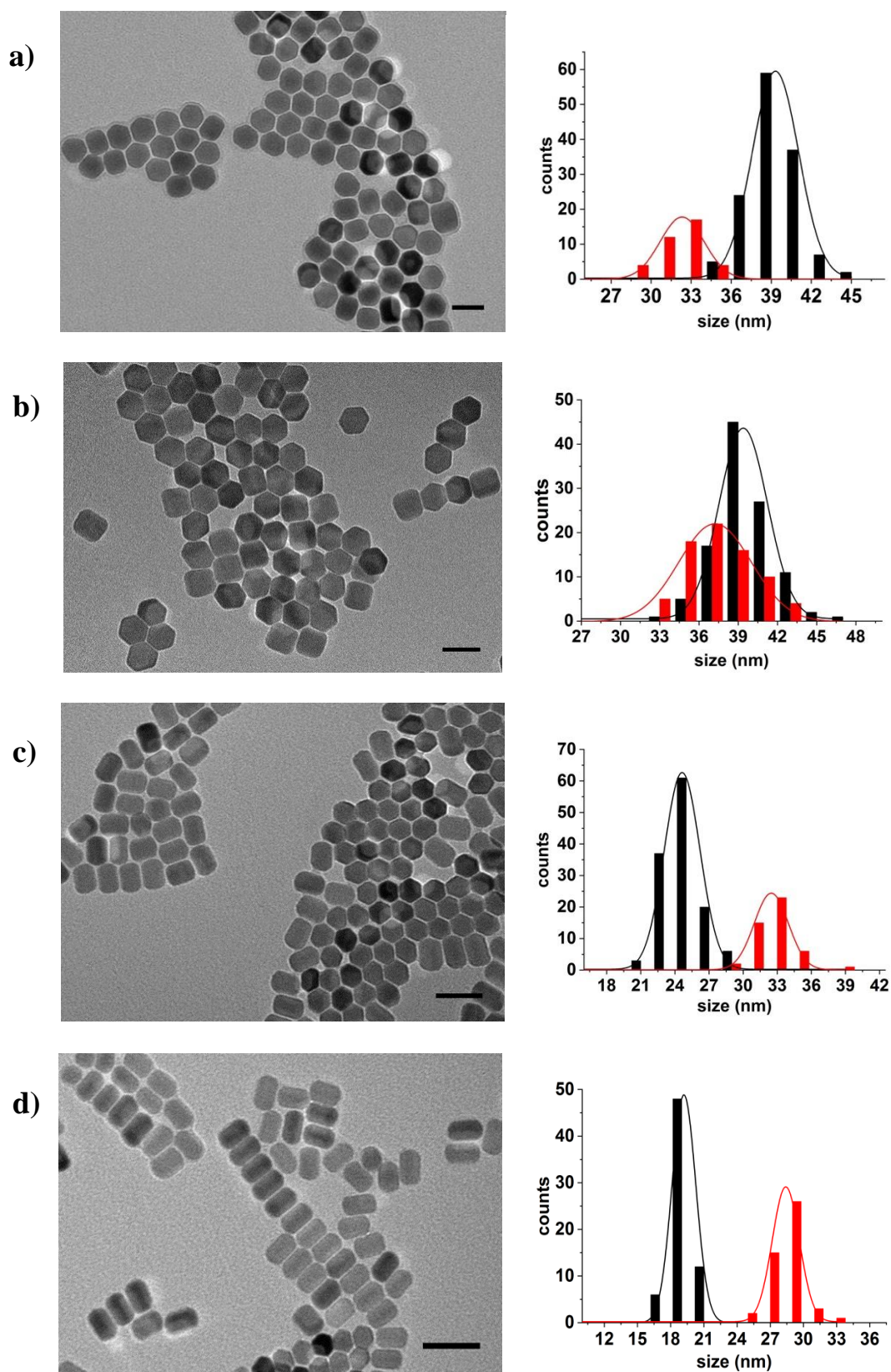
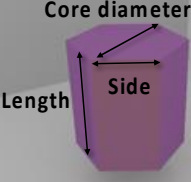


Figure 23. TEM images and size distribution of the different samples of β -NaYF₄: Yb³⁺(20%), Er³⁺(2%) UCNP obtained with (a) 6 ml (b) 12 ml (c) 17 ml and (d) 21 ml of OA. Scale bars are 50 nm. Black bars from the histograms indicate the size of core diameter meanwhile the red colour corresponds to the length. Samples (1-4).

The β -UCNPs synthesised with 6 ml, 12 ml, 17 ml and 21 ml of OA were conveniently named samples (1-4), and their dimensions and ARs (length/diameter) are summarized in **Table 4**. It should be considered that the total volume of the reaction and the OA: ODE volume ratio varied among the samples. The total volumes were 21 ml, 27 ml, 32 ml and 36 ml while the OA: ODE volume ratios were 0.4, 0.8, 1.13 and 1.4 for samples (1-4), respectively.

Table 4. Dimensions of the β -NaYF₄: Yb³⁺(20%), Er³⁺(2%) UCNPs obtained by using different amounts of OA in the reaction. Samples (1-4).

	Shape	Core diameter (nm)	Length (nm)	Side (nm)	AR
Sample 1	Hexagonal prism	39 ± 2	32 ± 2	18 ± 2	0.82
Sample 2	Hexagonal prism	39 ± 2	37 ± 3	19 ± 2	0.95
Sample 3	rod	25 ± 2	32 ± 2	12 ± 1	1.28
Sample 4	rod	19 ± 1	28 ± 1	10 ± 1	1.47

Images showed in **Figure 23** revealed nanocrystals of uniform size within each sample, which varied in shapes from hexagonal plates to short nanorods for the different experimental conditions employed here. Our results indicated that the concentration of OA as the capping ligand affected the preferential growth rate in different directions of the crystal. Results are in agreement to previous publications.^{54,237}

Observing the two-dimensional TEM images (**Figure 23c and d**), the actual morphology of the β -UCNPs can be misinterpreted, since it appears to be as a mixture between hexagons and nanorods. In order to observe the three-dimensional morphology, additional TEM images were taken at different tilting angles ($\pm \alpha$). See direction of the tilting TEM holder in **Figure 24**.

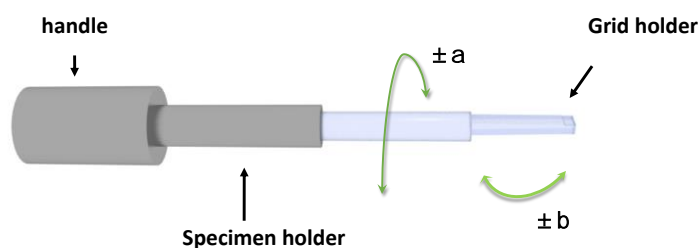


Figure 24. Illustration of TEM holder indicating in green line the ($\pm \alpha$) and ($\pm \beta$) tilting angles.

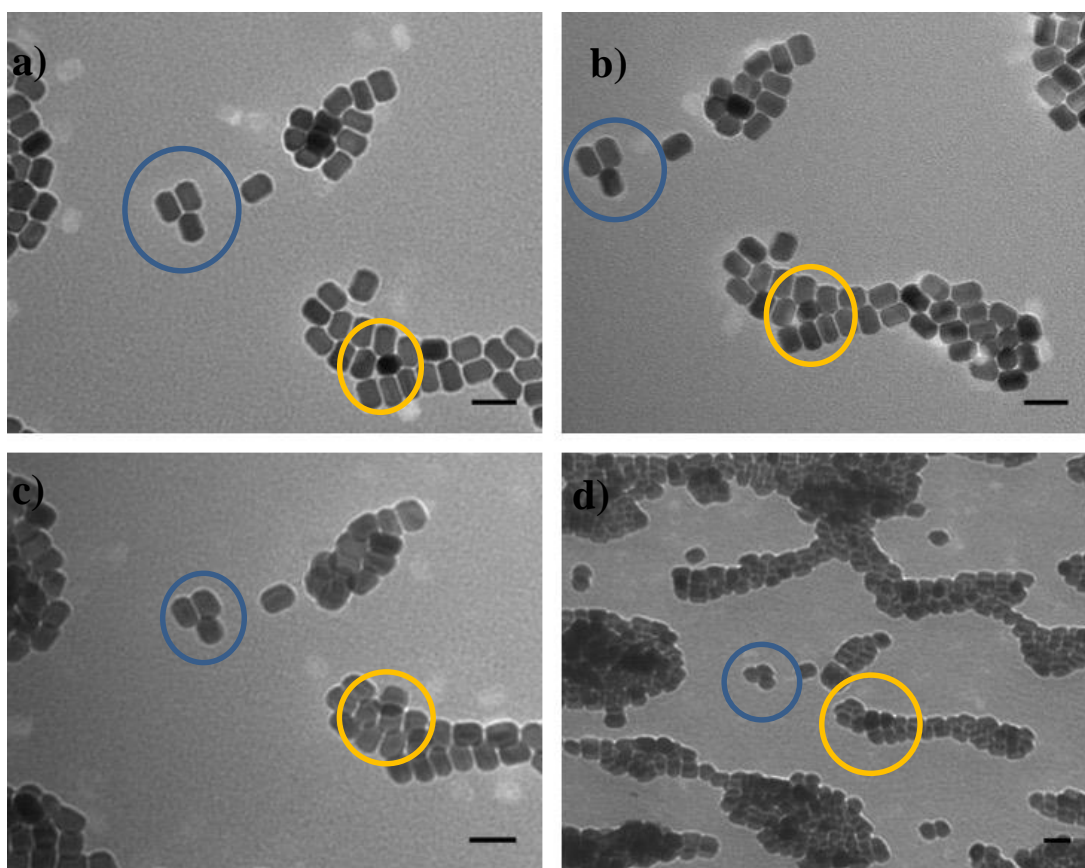


Figure 25. TEM images at different α tilting angles (a) 0° , (b) 20° , (c) 40° and (d) 60° of the synthesised $\beta\text{-NaYF}_4\text{: Yb}^{3+}(20\%), \text{Er}^{3+}(2\%)$ UCNPs using 17 ml of OA. Scale bars are 50 nm. Sample 3.

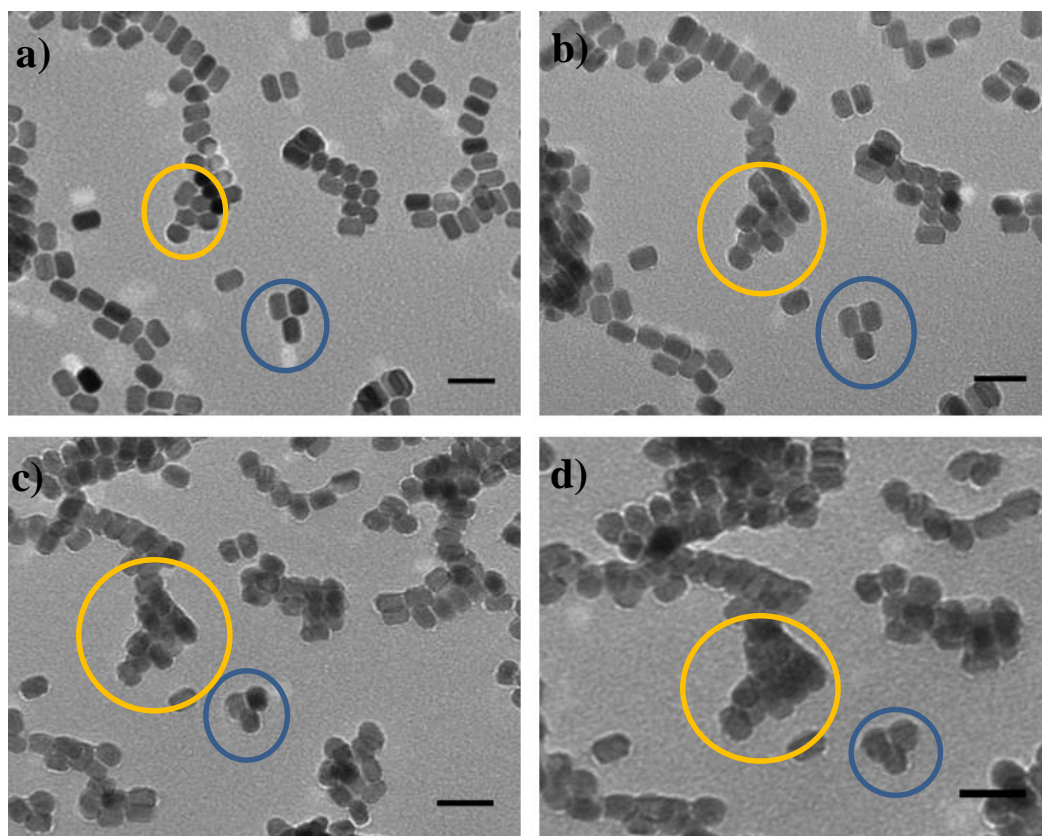


Figure 26. TEM images at different α tilting angles (a) 0° , (b) 20° , (c) 40° and (d) 50° of the synthesised β -NaYF₄: Yb³⁺(20%), Er³⁺(2%) UCNP using 21 ml of OA. Scale bars are 50 nm. Sample 4.

From **Figure 25 (a-d)** and **Figure 26 (a-d)** it is visible that after tilting, the hexagons resolve to a hexagonal prism and vice-versa. See blue and orange circles. **Figure 27** shows a simulation of the 3D morphology and its projected shadows of a representative UCNP for each synthesis.

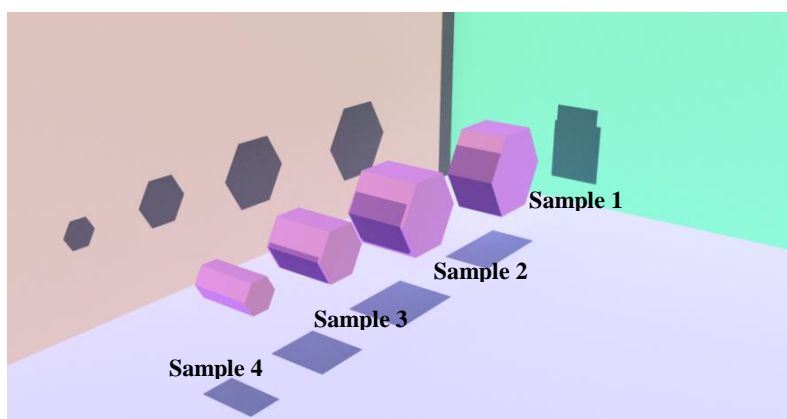


Figure 27. Graphic representation of the prism-shape β -NaYF₄: Yb³⁺(20%), Er³⁺(2%) UCNP from different perspectives. From right to left, the structures correspond to sample 1, 2, 3, and 4.

Next, the samples were characterized by the Fourier-transform infrared (FTIR) spectroscopy.

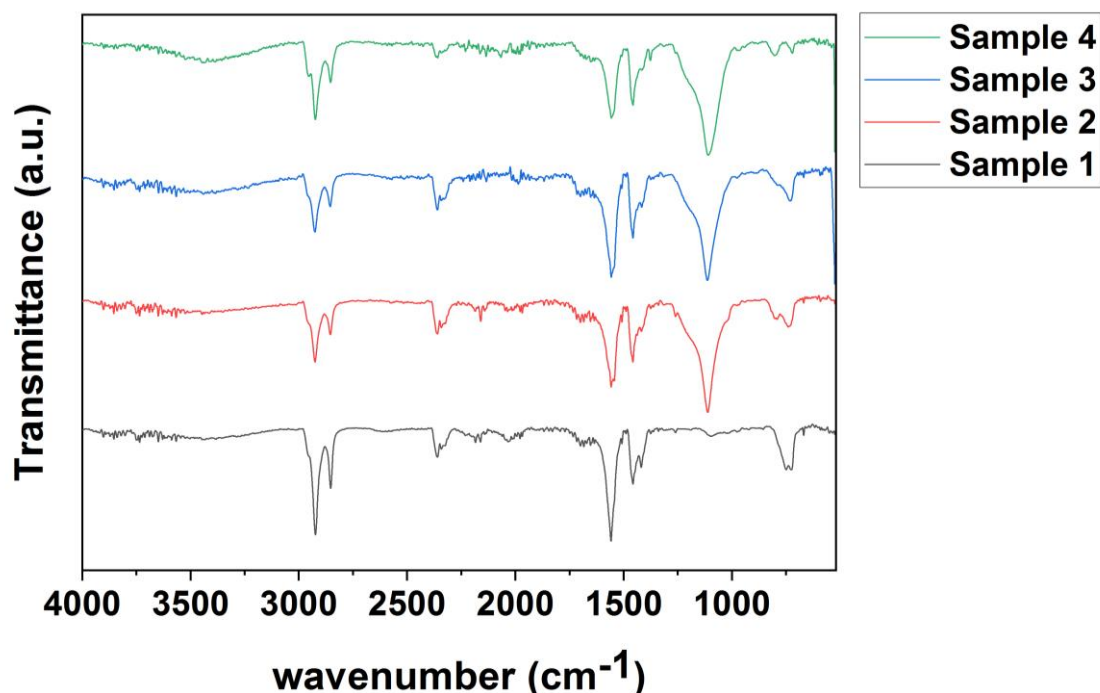


Figure 28. FTIR spectra of β -NaYF₄: Yb³⁺(20%), Er³⁺(2%) UCNP prepared with different OA concentrations. Samples (1-4).

Figure 28 shows the FTIR spectra of β -NaYF₄: Yb³⁺(20%), Er³⁺(2%) UCNP synthesized with different OA concentrations. The spectra show two main vibrations at 2924 cm⁻¹ and 2853 cm⁻¹, which were attributed respectively to the asymmetric and symmetric stretching modes of the methylene (-CH₂) groups of the OA molecule.¹⁰⁰ It is worth noting that the characteristic bands at ~1700 cm⁻¹, corresponding to stretching vibration of C=O from OA, were practically absent in all the spectra. Instead, two bands at 1559 cm⁻¹ and 1459 cm⁻¹ appeared, and were attributed to the asymmetric and symmetric stretching vibrations of the carboxylate group [(-COO-)₃Y³⁺] of the β -NaYF₄, respectively.

It is interesting that the absorption band of C-O at 1110 cm⁻¹ was very strong for samples (2-4) and became almost non-existent for the plate hexagonal structure (sample 1). This effect has been reported in the literature by Gao et al. and it appeared when doping the β -NaYF₄: Yb³⁺, Er³⁺ UCNP with other Ln³⁺ ions.²³⁸ Taking into account that in our work the Ln³⁺ ions and their concentration remained constant, we associated the intensity of this C - O peak with the high level of OA in the samples (2-4).

The as-synthesized samples were further examined by XRD to confirm the crystallographic phases. **Figure 29** reveals that the samples (1-4) presented pure hexagonal phase, without other impurity peaks, implying that high level of crystallinity can be obtained through this process.

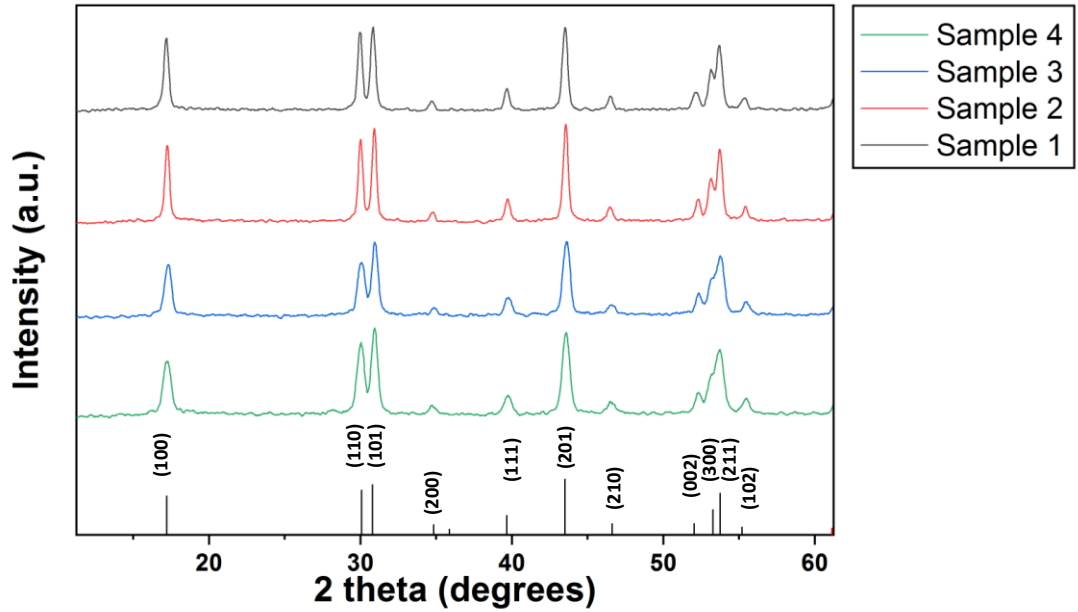


Figure 29. XRD patterns of β -NaYF₄: Yb³⁺(20%), Er³⁺(2%) UCNP prepared with different OA concentrations. Samples (1-4). Measurements were acquired using a Cu K- α source (with $\lambda = 1.54059 \text{ \AA}$). β -NaYF₄ (PDF card No.: 00-016-0334).

From the line broadening of the diffraction peaks, nanocrystalline domain sizes were estimated using the Debye–Scherrer equation:²³⁹

$$D = \frac{0.94 \lambda}{\beta \cos(\theta)} \quad (2)$$

, where D is the mean size of the crystalline domains, which is different from the particle size and refers to the size of a single crystal inside a particle. β is the full width at half maximum intensity (FWHM), λ is the X-ray wavelength and θ is the Bragg angle.²³⁹

The (100) diffraction peaks of the XRD patterns were fitted with a Lorentzian function and the crystallite domain sizes (D) were calculated using eq (2). The resulting crystalline sizes of each sample are presented in **Table 5**. It is important to mention that these calculations are a very rough size estimation. When calculating the crystallite size via XRD peak width, there are a variety of factors which can contribute to the width of a diffraction peak including the inhomogeneous tension, the imperfections of the crystal lattice, in addition to the

instrumental effects.¹³ The results indicate that our samples are not single crystallite.

Table 5. Crystallite sizes computed by the Debye-Scherrer equation, for samples (1-4).

	Crystallite Size (nm)
Sample 1	25
Sample 2	26
Sample 3	17
Sample 4	15

3.1.2 Influence of oleic acid ligands on the growth kinetics

The β -NaYF₄ generally features the (0001) crystal planes for the top/bottom and six equivalent $\pm (10-10)/ \pm (1-100)/ \pm (01-10)$ planes, usually simplified as (10-10).^{240–242}

Figure 30a shows a representation of the different crystallographic planes and **Figure 30b** shows the unit cell of the Na_{1.5}Y_{1.5}F₆ structure with P6-symmetry. It is visible that there are only three cation sites in the structural model of Na_{1.5}Y_{1.5}F₆: one for Y³⁺ ions (green balls), one for Na⁺ ions and vacancies (yellow-white balls), and the last one for both Y³⁺ and Na⁺ ions (yellow-green balls).^{49,243}

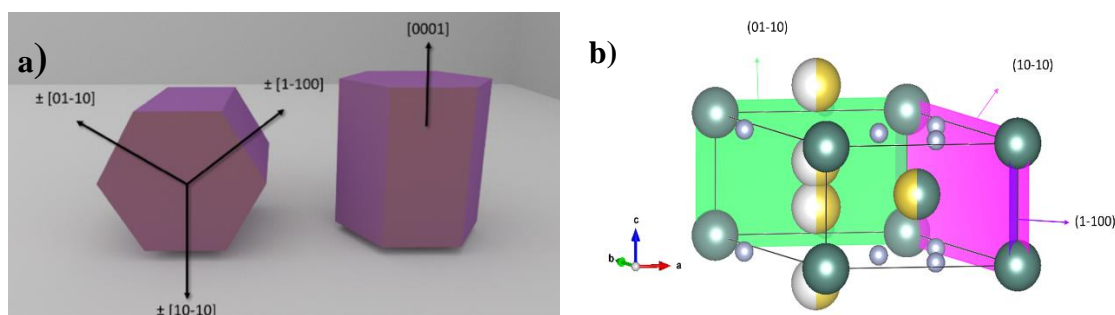


Figure 30. (a) Graphic representation of different families of plane for the β -NaYF₄ with hexagonal prism shape. (b) Representation of the hexagonal unit cell (Na_{1.5}Y_{1.5}F₆), showing the ions distribution and different set of planes. Green, yellow and light blue balls refer to Y³⁺ ions, Na⁺ ions and F⁻ ions, respectively. Figure was created with the open-source software package VESTA. Crystal structures were drawn based on the structural data reported by Grzechnik et al.²⁴³ but adapted to our experimental lattices constant. $a=b=5.96$ Å, $c=3.51$ Å and $\alpha=\beta=90^\circ$, $\gamma=120^\circ$. See **Appendix C** for the theoretical calculations of the lattice constant.

Using the hydrothermal method, β -NaYF₄ have been extensively synthesised with controllable size and morphology, by adjusting the pH and molar ratio of NaNO₃/Y³⁺, NaF/Y³⁺, and F/Y³⁺.^{241,244,245} Studies revealed that the selective adhesion of ions on different crystal facets can control the growth rate along different directions producing various shapes of the nanocrystals.^{244,245} Unfortunately, and to our knowledge, there is not much information on the synthesis carried out with the co-precipitation method and adjusting only the OA concentration.⁵⁴ Based on the above statements, the obtained size and morphology in our experiments were attributed to the preferential adhesion of OA on different facets of the β -NaYF₄. Although the exact mechanism is not very clear at present, the explanation for the change of morphology can be provided as follows.

In agreement to previous studies,⁴⁴ we believe that the OA ligands are chemically adsorbed through the coordination between the COO⁻ group and the Y³⁺ ions on the surface of the β -NaYF₄. This has been observed previously for OA coated iron oxide NPs,²⁴⁶ and it is supported by the two bands at 1463 cm⁻¹ and 1551 cm⁻¹ presented in the FTIR spectra (**Figure 28**), attributed to the stretching vibrations of the carboxylate group $[(-\text{COO}-)_3\text{Y}^{3+}]$.

According to the general principle of crystal growth, the growth of a crystal is related to the relative growth rate of different crystal planes.^{242,247,248} In addition, it is known that the most representative and common shape for hexagonal compounds is hexagonal prism.^{240,242} Therefore, if the growth rate on the [10-10] directions is quicker than the growth rate on the [0001] directions, the crystal takes a hexagonal plate morphology. Otherwise, in the case that the growth rate along the [0001] directions is quicker than the growth rate along the [10-10] it is likely that the crystal is a long and thin hexagonal prism.^{240,242}

We believe that the growth rate in different crystallographic facet could be influenced by the coordination effect between COO⁻ and Y³⁺ ions. With low concentration of ligands (synthesis with just 6 ml of OA), COO⁻ would bind preferentially to the (0001) facets, which would lead to the fast growth of the β -NaYF₄ along one of the (10-10) family facets and thus, producing β -NaYF₄ with a hexagonal plate shape and low AR (0.82). By increasing the amount of OA to 12 ml, the ligands could adhere to the (0001) facets as well as to the less preferred (10-10) facets, and as a result, the growth rates would be comparable along both directions. In our experiments, the ratio between the diameter and length was very close to 1, more precisely AR= 0.95.

Studied have revealed that the Y³⁺ density on different crystal planes of β -NaYF₄ is different. The density of Y³⁺ on the (10- 10) planes is bigger than the density of Y³⁺ on the top/bottom

facets of the (0001) planes.^{240,241} Consequently, when the concentration of OA is very high (17 ml and 21 ml), it is reasonable to think that the COO⁻ would adhere selectively more on the (10-10) prismatic facets of the β -UCNPs, lowering their surface energy, and therefore the growth in those last directions would be sterically prohibited. As a result, β -UCNPs would grow in the [0001] direction, leading to the formation of longer and thin rod-shaped β -UCNPs with higher AR.

Our results are also supported by the XRD data shown in **Figure 29**. The relative intensities of some peaks varied from one sample to another, indicating the possibility of different growth orientations.²⁴² For instance, the relative intensity of the (100) peak varied from sample 1 and 2 with hexagon shapes, and sample 3 and sample 4 that contained nanorods. XRD data revealed that the (100) reflection was stronger for samples 1 and 2, matching with the preferred [10-10] growth direction and in agreement to the observed morphology of the final products.

Figure 31 illustrates the evolution in the β -NaYF₄ size. Synthetic protocols using 6 ml and 12 ml of OA were comparable and seemed to have similar effects on nuclei growth. In both cases, the process suggested dissolution, re-nucleation and ripening causing larger UCNPs *via* Ostwald mechanism.²⁴⁹ Increasing concentrations of OA drastically delayed particle ripening due to the β -NaYF₄ growth being completely restricted along all crystal planes.²⁵⁰ Consequently, when increasing the concentration of OA to 17 ml and 21 ml, the UCNPs did not grow much due to steric hindrance.

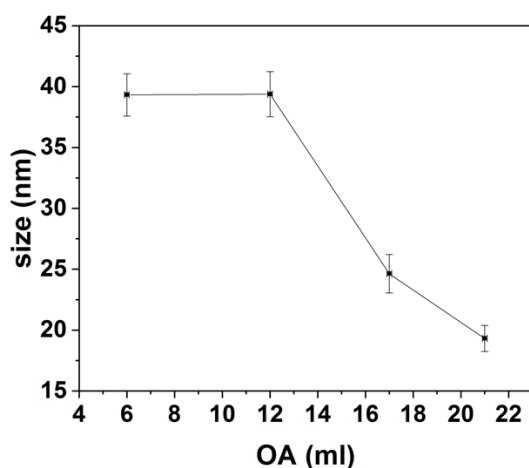


Figure 31. Changes in the particle size for β -NaYF₄: Yb³⁺(20%), Er³⁺(2%) UCNPs (samples 1-4) synthesised with different concentrations of OA. The Y axis represents the size of the core diameter and the X-axis is the OA volume added for each synthesis. (The OA volume were measured with an uncertainty of ± 0.1 ml, and error bars are very small to be seen).

3.1.3 Upconversion luminescence properties of nanoparticles β -NaYF₄ with different aspect ratio

In this section, we compare the UC luminescence spectra of the different β -NaYF₄ UCNPs discussed in the above section. The set-up used to measure the luminescence is schematically illustrated in **Figure 16**. In all cases, the doping percentage of the sensitizer (Yb³⁺) and activator (Er³⁺) was 20% and 2%, respectively. It is well-known that generally the level of activators shall be kept low, usually under 3%.^{34,251} However, the number of sensitizers must be high enough to allow an appropriate distance between sensitizers and activators to enable the energy transfer, but not so high to provoke the so-called “concentration quenching” effect due to cross-relaxation events.³⁴ Introducing a high level of Yb³⁺ dopants in the host lattice would decrease the Yb³⁺- Er³⁺ interatomic distance and thus would facilitate a back-energy-transfer from Er³⁺ to Yb³⁺. This process would reduce the population in excited levels of ²H_{9/2}, ²H_{11/2}, and ⁴S_{3/2} of Er³⁺ resulting in a low UC efficiency.⁴¹

Samples (1-4) were prepared in identical conditions with a final concentration of 1 mg/ml of β -UCNPs and were excited by a 980 nm CW laser (400 mW). The solvent used was always hexane where the β -UCNPs have a high colloidal stability and the acquisition period was 500 ms. The overall UC luminescence spectra of the samples (1-4) are shown in **Figure 32a** and the most relevant transitions that occur, including energy transfer, cross-relaxation, radiative, and non-radiative processes are illustrated in **Figure 32b**.²⁵²

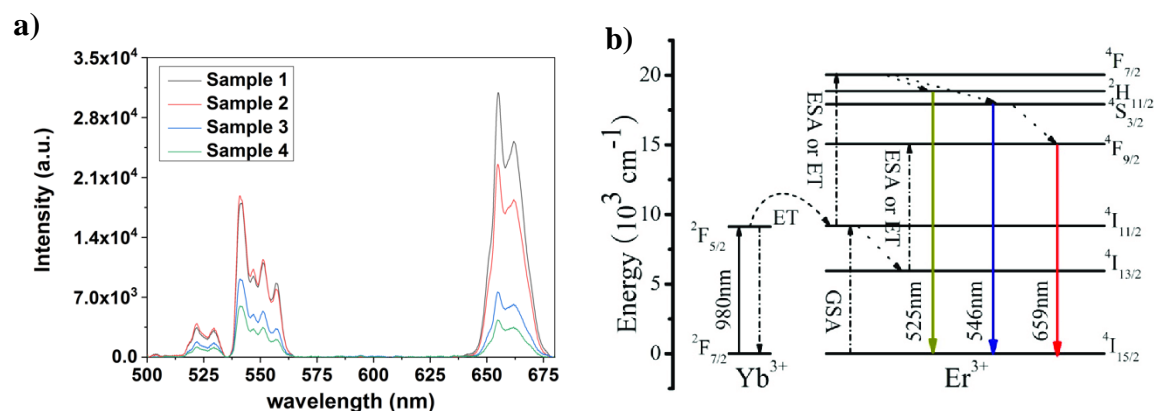


Figure 32. (a) UC emission spectra of β -NaYF₄: Yb³⁺(20%), Er³⁺(2%) UCNPs dispersed in hexane measured with a 980 nm CW laser excitation and 400 mW. (b) Energy transfer mechanism in NaYF₄: Yb³⁺(20%), Er³⁺(2%) adapted by Ref.²⁵²

From **Figure 32a**, it can be observed that although the UC emission intensities were quite different, there were always three bands centred at 525 nm, 540 nm, and 650 nm, which can be assigned to the $^2H_{11/2} \rightarrow ^4I_{15/2}$, $^4S_{3/2} \rightarrow ^4I_{15/2}$ and $^4F_{9/2} \rightarrow ^4I_{15/2}$ transition of Er^{3+} ion.³⁴

It can be seen that the ranking in the emission intensity was sample 1 > sample 2 > sample 3 > sample 4. Sample 4 showed the lowest UC luminescence in both, red and green emissions when excited at 980 nm with the CW laser. It is known that the quantum confinement effect is not suitable UCNPs.²⁵³ Thus, unlike quantum dots, the size-dependent emission cannot be interpreted by quantum mechanics. In general, we attribute the change in the emission intensity as a function of particle size to the surface quenching effect. β -UCNPs from sample 4 were the smallest and therefore had the highest surface area to volume (S/V) ratio. When the S/V ratio in β -UCNPs is high most of the Ln^{3+} dopants are exposed to surface deactivations (due to surface defects, as well as to ligands and solvents that possess high phonon energy).^{128,254,255}

For comparison, volumen (V), total surface area (SA_T), and S/V of the samples (1-4) were calculated according to the equations from **Appendix B** and the results are summarized in **Table 6**. Error were calculated according to eq. (44), eq. (45) and eq. (46) from **Appendix F**.

Table 6. Summary of the V, SA_T , and S/V for each of the as-synthesised β -NaYF₄: Yb³⁺(20%), Er³⁺(2%) UCNPs.

	V (nm ³)	SA_T (nm ²)	S/V (nm ² /nm ³)
Sample 1	27700 ± 15762	5240 ± 527	0.19 ± 0.04
Sample 2	36329 ± 8897	6281 ± 753	0.17 ± 0.05
Sample 3	12783 ± 2906	3185 ± 338	0.25 ± 0.06
Sample 4	6729 ± 1743	2101 ± 251	0.31 ± 0.09

In general, the UC luminescence intensity of the samples increased when decreasing the S/V ratio. It is noteworthy that the intensity in sample 1 was higher than in the sample 2 in the red area of the spectra. We attributed this observation to the better crystallization of sample 1 with reduced number of defects in the surface.

In addition, we observed a difference in the ratio of red to green (RGR) emission over the four samples. This is illustrated in **Figure 33a** and **b**, which show the RGRs obtained when integrating the areas under the peaks for green and red emission separately. We observed that smaller β -NaYF₄ had a brighter green emission thus a lower RGR, while bigger β -NaYF₄ with a brighter red emission had a higher RGR. Our results are in agreement with other experimental observations.^{15,256}

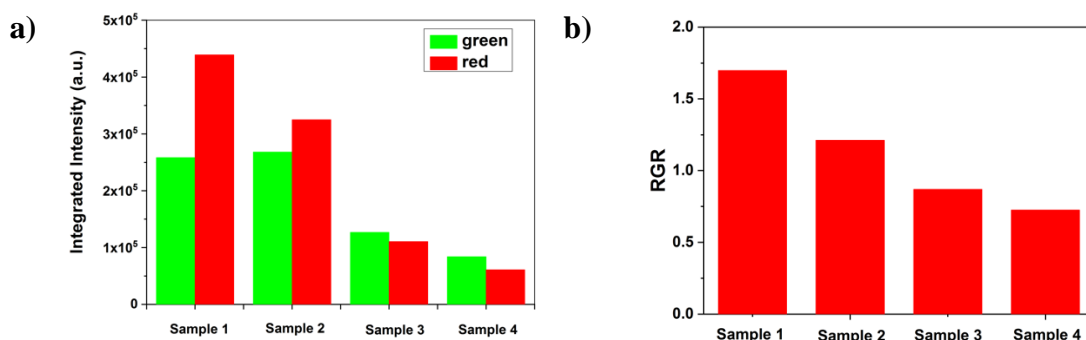


Figure 33. (a) Integrated intensity in the range of 510-570 nm (green bars) and 640-680 nm (red bars) and (b) RGR of the as-prepared samples (1-4).

The resulting RGRs greater than 1 in samples 1 and 2 can be justified by a much higher probability of an occurrence of multi-phonon relaxation $^4S_{3/2} \rightarrow ^4F_{9/2}$ and $^4I_{11/2} \rightarrow ^4I_{13/2}$ from the Er³⁺ ion.²⁵⁷ A digital photo of the different samples under a 980 nm laser pointer is shown in **Figure 34**.

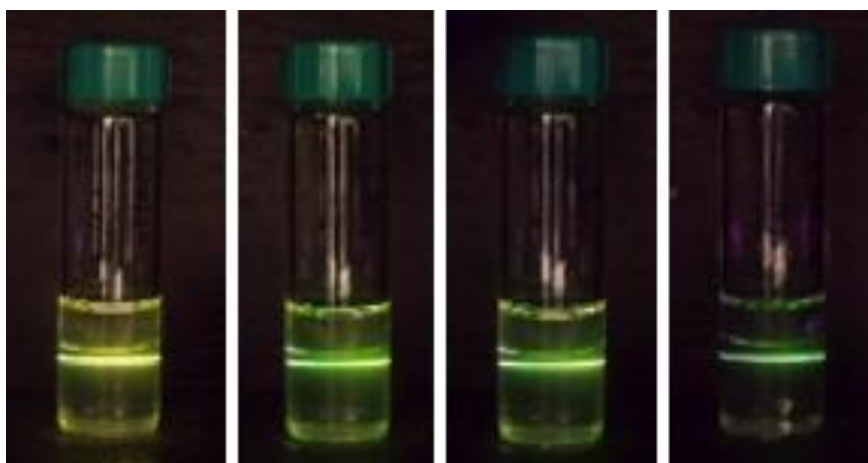


Figure 34. From left to right. Digital images for β -NaYF₄: Yb³⁺(20%), Er³⁺(2%) UCNP from samples (1-4) dispersed in hexane, under excitation wavelength of 980 nm.

At this point, it should be important to mention that achieving a sufficient accuracy in the concentration of β -UCNPs is a challenge. In our experiments we are working with mass concentrations (mg/ml). However, the different samples composed by the same total mass and different size contained a different number of β -UCNPs. The extinction coefficient is an adequate parameter that can be employed to evaluate the β -UCNPs concentration. Here, in order to calculate experimentally this value, transmission measurements for samples (1-4) were recorded.

We measured the power transmitted P at 980 nm through the different samples using the scheme illustrated in **Figure 17** and using 350 mW and 5 second of exposure time.

The transmittance coefficient T was obtained using the relation:

$$T = P/P_0 \quad (3)$$

where P_0 is the power density measured using only the solvent (hexane). The absorbance A was obtained for each of the samples according to the next equation:

$$A = \log\left(\frac{1}{T}\right) \quad (4)$$

Table 7 summarizes the absorbances for sample (1-4).

Table 7. Values of absorbances measured experimentally for β -NaYF₄: Yb³⁺(20%), Er³⁺(2%) UCNPs and calculated by equation (4). In all cases concentration was fixed to 1 mg/ml.

	Sample 1	Sample 2	Sample 3	Sample 4
Absorbance	0.078	0.083	0.107	0.069

We compared separately sample 1 and sample 2, which feature hexagon shapes, and sample 3 and sample 4 containing nanorods-shape. From **Table 7**, it can be seen that sample 1, composed of β -UCNPs slightly smaller but with larger surface area, absorbed less light than sample 2. Similarly, β -UCNPs from sample 4 with smaller size, absorbed less than sample 3 which was expected because large NPs scatter light more effectively.

In order to compare the UC emission intensity of the different samples taking into account their absorbances, we re-scaled the emission intensities from **Figure 32a**, in correlation to their relative absorbances. In detail, we re-scaled the intensity from sample 1 with respect to sample 2 and also sample 4 with respect to sample 3. The rescaling factors were of 1.06x and 1.55x for samples 1 and 4, respectively. Results are displayed in **Figure 35**.

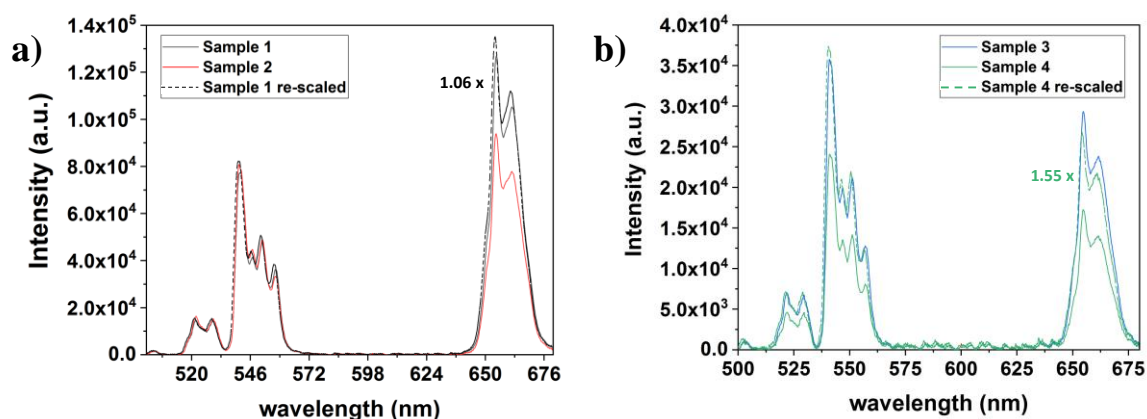


Figure 35. Emission spectra of β -NaYF₄: Yb³⁺ (20%), Er³⁺ (2%) UCNP in hexane measured with a 980 nm CW laser before and after the rescaling in accordance with their relative absorbance. (a) corresponds to sample 1 and 2, and (b) corresponds to sample 3 and 4. The measurements were taken at 350 mW and 5 second of exposure time. The rescaling factors are printed aside the curves for sample 1 and 4 in black and green, respectively.

The experiments revealed that the ranking in the emission intensity continued as: sample 1 > sample 2 > sample 3 > sample 4. Although in this case, it is noteworthy that the intensity in sample 4 was higher than in the sample 3 in the green area of the spectra.

In order to investigate the UC mechanism and give a reasonable explanation to our experimental results, we have also studied the pump power dependence of the red and green emission for samples (1-4). The results are displayed in **Figure 36** on a double logarithmic plot.

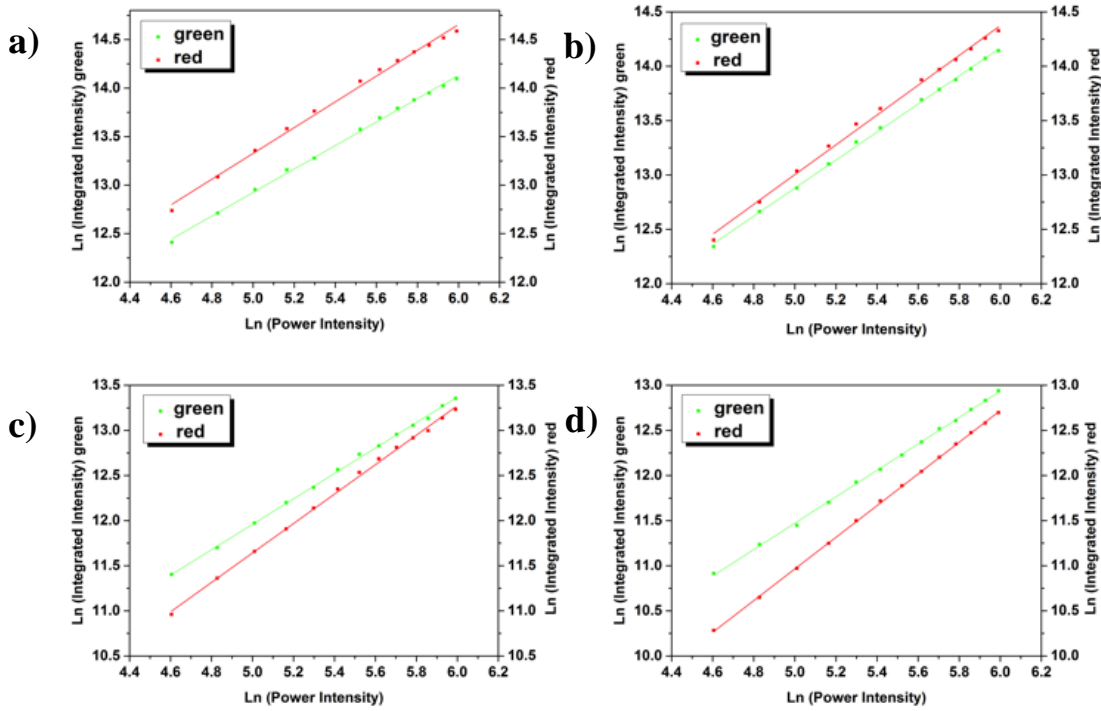


Figure 36. Dependence of the integrated intensity in the range of 510 – 570 nm (green line) and 640- 680 nm (red line) on pump power for β -NaYF₄: Yb³⁺(20%), Er³⁺(2%) UCNPs from (a) sample 1, (b) sample 2, (c) sample 3, and (d) sample 4. The excitation wavelength was fixed to 980 nm, and the PL spectra was recorded using different pump powers from 100 mW to 400 mW in steps of 25 mW. The acquisition time was fixed to 5 s.

It is known that the relation between the UC emission intensity and laser power can be approximately expressed as: ²⁵⁸

$$I_{UC} \sim P^n \quad (5)$$

, where I and P denote the UC emission intensity and pump power, respectively, and (n) refers to the number of photons absorbed per photon emitted, and its value can be derived from the slope of the fitted line of the plot $\log(I_{UC})$ vs $\log(P)$. ²⁵⁸

As visible in **Figure 36**, the UC emission changed gradually when increasing the pump power from 100 mW to 400 mW. The values of the exponent n of the β -UCNPs were extracted from a linear fitted of the experimental data.

Despite the identical experimental conditions and samples preparation, slightly different gradients of the characteristic curves for each sample were observed. The UC efficiency increased concomitantly with AR as following: sample 4 > Sample 3 > sample 2 > sample 1. In detail, the values of the parameter n (photons absorbed per photon emitted) for the

green and red emissions were found to be 1.21 and 1.33 for sample 1, 1.30 and 1.37 for sample 2, 1.41 and 1.63 for sample 3 and 1.47 and 1.76 for sample 4. In all the cases, the results indicated that both green and red UC emissions were originated from a two-photon process. In addition, for all of them, the (n) values extracted from the slope were higher for the red than for the green emissions.

From these experiments, and in contradiction to their relative emission intensities, it was concluded that the nanorod shape features the highest UC efficiency; meanwhile β -UCNPs with the hexagonal shape showed the lowest efficiency. In general, our results match with the literature. Several groups have examined the influence of the size and shape in the optical properties of the Ln^{3+} -doped UCNPs. Although no detailed explanations were given, Zhang et al. and Murray et al. reported that $\text{NaYF}_4:\text{Yb}^{3+}/\text{Er}^{3+}/\text{Tm}^{3+}$ nanoplates, nanospheres, and nanoellipses and $\text{NaYF}_4:\text{Yb}^{3+}, \text{Er}^{3+}/\text{Ho}^{3+}$ nanorods, nanoplates, and nanoprisms emitted varied UC luminescence.^{54,259} We believe that the variation in colours and UC efficiency might arise from their sizes and crystallisation degrees but also from the pathways of UC in different geometries as we will discuss below.

As it is well-known, the excited $^2\text{F}_{5/2}$ state of the Yb^{3+} ion is resonant with the $^4\text{I}_{11/2}$ excited state of Er^{3+} .⁴⁰ Thus, when β -UCNPs are excited at 980 nm there is an efficient absorption by sensitizers Yb^{3+} , producing an efficiency energy transfer to the activator Er^{3+} ions. Since each Er^{3+} ion is surrounded by many excited Yb^{3+} ions, the energy transfer from Yb^{3+} to Er^{3+} ions take place. In general, energy transfer migration depends on the strength of the ion-ion interaction and concentration of $\text{Yb}^{3+}-\text{Er}^{3+}$ and $\text{Er}^{3+}-\text{Er}^{3+}$ ions within the crystal. Therefore, we can assume that different particle shapes leading to different atom distributions within the crystal structure will favour more or less this energy transfer. The influence of β -UCNPs geometry on its luminescent properties has been recently considered as an interesting area of investigation since the pathways of UC could be different in one and three dimensional systems.²⁶⁰

It is indeed reasonable to think that the energy migration is affected by the spatial position of the ions in a structure and therefore the UC efficiency is different in case that one preferable direction exists.

Assuming the same distribution of Er^{3+} and Yb^{3+} ions, we can guess that the effective velocity is lower in sample 1 and 2 due to the energy migration happening in 3 directions inside the crystal. On the other hand, in a rod-shape UCNP (sample 3 and 4), the spatial position of the activator's molecules (Er^{3+}) are supposedly more accessible to sensitizers

molecules (Yb^{3+}), and the effective energy migration is higher compared with those where the migration occurs equally well in all 3 directions. This idea would explain our experimental results, albeit requiring certain assumptions. Further investigations on dimensionality of carrier migration in the UC mechanism would be necessary for a better understanding of this specific UCNP property, although beyond the scope of our work.

3.2 Synthesis of oleate coated $\text{Na}_x\text{ScF}_{3+x}$ upconversion nanoparticles

Among all the lanthanide-doped UCNPs, NaLnF_4 ($\text{Ln}=\text{Y}^{3+}$, La^{3+} , Ga^{3+} or Lu^{3+}) is one of the most studied host materials. However, UCNPs with Sc^{3+} have got some attention just in the last years and there are only few reports on the synthesis of $\text{Na}_x\text{ScF}_{3+x}$. Some of them are briefly summarized below.

Using the co-precipitation procedure, Huang and co-workers synthesised for the first time $\text{Na}_x\text{ScF}_{3+x}$ UCNPs with a controllable shape by adjustment of the $\text{NaF}:\text{Ln}^{3+}$ molar ratio.²¹⁶ Subsequently, the same group studied the solvent influence in the growth process, by modifying the OA:ODE volume ratio obtaining nanorods with length above 190 nm.²¹⁵ Recently, they studied the morphology and luminescence evolution of a new host material ($\text{KSc}_2\text{F}_7:\text{Yb}/\text{Er}$) *via* Li^{3+} doping and characterized the morphology evolution and the mechanism of UC emission enhancement.²⁶¹

Min Pang et al. synthesized $\text{Na}_x\text{ScF}_{3+x}$ UCNPs *via* the co-thermolysis of trifluoroacetates at high temperature for the first time. They tuned monoclinic phase to hexagonal phase by varying the Na/Sc^{3+} ratio.²⁶² J. Cao et al. prepared monodisperse ScF_3 and NaScF_4 employing a simple solvothermal method and tuned the phase, size and morphology by altering the ratio of $\text{Na}/\text{F}/\text{Sc}$ and Ln^{3+} doping.²⁶³ Ligang Zhang et al synthesized NaScF_4 -UCNPs by a hydrothermal route, whose UC emission from green to red was tuned gradually by adjusting the reaction time.²⁶⁴ Zhiqin Liang et al. synthesized for the first time tetragonal LiScF_4 -UCNPs employing a modified solvothermal method. The phase and morphology of the obtained samples were adjusted by varying the reaction time and temperature.²⁶⁵ Chen and co-workers determined for the first time the crystal structure of NaScF_4 crystals using single-crystal X-ray diffraction.²⁶⁶

Nevertheless, despite these studies it is still not enough on the study of Sc^{3+} -based UCNPs compared to that of Y^{3+} -based UCNPs. For this reason, it would be interesting to better control and understand the structural growth of these $\text{Na}_x\text{ScF}_{3+x}$ UCNPs.

Section 3.2.1 will look into the synthesis and characterization of $\text{Na}_x\text{ScF}_{3+x}$ through a co-precipitation procedure using NH_4F as the fluoride source. The UC luminescence is also briefly evaluated and discussed in **Section 3.2.2**. **Section 0** focuses on the same synthesis but using NaF as fluoride source. Here, the effects of experimental factors such as the reaction time and temperature, and the chemical composition in the fluoride source are discussed. The aim of this work is to further complement the research on Sc^{3+} -based UCNPs.

3.2.1 Synthesis of the $\text{Na}_x\text{ScF}_{3+x}$ UCNPs with NH_4F as a fluoride source

Four samples of $\text{Na}_x\text{ScF}_{3+x}$: Yb^{3+} (20%), Er^{3+} (2%) UCNPs were prepared following the experimental procedure described in **Section 2.1.1**, but using $\text{ScCl}_3 \cdot 6\text{H}_2\text{O}$ instead of $\text{YCl}_3 \cdot 6\text{H}_2\text{O}$ and a reaction temperature of 308 °C. The samples were prepared with increasing OA volume and fixed ODE volume in the reaction mixture. To facilitate the comparison, we chose similar volume of OA and ODE as in **Section 3.1.1** (6:15, 12:15, 17:15 and 21:15 of OA: ODE volume ratio). The remaining experimental parameters were kept the same for all samples.

The particle size and morphology were first evaluated using TEM and the results can be seen in **Figure 37**. The size distribution was analysed with ImageJ software considering over 100 NPs for the statistical analysis

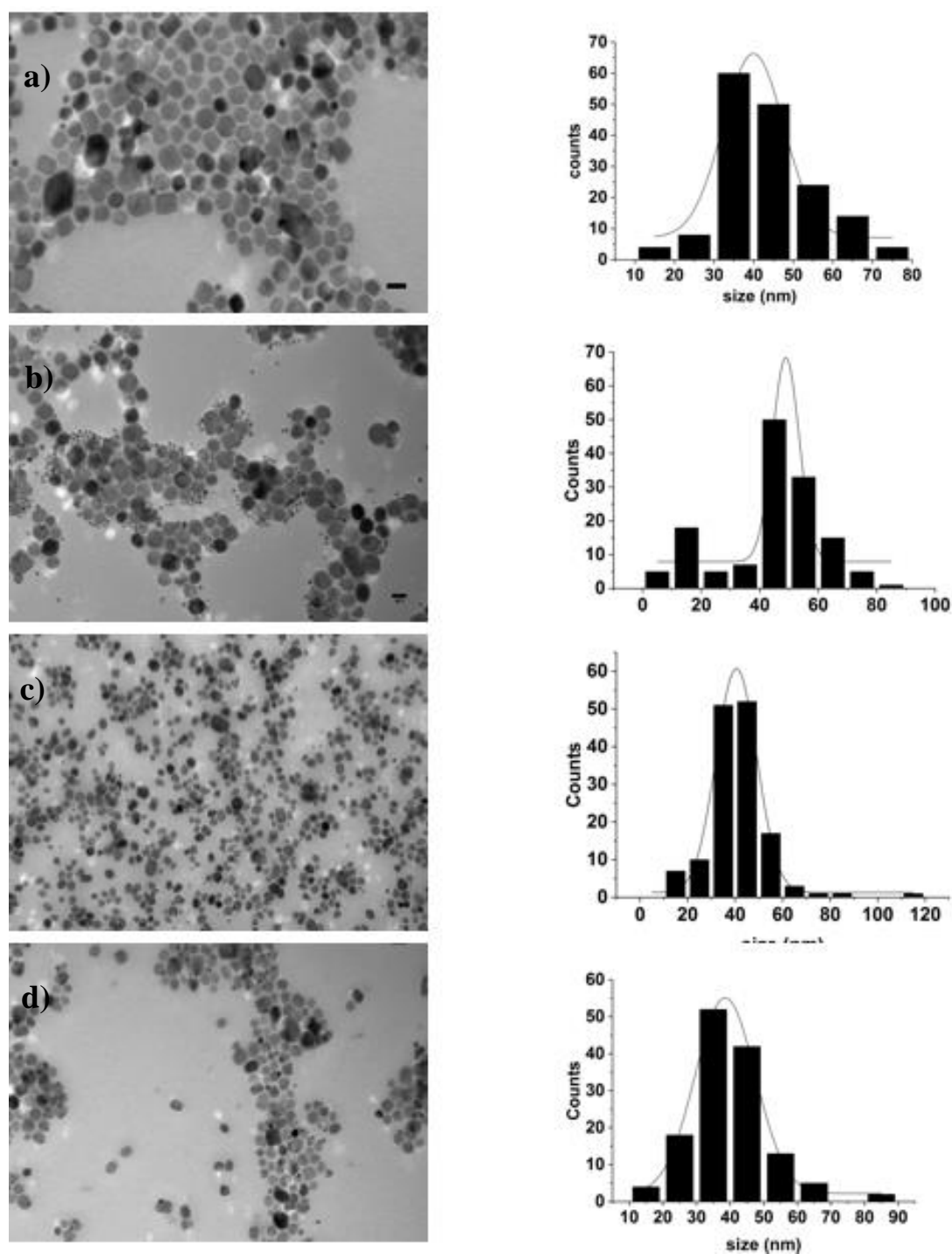


Figure 37. TEM images and size distribution of the different samples of $\text{Na}_x\text{ScF}_{3+x}:\text{Yb}^{3+}(20\%), \text{Er}^{3+}(2\%)$ UCNPs obtained using (a) 6 ml (b) 12 ml (c) 17 ml and (d) 21 ml of OA. Scale bars are 50 nm. Samples (5-8).

The samples synthesised with 6 ml, 12 ml, 17 ml, and 21 ml of OA were named conveniently samples (5-8). The size distribution and **standard deviation** were $40 \text{ nm} \pm 8 \text{ nm}$, $49 \text{ nm} \pm 5 \text{ nm}$, $41 \text{ nm} \pm 9 \text{ nm}$, and $39 \text{ nm} \pm 9 \text{ nm}$ for samples (5-8), respectively.

Next, we have performed XRD for the crystallographic phase confirmation. It can be seen that all peaks from the XRD patterns (**Figure 38**) belong to a mixture of hexagonal (NaScF_4) and monoclinic (Na_3ScF_6) phase, in agreement with the broad size and morphology distribution observed in TEM images.

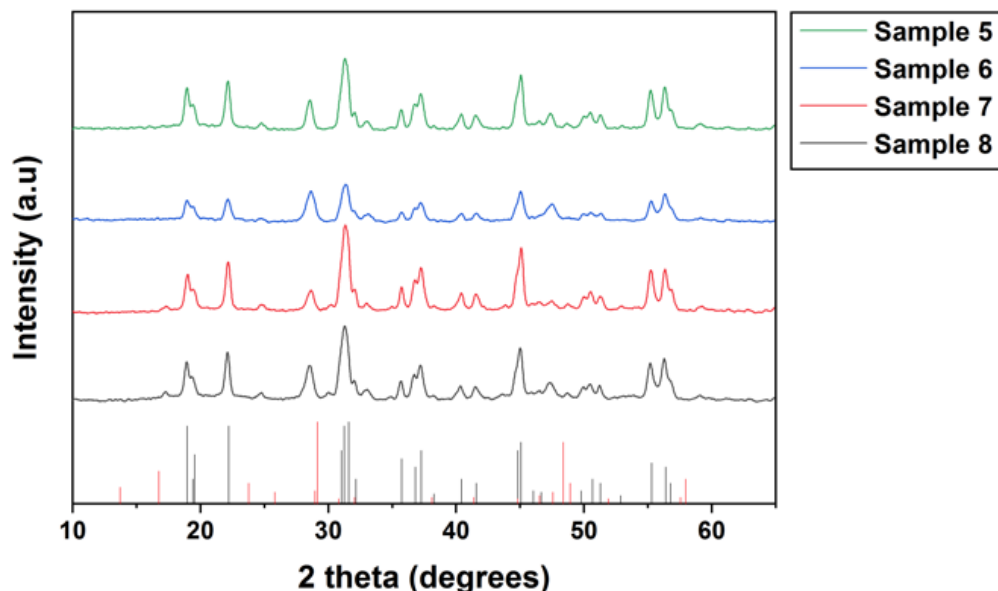


Figure 38. XRD patterns of $\text{Na}_x\text{ScF}_{3+x}$: Yb^{3+} (20%), Er^{3+} (2%) UCNP samples prepared with different OA concentrations. Samples (5-8). Measurements were acquired using a Cu K- α source. Black and red reference lines correspond to the hexagonal NaScF_4 (PDF card No.: 00-020-1152) and monoclinic Na_3ScF_6 phase (PDF card No.: 00-020-1153), respectively.

Previously when characterizing NaYF_4 UCNP only the hexagonal phase was observed thus we can attribute the current structural diversity to the presence of Sc^{3+} . In the present thesis, we have also performed some experiments using $\text{Na}_x\text{ScF}_{3+x}$ with NaF as fluoride source in order to confirm that this behaviour is indeed characteristic of Sc^{3+} . Those results will be discussed in **Section 0**.

3.2.2 Upconversion luminescence properties of $\text{Na}_x\text{ScF}_{3+x}$

Samples (5-8) were prepared in identical conditions, with a final concentration of 20 mg/ml in hexane and were excited by a 980 nm CW laser (500 mW). The overall UC luminescence spectra of the samples prepared with different amount of OA are presented in **Figure 39a** and the obtained RGRs are shown in **Figure 39b**.

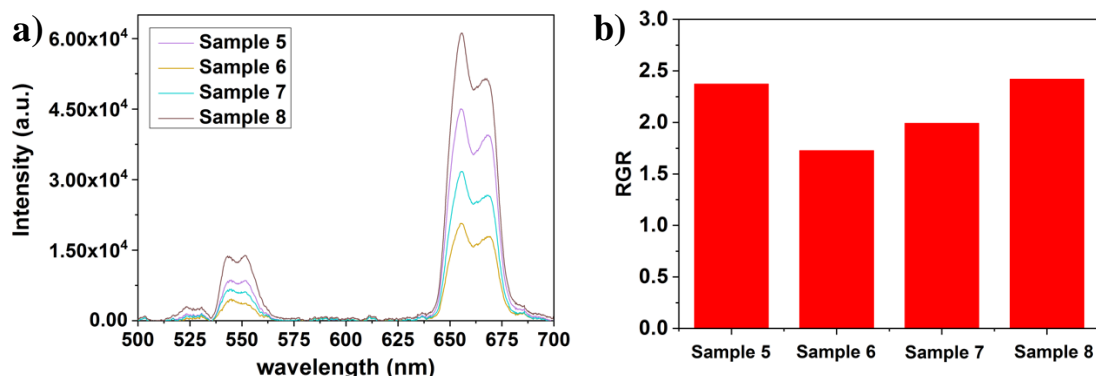


Figure 39. (a) Emission spectra and (b) RGR for $\text{Na}_x\text{ScF}_{3+x}$: Yb^{3+} (20%), Er^{3+} (2%) UCNPs synthesised with different concentrations of OA under 980 nm excitation wavelength. Samples (5-8).

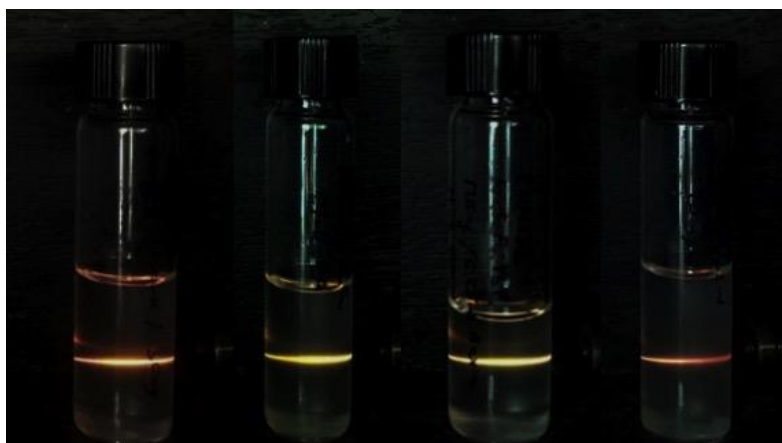


Figure 40. From left to right. Digital images for $\text{Na}_x\text{ScF}_{3+x}$: Yb^{3+} (20%), Er^{3+} (2%) UCNPs from samples (5-8), under excitation wavelength of 980 nm.

Overall, samples (5-8) did not follow any trend regarding the UC luminescence, but it was clearly observed that the synthesised $\text{Na}_x\text{ScF}_{3+x}$ showed a stronger red emission and thus higher RGRs than those of UCNPs based NaYF_4 (**Section 3.1.3**). This difference can be explained by the smaller ionic radius of Sc^{3+} compared to Y^{3+} ion and thus a shorter distance

Sc-Sc compared to Y-Y.²¹⁶ According to Wang and co-workers,²¹⁶ the short distance between Ln^{3+} could enhance the cross relaxation ($^4\text{F}_{7/2} + ^4\text{I}_{11/2} \rightarrow ^4\text{F}_{9/2} + ^4\text{F}_{9/2}$). The dominance in red emission and the quenching in green emission of samples (5-8) were associated to the increased cross relaxation (CR) effect among the activators.

Our observations indicated that by substituting different Ln^{3+} in the same matrix $\text{Na}_x\text{LnF}_{3+x}$ ($\text{Ln}^{3+} = \text{Sc}^{3+}, \text{Y}^{3+}$) and keeping the other experimental parameters the same during the synthesis, it was possible to have a transition from a brighter NaYF_4 hexagonal phase to a mixture of hexagonal NaScF_4 and monoclinic Na_3ScF_6 phases. Importantly, it has been found that this host material results in multicolour emissions ranging from red-orange to yellow and green. **Table 8** summarises the outcomes of the experiments carried with samples 1-8.

Table 8. Summary of RGR, UC emission multicolour and crystallographic phases obtained for $\text{Na}_x\text{LnF}_{3+x}$ ($\text{Ln} = \text{Sc}^{3+}, \text{Y}^{3+}$) UCNPs synthesised under the same co-precipitation experimental route and same fluoride source (NH_4F) but different volume of OA.

Method	Fluoride source	Matrix	Sample Name	OA(ml)	ODE (ml)	RGR	Colour Output	Crystallographic phase
Co-precipitation	NH_4F	NaYF_4	Sample 1	6	15	1.70	yellow	NaYF_4
			Sample 2	12	15	1.21	Yellow-green	NaYF_4
			Sample 3	17	15	0.87	green	NaYF_4
			Sample 4	21	15	0.73	green	NaYF_4
		$\text{Na}_x\text{ScF}_{3+x}$	Sample 5	6	15	2.37	orange	$\text{NaScF}_4 + \text{Na}_3\text{ScF}_6$
			Sample 6	12	15	1.73	yellow	$\text{NaScF}_4 + \text{Na}_3\text{ScF}_6$
			Sample 7	17	15	1.99	yellow	$\text{NaScF}_4 + \text{Na}_3\text{ScF}_6$
			Sample 8	21	15	2.42	red	$\text{NaScF}_4 + \text{Na}_3\text{ScF}_6$

3.2.3 Synthesis of $\text{Na}_x\text{ScF}_{3+x}$ UCNPs with NaF as a fluoride source.

3.2.3.1 Effect of the NaF: Ln^{3+} molar ratio to the morphology of upconversion nanoparticles.

$\text{Na}_x\text{ScF}_{3+x}$: Yb^{3+} (20%), Er^{3+} (2%) UCNPs were prepared following the experimental procedure described in **Section 2.1.5**. Here a reported protocol^{215,216} with minor modifications was followed, where NaF was used as fluoride source. Four samples were prepared by adjusting the NaF: Ln^{3+} molar ratio to 1, 1.5, 2 and 2.5. The remained experimental conditions were kept unchanged, and time and temperature reaction were fixed to 1 hour and 20 min and 308 °C respectively. The $\text{Na}_x\text{ScF}_{3+x}$ sizes and morphologies were first characterized using TEM. The NPs size distribution was analysed with ImageJ software considering over 100 NPs for the statistical analysis

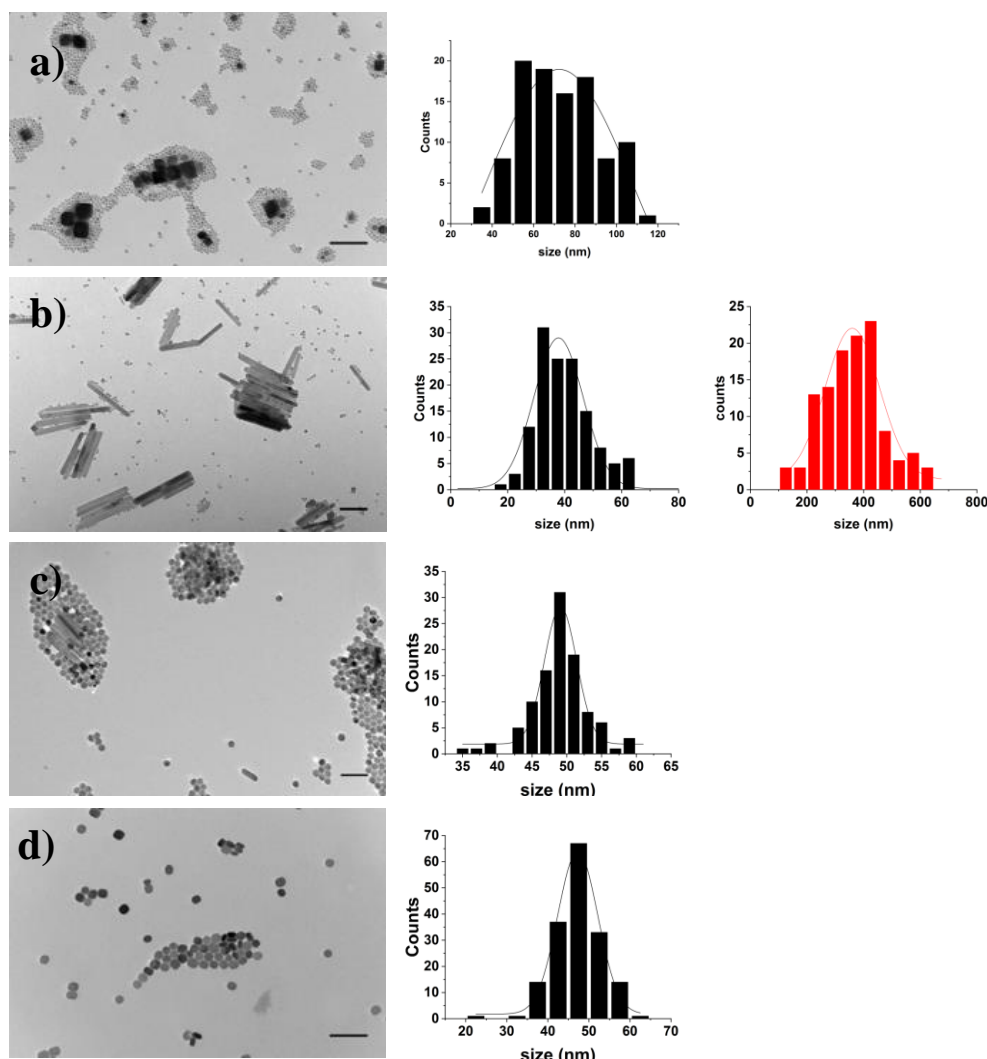


Figure 41. TEM images and size distribution of the $\text{Na}_x\text{ScF}_{3+x}$: Yb^{3+} (20%), Er^{3+} (2%) UCNPs synthesized at different NaF: Ln^{3+} ratio of (a) 1.0, (b) 1.5, (c) 2.0 and (d) 2.5. Scale

bars are 200 nm. Black bars from the histograms indicate the diameter and the red colour corresponds to the length of the rods.

Images from **Figure 41** reveal that by adjusting the NaF: Ln^{3+} molar ratio to 1, 1.5, 2 and 2.5, different morphologies and shapes of UCNPs were obtained. The resulting morphology varied from a) large cubes to b) long rods, c) mixture of rods/nanospheres and d) nanospheres. The dimensions and shapes of the as synthesised samples are summarized in **Table 9**.

Table 9. Dimensions of the $\text{Na}_x\text{ScF}_{3+x}$: Yb^{3+} (20%), Er^{3+} (2%) UCNPs synthesized at different molar ratio NaF: Ln^{3+} . The measured sizes correspond to the nanobubes for the NaF: $\text{Ln}^{3+}=1$, to the nanorods for the NaF: $\text{Ln}^{3+}=1.5$, and to the nanospheres for the NaF: $\text{Ln}^{3+}=2$ and NaF: $\text{Ln}^{3+}=2.5$.

NaF: Ln^{3+}	Shape	Size (nm)
1	Nanocubes + tiny NPs	72 ± 36
1.5	Nanorods + tiny NPs	$(360 \pm 96) \times (38 \pm 9)$
2	Nanospheheres + a few nanorods	49 ± 2
2.5	Nanospheres	47 ± 5

It is worth to mention that when the molar ratio was as low as 1, a considerable quantity of tiny NPs with a mean size of ~ 13 nm was obtained together with the cubes. When the molar ratio was 1.5 the number of tiny NPs (~ 5 nm) decreased considerably and above the molar ratio 1.5 the small NPs did not form. This broad distribution of morphologies has been also reported by Huang and co-workers, and could indicate a mixture of crystallographic phases.

The morphologies obtained in our experiments were compared with those reported in the literature.^{216,263} The morphologies obtained in Huang and co-worker's work are compared to our results in **Table 10**.

Observation of the data did not match with literature; however, our reaction conditions were not precisely mapped to Huang's experiments. Further investigation was therefore required to confirm the validity of our results. In the following sections we investigate how temperature and reaction time influenced the morphologies of the UCNPs.

Table 10. Huang and co-workers results ²¹⁶(working at 300 °C and 1 hour and 30 min) vs our results (when working at 308 °C and 1 hour and 20 min).

NaF: Ln ³⁺	Huang and co-worker. ²¹⁶	Our results
	Shape	Shape
1	Spheres	Cubes + tiny spheres
1.5	Cubes	Rods + tiny spheres
2	Rods	Spheres + a few rods
2.5	Spheres	Spheres

Clearly, different results were obtained by synthesizing Na_xScF_{3+x} UCNPs with NH₄F (**Section 3.2.1**) and NaF (current **Section 0**) as the fluoride source. Although the exact reason of the resulted structures is not very clear, an explanation for the change in the morphology can be provided as consequence of both, the addition temperature of fluoride precursors and the nature of the cation source.

The mechanism of growth of the UCNPs is generally based on the separation of the nucleation process that occur at the time of the addition of the precursors and the subsequent growth of the UCNP as the temperature rises.¹³ Hence, we should consider that in our experiments the reactions conditions were not exactly the same. In terms of the fluoride source addition temperature, NaF was added at 160° while NH₄F was injected along with NaOH at room temperature.

It is known that different crystals facets need different energies to grow. We believe that when the addition temperature was high (160°), all the facets could grow equally because energy was high, however when the addition temperature was lower, the energy was also low and the different energies required by each facet became a limiting factor. Therefore, lower addition temperatures produced more anisotropic Na_xScF_{3+x} UCNPs as seen in **Figure 37**, while higher addition temperature produced more symmetric structures as seen in **Figure 41**.

From another point of view, Wang and co-workers suggested that cations of the fluoride sources XF ($X = K^+, H^+, NH_4^+, Na^+, Rb^+$, and Cs^+) were responsible for their observed crystal structures and morphologies for EuF_3 .²⁶⁷ Although the exact role of these sources was not revealed, they suggested that it is probable that cations adhere differently to the initially formed tiny EuF_3 surface. They proposed that the number of cations ($K^+, H^+, NH_4^+, Na^+, Rb^+$, and Cs^+) with different sizes absorbed on the EuF_3 crystal faces might be different and therefore, different morphologies were obtained.²⁶⁷ Based on this idea, it could be equally assumed that the XF ($X = Na^+$ and NH_4^+) in our experiments adhered on the surface of the Na_xScF_{3+x} UCNP's nuclei differently giving rise to different morphologies.

3.2.3.2 Influence of reaction time upon the morphology of upconversion nanoparticles.

Na_xScF_{3+x} : Yb^{3+} (20%), Er^{3+} (2%) UCNPs were prepared following the experimental procedure detailed in **Section 2.1.5**. In this section, six samples in total (3 samples with NaF : $Ln^{3+} = 1.5$ and 3 samples with NaF : $Ln^{3+} = 1$) were prepared by changing the reaction time to 1 hour, 1 hour and 20 min and 1 hour and 40 min. The rest of the experimental conditions were kept unchanged.

The particle size and morphology were first observed using TEM (see **Figure 42** and **Figure 43**). The size distribution was analysed with ImageJ software considering over 100 NPs for each of the samples.

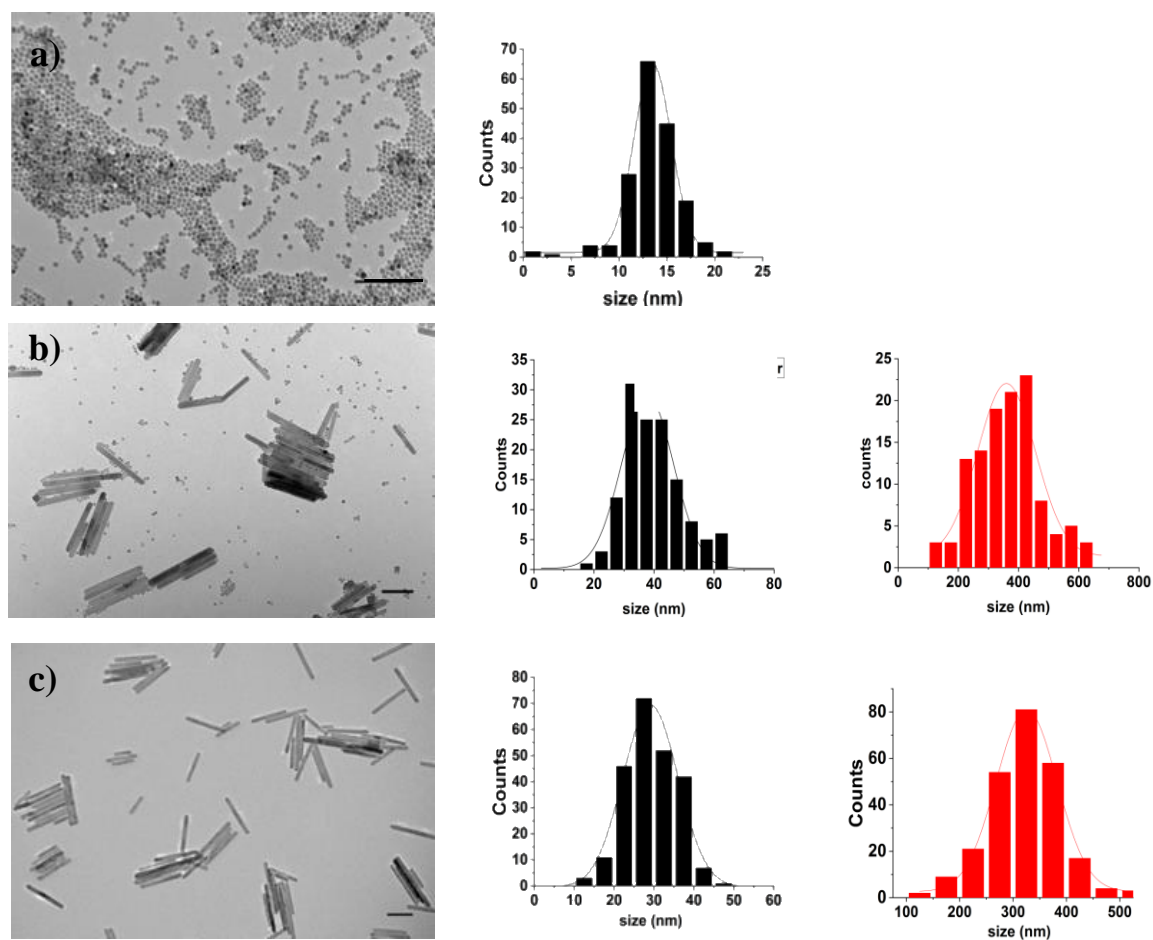


Figure 42. TEM images of the $\text{Na}_x\text{ScF}_{3+x}:\text{Yb}^{3+}(20\%), \text{Er}^{3+}(2\%)$ UCNPs synthesized at different reaction times of (a) 1 hour, (b) 1 hour and 20 min and (c) 1 hour and 40 min. $\text{NaF}:\text{Ln}^{3+} = 1.5$ molar ratio. Scale bars are 200 nm. Black bars from the histograms indicate the diameter size meanwhile the red colour corresponds to the length of the rods.

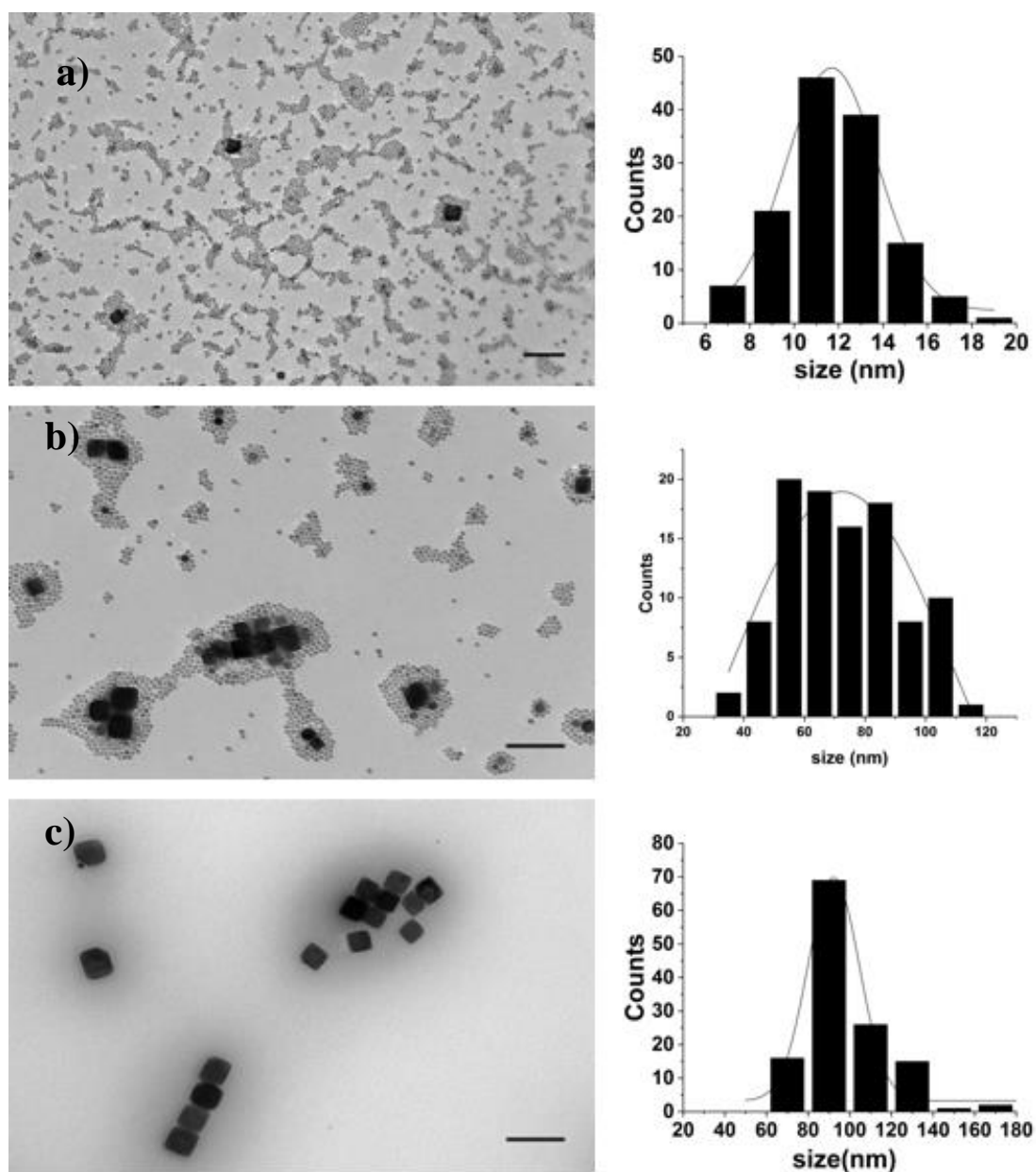


Figure 43. TEM images of the $\text{Na}_x\text{ScF}_{3+x}:\text{Yb}^{3+}(20\%), \text{Er}^{3+}(2\%)$ UCNP synthesized at different reaction times of (a) 1 hour, (b) 1 hour and 20 min and (c) 1 hour and 40 min. $\text{NaF}:\text{Ln}^{3+}=1$ molar ratio. Scale bars are 200 nm. Black bars from the histograms indicate the size in edge length.

It can be seen that small $\text{Na}_x\text{ScF}_{3+x}$ UCNP's were formed at earlier stages of the reaction (1 hour) and gradually converted into bigger structures. It was observed that $\text{Na}_x\text{ScF}_{3+x}$ synthesised with a lower molar ratio $\text{NaF}:\text{Ln}^{3+} = 1$ (see **Figure 43**) tended to form cubes while higher molar ratios of $\text{NaF}:\text{Ln}^{3+} = 1.5$ (see **Figure 42**) favoured the rod-shaped $\text{Na}_x\text{ScF}_{3+x}$. The size and morphology are summarized in **Table 11**.

Table 11. Summary of dimensions of the $\text{Na}_x\text{ScF}_{3+x}:\text{Yb}^{3+}(20\%), \text{Er}^{3+}(2\%)$ UCNP's synthesized at different reaction times of 1 hour, 1 hour and 20 min and 1 hour and 40 min and using molar ratios of $\text{NaF}:\text{Ln}^{3+} = 1$ and 1.5.

$\text{NaF}:\text{Ln}^{3+}$	Time	Shape	Size (nm)
1.5	1 hour	Tiny spheres	14 ± 2
	1 hour and 20 min	Rods + tiny spheres	$(360 \pm 96) \times (38 \pm 9)$
	1 hour and 40 min	Rods	$(325 \pm 57) \times (29 \pm 7)$
1	1 hour	Tiny spheres	12 ± 2
	1 hour and 20 min	Cubes + tiny spheres	72 ± 36
	1 hour and 40 min	Cubes	92 ± 12

XRD patterns were collected for phase identification and to understand the growth evolution. For the case of $\text{Na}_x\text{ScF}_{3+x}$ synthesised at $\text{NaF}:\text{Ln}^{3+} = 1.5$ molar ratio, (see **Figure 44**) it was found that pure hexagonal phase (NaScF_4) was only observed at the early stages of the reaction (1 hour). After 1 hour and 20 min of reaction a new phase (monoclinic Na_3ScF_6) appeared, which resulted in a mixture of both NaScF_4 and Na_3ScF_6 phases at the same ratio. When we stopped the reaction at 1 hour and 40 min, the intensity of the relative diffraction peaks of the NaScF_4 phase decreased dramatically in agreement to the morphological evolution, suggesting that at this stage, the sample was composed mainly by Na_3ScF_6 crystals.

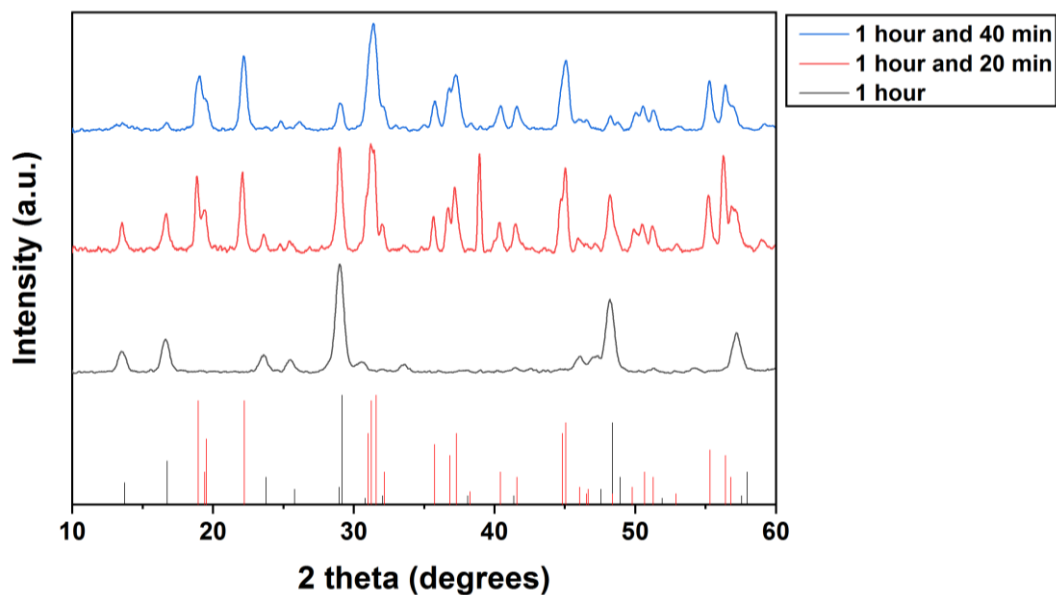


Figure 44. XRD patterns of the $\text{Na}_x\text{ScF}_{3+x}$: Yb^{3+} (20%), Er^{3+} (2%) UCNPs synthesized at different reaction time of 1 hour, 1 hour and 20 min and 1 hour and 40 min. $\text{NaF}:\text{Ln}^{3+}=1.5$ molar ratio. Measurements were acquired using a Cu K- α source. Black and red reference lines correspond to the hexagonal NaScF_4 (PDF card No.: 00-020-1152) and monoclinic Na_3ScF_6 phase (PDF card No.: 00-020-1153), respectively.

Results indicate that short reaction time favoured a NaScF_4 phase, while a longer reaction time favoured the Na_3ScF_6 phase. The crystallographic phase evolution matches our observations by TEM (see **Figure 42**). The NaScF_4 phase is usually associated with spheres and hexagonal plates, while the Na_3ScF_6 phase is characteristic of rod-shape structures.²¹⁶ It is interesting that after 1 hour and 40 min, some impurities from the NaScF_4 phase were still visible in the XRD pattern but neither spheres or any other shape different from the rods were observed in the TEM images.

One possible explanation is that the reaction was stopped before the $\text{NaScF}_4 \rightarrow \text{Na}_3\text{ScF}_6$ phase transition was completed. However, according to the TEM images from **Figure 42c**, only rods shapes were observed; therefore, we hypothesise that this low fraction of the NaScF_4 phase could indicate that as the reaction proceeds, some nanorods could be formed by aggregation of small UCNPs that eventually merged into one. Therefore, it is still possible that different crystallite sizes (domains) coexist inside the same particle. The broadening of the XRD peaks (see blue line in **Figure 44**) is also consistent with this hypothesis, since this is a feature of strains and lattice deformations within the crystal.²⁶⁸

Figure 45 displays the XRD pattern of $\text{Na}_x\text{ScF}_{3+x}$ synthesised at $\text{NaF}:\text{Ln}^{3+}=1$ molar ratio for a reaction time of 1 hour and 40 min. In general, samples with a molar ratio of $\text{NaF}:\text{Ln}^{3+}=1$ produced a low yield of product, which prevented XRD analysis for the first two stages.

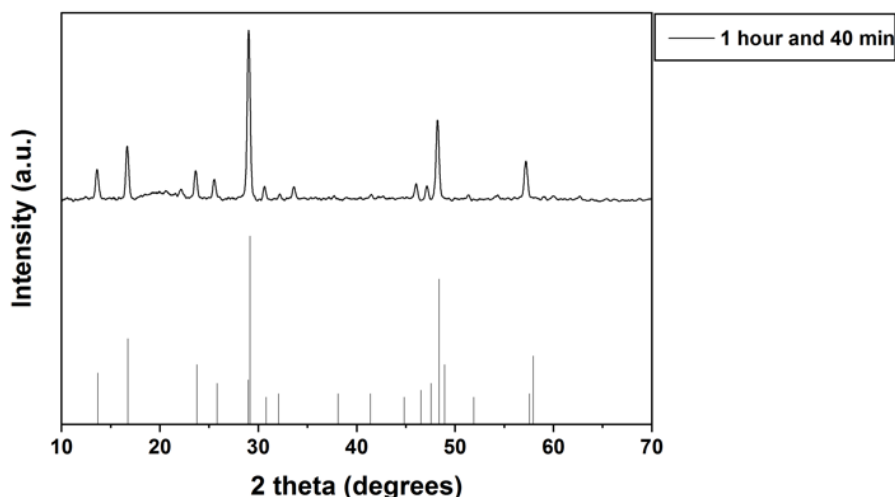


Figure 45. XRD pattern of the $\text{Na}_x\text{ScF}_{3+x}:\text{Yb}^{3+}(20\%),\text{Er}^{3+}(2\%)$ UCNPs synthesized for 1 hour and 40 min at $\text{NaF}:\text{Ln}^{3+}=1$. Measurements were acquired using a Cu K- α source. Black reference line is the hexagonal NaScF_4 phase (PDF card No.: 00-020-1152).

When using $\text{NaF}:\text{Ln}^{3+}=1$ molar ratio only a pure NaScF_4 phase of UCNPs was observed and at the end of the reaction no impurities from other phases were present. Therefore, we conclude that with this molar ratio, the NaScF_4 structure is thermodynamically more stable and that this phase dictates the entire growth evolution.

We hypothesize an Ostwald-ripening mechanism for the narrowing of the sizing distribution as illustrated in **Figure 46**. At the early stage of the reaction smaller $\text{Na}_x\text{ScF}_{3+x}$ with large SA are created and consequently the mixture initially is not in thermodynamic equilibrium. During the ripening, the smaller $\text{Na}_x\text{ScF}_{3+x}$ nuclei re-dissolve so that their mass is released into the solution to further create larger nanocrystals. The configuration with fewer larger nanocrystals is thermodynamically favoured. This growth pattern continues until thermodynamic equilibrium is reached.²⁶⁹

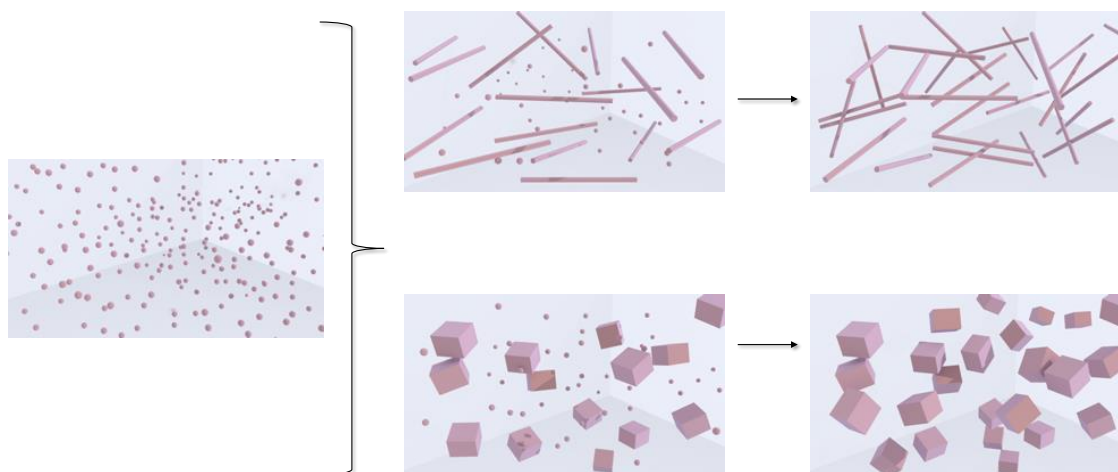


Figure 46. Illustration of the growth process of $\text{Na}_x\text{ScF}_{3+x}$: Yb^{3+} (20%), Er^{3+} (2%) UCNP via Ostwald ripening mechanism. NaF: Ln^{3+} = 1.5 molar ratio (top) and NaF: Ln^{3+} = 1 molar ratio (bottom).

In general, time-dependent experiments revealed that when using NaF: Ln^{3+} = 1.5 molar ratio, the monoclinic Na_3ScF_6 phase was thermodynamically more stable and favoured the formation of rods. On the other hand, when using NaF: Ln^{3+} = 1 molar ratio, cubes were formed and the hexagonal NaScF_4 phase seemed to be predominant throughout the whole process.

Independently of the NaF: Ln^{3+} molar ratio, we can conclude that the growth of the $\text{Na}_x\text{ScF}_{3+x}$ was *via* the Ostwald ripening. For the NaF: Ln^{3+} = 1, we believe that the smaller particles re-dissolved and diffused onto the surface of bigger particles for their growth. In the case of molar ratio NaF: Ln^{3+} of 1.5 we believe that phase transition ($\text{NaScF}_4 \rightarrow \text{Na}_3\text{ScF}_6$) occurred mainly with a dissolution and recrystallization process and not a direct phase transformation process on the surface of the particles.

3.2.3.3 Reaction temperature effect on the synthesis of upconversion nanoparticles

Five new samples of $\text{Na}_x\text{ScF}_{3+x}$: Yb^{3+} (20%), Er^{3+} (2%) UCNP were prepared following the experimental procedure detailed in **Section 2.1.5**. The temperature of the reaction was varied for each sample (288 °C, 298 °C, 303 °C, 308 °C and 318 °C) and the NaF: Ln^{3+} molar ratio (1.5) and reaction time (1 hour and 40 min) were kept the same for all five samples. The particles sizes and their morphologies were first characterized by TEM. The size distribution was analysed with ImageJ software considering over 100 NPs for each of the samples.

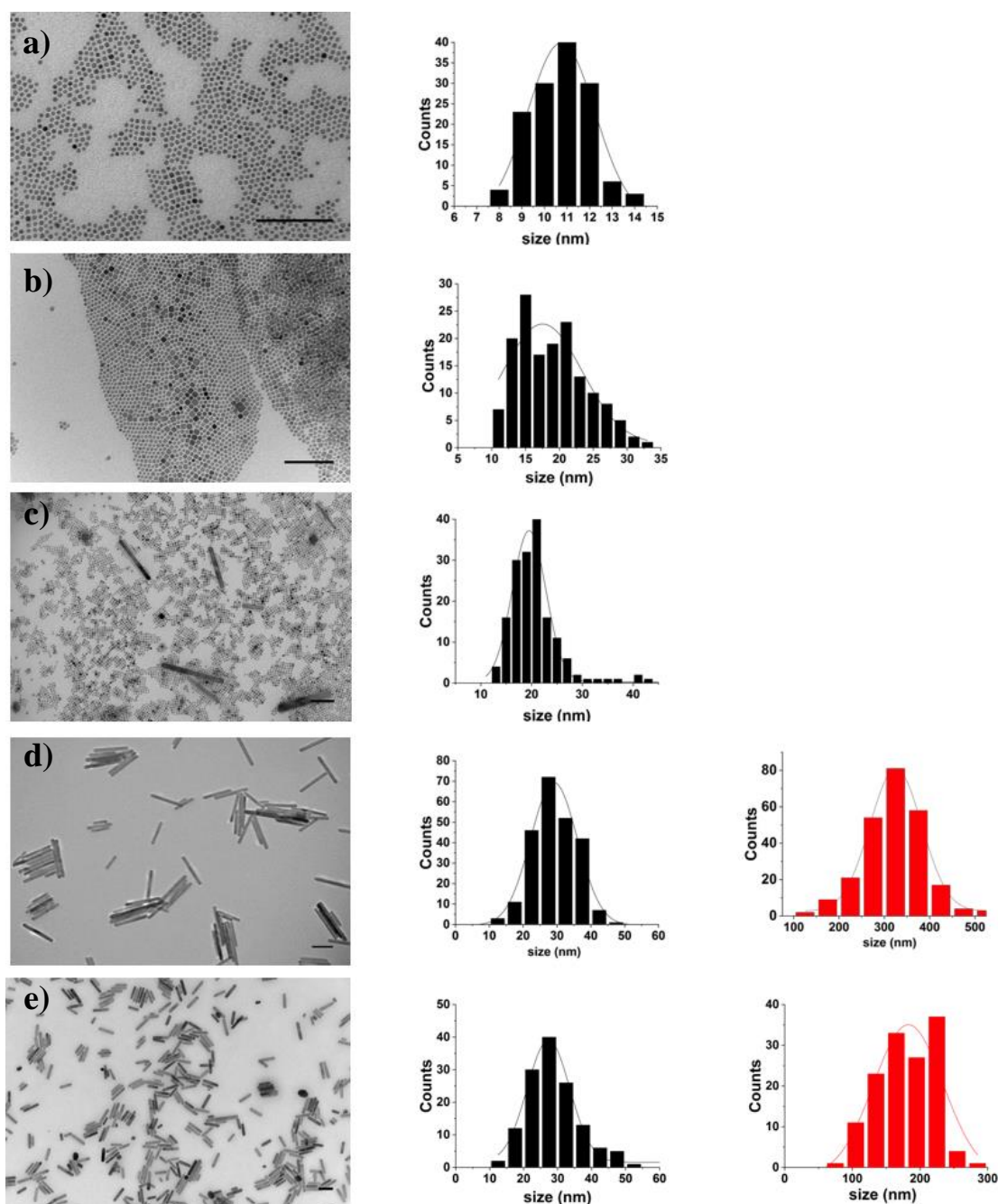


Figure 47. TEM images of the $\text{Na}_x\text{ScF}_{3+x}$: Yb^{3+} (20%), Er^{3+} (2%) UCNPs synthesized at different temperatures of (a) 288 °C, (b) 298 °C, (c) 303 °C, (d) 308 °C and (e) 318 °C. $\text{NaF}:\text{Ln}^{3+} = 1.5$. Scale bar are 200 nm. Black bars from the histograms indicate the diameter size meanwhile the red colour corresponds to the length of the rods.

The temperature dependence of the $\text{Na}_x\text{ScF}_{3+x}$ synthesized at 288 °C showed small spheres with a mean size of $11 \text{ nm} \pm 1 \text{ nm}$, which transformed into $18 \text{ nm} \pm 6 \text{ nm}$ small cubes when the temperature was adjusted to 298 °C. As the temperature increased, a morphology evolution pattern started to appear. Reaction at 303 °C produced a mixture of long rods but mostly cubes ($20 \text{ nm} \pm 3 \text{ nm}$). At 308 °C almost all the $\text{Na}_x\text{ScF}_{3+x}$ had rod-like shapes with

lengths of $(325 \text{ nm} \pm 57 \text{ nm})$ and diameters of $(29 \text{ nm} \pm 7 \text{ nm})$. Slightly shorter rods with a mean size of $(188 \text{ nm} \pm 51 \text{ nm}) \times (27 \text{ nm} \pm 6 \text{ nm})$ were obtained when the temperature was kept at 318°C .

Table 12. Dimensions of the $\text{Na}_x\text{ScF}_{3+x}:\text{Yb}^{3+}(20\%), \text{Er}^{3+}(2\%)$ UCNPs synthesized at different temperatures of 288°C , 298°C , 303°C , 308°C and 318°C . $\text{NaF}:\text{Ln}^{3+}=1.5$.

$\text{NaF}:\text{Ln}^{3+}$	Temperature ($^\circ\text{C}$)	Shape	Size (nm)
1.5	288	Tiny particles	11 ± 1
	298	Tiny cubes	18 ± 6
	305	Tiny cubes + rods	20 ± 3
	308	Rods	$(325 \pm 57) \times (29 \pm 7)$
	318	Rods	$(188 \pm 51) \times (27 \pm 6)$

XRD patterns were collected to characterize the phase of the $\text{Na}_x\text{ScF}_{3+x}$ UCNPs and they are shown in **Figure 48**. It was observed that pure hexagonal NaScF_4 phase was formed only when the temperature of the reaction was kept as low as 288°C . At 298°C the monoclinic Na_3ScF_6 phase appeared and the resulting mixture of the two phases produced cube-shaped particles with different sizes as shown in the TEM image from **Figure 47b**. At 308°C the intensity of the relative diffraction peaks of the hexagonal NaScF_4 phase decreased dramatically, suggesting that the sample was composed mainly of the monoclinic Na_3ScF_6 phase. However, when the temperature is as high as 318°C the $\text{Na}_3\text{ScF}_6/\text{NaScF}_4$ ratio seemed to decrease.

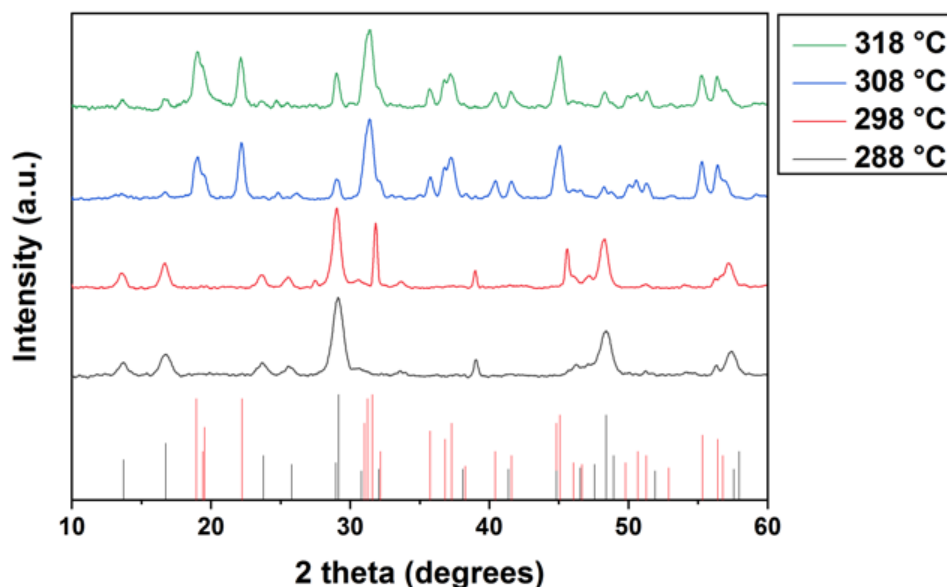


Figure 48. XRD patterns of the $\text{Na}_x\text{ScF}_{3+x}$: Yb^{3+} (20%), Er^{3+} (2%) UCNPs synthesized at different temperatures of 288 °C, 298 °C, 308 °C and 318 °C. $\text{NaF}:\text{Ln}^{3+} = 1.5$. Reaction time reaction was adjusted to 1 hour and 40 min. Black and red reference lines correspond to the hexagonal NaScF_4 (PDF card No.: 00-020-1152) and monoclinic Na_3ScF_6 phase (PDF card No.: 00-020-1153), respectively.

We have observed in **Section 3.2.3.2** that UCNPs ($\text{NaF}:\text{Ln}^{3+} = 1.5$) followed a $\text{NaScF}_4 \rightarrow \text{Na}_3\text{ScF}_6$ transition process as function of the reaction time and driven by the Ostwald ripening process. Stopping the reaction in the middle of the transition (before 1 hour and 40 min in our case) produced a mixed phase with non-uniform size distribution. To achieve pure Na_3ScF_6 , the reaction had to be stopped after the $\text{NaScF}_4 \rightarrow \text{Na}_3\text{ScF}_6$ phase transition was completed. We speculate that when the temperature was very high (318 °C) the growth evolution was driven by a distinct kinetic trend and therefore, longer reaction time would be necessary to obtain pure Na_3ScF_6 .

The effect of the temperature in the growth of NaYF_4 -UCNPs has been studied by different groups.^{56,237,270} They reported that the irregular cubic-phase (α - NaYF_4), formed at low temperature, can turn into the hexagonal-phase (β - NaYF_4) at high temperature. The phase transition $\alpha \rightarrow \beta$ occur with a dissolution and recrystallization process and not a direct phase transformation process on the surface of the β -UCNPs. Based on our observation and the above statement, we believe that the phase transition from hexagonal to monoclinic ($\text{NaScF}_4 \rightarrow \text{Na}_3\text{ScF}_6$) in our work occurred with a similar dissolution and recrystallization process.

The hexagonal NaScF₄ phase is expected to quickly nucleate after the RE reagents are mixed with NaF. Owing to the existence of a high energy barrier between the NaScF₄ and Na₃ScF₆ phases, the former one is quite stable and the NaScF₄ → Na₃ScF₆ transition cannot take place when the reaction temperature is lower than 288 °C. In the temperature window from 288 °C to 308 °C, we observed that both of the phases can coexist. Only when the reaction temperature exceeded 308 °C, the complete transformation to Na₃ScF₆ phase can be obtained. Our results follow a similar growth kinetics than the ones reported for the well-known matrix NaYF₄-UCNPs.²⁷¹

In general, the temperature dependent experiments revealed that small spherical Na_xScF_{3+x} formed at low temperature can transform into cubes and eventually into long rods at high temperature. Moreover, it was observed that at low temperature the pure hexagonal NaScF₄ phase dominates, while at high temperature the monoclinic Na₃ScF₆ phase takes over.

3.3 Fabrication of a shell around a core of upconversion nanoparticles.

Creating an inorganic shell around the core of UCNPs is a common approach to improve the UC efficiency of UCNPs.^{272–275} This improvement derives from passivation of the surface defects.²⁷⁶ The synthesis consist in the fabrication of a core@shell structure where a shell of the same or similar material as the core is grown on the surface of the core.^{126,138,277}

Section 3.3.1 will look at the synthesis and characterization of different inorganic shells around the β-UCNPs. Moreover, we will see how compressive and tensile strains affect the final geometry, and we will characterise their structural properties using XRD. We also performed optical measurements to understand how surface quenching was reduced. The UC luminescence is discussed in **Section 3.3.2**.

3.3.1 Effect of Epitaxial shelling on UCNPs

The synthesis of the core β-NaYF₄: Yb³⁺(20%), Er³⁺(2%) UCNPs was performed following the standard protocol described in **Section 2.1.1**.

In this case, a large batch of β-UCNPs was synthesised using double the quantities of reagents as specified in the original procedure. This was then split into four samples. One of the samples was kept for control experiments while the other three samples were used as the core's host material to prepare the core@shell structures.

In our experiments, β -NaYF₄, β -NaGdF₄, and β -NaLuF₄ were utilized as the shell materials and were coated on the surface of the β -NaYF₄ core following the experimental procedure detailed in **Section 2.1.2**.

TEM of core and core@shell are shown in **Figure 50**. The size distribution was analysed with ImageJ software considering over 100 NPs for the statistical analysis. The size distribution of the core β -NaYF₄ UCNPs was $27 \text{ nm} \pm 1 \text{ nm}$. The morphology of the core@shell created with β -NaYF₄ as the coating material was elliptical and presented an average size of $39 \pm 2 \text{ nm}$ (length) \times $28 \pm 2 \text{ nm}$ (diameter). Core@shell synthesized with β -NaGdF₄ shell produced dumbbell-shaped nanostructures with length of $31 \pm 2 \text{ nm}$, diameter of $30 \pm 2 \text{ nm}$ for the two ends, and 25 ± 2 for the middle-diameter. Core@shell fabricated with β -NaLuF₄ produced spherical particles with a mean diameter of $34 \pm 3 \text{ nm}$.

For clarity purposes, the geometry and measured distances of the different core@shell nanostructures are schematically represented in **Figure 49**.

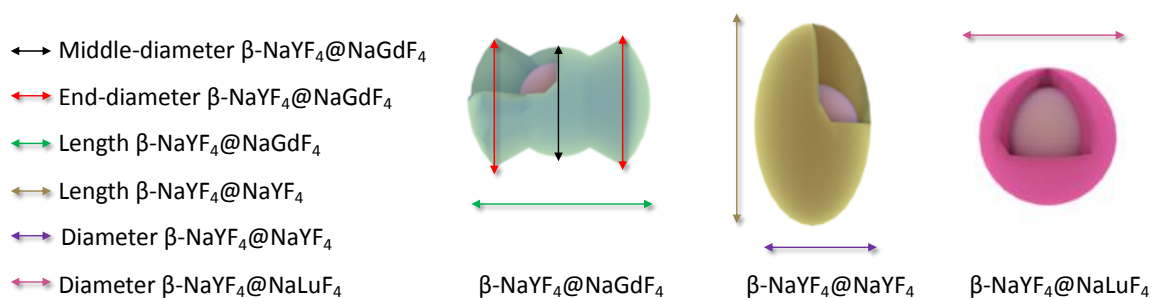


Figure 49. Cartoon showing the geometry of the different core@shell nanostructures. The measurements that were carried out are represented by coloured arrows.

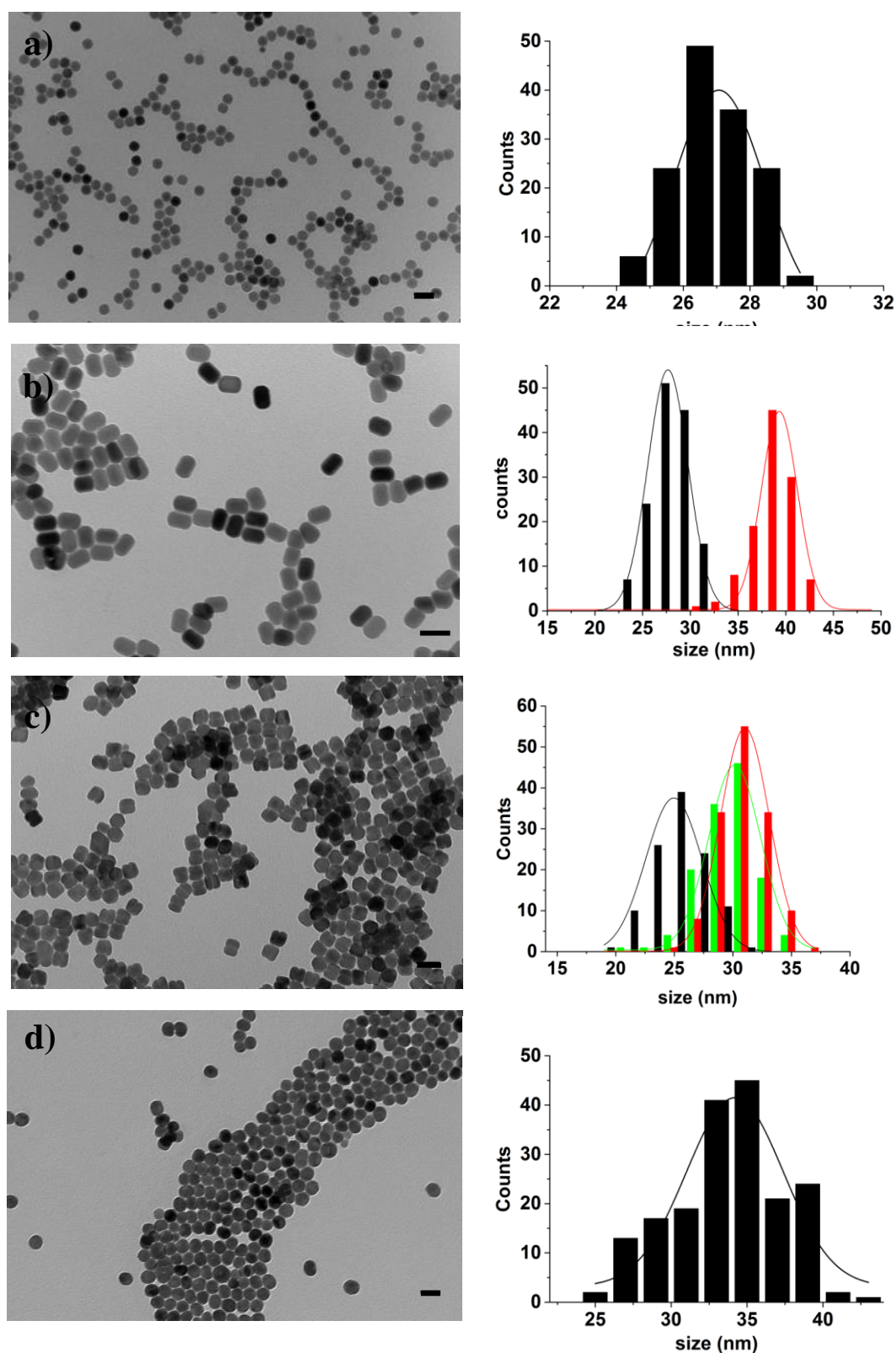


Figure 50. TEM images of the core (a) β -NaYF₄ and core@shell (b) β -NaYF₄@NaYF₄ (c) β -NaYF₄@NaGdF₄, and (d) β -NaYF₄@NaLuF₄. Scale bars are 50 nm. Black and red bars at the histograms indicate the diameter and the length of the UCNP, respectively. Additionally, the green bars refer to the end diameters of β -NaYF₄@NaGdF₄ structures.

Our experiments revealed that when β -NaLuF₄ was deposited around the β -NaYF₄ core, a uniform ~ 4 nm thick shell was obtained. If β -NaGdF₄ was the shell, particles grew in length and end-diameters ~ 2 nm and ~ 1.5 nm, respectively. A subtractive growth was observed in their middle-diameter size which decreased from 27 nm to 25 nm, producing the known dumbbell-shaped nanostructures.²⁷⁸ The resulting core@shell obtained with β -NaYF₄ showed no apparent change in thickness but increased ~ 6 nm in length.

Figure 51 illustrate how a tensile strain in the NaLuF₄ shell growth led to a highly isotropic shape compared to the compressed NaGdF₄ shell growth, which generated a more anisotropic structure.²⁷⁹ Our results indicate that core@NaLuF₄ did not show any preferred growth direction and consequently, the shell material distributed homogenously around the core.

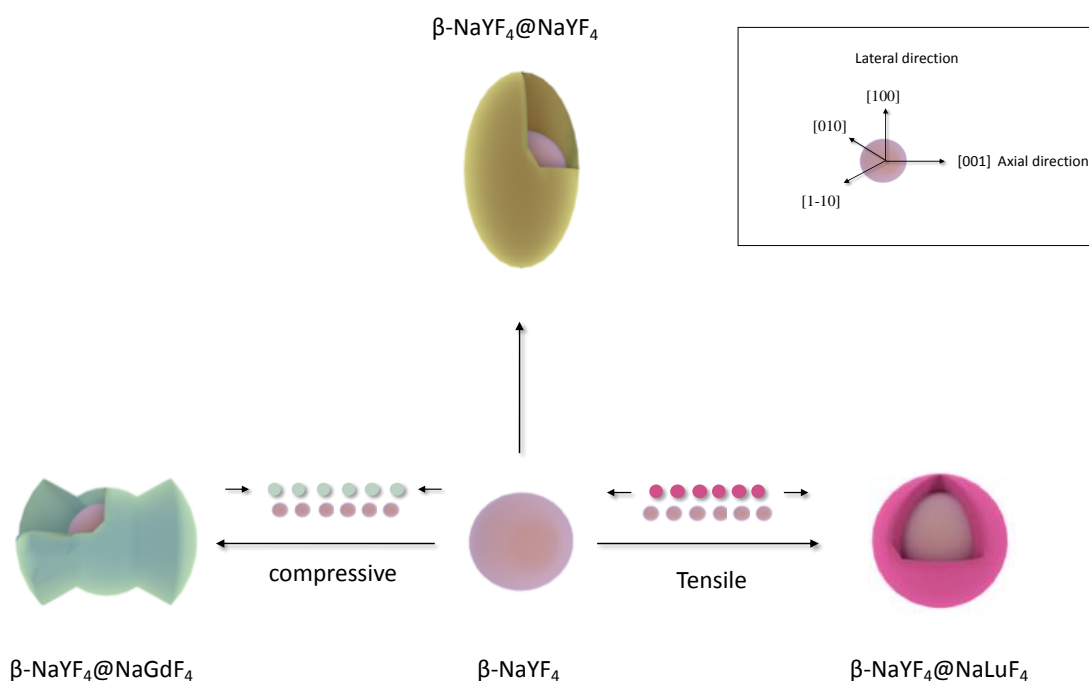


Figure 51. Schematic illustration of core@shells obtained through the same core. It reflects how the shape of β -UCNPs changes during compressive or tensile strains.

Shell growth with NaYbF₄ (which closely matched parameters to NaYF₄) was studied by Zhang et al.²⁸⁰ and our results match to their observations. They found that the epitaxial growth of the shell layer was faster in the lateral directions than in the [001] axial direction. Additionally, and in agreement to our results, they observed that in some cases, a complete shell enclosure could not even be formed.

Hui-Qin Wen and co-workers studied the growth mechanism of NaYF₄@NaGdF₄ and concluded that at first stage the core preferentially grows along the [001] direction and then

only afterwards, along the [010] or [100] direction resulting in nano-dumbbells-like nanostructures.²⁷⁸ The subtractive growth from the (100) side observed in our experiments is in agreement with other experimental observations.^{278,281}

Then, XRD patterns were collected to characterize the phase of the prepared samples and the results are shown in **Figure 52a**. It shows that all of the characteristic diffraction peaks match well with the standard hexagonal phase β -NaYF₄ (PDF card No: 00-016-0334). To study the different epitaxial growth, we zoomed into selected diffraction peaks. In epitaxial growth, as the shell lattice adapts to the core lattice, the XRD pattern of the resulting core@shell structure is expected to match with the core diffraction pattern.²⁷²

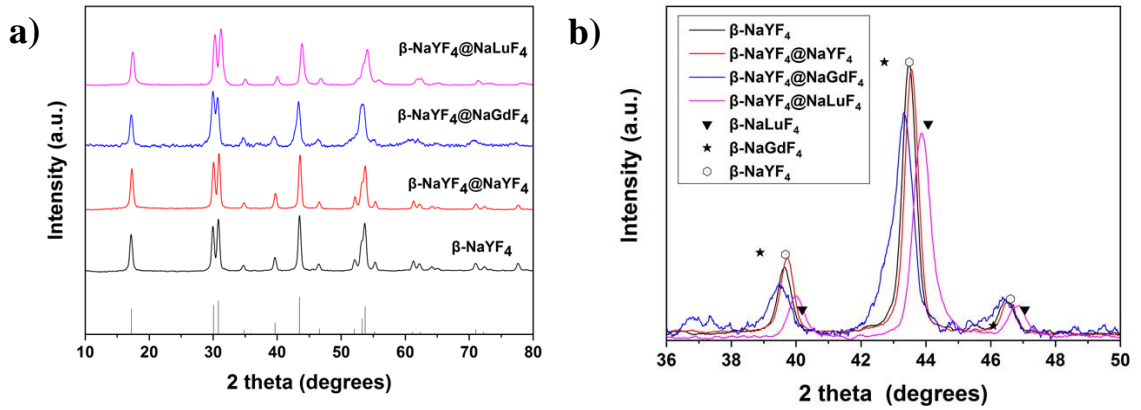


Figure 52. (a) XRD patterns of core (β -NaYF₄) and core@shell (β -NaYF₄@NaYF₄, β -NaYF₄@NaGdF₄, and β -NaYF₄@NaLuF₄). Measurements were acquired using a Cu K- α source. (b) Zoom into the (201) diffraction peak area. Black reference line in figure a corresponds to the β -NaYF₄ (PDF card No: 00-016-0334). Black triangle, black star and empty circle in figure b are the references of the β -NaLuF₄, (PDF card No: 00-027-0726), β -NaGdF₄ (PDF card No: 00-027-0699) and β -NaYF₄ (PDF card No: 00-016-0334), respectively.

According to the Bragg equation, $\lambda = 2d \sin \theta$, since the wavelength (λ) is fixed, a smaller scattering angle (θ) indicates larger distances between lattice planes (d). Indeed, Gd³⁺ ions, which have a larger ionic radius compared to Y³⁺ ions, will form unit cells with bigger d-spacing, and therefore Gd³⁺ ions will need to be compressed to fit around the β -NaYF₄ core. It can be seen that (111), (201) and (210) peaks from **Figure 52** were shifted to lower 2 theta angles. Contrary, β -NaLuF₄ which has a smaller lattice constant, experienced tension, which resulted in slightly shifted peaks to higher values. When β -NaYF₄ is used, the shell growth

followed the lattice of the core and therefore the resulted diffraction pattern was very similar to the ones of the core. Our results (TEM and XRD) are consistent to the ones reported by others groups.^{272,278,280,281}

3.3.2 Upconversion luminescence properties of UCNPs coated with an inorganic shell

We also compared the emission spectra of core vs shelled β -NaYF₄. The as-prepared core and core@shell β -UCNPs were suspended in hexane with the same concentration (5 mg/ml) and illuminated with a 980 nm CW at 300 mW. Results are displayed in **Figure 53**.

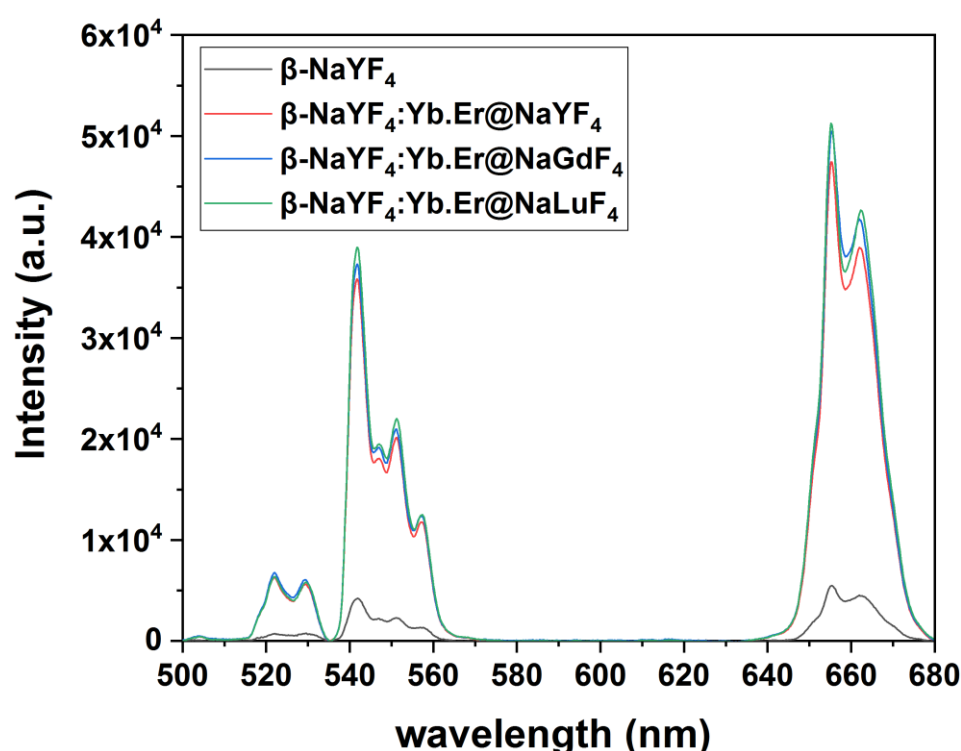


Figure 53. UC emission intensity of core (β -NaYF₄) and core@shell (β -NaYF₄@NaYF₄, β -NaYF₄@NaGdF₄, and β -NaYF₄@NaLuF₄) excited by a 980 nm CW laser. 300 mW and 500 ms integration time.

The core and core@shell emitted with peaks at 525 nm, 540 nm, and 650 nm, which can be assigned to $^2\text{H}_{11/2} \rightarrow ^4\text{I}_{15/2}$, $^4\text{S}_{3/2} \rightarrow ^4\text{I}_{15/2}$, and $^4\text{F}_{9/2} \rightarrow ^4\text{I}_{15/2}$ transitions of Er³⁺ ions.³⁴ From **Figure 53** it is clear that the core@shells are much brighter than the sole core. We found that the green emission intensity increased by a factor of ~8.5, ~8.9, and ~9.1 when using core@shell of β -NaYF₄, β -NaGdF₄, and β -NaLuF₄, respectively. The emission intensity

increased in the red area by a factor of ~8.8, ~9.4, and ~9.5, when using core@shell of β -NaYF₄, β -NaGdF₄, and β -NaLuF₄, respectively.

The relatively weak UC luminescence from the sole core was attributed to the surface quenching effect. We observed that the quenching from the core was reduced by the deposition of a shell, which helped to protect the Er³⁺ ions located in the surface of the core from non-radiative losses caused by surface defects and high-energy vibrational modes.

^{277,282}

From the spectra, we observed that particles coated with β -NaLuF₄ got the highest UC luminescence while particles coated with β -NaYF₄ got the lowest. This could be explained by their morphology. Particles treated with β -NaLuF₄ produced very isotropic and uniform shell structures while core@NaGdF₄ and core@NaYF₄ produced structures with higher anisotropy. Since β -NaYF₄ is unlikely to provide a complete shell closure, it is expected that the reduction in quenching effect was only realized partially.

Another important variable that affects the enhancement factor, but without direct impact on our work, is the shell thickness. Zhang et al.¹²³ investigated the effect of various NaGdF₄ coating in the 0-2.5 nm range and established a strong lineal dependence between the UC emission intensity and the shell thickness in NaYF₄@NaGdF₄ UCNPs.¹²³ It has been reported that a steady enhancement in UC emission is generally unexpected by using very thick shells and generally, the UC emission intensity reaches a plateau at a shell thickness of ~3 nm.²⁷⁷

Chapter 4 Results and discussion on inorganic functionalization of upconversion nanoparticles

4.1 Silica coating on upconversion nanoparticles

Silanization is a popular technique for surface modification of NPs since silica is highly biocompatible. To date, the Stöber synthesis and reverse microemulsion are the two most common procedures for silica coating regardless of the chemical composition of NPs to be coated as the procedure depends on the polarity of their capping ligands. The first one is commonly applied to hydrophilic NPs whereas the second one can also be applied to oil dispersed NPs.^{283–285}

One of the major drawbacks regarding silica coating is that the conditions must be thoroughly optimized to avoid the production of pure silica NPs and the formation of aggregates of particles coexisting under the same silica layer. Although reverse microemulsion has been employed by many groups for the silanization of UCNPs with adequate success, a well-defined universal protocol to produce a high yield of silica-coated UCNPs that takes into consideration the morphology of the particles has yet to be developed.

In this section, we introduce an approach that prevents the production of pure silica NPs and encapsulates single β -UCNPs within monodisperse silica spheres using a reverse microemulsion technique. More importantly, the procedure takes into account different sizes and morphologies of β -UCNPs, therefore it could be broadly applied to other hydrophobic materials synthesized in non-aqueous solvents. This topic is covered throughout **Section 4.1.1**. After that, we will discuss how the thickness of the silica shell can be adjusted by varying the content of ammonia and TEOS, according to a method introduced by Ding et al.²²⁰ See **Section 4.1.2**.

It is well known that aggregation of NPs arises due to poor dispersibility. In order to overcome this issue and obtain homogeneous β -UCNPs coatings, a wet-annealing treatment prior to the silica coating was followed.²¹⁹ The method is explained in **Section 4.1.3**.

For further use of β -UCNPs in biological environments they must be rendered water dispersible. The functionalization of β -UCNPs with amines for water dispersibility is discussed throughout **Section 4.1.4**. Then, we performed optical measurements to understand how the luminescence properties of the β -UCNPs were affected by the silica and

water dispersibility. The results are discussed in **Section 4.1.5**. We conclude the topic about silanization in **Section 4.1.6**, proposing a mechanism to explain the coating process of silica shell on the β -UCNPs.

4.1.1 Synthesis of silica coated upconversion nanoparticles

The formation of pure silica NPs besides the coating of the UCNPs is a side effect and very difficult to control. The focus of this work is the synthesis of silica coating UCNPs without the formation of free silica NPs. There exist two possible methods to achieve this. The first exploits the adjustment of the concentrations of both TEOS precursor and ammonia catalyst to suppress the development of the secondary nuclei. The second, instead is based on setting all the coating parameters and regulating the number of UCNPs according to the established conditions. We assume that the second option is more appropriate because it implies the variation of a single parameter; the following results have been obtained following this approach.

Synthesis of the β -NaYF₄: Yb³⁺(20%), Er³⁺(2%) UCNPs were prepared following the experimental procedure detailed in **Section 2.1.1**. A representative TEM image of the resulting β -UCNPs and the corresponding size histogram are illustrated in **Figure 54**, indicating a narrow size distribution of $23 \text{ nm} \pm 1 \text{ nm}$. The size distribution was analysed with ImageJ software considering over 200 NPs for the statistical analysis. The sample was named sample 9.

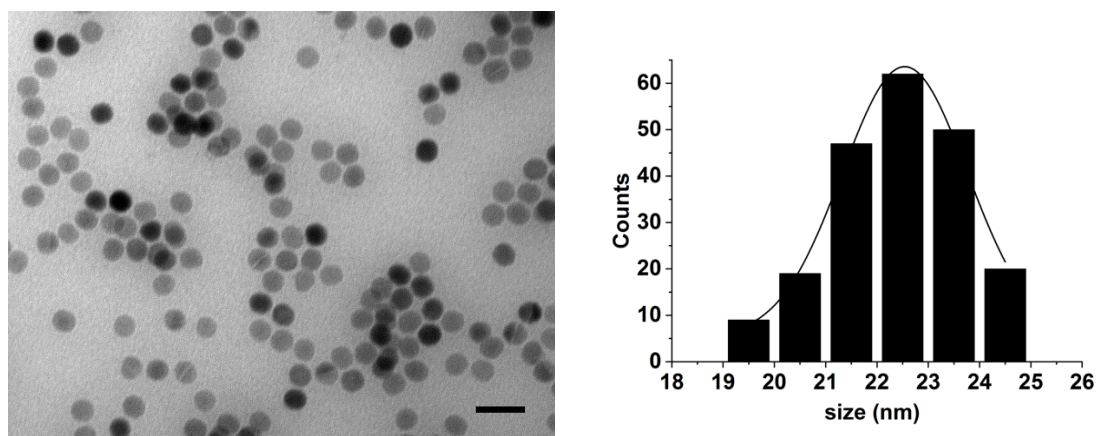


Figure 54. TEM image and size distribution of β -NaYF₄: Yb³⁺(20%), Er³⁺(2%) UCNPs. Scale bar is 50 nm.

The surface of this sample was coated with silica using a reverse microemulsion method with slight modifications, following the experimental procedure from **Section 2.3.1**. The amounts of Igepal CO-520, NH_4OH (35%), and TEOS were fixed to 0.5 g, 100 μl , and 75 μl , respectively and established according to the literature.²²⁰

In order to regulate the silica coating, it was essential to adjust the concentration of the UCNPs to the aforementioned conditions. Four samples of β -UCNPs coated with SiO_2 were prepared, where the concentration of the β -UCNPs was varied for each sample (2, 6, 10, and 13 mg/ml) whilst the other parameters were kept constant.

The samples were characterized by TEM and the corresponding micrographs are shown in **Figure 55**. With a low concentration of β -UCNPs (2 mg/ml), it was found that there was a large number of free silica NPs as shown in **Figure 55a**. As the concentration of β -UCNPs was progressively increased, the number of free silica NPs was reduced until it disappeared. (**Figure 55b, c and d**).

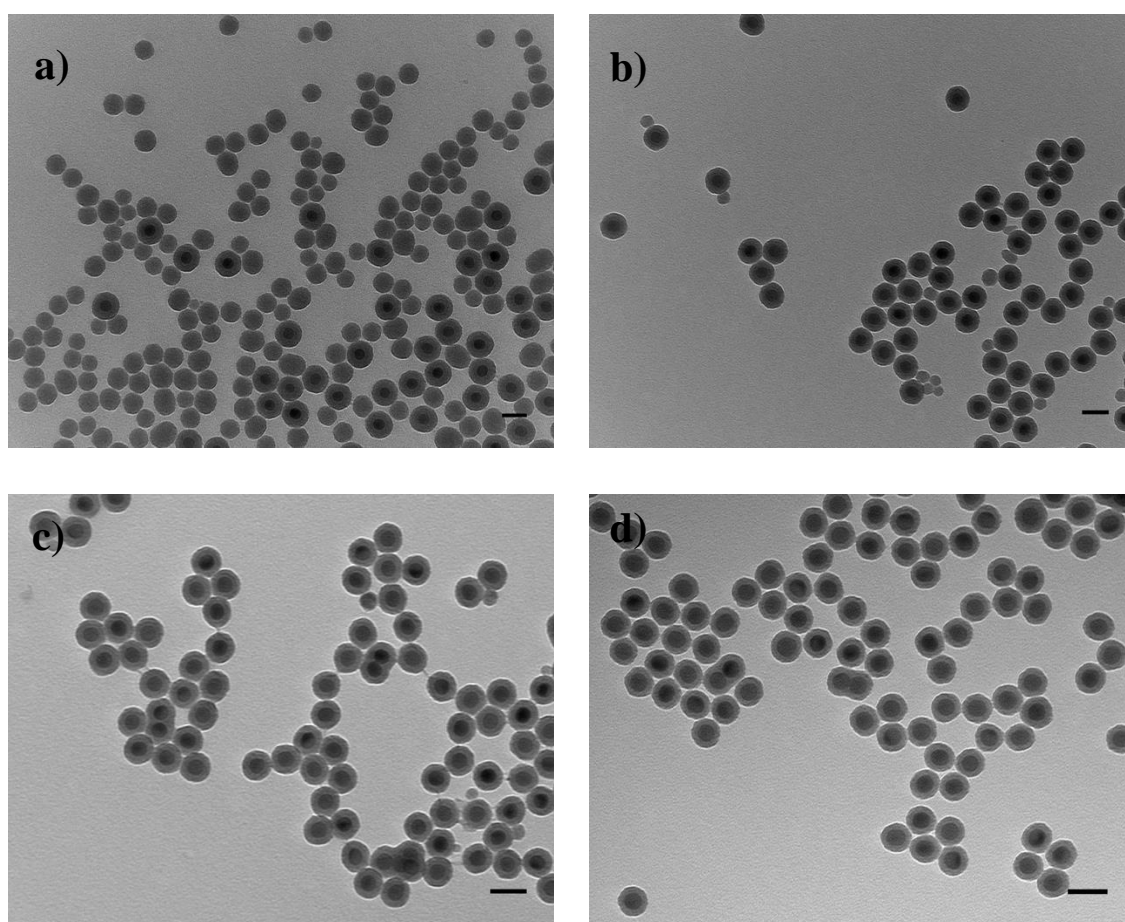


Figure 55. TEM image of silica coated β - NaYF_4 : Yb^{3+} (20%), Er^{3+} (2%) UCNPs (β -UCNPs@ SiO_2) using in the synthesis (a) 2 mg/ml, (b) 6 mg/ml, (c) 10 mg/ml and (d) 13 mg/ml of β -UCNPs. Scale bars are 50 nm.

The presence of the silica shell on the β -NaYF₄: Yb³⁺(20%), Er³⁺(2%) UCNPs was further confirmed by comparing the Fourier-transform infrared (FTIR) spectra of the β -UCNPs surfaces before and after silica coating. From the spectra shown in **Figure 56** it is visible that β -UCNPs prior to silica coating (see black line) presented two main vibrations at 2923 cm⁻¹ and 2858 cm⁻¹ which can be attributed respectively to the asymmetric and symmetric stretching modes of the methylene (-CH₂) groups in the long alkyl chain of the OA molecule. The low intense peak at 1710 cm⁻¹ was assigned to the stretch mode of the C=O. The bands at 1551 cm⁻¹ and 1463 cm⁻¹ were attributed to the asymmetric and symmetric stretching vibrations of the carboxylate group [(-COO-)₃Y³⁺] respectively.¹⁰⁰ This data confirms the presence of OA on the surface of the β -UCNPs before silanization. Following silica treatment, the aforementioned bands disappeared and a new set of bands at 1075 cm⁻¹, 950 cm⁻¹ and 795 cm⁻¹ appeared (see red line). The bands at 1075 cm⁻¹ and 795 cm⁻¹ were associated to asymmetric and symmetric stretching vibrations of (Si-O-Si) whereas the band at 950 cm⁻¹ was linked to the asymmetric bending and stretching vibration of (Si-OH).^{76,286}

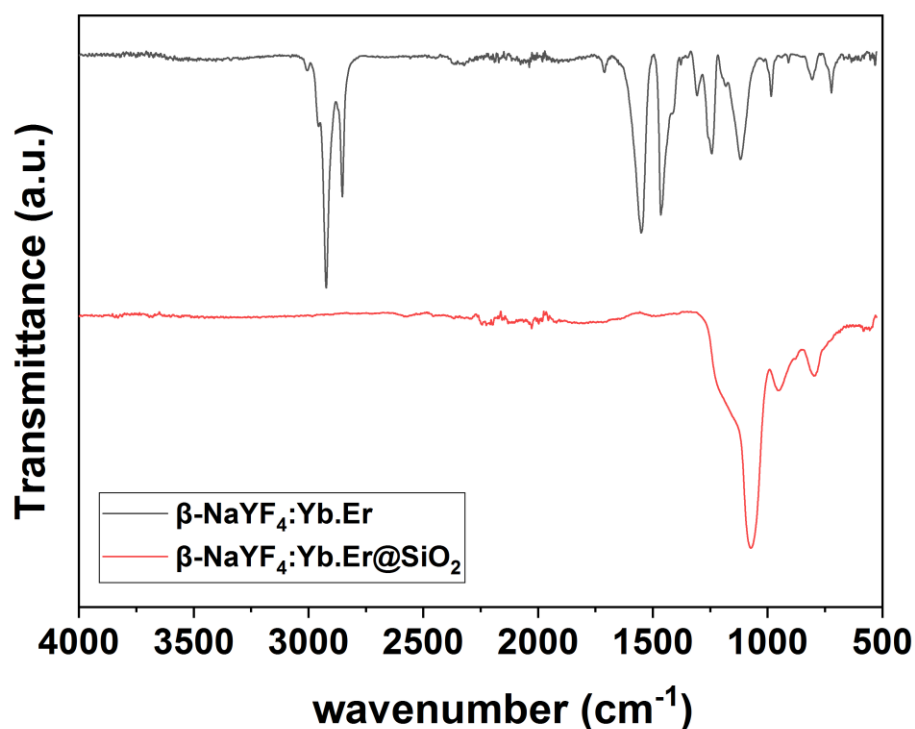


Figure 56. FTIR spectra of β -NaYF₄: Yb³⁺(20%), Er³⁺(2%) UCNPs (black line) and β -NaYF₄: Yb³⁺(20%), Er³⁺(2%) UCNPs coated by SiO₂ (red line).

4.1.1.1 Silica coating regulations

As we will discuss in **Section 4.1.6**, in a reverse microemulsion system, the ratio between Igepal and ammonia is crucial and determine the number and size of aqueous micelles due to the nature of the reaction mechanism.²²⁰ If the number of UCNPs equals to the number of the aforementioned micelles, a one to one correspondence between the number of UCNPs and micelles would ensure that no free silica NPs would appear.

It has been reported that the coating parameters suitable for a certain mass concentration of NPs are not transferable to other sizes.²²⁰ If the size of the UCNPs is varied, also their number should be adjusted, to ensure the one-to-one correspondence between silica and UCNPs.

In this section, we discuss our efforts into constructing a general calibration curve, which estimates the appropriate mass concentration of UCNPs needed for successful silica coating whilst avoiding the formation of free silica NPs. Samples (1-4) discussed in **Section 3.1.1** with varying sizes and shapes of NPs were taken as the standard samples of known concentration to construct the calibration curve.

The size of the UCNPs is clearly an important parameter to establish the appropriate reaction conditions. However, we considered that a general approach should take into account not only the size, but also the shape of the UCNPs (hexagonal, rod-like, etc). For this reason, we assume that the total surface area (SA_T) is the most relevant parameter which determines the appropriate concentration of UCNPs.

The SA_T of spherical 23 nm β -UCNPs (sample 9), was calculated according to the following equation.

$$(SA)_{sphere} = 4\pi r^2 \quad (6)$$

where r is the radius of the particles. From our observation, spherical 22 nm UCNPs (corresponding to a $SA_T = 1596 \text{ nm}^2$) required to be at a concentration of 13 mg/ml in order to prevent the production of free core silica, while keeping the rest of precursors fixed. Using this result as a reference and assuming a linear relationship, the concentration for the new set of UCNPs can be estimated from their SA_T .

Four samples of β -UCNPs coated with SiO_2 were prepared following the experimental procedure detailed in **Section 2.3.1** and using samples (1-4) as the cores. The concentrations of these β -UCNPs were estimated in linear proportion to the SA_T of the spherical 22 nm

UCNPs and the rest of coating parameters were kept the same for each of the synthesis. SA_T for samples (1-4) were calculated according to the general formula for right prisms:

$$(SA)_{prism} = 2A + M \quad (7)$$

$$A = 1.5\sqrt{3} l^2 \quad (8)$$

$$M = hl6 \quad (9)$$

where A and M indicate the surface area of the base and lateral prim and l and h are the prism side length and its height, respectively. The estimated concentrations for samples (1-4) to satisfy the one-to-one relationship, are summarized in the following **Table 13** along with their SA_T .

Table 13. SA_T and concentrations of β -NaYF₄: Yb³⁺(20%), Er³⁺(2%) UCNPs in samples (1-4).

Sample used as core	Total Surface Area SA_T (nm ²)	β -UCNPs (mg/ml)
Sample 1	5240	4.3
Sample 2	6281	5.1
Sample 3	3185	2.6
Sample 4	2101	1.7

The particle sizes and morphologies were first characterized by TEM. From **Figure 57**, it can be observed that β -UCNPs@SiO₂ were monodisperse in size and no free silica was obtained. The silica shell appeared very uniform in thickness and regular in surface. The diameter was measured to be: 61 nm \pm 2 nm, 60 nm \pm 3 nm, 49 nm \pm 2 nm and 52 nm \pm 2 nm for samples (1-4).

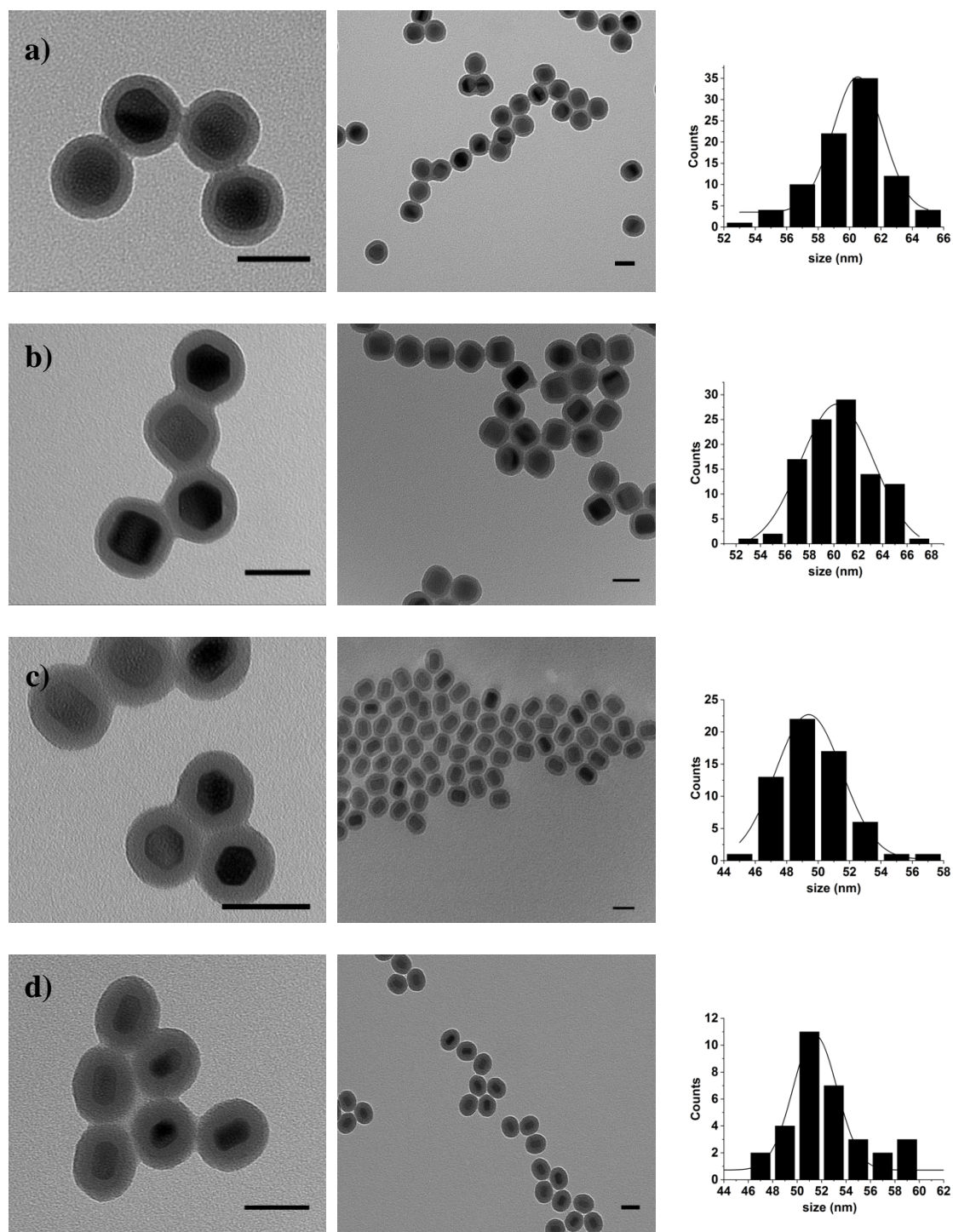


Figure 57. TEM images and size distribution of β -UCNPs@SiO₂ using as a core β -NaYF₄: Yb³⁺(20%), Er³⁺(2%) UCNPs from (a) sample 1, (b) sample 2, (c) sample 3 and (d) sample 4. Scale bars are 50 nm and black bars at the histograms indicate the diameter of the β -UCNPs@SiO₂ structures.

We plotted the calculated SA_T versus the concentration of samples (1-4). **Figure 58** shows the concentration on the X axis and the SA_T on the Y axis. Data were fitted with a straight-line using Origin and error bars for SA_T and concentrations were calculated using eq. (38) and eq.(44) from **Appendix F**.

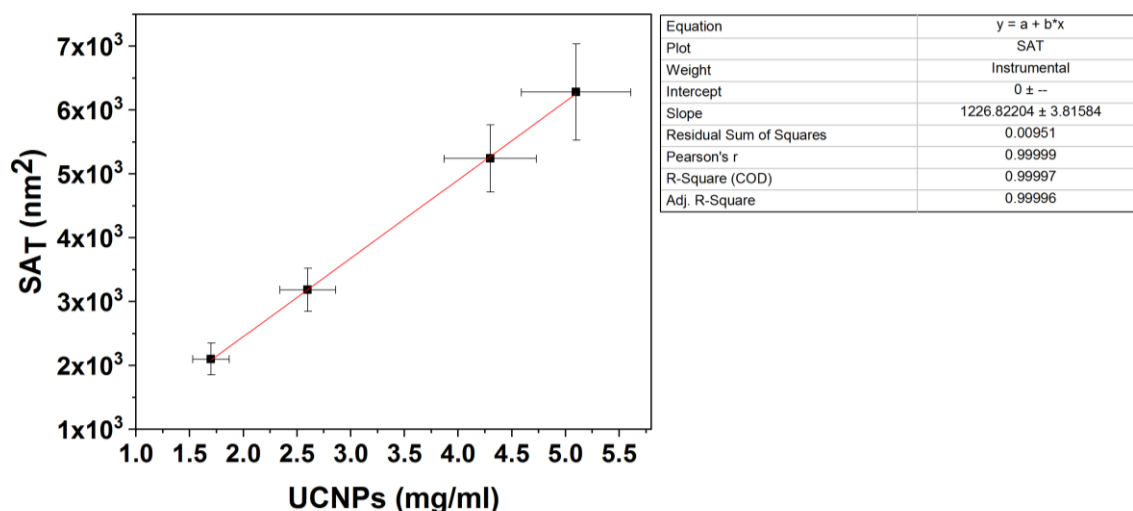


Figure 58. General calibration curve to estimate the amount of UCNPs core material to be used for silanization regardless of the morphology of the initial particles and only in accordance to its SA_T .

Under the working coating parameters, we hypothesize that the regression line from **Figure 58** (with R^2 value= 0.999) could be broadly used to estimate the content of UCNPs required to achieve a one-to-one silica coating without the production of free silica. More importantly, this calibration curve takes into consideration any kind of UCNP indistinctly of their size and shape and just based on their SA_T .

In order to test the calibration curve, two additional samples of β -NaYF₄: Yb³⁺(20%), Er³⁺(2%) UCNPs were prepared (named as sample 10 and sample 11). Sample 10 was prepared following the standard protocol detailed in **Section 2.1.1** and sample 11 was doped with 20% lutetium according to the procedure of **Section 2.1.4** to obtain larger particles. It has been demonstrated that the electron charge density of the surface of the UCNPs decreases when Y³⁺ is replaced by a smaller radius ion such as Lu³⁺. This effect would result in a greater attraction toward the negatively charged F⁻ ions, allowing the growth process to form larger sized UCNPs.^{101,214}

The UCNPs were characterized by TEM before silanization and showed a size distribution of $31 \text{ nm} \pm 2 \text{ nm}$ and $83 \text{ nm} \pm 4 \text{ nm}$ for sample 10 and sample 11, respectively. The size distribution was analysed considering over 100 NPs for both of the samples.

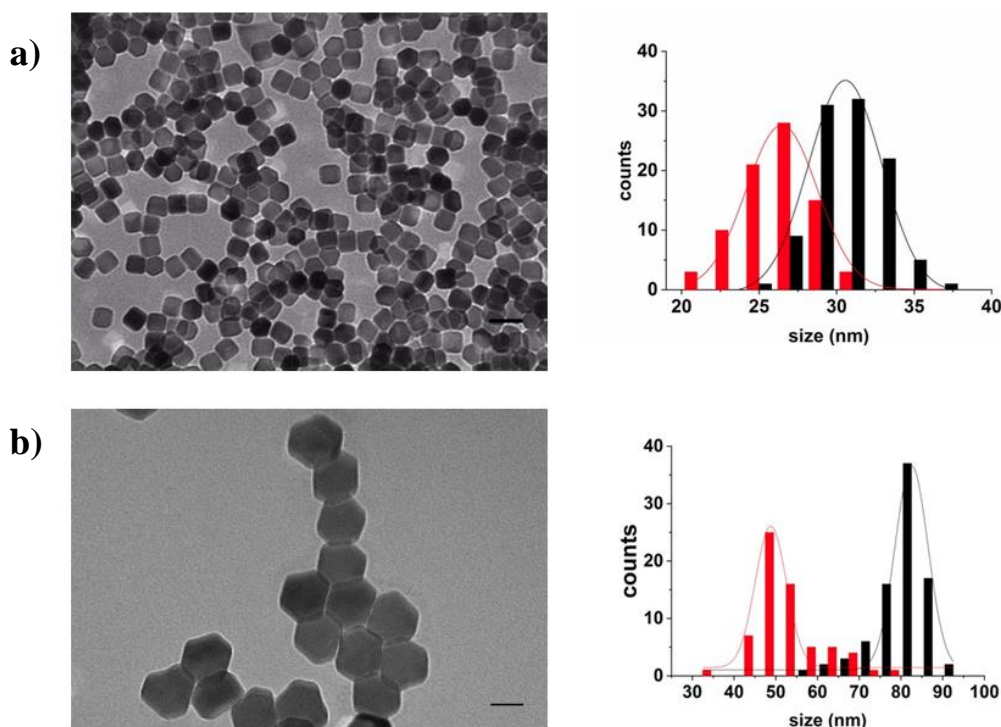


Figure 59. TEM images and size distribution of (a) $\beta\text{-NaYF}_4$: Yb^{3+} (20%), Er^{3+} (2%) UCNPs and (b) $\beta\text{-NaY(28%)/Lu(50%)F}_4$: Yb^{3+} (20%), Er^{3+} (2%) UCNPs. Scale bars are 50 nm. Black bars at the histograms indicate the diameter and the red colour corresponds to the length of β -UCNPs.

The silica coating was performed following the experimental protocol described in **Section 2.3.1** and the concentration of the β -UCNPs was estimated directly from their $(\text{SA})_{\text{T}}$ according to the calibration curve from **Figure 58**.

The resulted β -UCNPs coated by silica are illustrated in **Figure 60** and showed a size distribution of $52 \text{ nm} \pm 3 \text{ nm}$ and $93 \text{ nm} \pm 4 \text{ nm}$ for sample 10 and 11, respectively. As expected, silica coated β -UCNPs were obtained without the formation of free silica NPs.

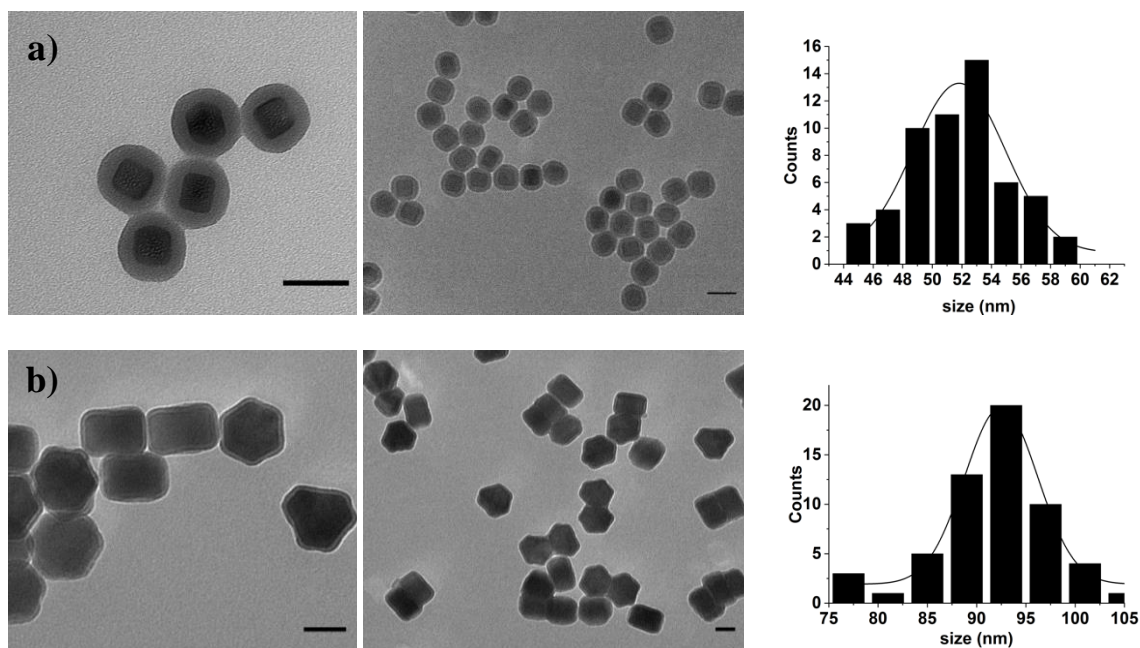


Figure 60. TEM images and size distribution of β -UCNPs coated with silica using as a core β -NaYF₄: Yb³⁺(20%), Er³⁺(2%) UCNPs from (a) sample 10 and (b) sample 11. Scale bars are 50 nm and black bars at the histogram indicate the diameter of the resulting β -UCNPs@SiO₂ structures.

We noticed that although the TEOS amount was kept the same for all samples, the thickness of the silica shells increased noticeably due to the decreasing surface area of the β -UCNPs. The thickness of the silica shell was estimated from the difference between the mean diameters of β -UCNPs coated with silica and β -UCNPs cores.

Table 14 summarizes the silica thickness obtained for the different samples along with the concentrations and calculated SA_T (listed in ascending order of silica thickness).

Table 14. Comparison for the silica thickness with the decreasing SA_T of UCNPs.

SA _T (nm ²)	β -UCNPs (mg/ml)	Silica thickness (nm)
20850	17.0	~5
6281	5.1	~11
5240	4.3	~11
3645	3.0	~11
3185	2.6	~14
2101	1.7	~17

4.1.2 Control of the silica thickness on upconversion nanoparticles.

Herein, the roles and effects of TEOS and NH_4OH are analysed. It is rational that the thickness of the silica shell increases as the amount of TEOS increases, but free silica spheres inevitably appear when the TEOS content is increased to a certain extent.^{287–289}

In this section we followed a strategy originally reported by Din and co-workers²²⁰ to tune the thickness of the shell. This strategy relies on increasing the shell thickness by increasing the content of TEOS in fractionated drops, which means that fresh TEOS is added after the previous TEOS is consumed in order to avoid the production of free silica. Concerning the production of a thin layer, it is required that the micelles around the β -UCNPs are sufficiently small. By reducing the NH_4OH content with a consistent decrease in the TEOS content, ultrathin silica shells can be obtained without the presence of free silica.²²⁰

A fresh batch of $\beta\text{-NaYF}_4\text{: Yb}^{3+}(20\%), \text{Er}^{3+}(2\%)$ UCNPs was prepared following the experimental procedure detailed in **Section 2.1.1**. The resulting β -UCNPs size was characterised by TEM, which indicated a narrow distribution in size of $34 \text{ nm} \pm 2 \text{ nm}$ (see **Figure 61**). The size distribution was analysed considering over 100 NPs. This sample was named sample 12.

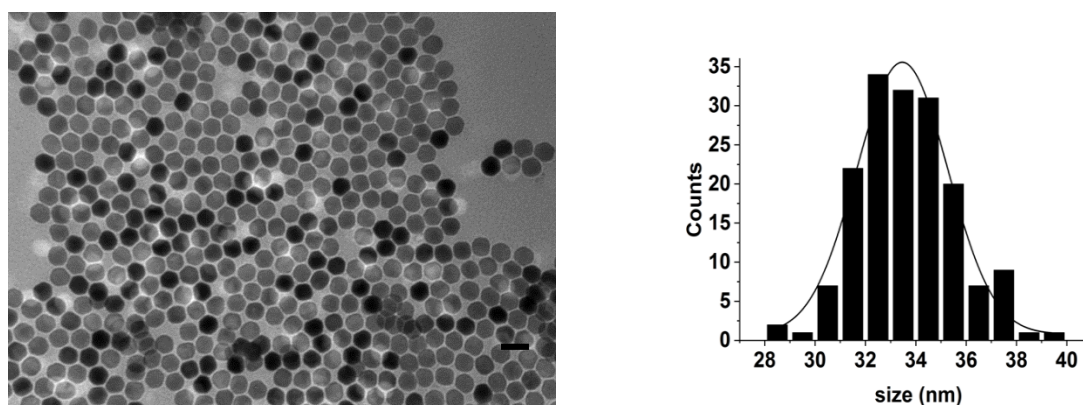


Figure 61. TEM image of the initial $\beta\text{-NaYF}_4\text{: Yb}^{3+}(20\%), \text{Er}^{3+}(2\%)$ UCNPs with a size distribution of $33 \text{ nm} \pm 2 \text{ nm}$.

Chapter 4

Sample 12 was used to create three different silica coated batches of β -UCNPs following the protocol described in **Section 2.3.3**. The resulting samples were named conveniently sample 12.1s, sample 12.2s and sample 12.3s.

Sample 12.1s was prepared employing the same coating parameters from the previous section and adjusting the β -UCNPs to these quantities. Sample 12.2s and sample 12.3s were synthesised with the same experimental procedure but modifying the TEOS and NH_4OH content according to the work of Din and co-workers. The experimental parameters applied for the silica coating are summarized in **Table 15**.

Table 15. Parameters for adjusting the thickness shell of the silica, using in all cases sample 12 as the core.

Name	β -UCNPs (mg/ml)	Solvent	Total volume	IGEPAL	NH_4OH	TEOS
Sample 12.1s	4.2	Hexane	10 ml	500 mg	100 μl	75 μl
Sample 12.2s	4.2	Hexane	10 ml	500 mg	50 μl	25 μl
Sample 12.3s	4.2	Hexane	10 ml	500 mg	100 μl	150 μl +150 μl

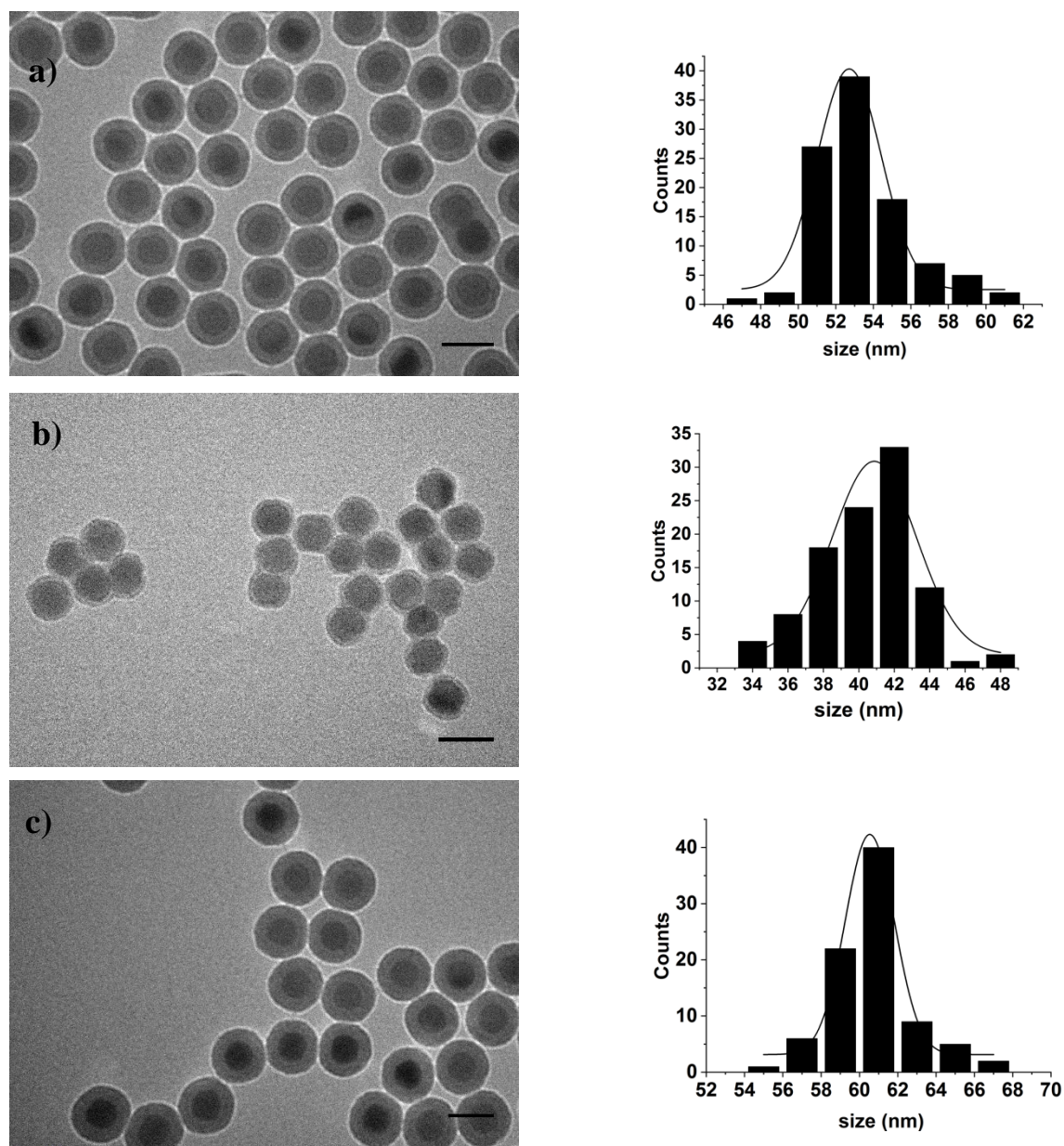


Figure 62. TEM image and size distribution of the β -NaYF₄: Yb³⁺(20%), Er³⁺(2%) UCNP@SiO₂ for (a) sample 12.1s, (b) sample 12.2s and (c) sample 12.3s according to the experimental parameters from **Table 15**. Scale bars are 50 nm.

TEM images from **Figure 62** (a-c) illustrate how the silica shell thickness can be easily modified when the TEOS and NH₄OH amount is varied. The resulting β -UCNPs coated by silica were measured to be respectively, $53 \text{ nm} \pm 2 \text{ nm}$, $42 \text{ nm} \pm 2 \text{ nm}$ and $61 \text{ nm} \pm 1 \text{ nm}$.

By increasing the ammonia content, the concentration of hydroxyl anions (OH^-) that catalyses both hydrolysis and condensation reaction increases, resulting in an increase in the hydrolysis rate of TEOS. On the contrary, low ammonia reduces the hydrolysis rate of TEOS accordingly.^{284,290–292} In sample 12.2s, the low ammonia content created a small aqueous micelle around the β -UCNPs producing a thin SiO_2 shell, due to the restriction of silica growth. The content of TEOS was reduced simultaneously in order to have a suitable match between these two components and to avoid the formation of free silica NPs. By decreasing the amount of ammonia under the condition that the corresponding TEOS content was decreased simultaneously the shell thickness decreased from ~ 10 nm to ~ 4 nm **Figure 62 (a, b)**.

In sample 12.3s, increasing only the amount of TEOS as fractionated drops while maintaining the same ammonia content, produced an increase in the shell thickness from ~ 10 nm to ~ 14 nm **Figure 62 (a, c)**, while preventing the formation of free silica NPs. It is speculated that the silica shell can be further increased by continuing increasing the TEOS content with more fractionated drops.²²⁰ Although we did not try in our experiments, we would like to emphasize that a thicker silica coating could be also achieved by increasing the ammonia content accompanied by an appropriate decrease in the TEOS content.²²⁰

Possible future efforts could be directed to achieve a finer control on the thickness of the silica shells. Nonetheless, these results further complement our optimal silica coating regulation already obtained in **Section 4.1.1.1** achieving a better control on the silica thickness.

4.1.3 Prevention of nanoparticle aggregation during silanization

Formation of aggregates of NPs coexisting under the same silica layer is one of the major drawbacks that arise during the silanization. For practical applications, it is imperative that every NP is coated homogeneously and individually. We observed that in our experiments β -UCNPs easily agglomerated and bundled together producing occasionally an inhomogeneous silanization. We believe that this effect could be related to their large size but also to a loss of OA caused in the stage of purification. It has been reported indeed, that the OA can be easily removed by treating the UCNPs by excess of ethanol under sonication.⁷⁵

Wenjuan Bian and co-workers reported a synthesis to improve the crystallinity of the α -UCNPs, reconstructing the crystal edges by a wet chemical annealing in the presence of OA. In addition, their experiments demonstrated for the first time that recovery from surface defects could also enhance the PL properties of the α -UCNPs by an order of magnitude.²¹⁹ We speculated that this treatment could also help to improve the silica coating of the β -UCNPs.

Sample 10 was taken as an example to illustrate this effect. The β -UCNPs were annealed before silica coating, following the experimental protocol described in **Section 2.3.1**. For optical testing, the resulting annealed β -UCNPs were compared with the non-annealed β -UCNPs at the same concentration and same conditions.



Figure 63. From left to right. Digital images of β -NaYF₄:Yb³⁺(20%), Er³⁺(2%) UCNPs dispersed in hexane under ambient light and under a 980 nm laser pointer before and after annealing at 240 °C for 1.5 hour.

We observed that the post-treatment helped to increase the colloidal stability of the β -UCNPs in organic solvents. From **Figure 63** it can be seen that prior to annealing, a turbid solution of β -UCNPs was obtained, probably due to a poor dispersibility. The annealing treatment resulted in a change in the transparency of the solution from turbid to clear indicating the formation of colloidal stable β -UCNPs.

In order to illustrate the surface quenching effect, we measured the UC emission spectra on each sample. Annealed and non-annealed β -UCNPs were suspended in hexane with the same concentration (5 mg/ml) and illuminated with a 980 nm CW at 365 mW. Results are shown in **Figure 64a**.

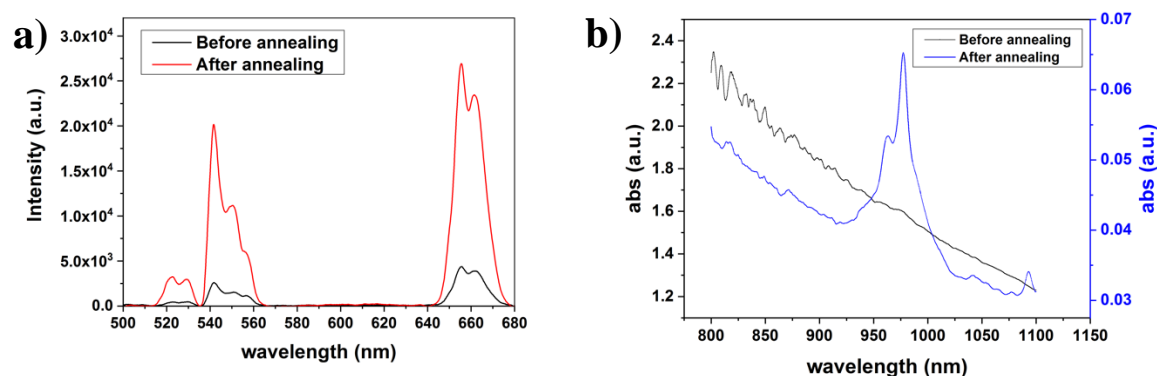


Figure 64. (a) Emission intensities of β -NaYF₄: Yb³⁺(20%), Er³⁺(2%) UCNP before (black line) and after the annealing (red line) measured by a 980 nm CW laser (365 mW, 500 ms), and (b) UV spectra of the β -NaYF₄: Yb³⁺(20%), Er³⁺(2%) UCNP before (black line) and after annealing (blue line).

Green emissions centred at 525 nm and 550 nm and red emission centred at 660 nm were observed, which were assigned to $^2H_{11/2} \rightarrow ^4I_{15/2}$, $^4S_{3/2} \rightarrow ^4I_{15/2}$ and $^4F_{9/2} \rightarrow ^4I_{15/2}$ transitions of Er³⁺ ions, respectively.³⁴ It can be seen from the emission spectra that annealed β -UCNPs (red line) showed a higher UC emission intensity. In our work, the emission intensity of the green and red peaks increased by ~6.5 times and ~5.6 times, respectively. We attribute the change in the intensity of UC emissions to the restore process of the surface of β -UCNPs from surface defects (i.e., disorder, vacancy, and interstitial defects).²¹⁹

Then, NIR absorption spectroscopy was used to measure the absorbance for the annealed and non-annealed β -UCNPs and the results are showed in **Figure 64b**. The NIR absorption spectra was recorded on a Jasco FT-IR 620 spectrometer with a 0.2 nm resolution from 800 to 1100 nm. NIR spectroscopy revealed that the scattering produced by the turbid non-annealed solution masked the absorption intensity of the β -UCNPs. On the contrary in the annealed β -UCNPs a well resolved absorption peak was visible. The broad absorption band observed in the region of 900-1050 nm with a sharp peak at ~975 nm can be ascribed to the characteristic $^2F_{7/2} \rightarrow ^2F_{5/2}$ transition of Yb³⁺.²⁹³

We envisioned that this strategy might also improve the homogeneity in the silica coating of UCNP. Hence, annealed and non-annealed samples were further used for the process of silanization (concentration was calculated based on the calibration curve from **Figure 58**) and their representative TEM images are shown in **Figure 65**.

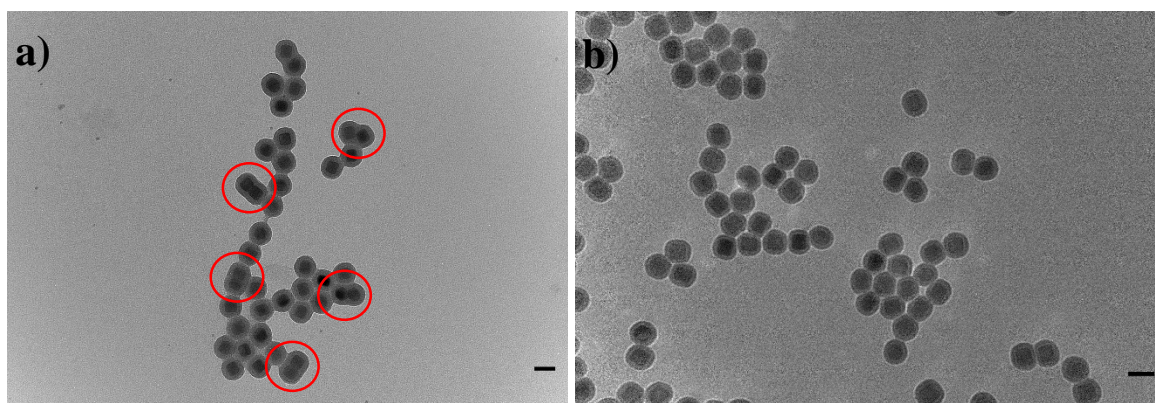


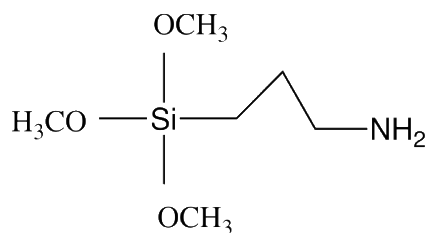
Figure 65. TEM images of β -UCNPs@SiO₂ (a) before and (b) after annealing at 240 °C for 1.5 hour. Scales bars are 50 nm.

Red circles from **Figure 65a** show some examples of some β -UCNPs coexisting under the same silica layer. In general, we observed that the number of β -UCNPs coated by the same silica shell decreased considerably after the annealing treatment. Extra images of the silica coating can be seen in **Appendix I**. We believe that the dispersibility of the initial core β -UCNPs was improved using the pre-annealing treatment and consequently a more homogenous silanization of β -UCNPs was obtained through them.

Overall, our optimal silica coating regulation obtained from the previous **Section 4.1.1.1** has been improved, applying a wet chemical annealing of the original core β -UCNPs. The challenging to directly make uniform and individual silica coating of the β -UCNPs has been preliminary achieved. Our results further complement the exploration of the silica coating on UCNPs.

4.1.4 Surface functionalization of Silica coating UCNPs

The surfaces of the as-prepared β -UCNPs@SiO₂ (sample 12.1s) were modified to various degrees of hydrophobicity adding 3-aminopropyltrimethoxysilane (APTMS) (see **Scheme 1**). The APTMS functionalization can be found in detail in **Section 2.3.3**. The functional groups at the surface of the silica are predominantly silanol (Si-OH) or ethoxy groups (-OR) and when those groups are treated with APTMS, surfaces terminated with amine are produced. After surface modification, amine-functionalized β -UCNPs@SiO₂-NH₂ were dispersible in water with good chemical stability, which was indicative from the clear colloidal solution that was formed. The resulting sample was named sample 12.1sAm.



Scheme 1. Chemical structure of APTMS.

A Malvern Instruments Nano-Zetasizer was used to determine the z-potential for the sample 12.1sAm. The Z-potential of the β -UCNPs@SiO₂ turned from -42.4 ± 6.70 mV to $+14.6 \pm 6.23$ mV, characteristic of the presence of NH₂ groups on the surface of the silica.

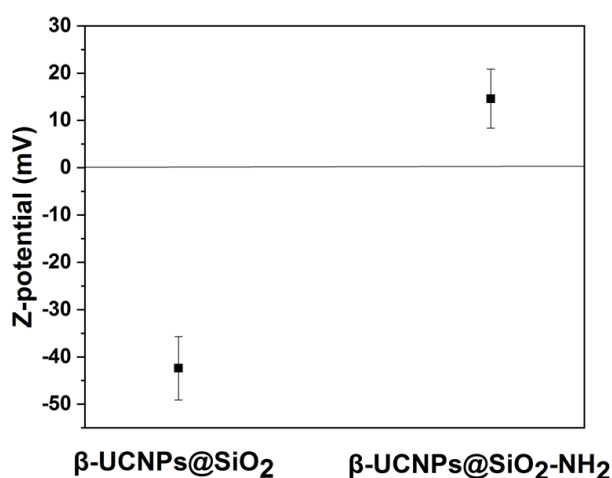


Figure 66. Z-potential measurements of the β -UCNPs@SiO₂ (sample 12.1s) and β -UCNPs@SiO₂-NH₂ (sample 12.1sAm) in Milli-Q water.

4.1.5 Quenching of the upconversion luminescence by water

In this section, we compared the spectra of water-dispersible amine-functionalized β -UCNPs@SiO₂-NH₂ to those of the initially prepared particles with OA coating dispersed in hexane.

In ambient conditions, under the excitation of a 980 nm laser, the UC luminescence of both OA coated β -UCNPs (Sample 12) and β -UCNPs@SiO₂-NH₂ (Sample 12.1sAm) was investigated. The set-up used is schematically illustrated in **Figure 16**. The samples were prepared under identical conditions, with a final concentration of 8 mg/ml. OA coated β -UCNPs were dispersed in hexane and β -UCNPs@SiO₂-NH₂ in Milli-Q water.

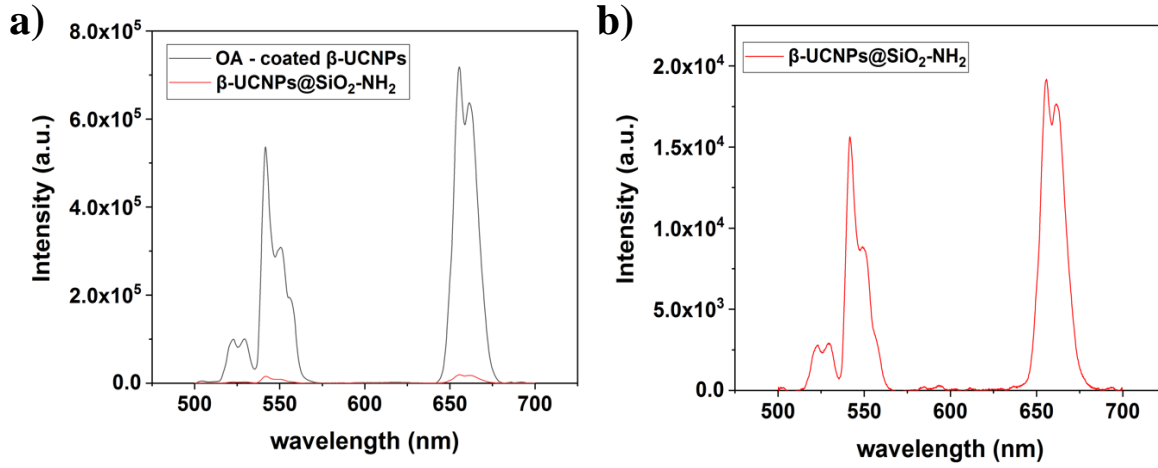


Figure 67. (a) Comparison between emission intensities for β -UCNPs@SiO₂-NH₂ dispersed in Milli-Q water and OA-coated β -UCNPs in hexane. (b) Zoom to the emission intensity of β -UCNPs@SiO₂-NH₂ dispersed in Milli-Q water. All measurements were taken after laser irradiation at 980 nm CW laser and 465 mW.

Results are shown in **Figure 67a** and **b**. Green emissions centred at 525 nm and 550 nm and red emission centred at 660 nm were observed, which were assigned to $^2H_{11/2} \rightarrow ^4I_{15/2}$, $^4S_{3/2} \rightarrow ^4I_{15/2}$ and $^4F_{9/2} \rightarrow ^4I_{15/2}$ transitions of Er³⁺ ions, respectively.³⁴ We observed that the green and red emission for the β -UCNPs@SiO₂-NH₂ dispersed in Milli-Q were ~97% quenched. The water quenching effect (η) was calculated using the equation from below.^{294,295}

$$\eta = 1 - \frac{I_Q}{I} \quad (10)$$

where I_Q is the UC luminescence intensity of the β -UCNPs@SiO₂-NH₂ dispersed in the water, and I is the UC luminescence intensity of the OA-coated β -UCNPs in hexane. The results clearly demonstrated a strong influence of the surrounding water/silica molecules on the intensity of the UC luminescence.

The quenching effect caused by water in NaYF₄: Yb³⁺, Er³⁺ UCNPs has been studied extensively in the literature.^{296–299} The main cause is associated to the non-radiative relaxation processes caused by high frequency vibrational groups such as (-OH, -CH₂, -CH₃). It has been reported that OH- groups quench the luminescence of NaYF₄: Yb³⁺, Er³⁺ UCNPs by relaxation of $^2H_{11/2}/^4S_{3/2} \rightarrow ^4F_{9/2}$ and $^4I_{11/2} \rightarrow ^4I_{13/2}$ transition of Er³⁺ ions. Both of these relaxation pathways favour the population of the $^4F_{9/2}$ state and therefore the red-to-green luminescence ratio RGR increases in the presence of water.^{44,71} (see **Figure 68** for a better understanding). In our case we measured an increase of the RGR only from 1.4 to 1.5.

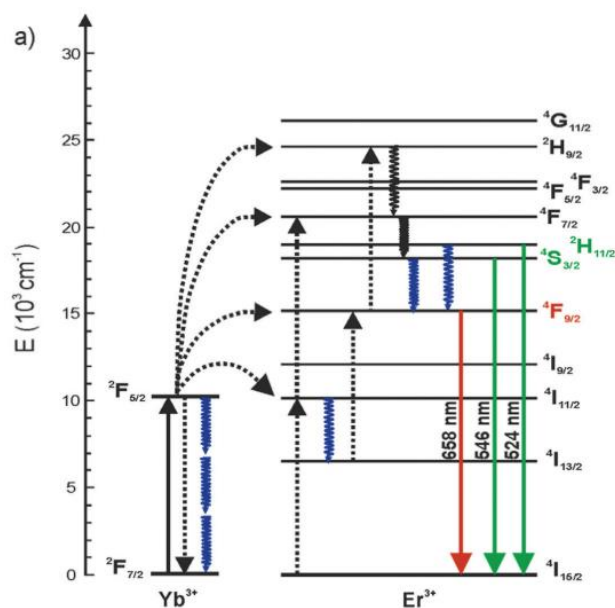


Figure 68. Energy level diagrams of NaYF₄:Yb³⁺, Er³⁺UCNPs. Solid, dotted and wavy arrows indicate photon absorption or emission, energy transfer and relaxation processes, respectively. The blue wavy arrows represent the increased multiphonon relaxations caused by OH⁻ vibrations. Picture adapted from Arppe et al.²⁹⁷

The non-radiative relaxation of Er³⁺ ions caused by high energy vibrational modes of OH⁻ groups is, however, only partly responsible for the strong quenching observed in the UC luminescence. Arppe and co-workers have studied the influence of the surrounding water molecules on the intensity and decay behaviours of the UCNPs and identified the sensitizer Yb³⁺ as the main source of non-radiative relaxation.²⁹⁷

The effect of the OH-vibrations was also studied by measurement of UC luminescence for β -UCNPs without any ligand capping and without silica. Herein, we compared the same core particles dispersed in water and in hexane without the existence of silica. Sample 12 was washed by acid following the detailed protocol in **Section 2.3.7** to produce water-dispersible ligand-free β -UCNPs and the resulting sample was named sample12_LF.

OA-coated β -UCNPs (sample 12) and ligand-free β -UCNPs (sample12_LF) were prepared in identical conditions, with a final concentration of 5 mg/ml of UCNPs. OA coated β -UCNPs were dispersed in hexane and ligand-free β -UCNPs in Milli-Q water. The emission spectra were obtained upon excitation with a 980 nm CW laser and are shown in **Figure 69a**.

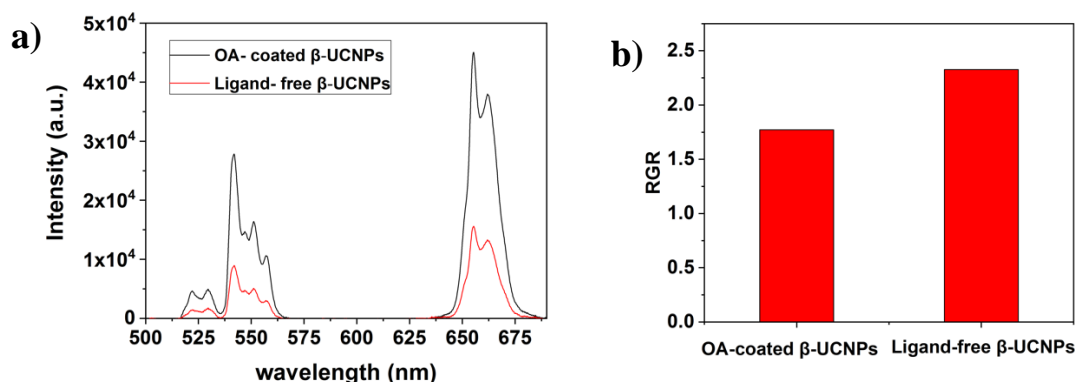


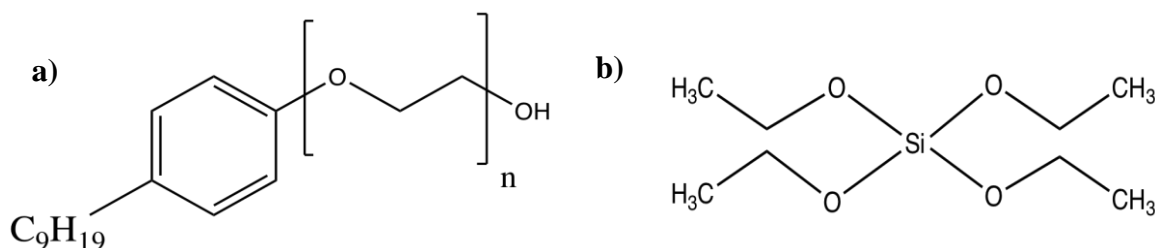
Figure 69. (a) Emission intensities and (b) RGR of OA free β -NaYF₄: Yb³⁺(20%), Er³⁺(2%) UCNPs dispersed in Milli-Q water and OA-coated β -NaYF₄: Yb³⁺(20%), Er³⁺(2%) UCNPs in hexane under a 980 nm CW laser at 480 mW.

The green and red emission intensities were quenched by ~75% and ~68% for the ligand-free UCNPs dispersed in Milli-Q water compared to the original hydrophobic β -UCNPs and accompanied by an increase in the RGR from 1.8 to 2.3 (**Figure 69b**). In general, our results are in agreement with other reports.³⁰⁰

As mentioned previously, this can be attributed to the non-radiative decay of the excited states of the dopant Ln⁺³ ions caused by water molecules. Indeed, in the presence of hydrophobic UCNPs, the OA ligands cover a high percentage of the UCNP surface and hinder partly the direct access of water molecules to the particle surface.

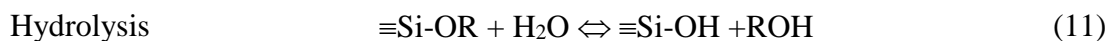
4.1.6 Mechanism of silanization on UCNPs

We carried out a reverse microemulsion strategy which enabled the encapsulation of individual β -UCNPs into SiO₂ spheres. In a typical reverse microemulsion strategy, a hydrophilic cavity (micelle) is first created and stabilized by Igepal CO-520, which acts as surfactant in the organic phase (see **Scheme 2a**). This micelle can then provide a water environment between the hydrophobic NPs and the organic phase.³⁰¹

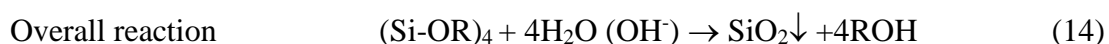


Scheme 2. Chemical structure of (a) Igepal CO-520 and (b) TEOS

Within this aqueous layer, silica can grow on the surface of UCNPs *via* hydrolysis of $\text{Si}(\text{OC}_2\text{H}_5)_4$ (TEOS) and condensation of the hydrolysed silica species in the presence of ammonia as the basic catalyst (see **Scheme 2b**).^{302–304} The hydrolysis and condensation mechanism of TEOS, where $\text{R}=\text{C}_2\text{H}_5$ is summarized below.²⁹⁰



The first reaction shows the hydrolysis of TEOS to silanol monomers. This process is catalysed by the presence of either an acid or a base. Under basic conditions, water dissociates to produce hydroxyl anions (OH^-) in a rapid first step, and then OH^- attacks the silicon atom. The alcohol and water condensation reaction represent the formation of siloxane bonds. The resultant siloxanes from the alcohol and water condensation are the same, except the by-product is either ethanol or water. Therefore, the global chemical reactions describing the hydrolysis and condensation of TEOS, involving the formation of silica can be briefly written as follows:



There are studies detailing the mechanism of silanization for others type of OA-coated NPs.³⁰⁵ Vogt and co-workers suggested a ligand exchange mechanism between OA and hydrolysed TEOS to transfer iron oxide NPs from the organic to the water phase using a reverse microemulsion method.³⁰⁶ Ding and co-workers reported evidence of an intermediate ligand exchange between OA and the surfactant Igepal on the surface of similar NPs.²²⁰

Based on the above statements and considering similarities between the surface of the UCNPs and the ones reported, we can propose a similar synthetic route resulting in β -UCNPs@ SiO_2 (see **Figure 70**)

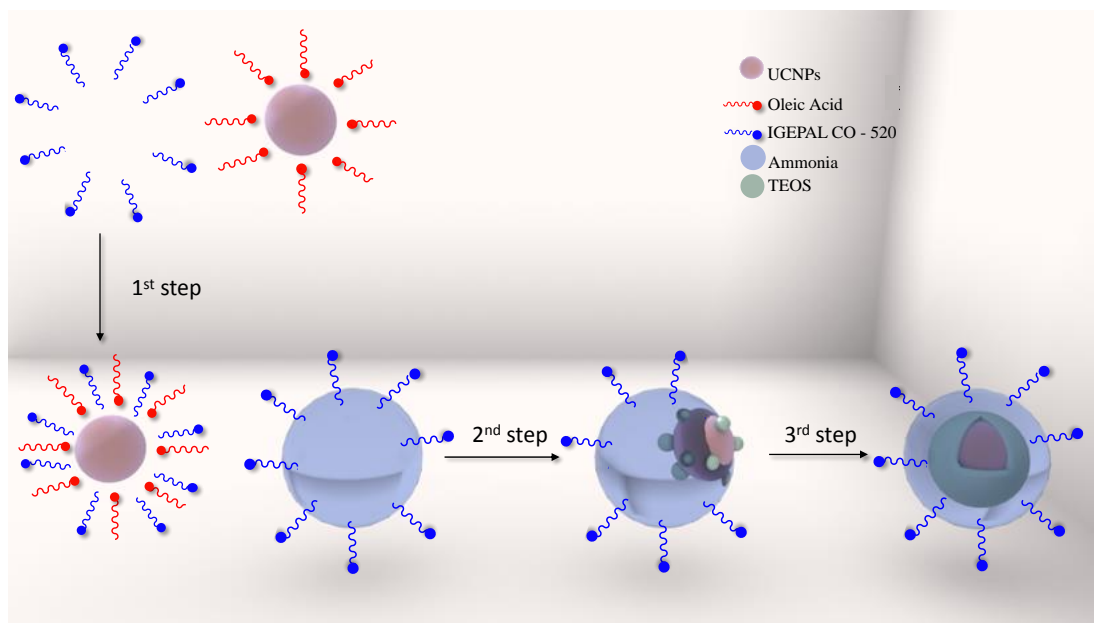


Figure 70. Proposed mechanism illustrating the synthetic route to produce hydrophilic β -UCNPs@SiO₂.

First, Igepal is added into the hexane organic phase where it spontaneously aggregates and forms the aqueous micelles. When OA-coated β -UCNPs are added into the solution, part of the Igepal could interact with their surface resulting in a ligand exchange (1st step). Then, ammonia is added to fill the rest of the empty Igepal micelles. The hydrolysis of TEOS occurs on the surface of the micelles, upon their addition. At this stage, a new ligand exchange between Igepal and hydrolysed TEOS may occur transferring the β -UCNPs into the reverse micelles (2nd step). Finally, the condensation process of TEOS forms the silica shell around the β -UCNPs (3rd step). This mechanism would explain the silica coating on β -UCNPs however, a more in-depth experimental analysis is needed for approbation.

4.2 Oligonucleotide functionalization of upconversion nanoparticles

In order to use UCNPs for different biological applications, it is crucial to couple the UCNPs with molecules that possess biological functions, such as antibodies, peptides, and nucleic acid ligands. This biofunctionalization step, also referred to as bioconjugation, can be realized by the attachment of biomolecules to the UCNP surface *via* physical adsorption or chemical conjugation.

In order to covalently couple the UCNPs with biomolecules and more specifically synthetic oligonucleotides, -COOH functional groups were introduced to the surface of UCNPs and used for binding to oligonucleotides. In our work, we employed a s-NHS/EDC coupling

strategy to functionalize the -COOH group of the β -UCNPs and successfully attached the amino functional group of the oligonucleotide strands to the β -UCNPs.^{225,307} The synthesis and characterization of the single strand oligonucleotides ssDNA-UCNPs are discussed in **Section 4.2.1**.

The incubation process of the obtained ssDNA-UCNPs with A549 cells and the method followed for the fixation and staining of cells on coverslips are explained in **Section 4.2.2** and **Section 4.2.3**, respectively. The fluorescence of the cells and the UC luminescence of the β -UCNPs in cells were detected using a confocal microscope and a built-home set-up, and the results are discussed in **Section 4.2.4** and **Section 4.2.5**, respectively.

4.2.1 Covalent construction of ssDNA-UCNPs structure

For the following experiments, we used the water-dispersible amine-functionalized β -UCNPs@SiO₂-NH₂ nanocomposite (Sample 12.1s.Am) synthesised in the previous **Section 4.1**. With these particles successfully transferred to an aqueous phase, and in order to prepare the NH₂-functionalized particles for the EDC coupling reaction, carboxylic groups were first created to their surface, using succinic anhydride. See the full experimental procedure in **Section 2.3.5**.

Following this strategy, the amine terminal group from the UCNPs reacts with the succinic anhydride through a ring opening reaction, yielding a terminal carboxyl group, where the amino groups acted as nucleophiles for the reaction with succinic anhydride (see **Figure 71**).

308–310

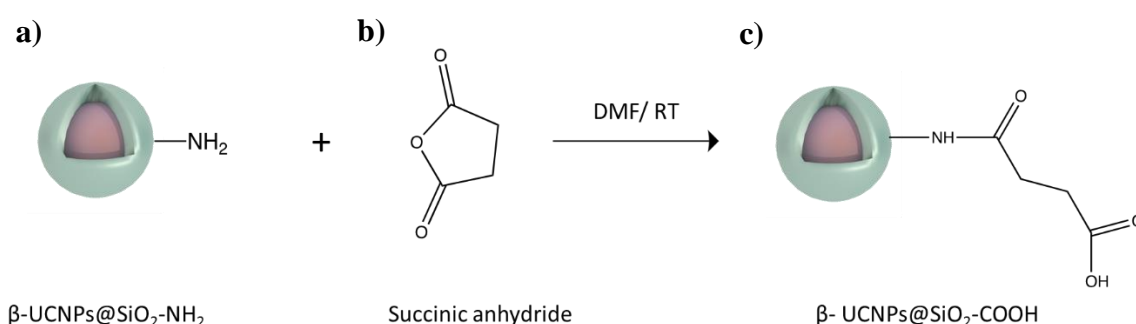


Figure 71. Schematic illustration of the synthetic route to produce β -UCNPs@SiO₂ functionalized with -COOH group. (a) Amine functionalized UCNPs denoted as β -UCNPs@SiO₂-NH₂, reacted with (b) succinic anhydride, in dimethylformamide (DMF) at room temperature and overnight to produce (c) NPs denoted as β -UCNPs@SiO₂-COOH. Pink and green colour spheres are referred to the core and silane layer on the surface of the β -UCNPs.

The charge of the β -UCNPs was monitored using ζ -Potential measurements. **Figure 72** shows the changes in the charge of the particles as they go through the different stages of functionalization. The ζ -potential of the initial β -UCNPs@SiO₂ was negative ($-42.4 \text{ mV} \pm 6.70 \text{ mV}$), while after attachment of amino groups, it became positive ($+14.6 \text{ mV} \pm 6.23 \text{ mV}$). Finally, following the ring opening reaction, the functional amino groups were transformed into carboxylic groups, and the ζ -potential of the NPs became negative again ($-14.1 \text{ mV} \pm 4.21 \text{ mV}$.)

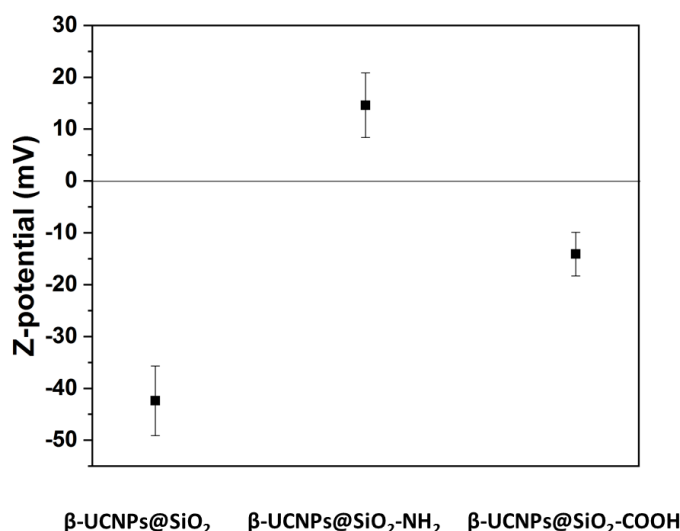


Figure 72. ζ -potential measurements of the β -UCNPs@SiO₂, β -UCNPs@SiO₂-NH₂ and β -UCNPs@SiO₂-COOH in Milli-Q water.

β -UCNPs@SiO₂ functionalized with -COOH groups can be further modified with amine containing biomolecules *via* simple coupling chemistry methods, e.g. using 1-ethyl-3-(3-dimethylaminopropyl)carbodiimide (EDC) as a catalyst.³¹¹

Carbodiimide chemistry is the most common method to covalently bind carboxylic acids with primary amine groups. Initially, EDC reacts with the carboxylic group to form an amine reactive intermediate (O-acylisourea). To avoid the hydrolysis of the O-acylisourea and regeneration to the carboxyl, N-hydroxysulfosuccinimide sodium salt (s-NHS) is often used to increase the efficiency of the reaction. The intermediate produced by s-NHS is significantly more stable than the O-acylisourea that is produced in reactions only with EDC. S-NHS is known to stabilise O-acylisourea, by converting it into amine reactive s-NHS ester intermediate.^{307,312}

Following this strategy, the β -UCNPs@SiO₂-COOH were conjugated to oligonucleotides that contained -NH₂ groups. See **Figure 73** for a schematic route process. The sequence of

the synthetic oligonucleotide employed in this work was: 5'-aminohexyl 2AAACGGGCTTTTTTTTTTTTTTTTTTTTTTTTTTTTTTTTTTT-3'. First, the terminal -COOH groups from the functionalized β -UCNPs were activated with (EDC) and the (s-NHS) in buffers. Then, the resulting intermediate products reacted with -NH₂ group from the oligonucleotides to complete the chemical bonding. With this method, an amide bond was created between the -NH₂ groups and a -COOH group; hence, between carboxy terminated β -UCNPs@SiO₂ and amine containing oligonucleotides. More information can be found in the experimental in **Section 2.3.6.2**.

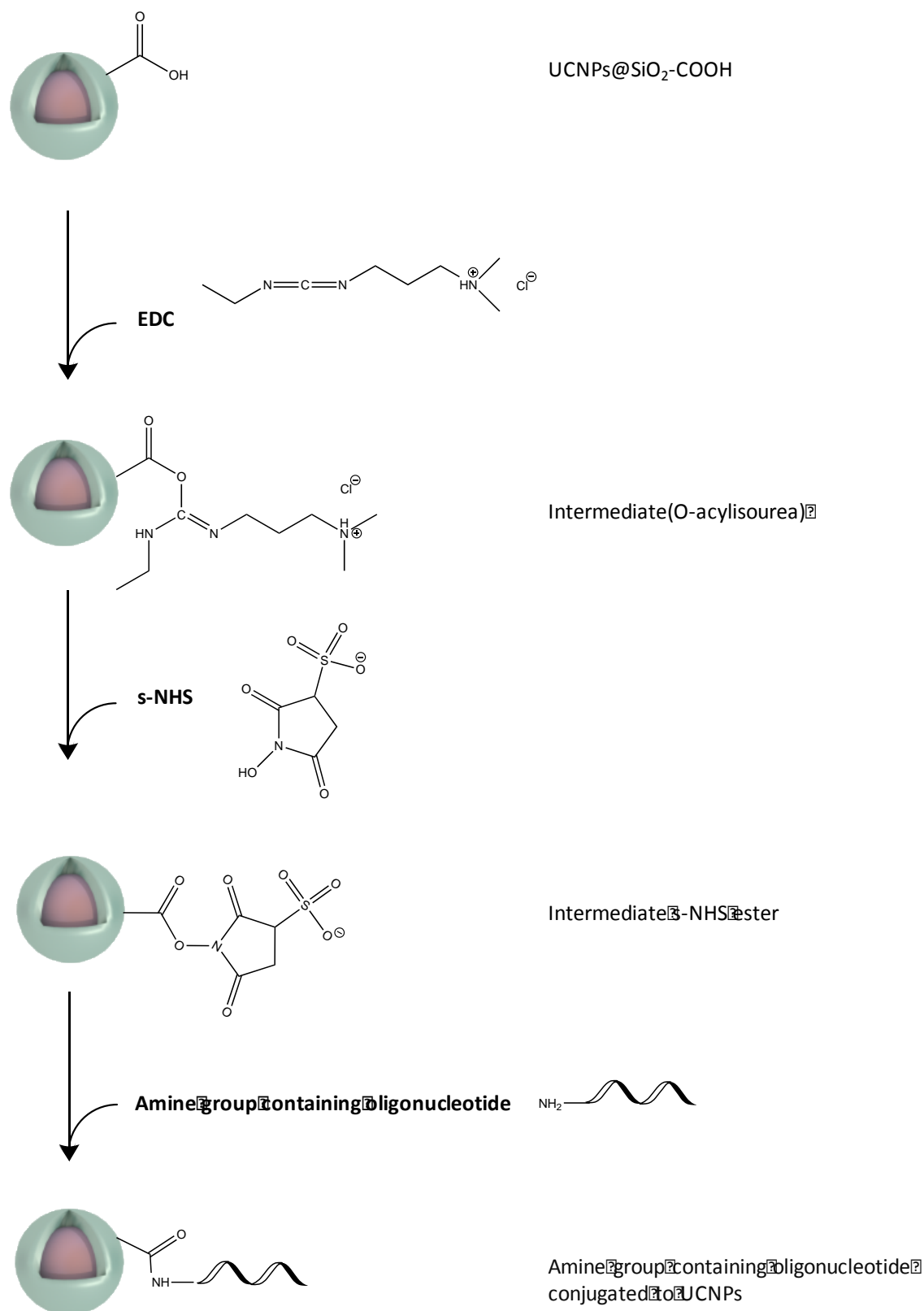


Figure 73. Schematic illustration of EDC/s-NHS coupling reaction between β -UCNPs@SiO₂-COOH and amine group containing oligonucleotide. For simplicity β -UCNPs@SiO₂-COOH cartoon only shows the terminal -COOH group.

Apart from ζ -potential measurements, FTIR spectroscopy was also used to evaluate coupling of the oligonucleotides. β -UCNPs coated with OA were compared to β -UCNPs coated with silica and after modification with oligonucleotides. **Figure 74** shows a double peak (blue line) occurring at 1544 cm^{-1} and 1653 cm^{-1} on the oligonucleotide-coated UCNPs. Although, the peaks intensity is not very high, we attributed them to the C=O and the N-H vibrating bonds of the amide groups, respectively thus ensuring the successful attachment of single strands from the oligonucleotide (ssDNA) to the surface of UCNPs.^{225,310}

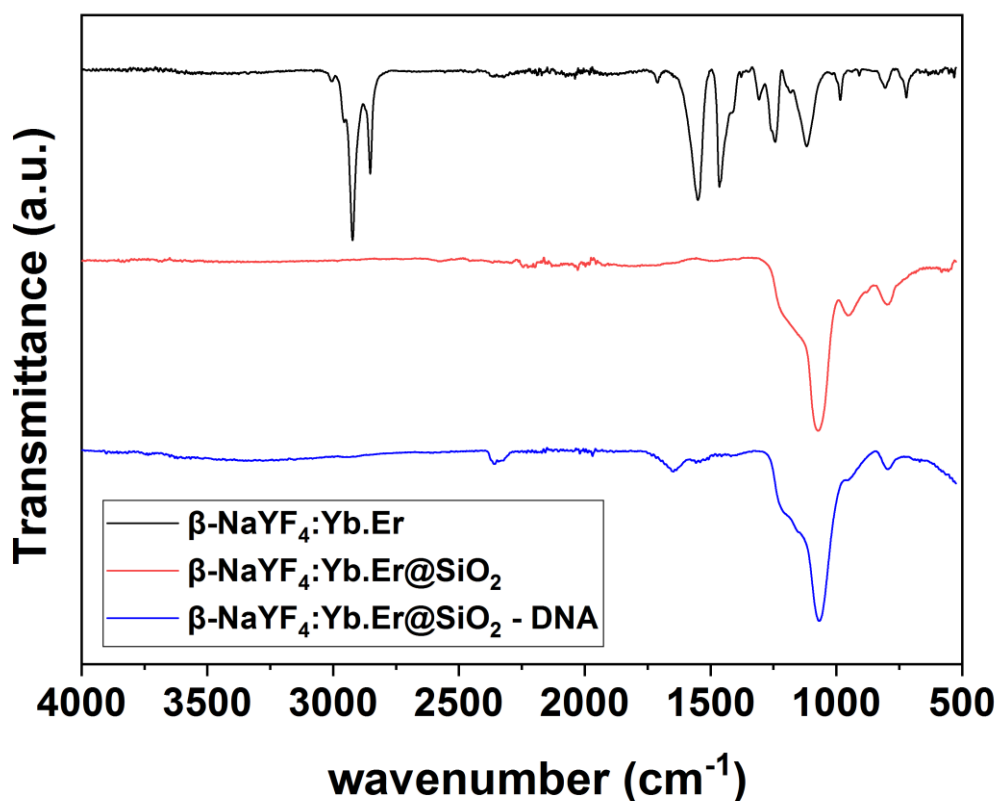


Figure 74. FTIR from sample before and after the oligonucleotides attached. Black line corresponds to the original OA coated β -NaYF₄: Yb³⁺, Er³⁺ UCNPs, red line shows the β -NaYF₄: Yb³⁺, Er³⁺@SiO₂ and blue line indicates the β -NaYF₄: Yb³⁺, Er³⁺@SiO₂-ssDNA.

4.2.2 Incubation of upconversion nanoparticles with A549 cells

The as-prepared β -UCNPs covered with synthetic oligonucleotides were incubated with A549 cells. The A549 cell line was isolated in 1973 by Giard et al. It was obtained by extracting and culturing cancerous lung tissue from the explanted tumour of a 58-year-old male.^{313,314} The importance in these cells lies in the fact that they can be used as a model for the study of lung cancer and the development of drug therapies against it.

See experimental detail in **Section 2.3.6.3** for the full incubation protocol. A schematic illustration containing the incubation procedure and a cartoon of the NPs incubated with cells is shown in **Figure 75**.

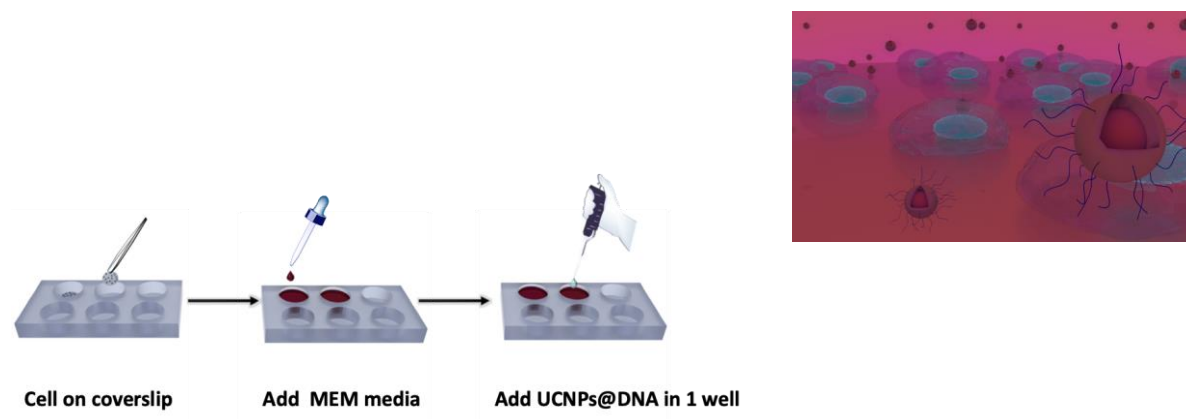


Figure 75. Illustration showing the incubation procedure and a representation of the β -UCNPs@SiO₂-ssDNA nanocomposite with the A549 cell during the incubation process.

4.2.3 Preparation fixation and staining of cells on coverslips for microscope imaging

After the incubation period, cells were fixed to help to preserve the architecture and composition of the cells and allow further examination. Aldehydes such as formaldehyde, formalin, paraformaldehyde and glutaraldehyde are the most commonly used fixatives and have been studied for decades.^{315 316} In our work we used paraformaldehyde (PFA) as fixative agent.

Then, cell nuclei were stained with DAPI, which is a blue fluorescent DNA stain. It is excited at the wavelength of 405 nm and is commonly used as a nuclear counterstain in fluorescence microscopy, which can be used to stain both live and fixed cells. For imaging, coverslips were removed from the wells and mounted onto glass microscope slides and set in place using a Mowiol solution which hardens overnight after slide preparation. See **Figure 76** for a scheme of the process and **Section 2.3.6.3.1** for the experimental details.

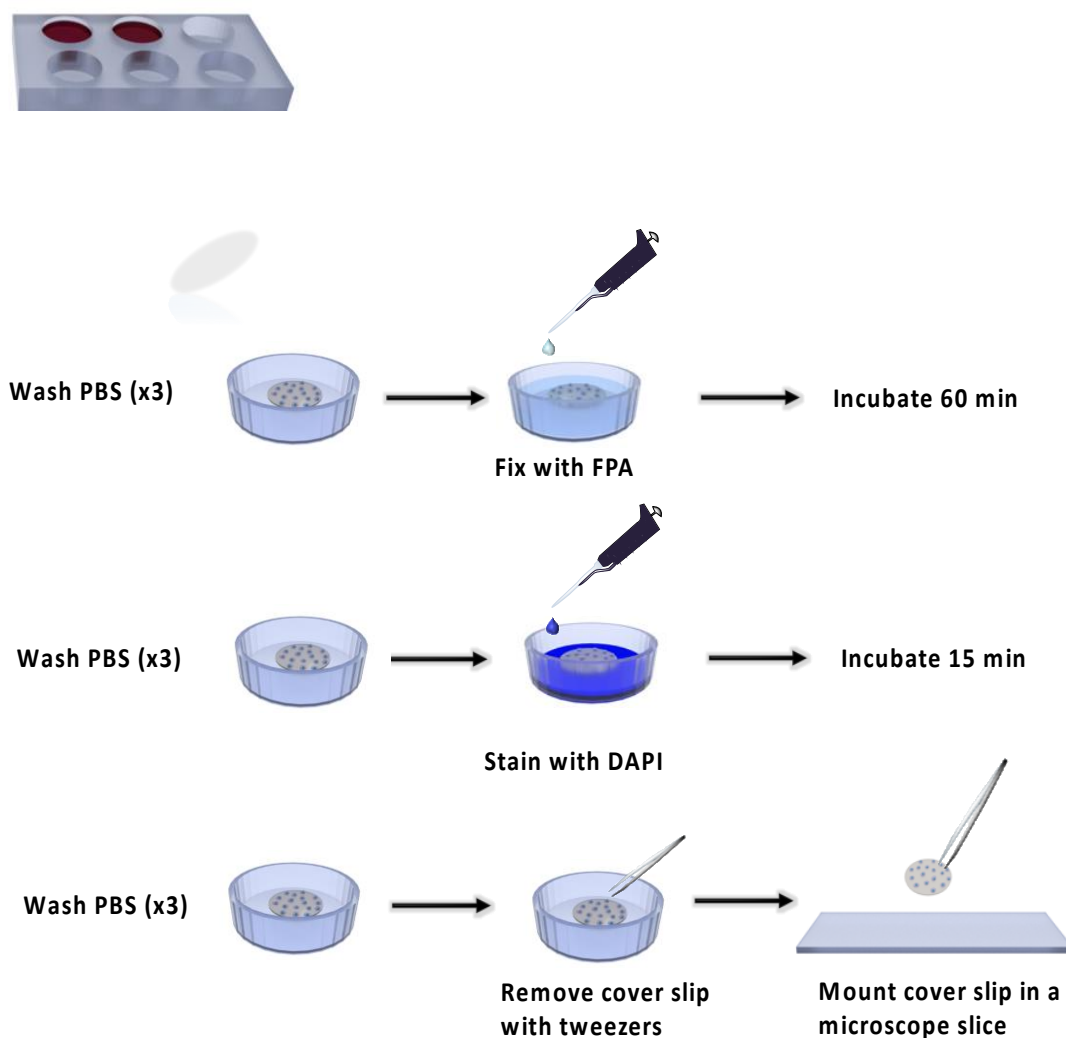


Figure 76. Preparation fixation and staining of cells on coverslips for confocal.

4.2.4 Confocal microscopy of upconversion nanoparticles with A549 cells

After incubation of the cells with the particles and their cell fixation in the cover slip, the cells were imaged using a Leica TCS SP8 confocal microscope. A $\times 63$ oil immersion objective and an excitation wavelength of 405 nm was used.

Figure 77 shows the confocal laser microscopy images of A549 cells incubated without UCNPs (**Figure 77a**) and with β -UCNPs@SiO₂-ssDNA (**Figure 77b**) after 12 hours. The images show that the nucleus morphology was intact after treatment with the UCNPs, indicating that cells were most likely not affected after the 24 hours' incubation period.

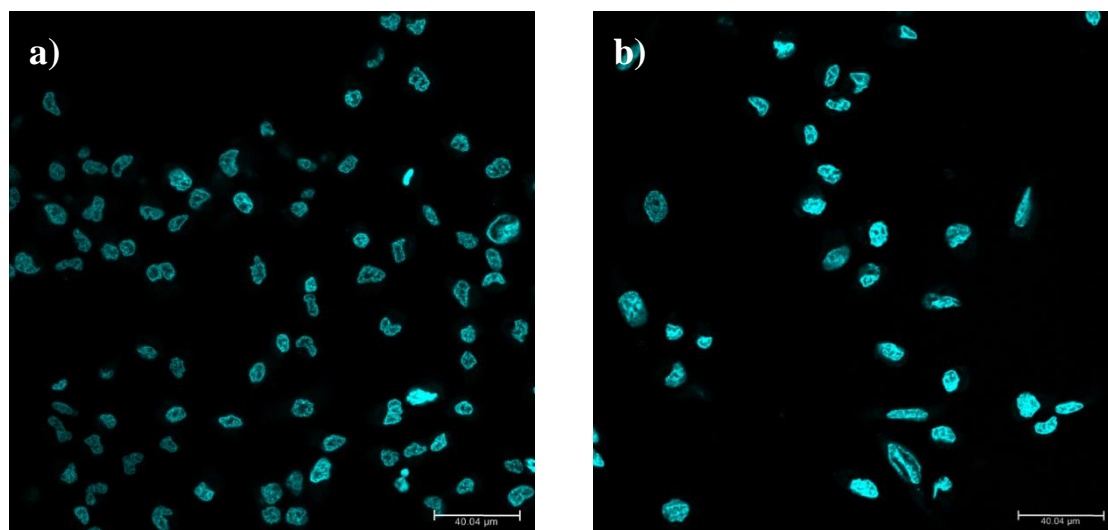


Figure 77. Confocal laser microscopy images of A549 cells (a) without treatment and (b) after the incubation with the β -UCNPs@SiO₂-ssDNA nanocomposite for 24 hours. 405 nm excitation for DAPI. Scale bars are 40.04 μ m.

4.2.5 Luminescence of upconversion nanoparticles incubated with A549 cells

The excitation wavelength of UCNPs is high and beyond the capacity of a normal confocal microscope. To study whether the β -UCNPs@SiO₂-ssDNA could effectively enter into A549 cells, the uptake of particles into A549 cells was visualized and imaged by a home-built setup which is presented in **Figure 19**. The built setup is equipped with a microscope to detect both the UC luminescence and fluorescence spectra from the DAPI. The UCNPs were excited under a 980 nm laser source, whereas DAPI was excited under a laser source of 405 nm.

Figure 78a shows a luminescence image of the cell nuclei after incubation with the β -UCNPs@SiO₂-ssDNA, obtained by exciting the sample at 405 nm. **Figure 78b**, on the other hand, shows the corresponding UC luminescence image when excited at 980 nm. Each bright spot in the image is thought to represent the UCNPs inside the cell. The image shows very high amount of luminescence of UCNPs around the cell nuclei, indicating a high number of uptaken particles. Unfortunately, knowledge of the interaction between UCNP and cells is still limited and their intracellular uptake pathways remain unexplored,³¹⁷ therefore further analysis such as cross-sectioning are still needed for understanding the uptake mechanism carried out by the cells.

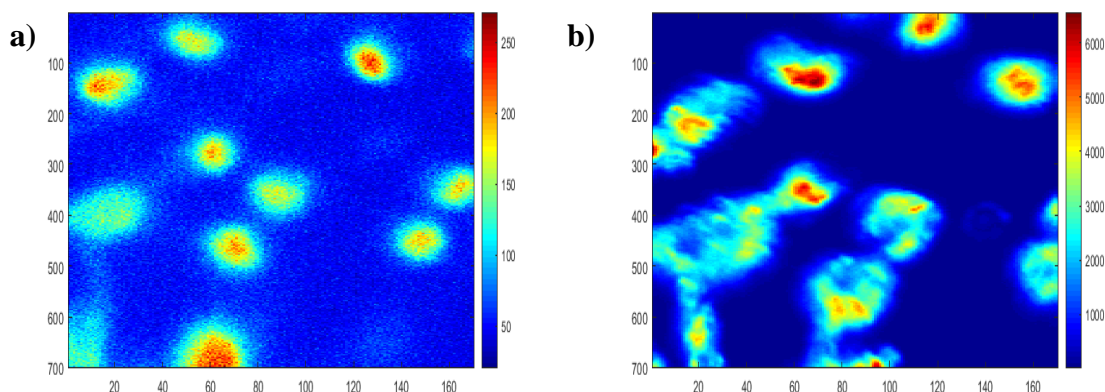


Figure 78. Luminescence images of cells incubated with β -UCNPs@SiO₂-ssDNA (a) using the DAPI excitation at 405 nm and (b) under 980 nm excitation.

We repeated the same experiment for the control sample (cells without particles) and the results are shown in **Figure 79**. The fact that no signal was detected when the control sample was excited by the 980 nm laser is a strong indication that the fluorescence signal detected in the case of cells incubated with β -UCNPs@SiO₂-ssDNA was due to the successful uptake of particles by the A549 cells.

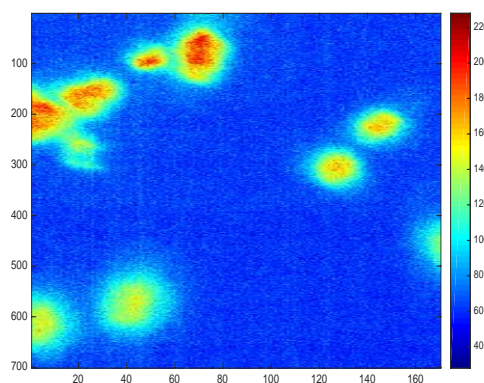


Figure 79. Luminescence image of the cell nuclei using the control sample, under the DAPI excitation wavelength of 405 nm. No observed image was obtained with the 980 nm excitation wavelength.

Overall, the β -UCNPs@SiO₂-ssDNA nanohybrid showed UC luminescence imaging after being incubated with A549 cells and therefore signs of good biocompatibility. Although the work is still ongoing we expect that the β -UCNPs@SiO₂-ssDNA nanohybrid could be applied for further biological applications and provide support on the existing knowledge of UCNP biocompatibility.

4.3 Functionalization of gold nanoparticle with upconversion nanoparticles

It has been reported that plasmonic modulation can enhance the low efficiency of UCNPs by coating the particles with an Au shell and tuning the surface plasmon resonance (SPR) peak to the NIR region. If the SPR peak is tuned to the NIR region and resonates with the absorption of UCNPs at 980 nm, the absorption cross-section of the UCNPs can be significantly enhanced.¹⁴² Interestingly, research has found that the Au shell encapsulation not only improves the UC properties, but enhances biocompatibility.³¹⁸ In **Section 4.3.1** we will look at the synthetic protocol to create the Au shell around the UCNPs. Additionally, we will study the tunability of the SPR peak.

Gold nanoparticles (AuNPs) and gold nanorods (AuNRs) are of great interest to study because of their shape-dependent optical properties, thus it is very important to maintain a precise control during their synthesis. It is well known that the optical properties are tuneable throughout the visible and NIR region of the spectrum as a function of NPs size and shape.^{217,319,320} Liu and co-worker carried out a theoretical study to investigate the luminescence enhancement of UCNPs in the vicinity of AuNRs.¹⁴³ Although the work was theoretical, the findings from their study could provide us with important guidelines for designing new UCNPs composite with AuNRs with significantly enhanced luminescence efficiency. **Section 4.3.2** will look at the synthesis of AuNRs whilst also varying their AR. AuNRs with very high AR were also synthesised and are discussed in **Section 4.3.3**.

4.3.1 Au shell coated UCNPs

Au shell coated β -UCNPs were prepared according to a method developed by Halas and co-workers with some modifications.³²¹

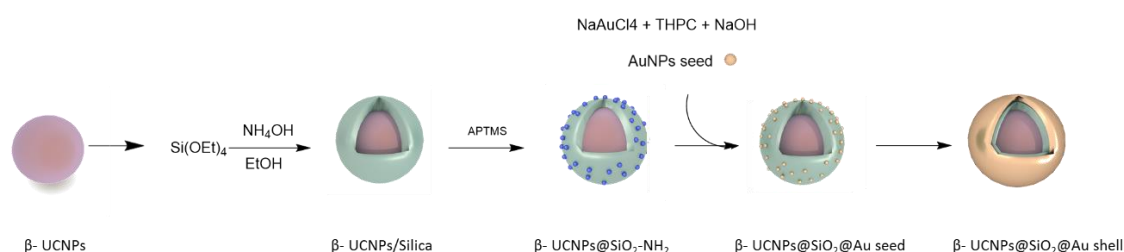
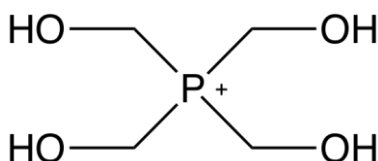


Figure 80. Schematic illustration of the synthetic route to produce β -UCNPs@SiO₂@Au shell dispersible in water.

This method involves three major steps; preparation of silica coated β -UCNPs, to which small Au seeds are subsequently attached and slow growth of the Au shell around the surface of the silica (**Figure 84**).

Three samples with different sizes of Au seeds were synthesised according to a well-defined synthetic route originally established by Duff, Daniel G. in 1993.²²³ This involves the reduction of an Au^{3+} salt with alkaline tetrakis(hydroxymethyl)phosphonium chloride (THPC) (See **Scheme 3**). The full synthetic protocol can be found in **Section 2.3.4**.



Scheme 3. Chemical structure of THPC.

To obtain different Au seeds, three different volumes of the Au precursor (1% sodium tetrachloroaurate (III) dihydrate solution) were added to the standard reducing mixture, precisely 0.75 ml, 1 ml and 1.5 ml.

UV-vis spectra of the seed solutions are shown in **Figure 81** along with a digital photo of their colloidal solutions. This spectrum should be very sensitive to changes in particle size and so was employed as a fingerprint to detect seed size.^{322,323} The bigger seeds solution exhibited a shoulder-like plasmon band (blue line), while the maximum absorbance peak of the smallest seeds (black line) was not visible.

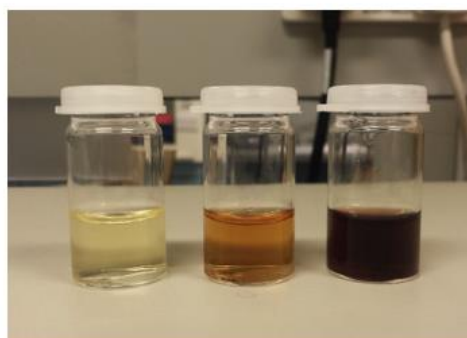
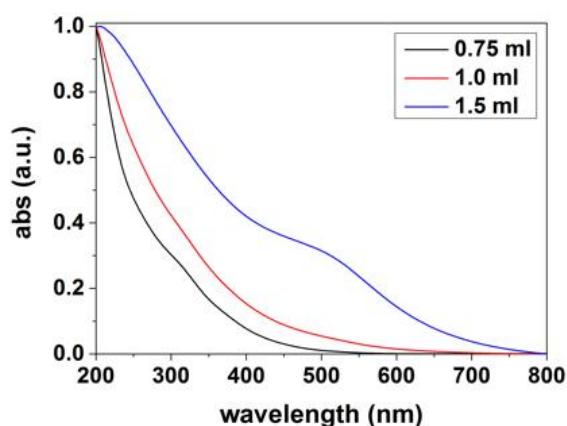
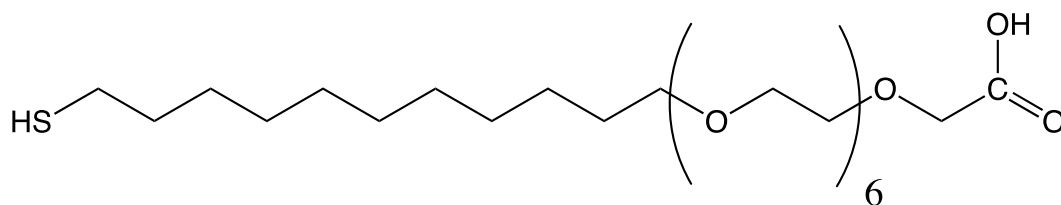


Figure 81. UV-vis spectra and corresponding digital image of THPC coated Au seeds. Black line from the spectra represents the smallest seeds (yellow solution), red line corresponds to the medium size (orange solution) and blue line to the largest seeds (brown solution).

The synthesis of β -UCNPs@SiO₂@Au seed was carried out by the reaction of amine-functionalized β -UCNPs@SiO₂ with the Au seed solution according to the experimental protocol detailed in **Section 2.3.3**. Amine-functionalized β -UCNPs@SiO₂-NH₂ (Sample 12.1.s.Am) (See **Figure 62**) was employed to attached the Au seeds, where the available amine groups served as binding sites.³²¹ Next, Au shells were grown on the top of the silica. Au seeds attached to the silica served as nucleation sites, so their initial size was crucial for the final thickness of the shell, which would also affect their optical properties. The growth was terminated by the addition of thiol containing molecule, monocarboxy (1-mercaptoundec-11-yl) hexaethylene glycol (OEG) with MW = 526.7, see **Scheme 4** for the chemical structure), which binds to the Au surface and prevents further growth of NPs.



Scheme 4. Chemical structure of OEG.

Significant differences in the optical properties were found due to the variation of the Au shells grown on the silica surface. The ratio of core diameter to shell thickness is altered and therefore the SPR peak is changed accordingly. The UV-Vis spectra of β -

UCNPs@SiO₂@Au shell are shown in **Figure 82** and contain a very pronounced peak at 525 nm (blue line), which corresponds to the plasmon band of the thickest Au shell. The medium size seeds produced Au shells, which exhibited a peak at 590 nm. The smallest seeds led to the formation of the thinnest Au shells producing a considerable and broad red-shift peak at 670 nm. The broad shape can be explained by the scattering effect deriving from a non-homogenous diameter of the resulting NPs ³²⁴ and is in a reasonably good agreement with the absorption spectra of bulk Au. ³²⁵

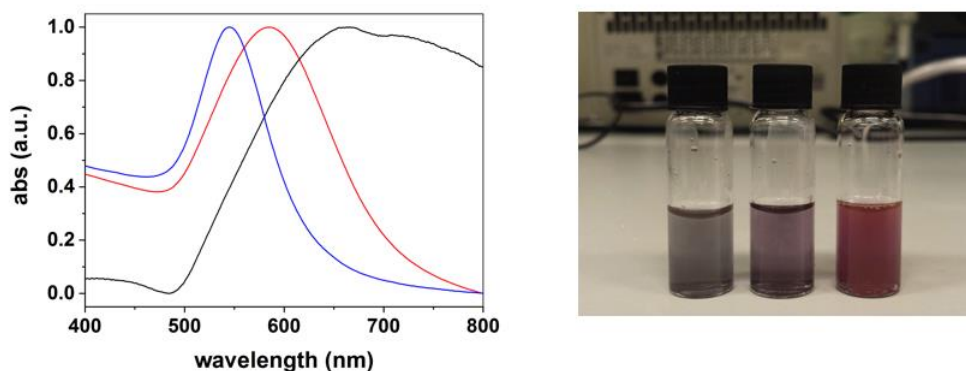


Figure 82. UV-Vis spectra and corresponding digital image of β -UCNPs@SiO₂@Au shell nanostructures. Black line represents the thinner shell (blue-grey solution), red line the middle thickness (purple solution) and blue line represent the thickest shell (red solution).

It is also worth highlighting that the yield was very low and only a few β -UCNPs@SiO₂@Au shell particles were found under TEM microscopy. **Figure 83** shows a representative TEM image of the Au shell evolution. From left to right, image shows a TEM image of Au seeds, Au seeds attached to β -UCNPS@SiO₂ and β -UCNP@SiO₂@Au shell.

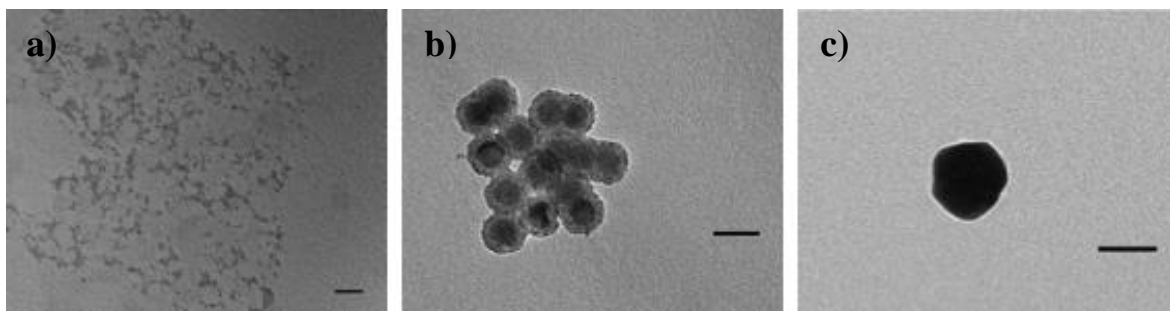


Figure 83. TEM figure of (a) Au seeds, (b) β -UCNPs@SiO₂@Au seeds and (c) β -UCNP@SiO₂@Au shell. Scales bars are 50 nm.

Although this work is still continuing, we hypothesize that the decrease of Au precursor would lead to a shift of the SPR to higher wavelengths, precisely to the region where UCNPs absorb, at 980 nm.

4.3.2 Synthesis of Gold nanorods

We synthesized AuNRs with varying AR by using different amounts of silver nitrate. Four samples of AuNRs coated with CTAB were synthesised following a seed-mediated protocol reported by El-Sayed and co-worker.²¹⁷ See **Section 2.2.1** for experimental details.

CTAB Gold seeds

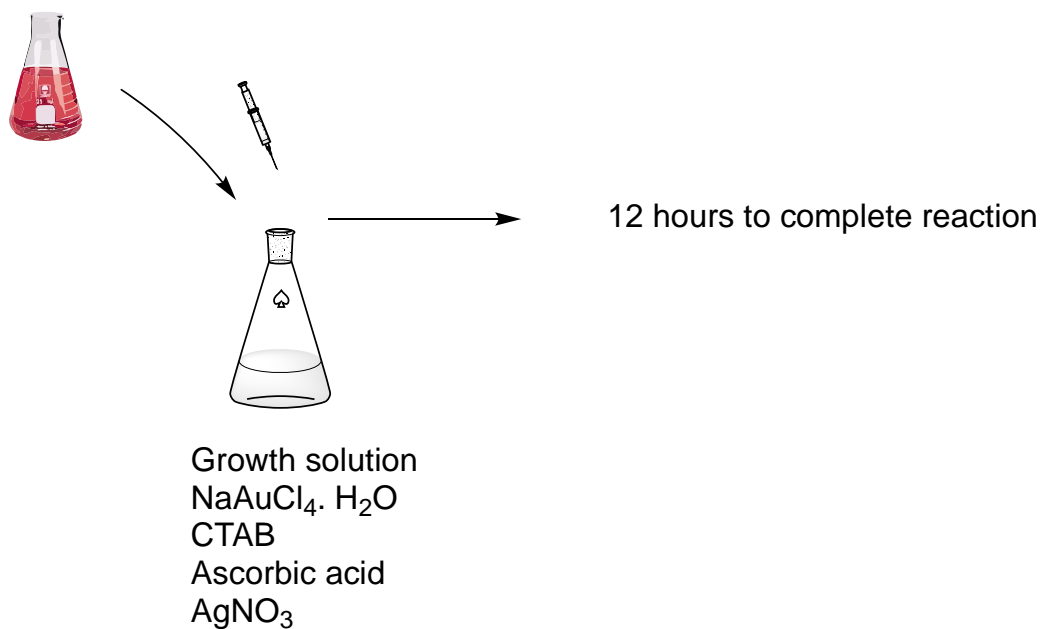


Figure 84. Schematic illustration for the formation process of AuNRs.

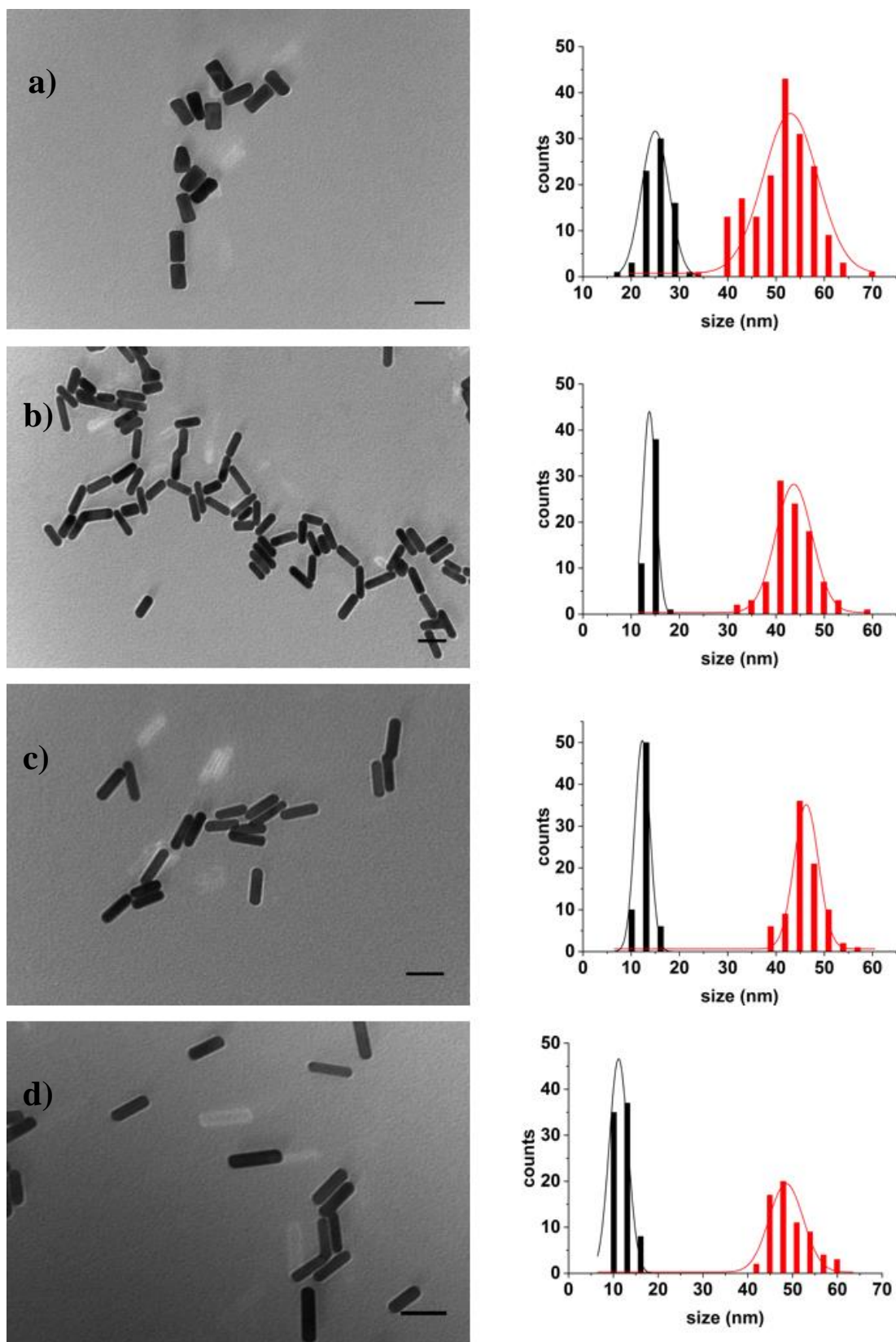


Figure 85. TEM of AuNRs synthesised with (a) 120 μl , (b) 300 μl , (c) 400 μl , and (d) 500 μl of AgNO_3 . Scales bars are 50 nm.

The AuNRs were first characterized by TEM. The size distribution was analysed considering over 100 AuNPs for each of samples. From TEM images (see **Figure 85**) it can be seen that there is an apparent increase in the AR accompanied with a decrease in the diameter when more silver was added. AuNRs increased in AR as following 2.12, 3.38, 3.76 and 4.38, whilst the average diameter gradually decreased (~25 nm, ~14 nm, ~13 nm and ~11 nm, respectively). It can be seen that through this method, the reaction produced a majority of NPs with rod-like shape, and only few spheres or cubes were visible from the TEM. **Table 16** summarizes the dimensions and AR of the four samples.

Table 16. Dimensions of the AuNRs obtained by using different AgNO_3 contents.

AgNO_3 (μl)	Length	Width	AR
120	53 nm \pm 6 nm	25 nm \pm 3 nm	2.12
300	46 nm \pm 4 nm	14 nm \pm 1 nm	3.38
400	46 nm \pm 2 nm	12 nm \pm 2 nm	3.76
500	49 nm \pm 4nm	11 nm \pm 2 nm	4.38

Then, UV-Vis spectroscopy was used to characterize the samples. From **Figure 86** it is visible that AuNRs exhibited two plasmon bands, which correspond to the localized surface plasmon resonance (LSPR) along the long axis of the particle (longitudinal plasmon band) and along the short axis of the particle (transverse plasmon band). Moreover, the colour of the resulting solution varied with the concentration of silver added, which is indicative of AuNRs with different AR due to the red shift of the longitudinal peak. The transverse plasmon band shifted as following: 620 nm, 710 nm, 750 nm and 790 nm, with increasing AR.

It can be concluded that the length and thus AR of the obtained AuNRs depended on the introduced quantity of silver. It is well known that with this method there is a critical level regarding the concentration of silver that can be added.³²⁶ In our work, the largest AR that we were able to achieve was 4.38.

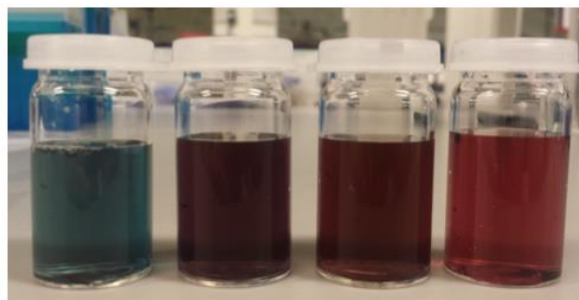
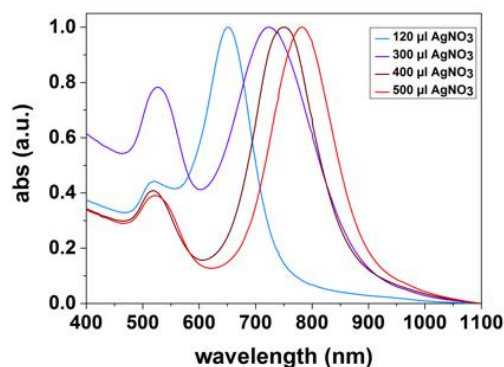


Figure 86. UV-Vis spectra and optical photography of AuNRs synthesised with 120 µl, 300 µl, 400 µl and 500 µl of AgNO₃.

As proposed by Mulvaney and co-workers, seeds originate with the reduction from Au³⁺ to Au⁺ by NaBH₄.³²⁷ In the growth process, CTA⁺ ions and Au³⁺ ions, form a CTA⁺-Au³⁺ complex. Subsequently, ascorbic acid (AA) reduces this complex to form CTA⁺-Au⁺. The formation of elemental Au occurs when CTA⁺-Au⁺ and AA react and are deposited on the surface of AuNPs.

In the presence of Ag⁺ ions, the reduction and deposition of Ag atoms occur on the AuNRs sides. The strong CTAB binding inhibits Au growth on the side of rods, and as a consequence AuNRs grow along the longitudinal [110] direction leading to AuNRs with different ARs.
328,329

4.3.3 Synthesis of high aspect ratio gold nanorods

More elongated AuNRs structures, were synthesised *via* a slightly modified procedure described in **Section 2.2.2**. In this method originally developed by Murphy and adapted by Huang, silver nitrate was discarded from the growth solution and seeds were grown by a fast and successive addition of growth solutions containing Au (see **Figure 87**). This led to the synthesis of AuNRs with a high AR and a length above 500 nm. Representative TEM images from the solution are shown in **Figure 88**.

Citrate Gold seeds

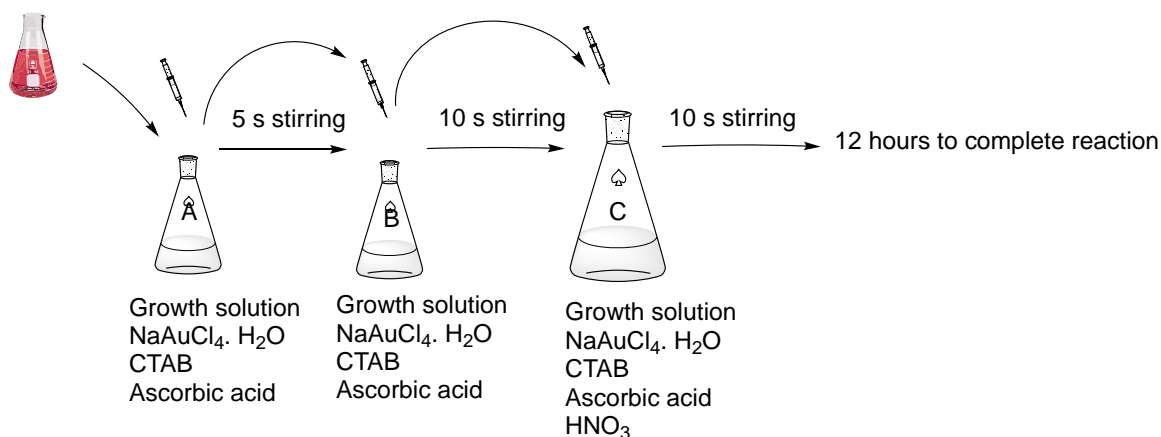


Figure 87. Schematic illustration for the formation process of high AR of AuNRs.

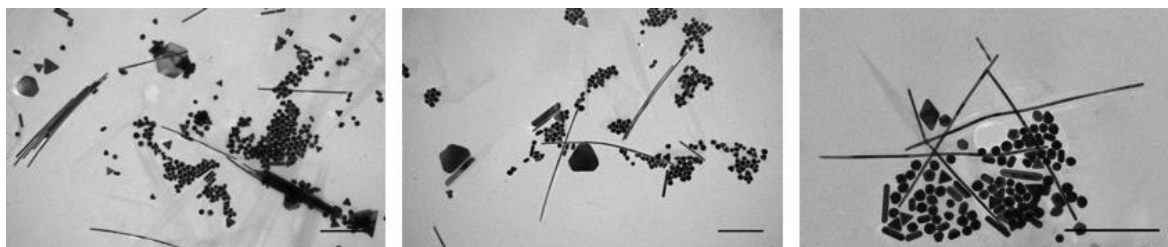


Figure 88. TEM images of long AuNRs. Scales bars are 500 nm.

The resulting solution contained a large fraction of spherical, triangular and hexagonal NPs, due to the low nanorods yield of the growth reaction.

The optical properties of these high AR AuNRs were characterized by uv-vis-NIR spectroscopy. The absorption spectra of AuNRs with high aspect ratio were recorded on a Jasco FT-IR 620 spectrometer with a 1 nm resolution from 400 to 1200 nm. The presence of high AR structures in colloidal solution resulted in even greater red-shift of the plasmon band (to 800-1200 nm). However, the overall reaction yield through this method was lower than in **Section 4.3.2**. **Figure 89** shows a broad longitudinal peak suggesting poly-dispersed NPs as indicated by the TEM images of **Figure 88** whereas the higher intensity of the transverse band at 510-520 nm matched with the presence of spherical NPs.

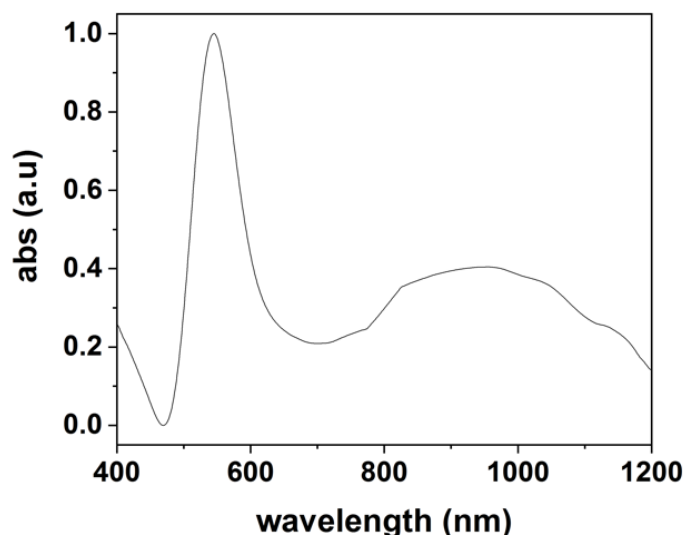


Figure 89. UV-Vis spectra of long AuNRs containing a large number of spheres and triangles.

Although the work is still ongoing, we expect that the presence of high AR AuNRs bound or in close proximity to the UCNPs can influence both its absorption in the NIR and emission in the Vis, and thus enhance the UC luminescence.

4.4 Photocatalysis of upconversion nanoparticles coated with a TiO₂ shell

Since Fujishima and Honda discovered the photocatalytic water-splitting on TiO₂ electrodes in 1972,³³⁰ research interest on TiO₂ photocatalysis has grown significantly due to their strong oxidizing power, extraordinary stability, environmentally friendly and biocompatibility features.^{331–333} However, one of the few limitations of TiO₂ (anatase phase) is its wide bandgap (~3.2 eV), which means that it can only be activated by UV excitation.^{334,335} In order to broaden the absorption spectra of the TiO₂ to the visible and NIR, UCNPs have been recently used. These particles absorb at 980 nm and can transmit in the UV-visible region. Therefore, they can serve as activators for the TiO₂.^{181,188,336}

Section 4.4.1 will look into the synthesis and characterization (TEM, XRD, EDX and luminescence spectroscopy) of β -NaYF₄: Yb³⁺(20%), Tm³⁺(0.5%) UCNPs coated with TiO₂.

We have studied the photocatalytic activity of the β -UCNPs/TiO₂ in the presence of several dyes and optimized the photocatalytic degradation conditions. Different effects including the β -UCNPs/TiO₂ dosage, recyclability and kinetics were investigated and will be discussed in **Section 4.4.2**.

Cobalt doped β -UCNPs/ TiO_2 were prepared by an impregnation method and its photocatalytic activity was also studied. This part of the research is explained throughout **Section 4.4.3**. The work concludes in **Section 4.4.4**, with a study based on the structural effects caused by annealing the β -UCNPs/ TiO_2 nanostructures at different temperature.

4.4.1 Synthesis and characterization of UCNPs coated with TiO_2

OA-coated β - NaYF_4 : Yb^{3+} (20%), Tm^{3+} (0.5%) UCNPs were synthesised following the experimental procedure detailed in **Section 2.1.1**. The particle size and morphology were first characterized by TEM. **Figure 90** shows that the β -UCNPs were monodispersed with a narrow size distribution of $39 \text{ nm} \pm 2 \text{ nm}$.

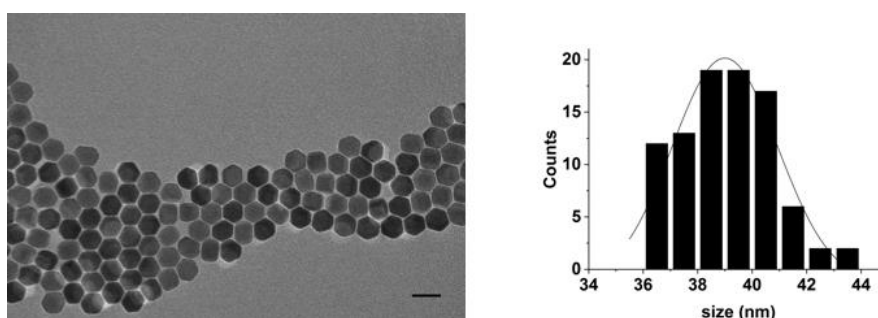


Figure 90. TEM images of the β - NaYF_4 : Yb^{3+} (20%), Tm^{3+} (0.5%) UCNPs with a size distribution of $39 \text{ nm} \pm 2 \text{ nm}$. Scale bar is 50 nm.

The as-prepared UCNPs were utilized as a core to grow a shell of TiO_2 . See **Figure 91** for a schematic route of the synthesis.

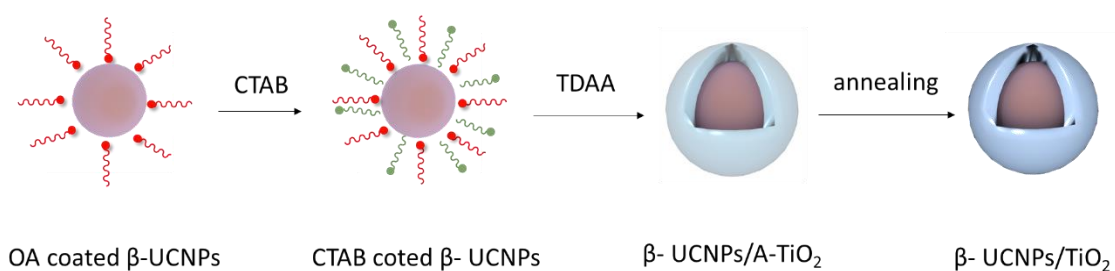
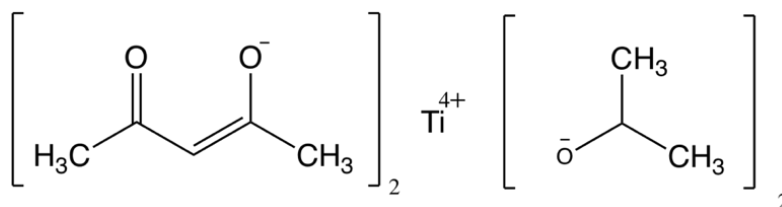


Figure 91. Schematic representation of β - NaYF_4 : Yb^{3+} (20%), Tm^{3+} (0.5%) UCNPs coated with TiO_2 . Red and green arrows indicate OA and CTAB respectively and A- TiO_2 means amorphous TiO_2 .

A reverse-micelle method was used to modify the surface of the particles with CTAB as a surfactant and make them hydrophilic by orienting the hydrophilic head of the surfactant outwards. The functionalisation step is of vital importance since the modification with

CTAB provides the β -UCNPs with an organic template for the growth of the TiO_2 shell, as well as dispersion in water and IPA, being the second one the solvent required during the TiO_2 coating step. Experimental details to fabricate the microemulsion CTAB-water-hexane can be found in **Section 2.3.9.1**.

Subsequently, the TiO_2 coating was performed by adding titanium diisopropoxide bis(acetylacetonate) (TDAA), a TiO_2 precursor with a slow hydrolysis rate.³³⁷ TDAA has an octahedral coordination with two isopropoxide and two acetylacetonate groups around a central titanium atom (see **Scheme 5**). Previous literature has shown that the first groups can easily hydrolyse compared to the acetylacetonate groups.^{338,339} The mild hydrolysis and condensation of TDAA resulted in β -UCNPs/ TiO_2 with a uniform core-shell. More information about this experimental stage of the reaction can be found in **Section 2.3.9.2**.



Scheme 5. Chemical structure of TDAA

β -UCNPs/ TiO_2 nanohybrid were characterized by TEM and two representative images are visible in **Figure 92**. It is worth highlighting that the as-prepared β -UCNPs coated with TiO_2 appeared as aggregates under TEM, probably due to the cross linking of the hydrolysed TDAA.¹⁸⁷

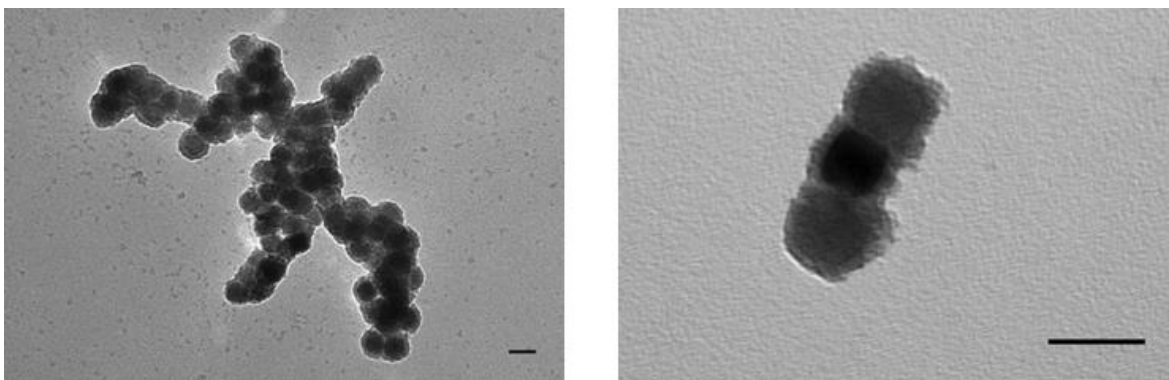


Figure 92. Two representative TEM images of β -UCNPs coated with TiO_2 before annealing. Scales bar are 50 nm.

In order to obtain a crystalline TiO_2 shell, the as-prepared coated β -UCNPs were annealed under atmosphere at 500 °C for 3 hours. After annealing, the products became highly crystalline as can be seen from the XRD characterization in **Figure 93**.

XRD spectra reveals pure β - UCNPs before the TiO_2 grown. When the latter one was created, two sets of peaks were clearly discernible. The first one corresponds to the β -UCNPs and the second one to the anatase phase of the TiO_2 .

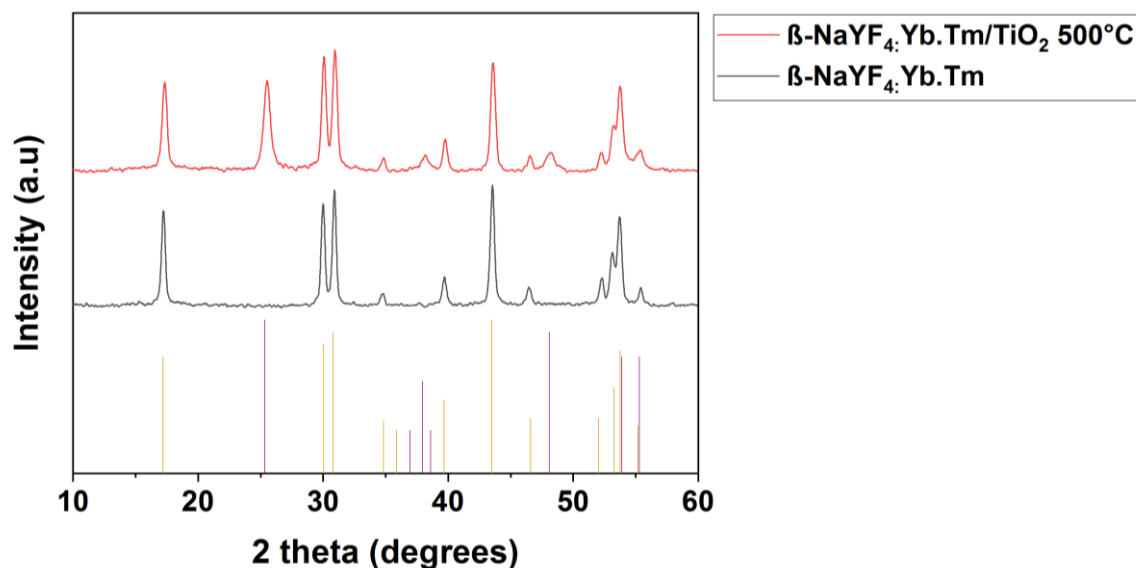


Figure 93. XRD patterns of β -UCNPs before and after the epitaxial growth of TiO_2 shell. Measurements were acquired using a Cu K- α source. Reference lines in yellow and purple correspond to β -UCNPs (PDF Card No.:00-016-0334) and TiO_2 anatase (PDF Card No.:00-002-0387), respectively.

EDX was then performed to characterize the composition of the sample. The spectra from **Figure 94** reveals the existence of Na, Y, F, Ti, O, Yb, and Tm apart from the signals related to the carbon-coated grids.

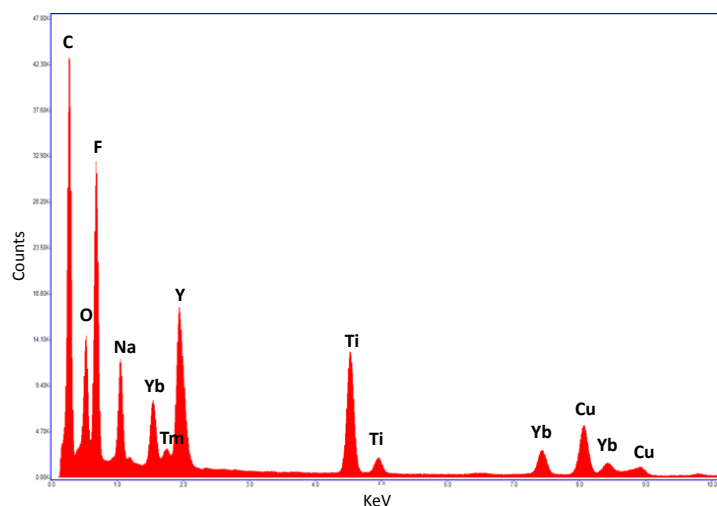


Figure 94. EDX of β -NaYF₄: Yb³⁺(20%), Tm³⁺(0.5%) UCNPs coated with TiO₂ on a carbon-film coated copper grid. The peaks labelled Na, Y, F, Yb and Tm originate from the core, while that of Ti and O come from the shell. The elements C and Cu are from the carbon-film coated copper grid used in the EDX characterizations.

Elemental mapping was used to further characterize the sample, proving that the particles were coated by TiO₂. The results are shown in **Figure 95**. Elemental mapping was consistent with EDX characterization.

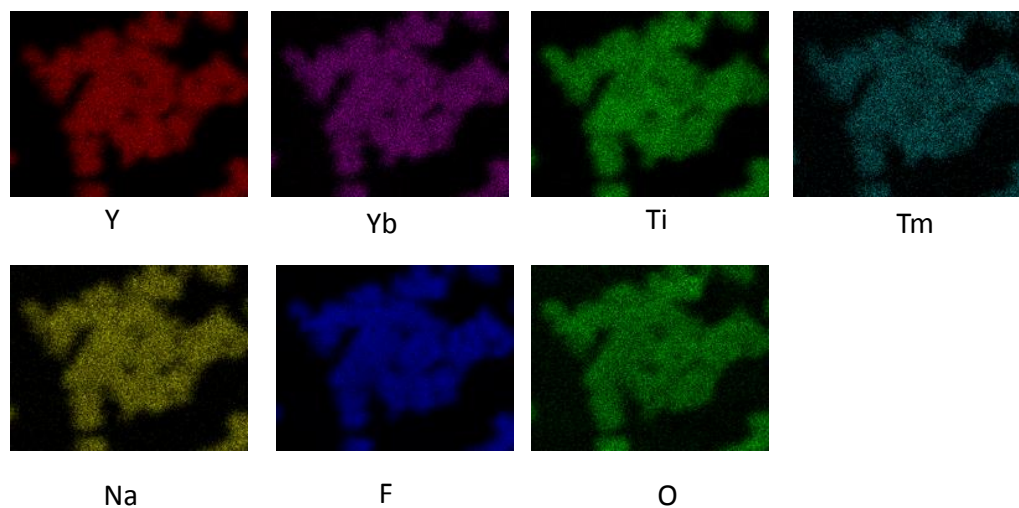


Figure 95. Elemental mapping of β -NaYF₄: Yb³⁺(20%), Tm³⁺(0.5%) UCNPs coated with TiO₂.

UV-vis spectra of the samples are shown in **Figure 96**, indicating no absorbance of the β -UCNPs in the UV region prior to titania coating. The absorbance spectrum of the sample coated with TiO₂, shows a peak at 400 nm corresponding to its bandgap absorption of ~ 3.2 eV (~ 380 nm).

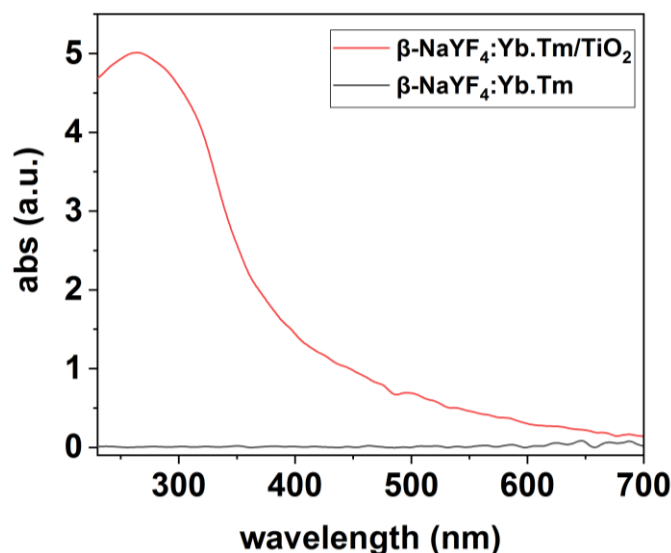


Figure 96. UV-vis absorbance of β -UCNPs with and without titania coating. Black line from the spectra represents the β -UCNPs before any coating, and red line represents the spectra of the particles coated with titania (β -UCNPs/ TiO_2 -anatase).

Then, we compared how the luminescence properties were affected by the TiO_2 coating. OA coated $\text{NaYF}_4: \text{Yb}^{3+}(20\%), \text{Tm}^{3+}(0.5\%)$ and $\text{NaYF}_4: \text{Yb}^{3+}(20\%), \text{Tm}^{3+}(0.5\%)/\text{TiO}_2$ samples were excited by a 980 nm CW laser (350 mW) using the set-up from **Figure 16**. OA coated $\beta\text{-NaYF}_4: \text{Yb}^{3+}(20\%), \text{Tm}^{3+}(0.5\%)$ UCNPs were dispersed in hexane and $\beta\text{-NaYF}_4: \text{Yb}^{3+}(20\%), \text{Tm}^{3+}(0.5\%)/\text{TiO}_2$ in Milli-Q water. **Figure 97** shows the UC luminescence spectra for both of the samples normalized in respect to the 476 nm peak.

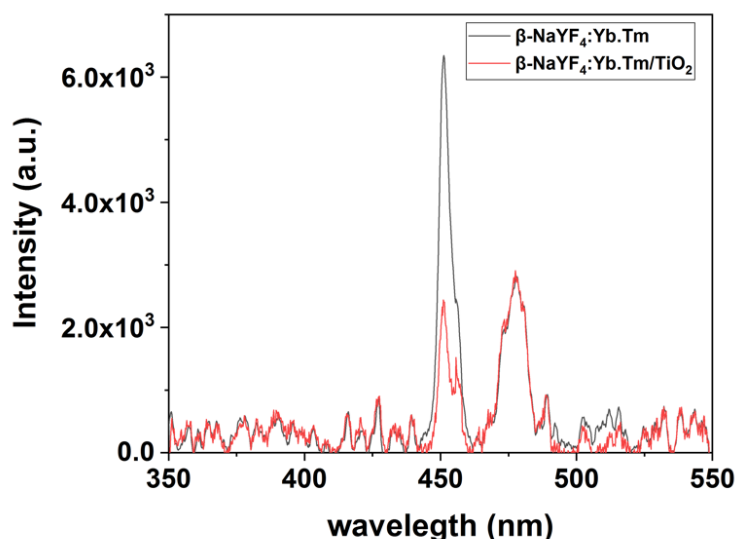


Figure 97. Emission spectra of β -UCNPs before and after coating the TiO_2 . Black line from the spectra represents the β -UCNPs before coating, and red line represents the spectra of the β -UCNPs after titania coating (980 nm laser excitation, 350 mW and 500 ms).

Under a 980 nm laser excitation, NaYF₄ co-doped with Yb³⁺ and Tm³⁺ ions emitted blue light. The two strong peaks centered at 452 nm and 476 nm corresponds to the ¹D₂ → ³F₄ and ¹G₄ → ³H₆ transitions of Tm³⁺, respectively. Once TiO₂ was coated around the surface of β-UCNPs, notable spectral differences were observed. The emission peak centered at 452 nm luminescence decreased significantly, suggesting that the TiO₂ can efficiently harvest the UC luminescence. Although we could not confirm and record the UV spectra at lower wavelengths with the current set-up, it is well known that Tm³⁺ ions also emit in the UV range (291 nm, 347 nm and 362 nm) assigned to the ¹I₆ → ³H₆, ¹I₆ → ³F₄ and ¹D₂ → ³H₆ transitions of Tm³⁺, respectively.³⁴⁰

Based on the results from **Figure 97** and **Figure 96**, we hypothesize that the UV energy generated from the β-UCNPs should be (fully or partially) absorbed by TiO₂ coating. However further characterization in the UV area should be carried out to clarify this hypothesis.

4.4.2 Photodegradation of different dyes using UCNPs@TiO₂

In previous work, Tang et al.¹⁸¹ proposed that the UV photon energy generated from the UC process of UCNPs is absorbed by the anatase TiO₂ shell *via* an energy transfer between the two materials. As long as UCNPs and TiO₂ are in close proximity and therefore Förster resonance energy transfer (FRET) is efficient, the energy can be transferred from the excited states of Tm³⁺ ions to TiO₂. The Förster mechanism can be defined as a dipole–dipole resonance interaction between the donor and acceptor, which requires spectral overlap between absorption of the acceptor and emission of the donor. The efficiency of the FRET process depends on the inverse sixth power of the distance between the donor and acceptor.

³⁴¹

The process of photodegradation on β-UCNPs/TiO₂ starts when the TiO₂ coating absorbs a UV radiation of energy equal or higher than its theoretical band gap (3.2 eV for anatase; 3.0 eV for rutile).^{181,342} This leads to the formation of free electrons (e⁻) in the conduction band (CB) and holes (h⁺) in the semiconductor valence band (VB) (see **Figure 98**). The energized electrons can either recombine with the holes (and then dissipate the absorbed energy as heat) or the electron-hole pairs can participate in redox reactions.³⁴² Then, h⁺ have a strong oxidizing capability to directly decolorize the dye solution. On the other hand, the generated e⁻ can capture O₂ molecules and produce superoxide (O₂⁻), serving as a reactive species in

the system. After successive free radical attack and fragmentation, most organics such as dyes are mineralized to water, carbon dioxide and mineral acids.

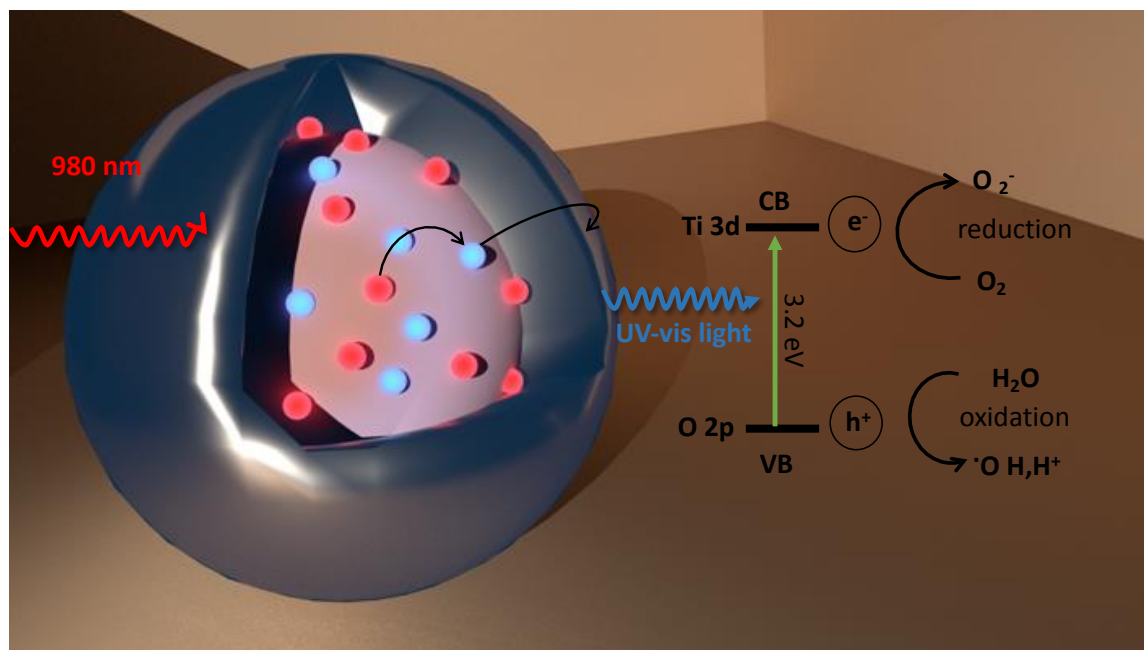


Figure 98. Schematic illustration of the working mechanism for the hybrid β -UCNPs/TiO₂. The β -UCNPs nuclei (in pink) absorbs the 980 nm light (red wiggled arrows) where UC is realized. Subsequently the β -UCNPs transfer the energy to the outer layer of the TiO₂. The blue arrow represents the visible energy emitted by the β -UCNPs.

Photocatalytic performance of the as prepared β -NaYF₄: Yb³⁺(20%), Tm³⁺(0.5%) UCNPs coated with TiO₂ were evaluated considering the degradation of different dyes under different irradiation bands of a Xe lamp: ultra violet (UV), near infrared (NIR) and upon unfiltered Xenon lamp (300-2500 nm). Digital images of the solar simulator can be seen in **Figure 22**. The UV irradiation band was obtained using a Glass UV-Passing Filter, 240 - 395 nm, and the NIR band was obtained with a 780 nm Longpass filter.

In a typical experiment, a solution was prepared by mixing the annealed β -UCNPs/TiO₂ (1 mg in 1 ml in Milli-Q water) together with a dye solution (80 μ M in 1 ml in Milli-Q water). The reaction mixture was magnetically stirred for 2 hours before photocatalytic measurements at room temperature in the dark. Then, the solution was transferred to a solar simulator station coupled with a digital timer and the reaction was conducted under vigorous agitation to ensure uniform distribution in the medium. The suspension was taken out at appropriate time intervals of 0, 2, 4, 6, 8 and 10 min and centrifuged to remove the powders before measuring the concentration of the dye by UV-Vis spectroscopy.

Chapter 4

Absorbance measurements of dyes and catalyst were carried out using a Denovix DS-11+spectrophotometer. The change in the dye absorbance was monitored using the transmission module scanning at wavelengths from 200 nm – 800 nm.

All experiments were carried out at natural pH and room temperature. The photodegradation was evaluated according to the C/C_0 value for the different dyes, where, C_0 (mg/ml) is the initial concentration of dye solution and C is the concentration of the dye after a specific irradiation time.³⁴³ Both C and C_0 are proportional to the measured absorbance according to the Beer-Lambert Law:

$$A = \epsilon bc \quad (15)$$

where, c is the concentration of the solution, b is the pathlength through the solution and ϵ is the molar absorptivity.

We chose the following commercially available dyes as candidates to study photodegradation activity: Methylene blue (MB), Rhodamine B (RB), Resazurin (Rz) and DCPIP. **Table 17** gathers relevant information about the dyes. It can be seen from their molecular structure that the nature of these dyes is quite different from each other; MB and RB are cationic dyes while Rz and DCPIP are anionic dyes. The absorbance and corresponding ϵ parameter for each of the dyes were: 664 nm and 74028 cm^{-1}/M for MB, 543 nm and 106000 cm^{-1}/M for RB, 602 nm and 35000 cm^{-1}/M for Rz, and 610 nm and 21000 cm^{-1}/M for DCPIP. The volume of solution used for each analysis was 1 ml contained in polystyrene cuvettes with a 10 mm window and a spectral range of 340 nm – 800 nm. The uncertainty of the " C/C_0 " value were obtained according to the calculations in **Appendix G**.

Table 17. List of dyes used in our experiments, including name (IUPAC), max λ_{abs} and molecular structure of Methylene blue (MB), Rhodamine B (RB), Resazurin (Rz) and 2,6-dichlorophenolindophenol (DCPIP).

Dye	IUPAC Name	λ_{abs} max (nm)	Molecular structure
Methylene blue	3,7-Bis(dimethylamino)phenothiazin-5-ium chloride	664	
Rhodamine B	[9-(2-carboxyphenyl)-6-diethylamino-3-xanthenylidene]-diethylammonium chloride	543	
Resazurin	7-hydroxy-10-oxidophenoxazin-10-ium-3-one	602	
DCPIP	2,6-Dichloro-N-(4-hydroxyphenyl)-1,4-benzoquinoneimine sodium salt	610	

4.4.2.1 Dye stability in the presence of light irradiation

Four solutions of pure dyes (MB, RB, Rz and DCPIP) were prepared in glass tubes with a similar concentration of 40 μM and natural pH. The samples were irradiated one by one using a solar simulator equipped with a full Xenon lamp (300-2500 nm). While conducting experiments, the tubes were kept closed to avoid evaporation of water during illumination. Aliquots were taken at an appropriate time interval of 0, 5, 10, 15 and 20 min for UV-Vis spectroscopy.

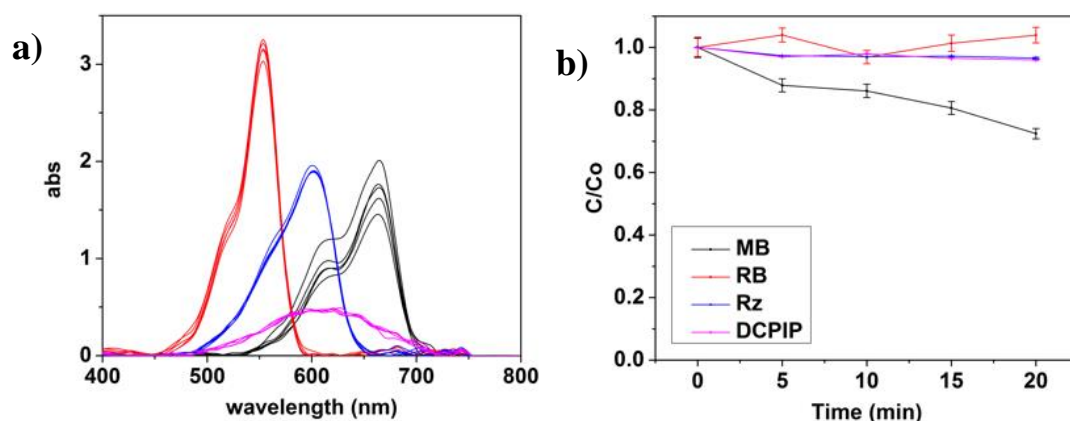


Figure 99. (a) Comparison of the absorbance spectra and (b) changes in the concentration (C/C_0) as a function of the time of different dyes. Samples were irradiated with the full spectrum source of a Xenon lamp (300-2500 nm).

Figure 99a shows the absorbance spectra of the four different dyes, while **Figure 99b** shows changes in the concentration (C/C_0) as a function of the irradiation time under full irradiation source (300-2500 nm). It can be seen from **Figure 99b**, that the absorption intensity of MB at 664 nm gradually decreased with the increase in the irradiation time (black line), leading to 27% degradation in 20 min. The photodegradation of DCPIP (pink line) and Rz (blue line) was minimal. We observed that the concentration remained constant over the time and only 3% of the dyes were degraded. It was found that the concentration of RB at 543 nm fluctuated sharply. This trend (red line) was accompanied by large error bars that imply huge instability and a poor reproducibility in the measurements.

This quick approach allowed us to observe how different dyes behave on the presence of the light. From the photoirradiation, we concluded that Rz and DCPIP are highly photostable dyes. On the other hand, it seems that MB is a dye with high sensitivity to the light; and RB has very little stability.

4.4.2.2 Dye adsorption/desorption equilibrium reactions

As the dye molecules come into contact with the photocatalyst, the molecules adsorb to and desorb from the surface of the catalyst until an equilibrium is established.³⁴⁴ The amount of adsorption of dye to the powdered photocatalyst surface prior to irradiation was monitored by comparing the concentration of dye after different times in the presence of the β -NaYF₄: Yb³⁺(20%), Tm³⁺(0.5%) /TiO₂ in the dark.

Four fresh samples were prepared by mixing a dye solution of known concentration (MB, RB, Rz and DCPIP) with a certain mass of β -NaYF₄: Yb³⁺(20%), Tm³⁺(0.5%) /TiO₂. In detail, the concentrations of β -UCNPs/TiO₂ and the dye solutions were 0.5 mg/ml and 40 μ M, respectively. All samples were prepared in glass containers at ambient pH, room temperature and similar concentrations. All the experiments were performed in the dark, so that the change in the concentration of the dyes were attributed only because of adsorption on the catalyst surface. At given time intervals of 30 min, 60 min and 120 min, aliquots were taken for UV measurements. In all the cases, aliquots were centrifuged to remove the catalyst before UV measurement.

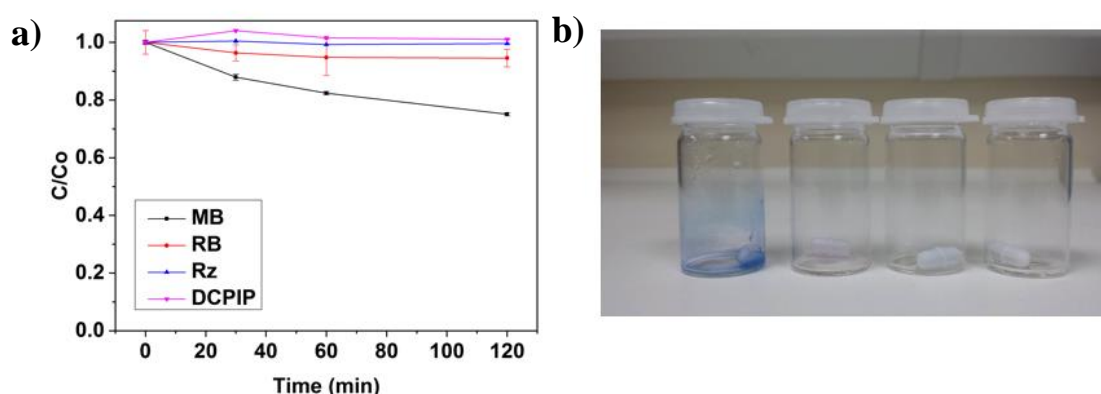


Figure 100. (a) Degradation of four different dyes in the presence of same initial concentration of β -UCNPs/TiO₂ under dark conditions. (b) Digital photograph of glass tubes after treatment with β -UCNPs/TiO₂. From left to right glass tube of β -UCNPs/TiO₂ with MB, RB, Rz and DCPIP.

Figure 100a shows the dark adsorption for the different dyes in the presence of β -UCNPs/TiO₂ and natural pH. The C/C_0 concentrations of RB, Rz and DCPIP remained constant over the time, however it was observed a gradual degradation of the MB which did not get stabilised after 2 hours. Adsorption study of MB on TiO₂ has been already reported in literature.^{345–347} In our case, the decomposition of MB was attributed to the adsorption of MB molecules on the surface of the β -UCNPs/TiO₂, but also to the adsorption phenomena of the dye with the glass surface.³⁴⁸ The latter phenomenon was deduced from the stained glass visible in **Figure 100b**.

Overall, our experiments revealed that RB was very unstable and had a very sensitive absorbance tendency. RB is a dye with a very rigid structure compared to the others. It does not degrade itself without any catalyst or semiconductor in visible light or even in UV light.

We speculate that the reason of the high instability may be the formation of RB dye aggregates, occurring at higher concentrations as a consequence of the chemical interactions that the molecules establish among themselves and with their surrounding environment.^{349,350} Among all of the proposed dyes, DCPIP and Rz were found to have the highest stability in the presence and absence of β -UCNPs/TiO₂.

4.4.2.3 Photocatalytic degradation of DCPIP under full solar radiation, IR and UV radiation

Andrew Mills's group developed an intelligent photocatalyst indicator ink to identify and measure the photocatalytic activities of thin semiconductor films.³⁵¹ This ink was specially designed for thin titania films and most self-cleaning products (e.g. glasses, tiles and paints) and permits a more rapid method of assessing photocatalytic activity. When in contact with TiO₂, the indicator ink changes colour upon UV illumination.

A general photocatalyst indicator ink is composed of a redox dye, glycerol and an aqueous solution of hydroxyethyl cellulose (HEC).³⁵² Glycerol acts as a sacrificial electron donor (SED); where the glycerol molecules act as "hole traps," preventing recombination of the photogenerated electron-hole pair by undergoing oxidation. Therefore, any of the photogenerated electrons are able to reduce the dye molecules in the ink when in contact with the photocatalyst. Overall, this ink functions *via* a photo-reductive mechanism in which the generated holes react irreversibly with the sacrificial electron donor (SED) (see **Figure 101**).

The general mechanism starts with the illumination of TiO₂ by UV light and the production of an electron-hole pair ($e^- - h^+$).^{352,353} Then, the hole oxidises the SED to SED_{ox}. The electron reduces the dye from its oxidised form, D_{ox}, to its reduced equivalent, D_{red}. It should be clarified that if D_{red} is oxygen sensitive, its undesirable oxidation (from D_{red} to D_{ox}) can occur.^{352,353}

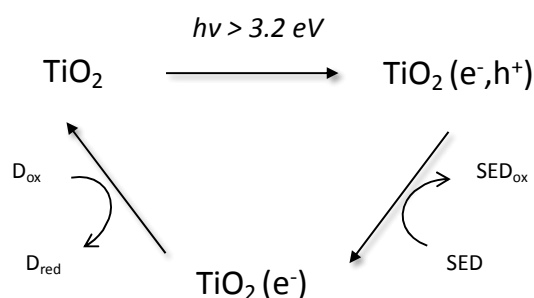


Figure 101. Schematic illustration of the mechanism by which a typical photocatalyst indicator ink works.

In this section we report the behaviour of two photocatalyst indicator inks, based on the redox dyes of DCPIP and Rz when mixing with the as-prepared β -NaYF₄: Yb³⁺(20%), Tm³⁺(0.5%) /TiO₂. DCPIP and Rz inks were prepared by mixing the corresponding dyes with glycerol following the experimental work of Andrew Mills et al.³⁵³ See the detailed procedure in **Section 2.3.9.4**. The concentration of β -UCNPs/TiO₂ and the dye inks solution were fixed to 0.5 mg/ml and 40 μ M, respectively. The overall process involving the glycerol with DCPIP is as follows:



When using this indicator ink, DCPIP is D_{ox}, leuco-DCPIP is D_{red}, and the reduction process (D_{ox} → D_{red}) seen from **Figure 101** is accompanied by a colour change from blue to colourless. The mechanism with the corresponding molecular structures of reduction for DCPIP is illustrated in **Figure 102**.

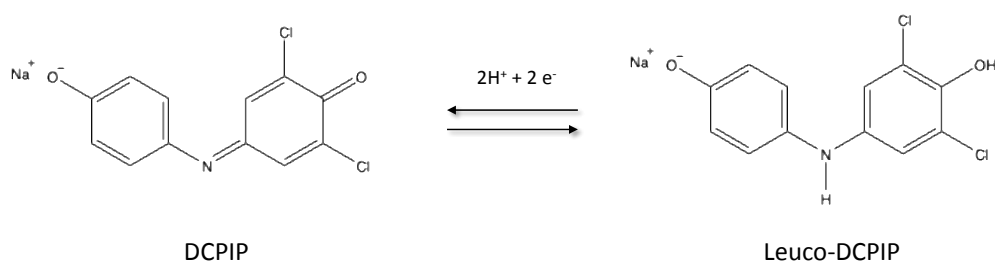


Figure 102. The structures of the sodium salt of DCPIP (left) and its reduced product, Leuco-DCPIP.

Two samples were prepared and measured under identical conditions. The first sample contained DCPIP with glycerol while the second one just DCPIP in an aqueous solution. As illustrated by the results in **Figure 103**, the DCPIP ink of both samples rapidly changed

colour from blue to colourless upon unfiltered Xenon lamp in the presence of β -UCNPs/ TiO_2 over a period of 10 min.

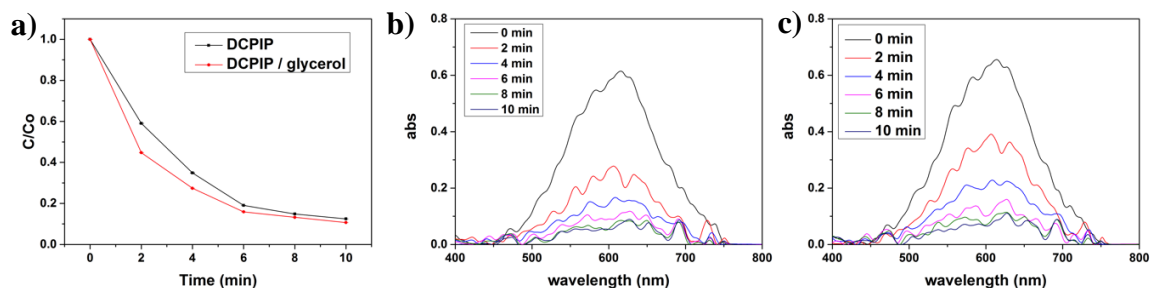


Figure 103. (a) Effect of glycerol on the photocatalytic activity of the β -UCNPs/ TiO_2 using DCPIP under unfiltered Xenon lamp radiation. (b) and (c) are the absorbance spectra of the DCPIP with and without glycerol, respectively as a function of the irradiation time.

It has been reported for TiO_2 , that when the ink is prepared without glycerol and irradiated with UV light there is no observed reduction of the dye.³⁵³ Removing the SED from the DCIP ink results in electron-hole recombination becoming the predominant process. In our experiments, it can be observed that the kinetics in the degradation of the DCPIP was slightly different but comparable for both samples. We hypothesise that in our experiments, only when the glycerol was present, the DCPIP molecules in the ink reduced to their respective leuco-DCPIP form. With no glycerol present, we believe that the dye molecules followed a different oxidative degradation mechanism based on hydroxyl radicals.³⁵⁴

The general reaction pathways for an oxidative degradation involve the formation of phenolic compounds as the primary intermediates. The formation of these intermediates are followed by the appearance of aromatic compounds such as hydroquinone, catechol and benzoquinone and then converted to acetic acid due to the opening of the benzene ring, before completely mineralized to CO_2 and H_2O .³⁴³ The proposed reaction pathways for the oxidative mechanism of DCPIP without glycerol is schematically shown in **Figure 104**.

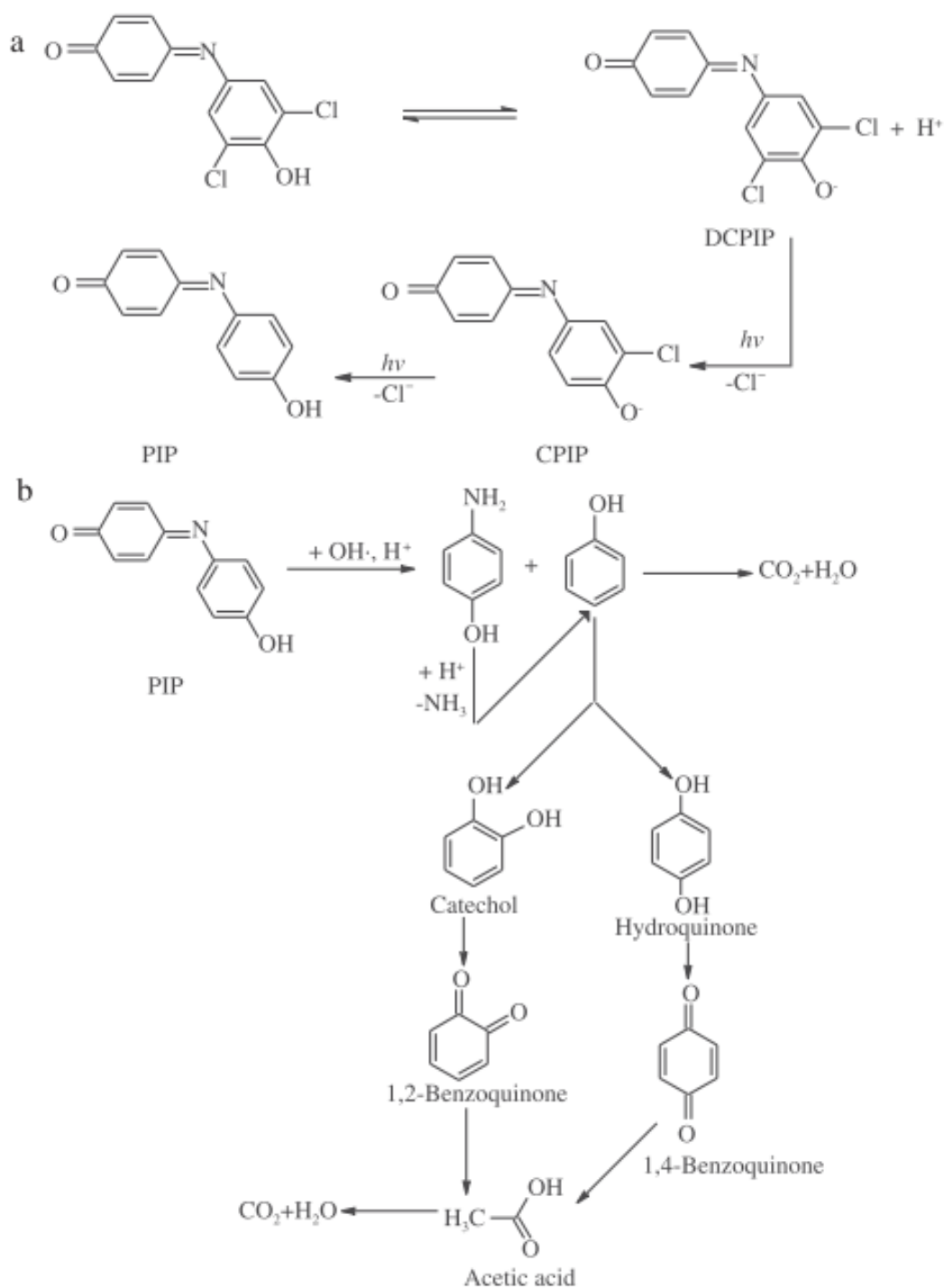


Figure 104. Proposed photocatalytic degradation pathways of DCPIP dye under the UV irradiation with no glycerol. (a) dechlorination and (b) intermediate. Image taken from H.A. Hamad's work.³⁴³

Photocatalytic activities were compared between the following four groups: just DCPIP/glycerol solution (no catalysis), bare β -UCNPs, TiO_2 Degussa (P25), and the as-prepared β -UCNPs/ TiO_2 . The concentrations of β -UCNPs, P25 and β -UCNPs/ TiO_2 were fixed to 0.5 mg/ml and the DCPIP/glycerol dye on solution to 40 μM .

The photocatalytic activity was evaluated for different irradiation bands of the Xenon lamp. The changes in the concentration of DCPIP/glycerol are summarized in **Figure 105**. **Figure 105a** shows the change in the concentration of the dye catalysed by the different samples under unfiltered Xenon lamp radiation (300-2500 nm) as function of the irradiation time. It can be observed that 100% of the dye was degraded with P25 and 83% by using β -UCNPs/ TiO_2 within 10 min.

To further evaluate this phenomenon, photocatalytic degradation activities for the same samples were tested under NIR and UV separately.

Using NIR light (780-2500 nm), the sample of β -UCNPs/ TiO_2 decolorized slightly the DCPIP/glycerol solution (13%) along with increasing irradiation time. Considering that the solutions of bare β -UCNPs and just the dye did not show any photocatalytic effect, this phenomenon was associated to the TiO_2 shell, indicating that UV photon energy generated from the β -UCNPs was absorbed by the TiO_2 shell via an energy transfer between them.

The activity of the sample was also evaluated under UV-visible light. (350-780 nm). The sample of β -UCNPs/ TiO_2 degraded the dye solution by 78% with respect to its initial concentration. This result implies that the TiO_2 shell can be also activated as TiO_2 powder and it is the main cause of the whole degradation of the DCPIP/glycerol system.

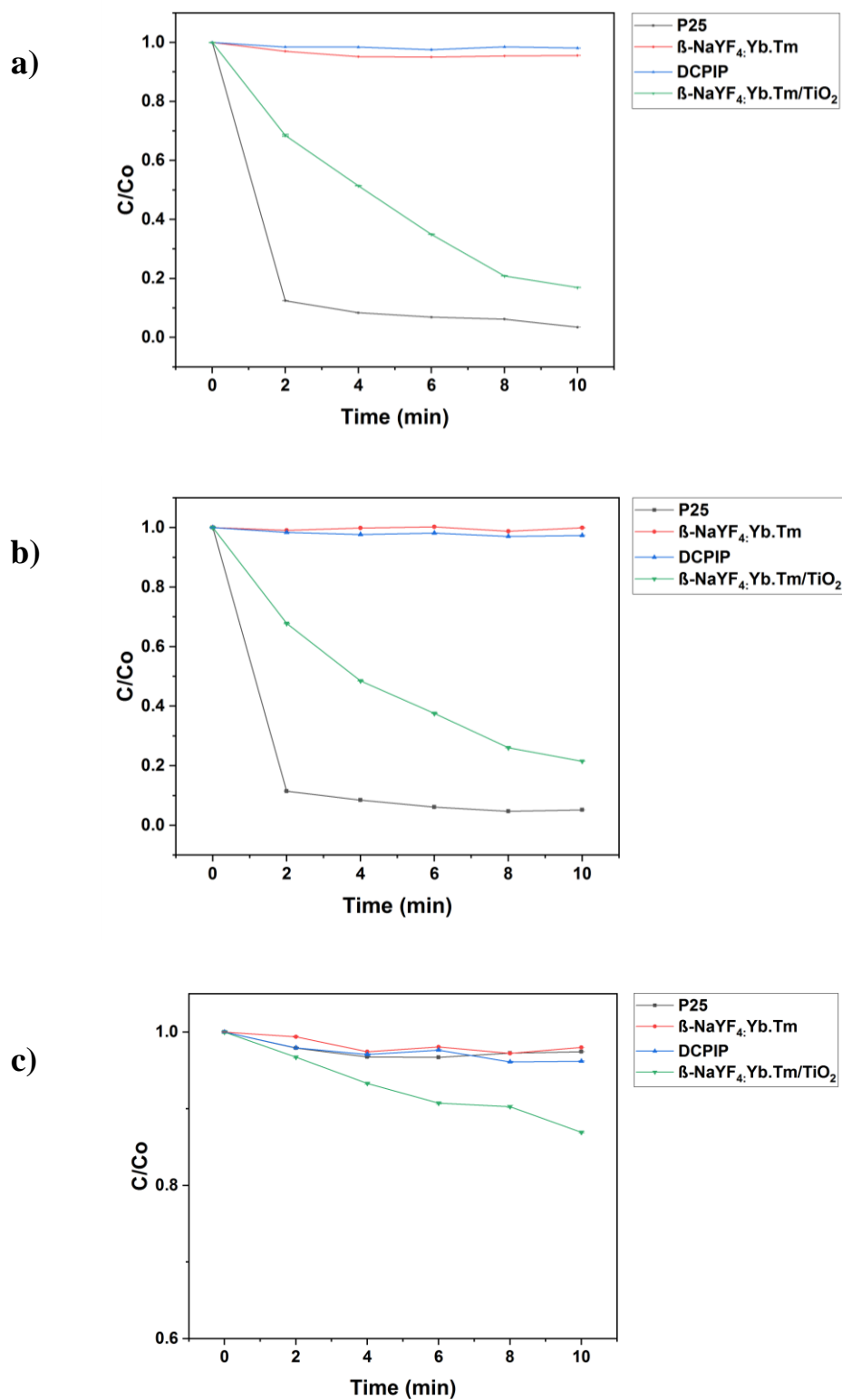
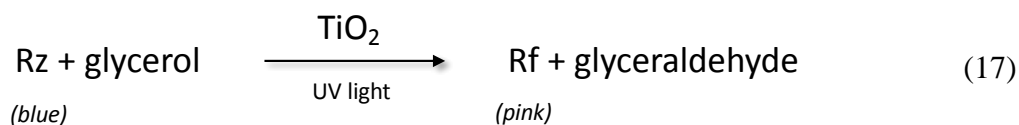


Figure 105. Comparison of samples under different irradiation bands using DCPIP/glycerol and β -UCNPs/TiO₂ as catalysts. (a) Full spectra of a Xenon lamp, (b) UV and (c) NIR.

4.4.2.4 Photocatalytic degradation of Resazurin under full, IR and UV radiation

In a similar way to **Section 4.4.2.3**, we have also used a redox ink with resazurin (Rz) and glycerol. The Rz ink has the feature that it is blue before UV irradiation, but pink, due to the photocatalyzed irreversible reduction to the Resorufin (Rf) dye.²²⁷ The overall process involving the glycerol with Rz is as follows:



A schematic illustration of the key processes can be seen in **Figure 106**.

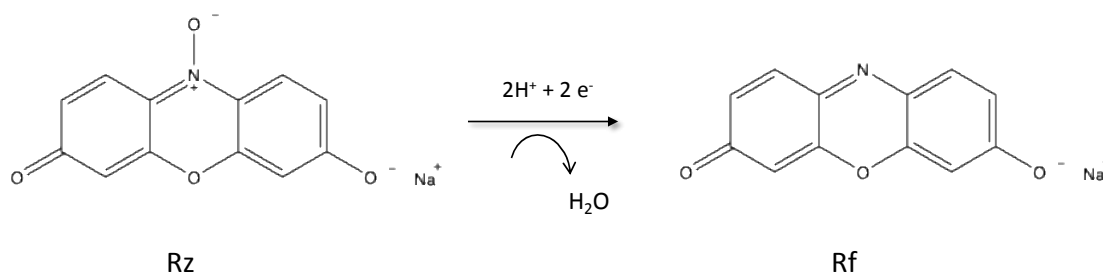


Figure 106. Photo-reduction of resazurin (Rz) to resorufin (Rf) by TiO₂.

The photocatalytic activity of the as-prepared β -NaYF₄: Yb³⁺(20%), Tm³⁺(0.5%) /TiO₂ was evaluated with the Rz ink using unfiltered Xenon lamp radiation (300-2500 nm). Two samples were again freshly prepared and measured under identical conditions. The first sample contained a Rz ink with glycerol while the second one just Rz in the aqueous solution. In both cases, the samples changed colour with increasing radiation times, but only when using glycerol, the sample turned into a bright pink colour, indicating the formation of the Rf form. In the case of no glycerol, the sample changed from blue to a faint pink colour.

From **Figure 107a** it can be observed that the kinetic followed the same tend; however, **Figure 107b** and **c** revealed spectral changes in the kinetic for the dye with and without glycerol when they were irradiated with the Xenon lamp. It was visible that only when glycerol was present, the reduced form Rf was formed.

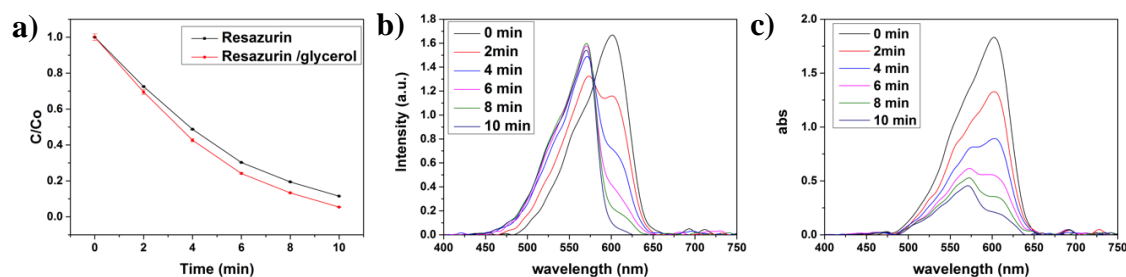


Figure 107. (a) Effect of glycerol on the photocatalytic activity of the β -UCNPs/TiO₂ using Rz under unfiltered Xenon lamp radiation. (b) and (c) are the absorbance spectra of the Rz with and without glycerol, respectively as a function of the irradiation time.

For the case of Rz with no glycerol, and thus with no sacrificial electron donor, we propose a photobleaching of the dye, *via* a photooxidative mechanism, in which the dye is oxidatively bleached by photogenerated hydroxyl radicals while the photogenerated electrons react with oxygen to produce superoxide, another possible source of hydroxyl radicals.³⁵⁵

The photocatalytic activities were also compared between the following four groups: just Rz/glycerol dye (no catalysis), bare β -UCNPs, P25, and the as-prepared β -UCNPs/TiO₂. The concentration of β -UCNPs, P25 and β -UCNPs/TiO₂ were fixed to 0.5 mg/ml and the Rz/glycerol dye on solution to 40 μ M.

The photocatalytic activity was evaluated for different irradiation bands of a Xenon lamp. The changes in the concentration of Rz/glycerol are summarized in **Figure 108**. **Figure 108a** shows the change in the concentration of the dye catalysed by the different samples under unfiltered Xenon lamp (300-2500 nm) as function of the irradiation time. It can be observed that 100% of the dye was degraded with P25 and 89% by using β -UCNPs/TiO₂ within 10 min.

To further evaluate this phenomenon, photocatalytic degradation activities for the same samples were tested under NIR and UV separately. Using NIR light (780-2500 nm), the sample of β -UCNPs/TiO₂ effectively decolorized the Rz/glycerol solution (42%) along with increasing irradiation time, showing that this photocatalyst can be driven by NIR. Considering that the solutions of bare β -UCNPs and the just dye ones did not show any photocatalytic effect, this phenomenon was associated one more time to the TiO₂ shell. β -UCNPs converted the NIR to UV light and the TiO₂ acted as the catalytic centre by absorbing the UV light.

The activity of the sample was also evaluated under UV-vis radiation. Under (350-780 nm), the sample of β -UCNPs/TiO₂ degraded the dye solution in a 53% with respect to its initial concentration. This result implies that TiO₂ shell can be also activated as TiO₂ powder.

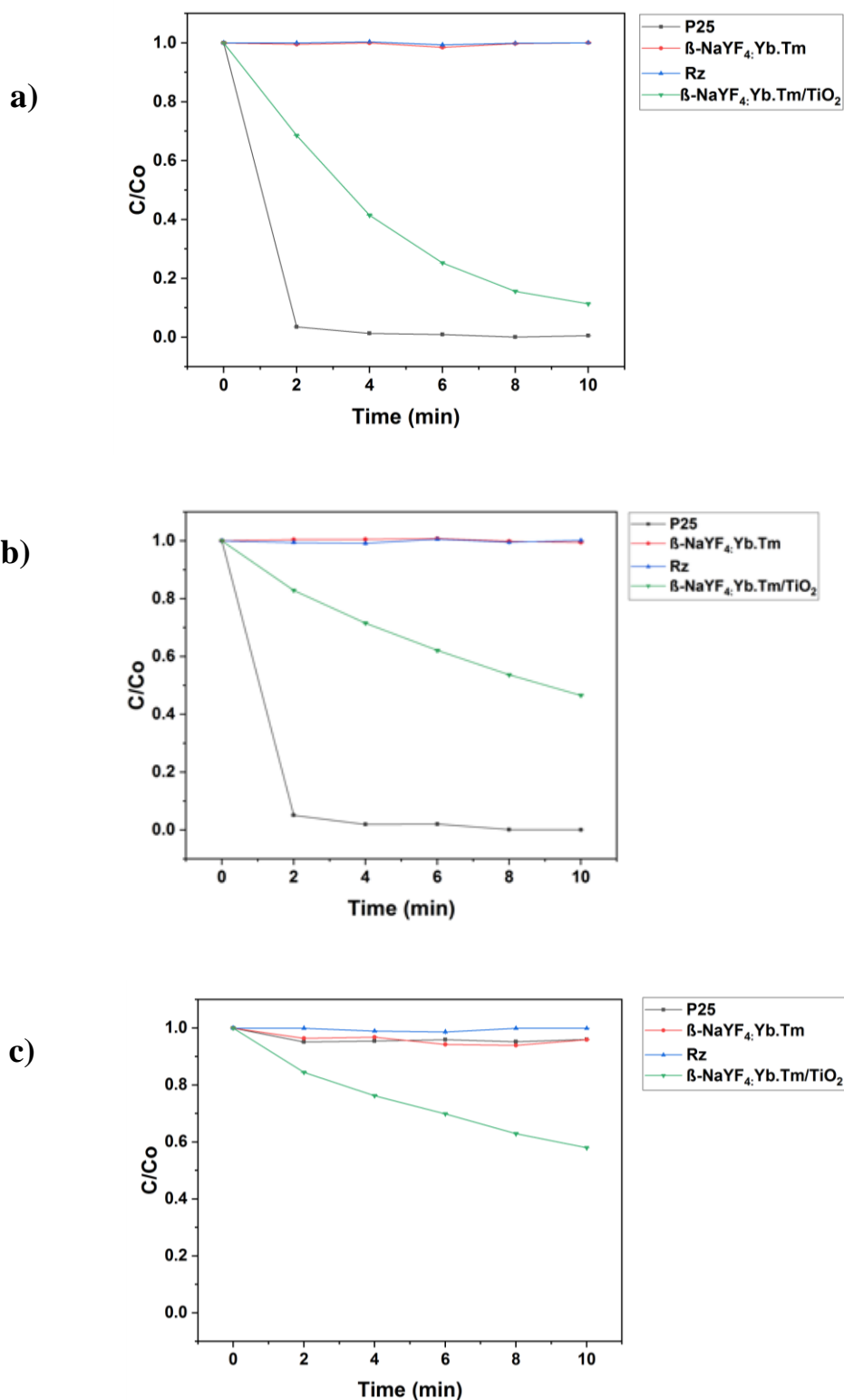


Figure 108. Comparison of samples under different irradiation bands using Rz/glycerol and β -UCNPs/TiO₂ as catalysts. (a) Full spectra of a Xenon lamp, (b) UV and (c) NIR.

It should be noted the lack of molecular weight information for β -UCNPs/TiO₂ was a considerable shortcoming in this work. A precise quantification of their concentration would be highly beneficial for the comparison of the study with TiO₂ (P25).

Overall, we have observed, that two types of photocatalyst indicator inks, based on a redox dye, can be used to assess the photocatalytic activity of β -UCNPs/TiO₂ *via* a NIR and UV-driven, accompanied by a colour change. We observed that with this system as catalyst and under the same conditions, Rz exhibited a higher degradation compared to DCPIP. Still further investigations are necessary to find out the causes that provoked differences in the behaviour for both of dyes.

4.4.2.5 Effect of β -UCNPs/TiO₂ dosage on the photocatalytic activities

In this section, the effect of β -UCNPs/TiO₂ loading on the degradation of Rz and DCPIP is discussed. A kinetic study of the reactions is considered and the kinetic parameters are determined in detail. For that, we applied the pseudo first-order model, which has been widely used to evaluate the photocatalytic degradation rate. The degradation rate was calculated by plotting the $\ln(C/C_0)$ versus the irradiation time, according to the following equation:

$$\ln\left(\frac{C}{C_0}\right) = -k_{app}t \quad (18)$$

Where k_{app} is the apparent first-order rate constant of the photocatalytic degradation and t is the reaction time.

Figure 109 shows the effect of the increasing β -UCNPs/TiO₂ loading in the degradation of DCPIP and Rz, respectively as function of the time with a constant concentration of dye.

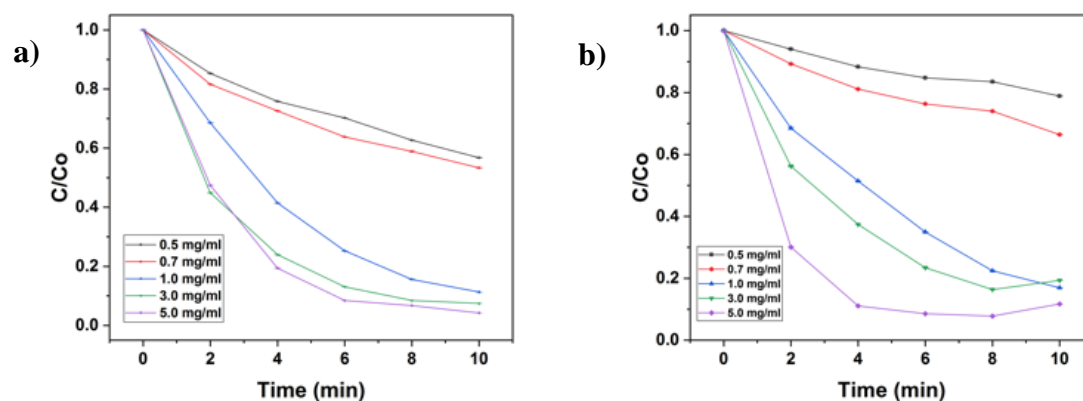


Figure 109. Effect of the β -UCNPs/TiO₂ dosage on the (a) Rz and (b) DCPIP photodegradation tested under full spectrum of a Xenon lamp.

Figure 110 represents the photocatalytic degradation $\ln(C/C_0)$ as function of the irradiation time. It was observed that initial slopes of the curves rapidly increased by increasing catalyst loading from 0.5 mg/ml to 5.0 mg/ml, so that reaction rates k_{app} were enhanced as shown in **Table 18** and **Table 19**.

This is due to the increase in the number of photons absorbed by the TiO₂, leading to excitation of more electrons from the valence to the conductor band.³⁵⁶

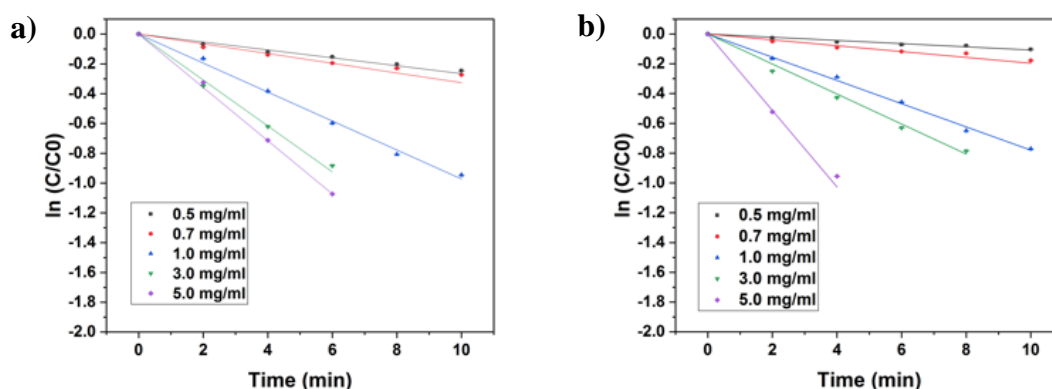


Figure 110. Comparison of photocatalytic activity for different β -UCNPs/TiO₂ dosage treated with (a) Rz and (b) DCPIP after 10 min of photoirradiation with full spectrum of a Xenon lamp.

Table 18. Kinetic parameters of photocatalytic degradation of DCPIP at varying the β -UCNPs/TiO₂ concentration.

Dye indicator	β -UCNPs/TiO ₂ (mg/ml)	K_{app} (min ⁻¹)	R^2
DCPIP	0.5	0.0096	0.950
	0.7	0.0179	0.949
	1.0	0.0781	0.998
	3.0	0.0972	0.994
	5.0	0.2560	0.997

Table 19. Kinetic parameters of photocatalytic degradation of Rz at varying the β -UCNPs/TiO₂ concentration.

Dye indicator	β -UCNPs/TiO ₂ (mg/ml)	K_{app} (min ⁻¹)	R^2
Rz	0.5	0.0265	0.990
	0.7	0.0326	0.985
	1.0	0.0973	0.999
	3.0	0.1541	0.996
	5.0	0.179	0.999

In general, it has been shown that above a certain level, no further molecules to react are available, and the photodegradation efficiency can be reduced. When the loading concentration is high, aggregation and sedimentation of particles would take place, and the photocatalytic efficiency would be reduced.³⁵⁷ In our work, the highest efficiency we were able to get was $k_{app} = 0.256$ (min⁻¹) at a concentration of 5 mg/ml and using DCPIP/glycerol as indicator. With the working loading of catalyst, we did not observe the shielding effect of the β -UCNPs/TiO₂ for any of the dyes. As we did not test the experiments with higher concentrations, it is worth noting that this is probably not the optimal condition.

4.4.2.6 Recyclability of the samples

We also investigated the reusability of the as-prepared β -UCNPs/TiO₂ photocatalyst. The particles were recycled from the solution after photocatalysis by centrifugation, washed with Milli-Q water and dried before the next use.

As shown in **Figure 111**, the samples had a considerably good recyclability. The efficiency of the photocatalytic activity for both Rz and DCPIP, were above 50% after the second round. Even after three cycles, the samples were still able to decompose ~30% of the dyes under full irradiation.

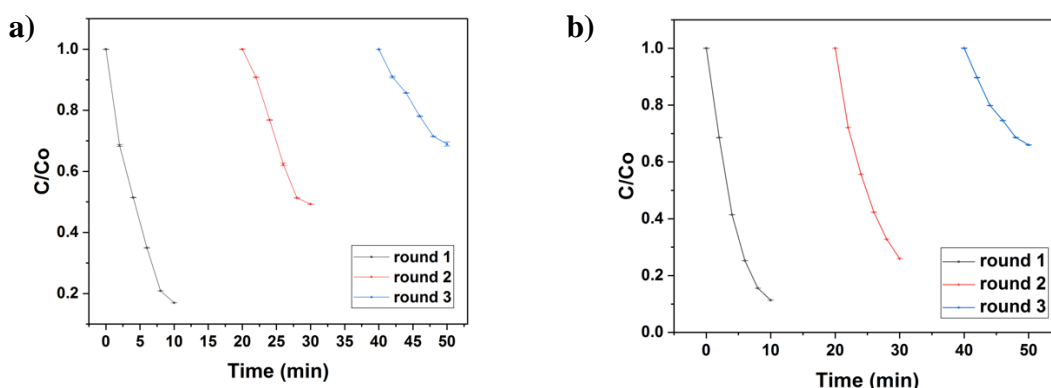


Figure 111. Recyclability of β -UCNPs/TiO₂ with (a) DCPIP/glycerol and (b) Rz/glycerol under full radiation. Using an initial concentration of 1 mg/ml of material.

4.4.3 Effect of Cobalt as dopant on the photocatalytic activities of the samples

TiO₂ modified by noble metal deposition has been widely proved to be one of the best systems in photocatalysis; mainly for its ability to suppress charge recombination, and thus to facilitate the separation of electron–hole pairs in TiO₂.^{331,358,359} This is mainly because the Fermi level of the noble metal is lower in energy than the conduction band of TiO₂.³⁶⁰ The photo promoted electrons can efficiently migrate to the metal, leaving the holes in the TiO₂ valence band.³⁶¹ Various transition metals including Fe, Cu, Ni, Cr, and Co have been successfully doped on TiO₂ to promote the photocatalytic activity and to minimize the electron hole recombination. Among these, cobalt doped TiO₂ has been studied in various applications like oxidation of NO and CO,^{362,363} degradation of the methylene blue,³⁶⁴ methyl orange,³⁶⁵ 2- chlorophenol,³⁶⁶ and 4-chlorophenol.³⁶⁷ Recently, Kazuhiko et al.²²⁶ also studied the photocatalytic activity during water oxidation of rutile (R)-TiO₂ loaded with various cobalt loadings as catalytic and observed a significant enhancement of the photocatalytic activity when using certain annealing temperature for the cobalt.

In the present course of investigation, cobalt doped β -UCNPs/ TiO_2 photocatalyst were prepared and employed for Rz and DCPIP degradation. The effect of cobalt loading was investigated with both dyes. The objective was to develop an efficient photocatalyst and optimize the photocatalytic conditions.

Cobalt was loaded onto β -UCNPs/ TiO_2 and P25 (TiO_2) following an impregnation method²²⁶ which is schematically shown in **Figure 112**. In a typical experiment, the as-prepared β -UCNPs / TiO_2 -anatase or P25 were added to a solution of $\text{Co}(\text{NO}_3)_2 \cdot 6\text{H}_2\text{O}$ dissolved in acetone. After solvent evaporation, the loaded nanoparticles were collected, placed in an appropriate alumina boat and calcined under air. See details of the experimental conditions in **Section 2.3.9.3**.

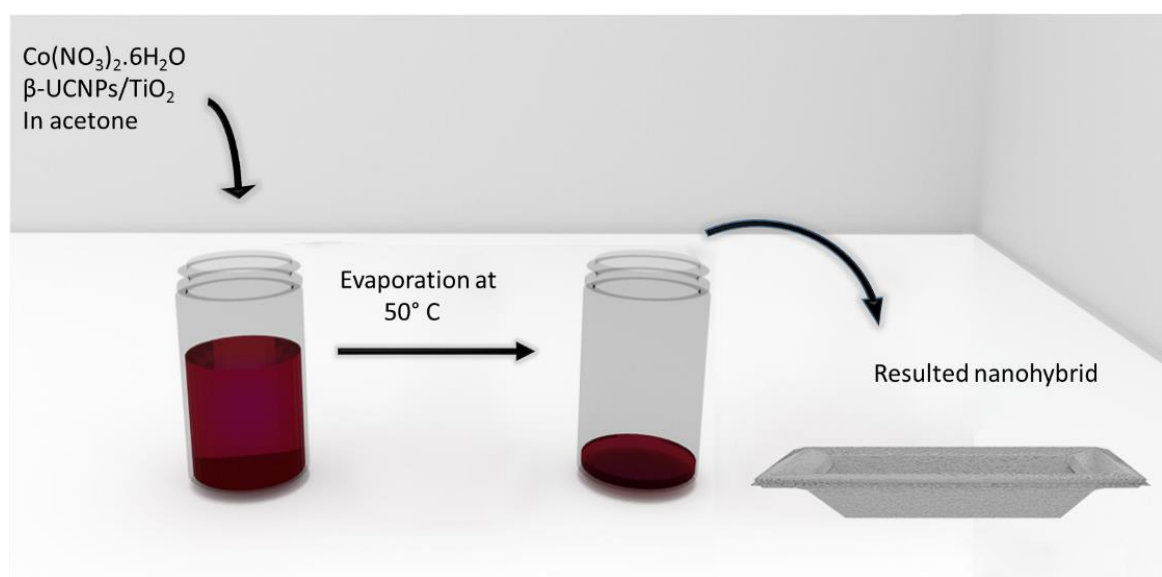


Figure 112. Schematic illustration of the process to obtain β -UCNPs/ TiO_2 nanohybrid load of cobalt species by an impregnation method.

Degradation of DCPIP and Rz inks under full radiation of a Xenon lamp was studied by UV-vis spectroscopy. **Figure 113** shows the photodegradation of DCPIP and Rz for TiO_2 (P25) at constant TiO_2 concentration of 0.5 mg/ml and variable cobalt loadings of 0%, 0.3%, 0.7%, 1%, 2% and 3% wt. cobalt. Overall, it can be observed that under full irradiation source, Co-undoped TiO_2 showed better results than Co-doped TiO_2 .

Our experiments revealed that both dyes degraded 100% in a period of 4 min when using Co-undoped TiO_2 . On the other hand, Co-doped TiO_2 (0.3% wt.) degraded only 20% of DCPIP and Rz and less than 10% when using Co-doped TiO_2 (0.7% wt., 2% wt. and 3% wt.).

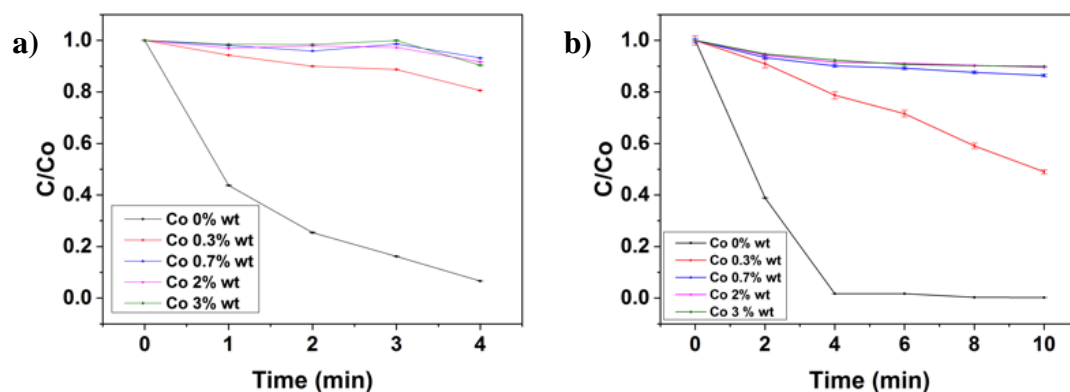


Figure 113. Photocatalytic degradation of (a) DCPIP and (b) Rz in the presence of TiO₂ co-doped with cobalt under full irradiation of a Xenon lamp.

Photodegradation of DCPIP ink under full spectrum was also studied in the presence of β -UCNPS/TiO₂ as catalyst and the results are shown in **Figure 114**. Correspondingly, the concentration of β -UCNPS/TiO₂ was fixed to 0.5 mg/ml and cobalt loading was varied as following: 0%, 1%, 2% and 3% wt. cobalt. **Figure 114** revealed one more time that under full irradiation source of a Xenon lamp, Co-undoped β -UCNPs/TiO₂ possess better photocatalytic activity than Co-doped β -UCNPs/TiO₂.

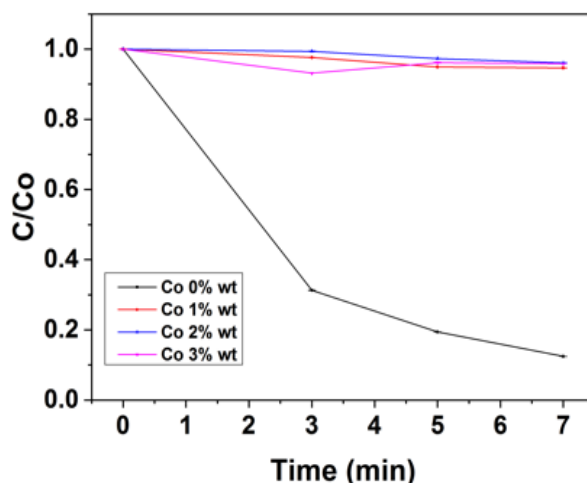


Figure 114. Photocatalytic degradation of DCPIP in the presence of β -UCNPs/TiO₂ co-doped with different loadings of cobalt using the full spectra irradiation of a Xenon lamp.

It has been reported that Co doping has two opposite effects in TiO₂: light absorption capacity and surface area; and the photocatalytic activity will depend on which of these is the dominant factor.³⁶⁵ Most of the metal doped TiO₂ samples absorb in the visible region, so it increases light absorption. However, we speculate that in our work, the Co concentrations produced undesired agglomeration of NPs on the TiO₂ surface which resulted

in a decreased of the surface area leading to a reduction in the photocatalytic activity. Recombination of photogenerated electrons-holes is another significant factor to consider, which deteriorates the photocatalytic activity of TiO_2 .³⁶⁸ It may be that in our experiments, cobalt NPs are sites for recombination of the generated electron-holes and thus, decreased the photocatalytic activity.

Future strategies could focus on optimizing the synthesis of Co-doped β -UCNPs/ TiO_2 able to respond in visible light. In order to understand the structure - activity relationship during photocatalytic experiments by these Co-doped photocatalysts, the synthesized materials should be investigated by XRD, UV-vis absorbance spectroscopy, high resolution (HR)-TEM, X-ray absorption fine structure (XAFS), and X-ray photoelectron spectroscopy (XPS).

4.4.4 Effect of varying the annealing temperatures on the photocatalysts

In this section, we studied the effect of annealing temperature on the structure, on the luminescent properties and on the photocatalytic activity of β -UCNPs/ TiO_2 . First, the temperature-dependence for the as-prepared β -UCNPs/ TiO_2 have been studied in the range of (500 °C – 1000 °C). **Figure 115** displays the XRD patterns of the β -UCNPs (black line) and β -UCNPs/ TiO_2 annealed at 500 °C (red line), 700 °C (blue line), 900 °C (green line), and 1000 °C (purple line).

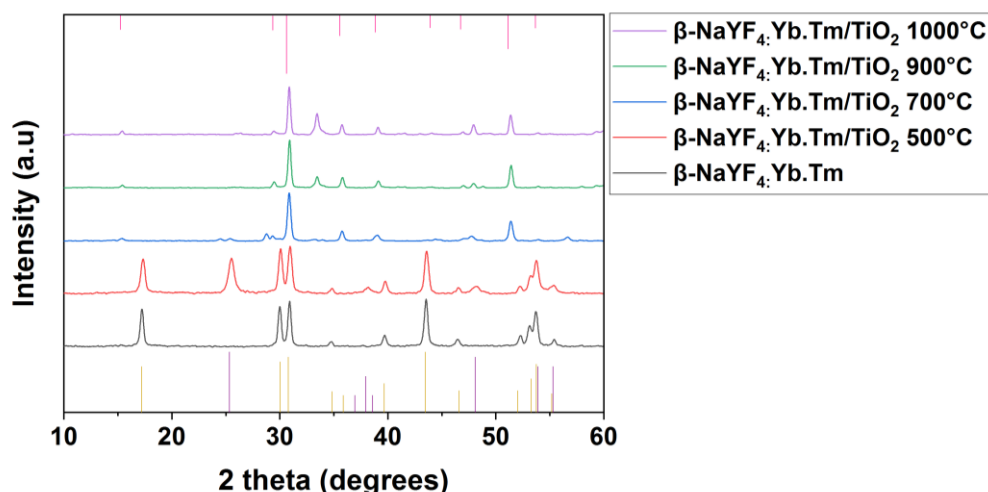


Figure 115. XRD patterns of β -UCNPs and β -UCNPs/ TiO_2 annealed at 500 °C, 700 °C, 900 °C and 1000 °C. Measurements were acquired using a Cu K- α source. Yellow, purple, and pink reference lines from the top correspond to β -UCNPs (PDF Card No.:00-016-0334), TiO_2 anatase and $\text{Y}_2\text{Ti}_2\text{O}_7$ (PDF Card No.:00-027-0982), respectively.

The XRD patterns indicated that the anatase phase of the TiO_2 was stable up to 500 °C and started to change above this temperature. Further increase in the annealing temperature induced a structural deformation. Several new diffraction peaks appeared at 700 °C, 900 °C and 1000 °C. Above 700 °C, there was no peak related to β -UCNPs or TiO_2 and the cubic- $\text{Y}_2\text{Ti}_2\text{O}_7$ phase dominated in the XRD pattern. All of the diffraction peaks are in good agreement with the standard values of $\text{Y}_2\text{Ti}_2\text{O}_7$ (PDF Card No.:00-027-0982), which is pyrochlore phase with the face-centred cubic crystal structure.³⁶⁹ Above 900 °C, XRD patterns showed traces of unknown phases likely due to the presence of impurities. In any case, it was noticeable that all diffractions peaks became sharper with increasing temperatures, which imply better crystallinity. It was interesting to observe how pyrochlore-type $\text{Y}_2\text{Ti}_2\text{O}_7$ NPs were obtained by annealing β -UCNPs/ TiO_2 above 700 °C. This research could provide an alternative-chemistry route to synthesize nanoscale pyrochlore-oxide $\text{Y}_2\text{Ti}_2\text{O}_7$.

As a control, the influence of the annealing temperature was also investigated on the structure of β -UCNPs without the titania coating. **Figure 116** displays the XRD patterns of the β -UCNPs annealed at 500 °C (red line), 700 °C (blue line) and 900 °C (pink line), compared to the non-annealed β -UCNPs (black line).

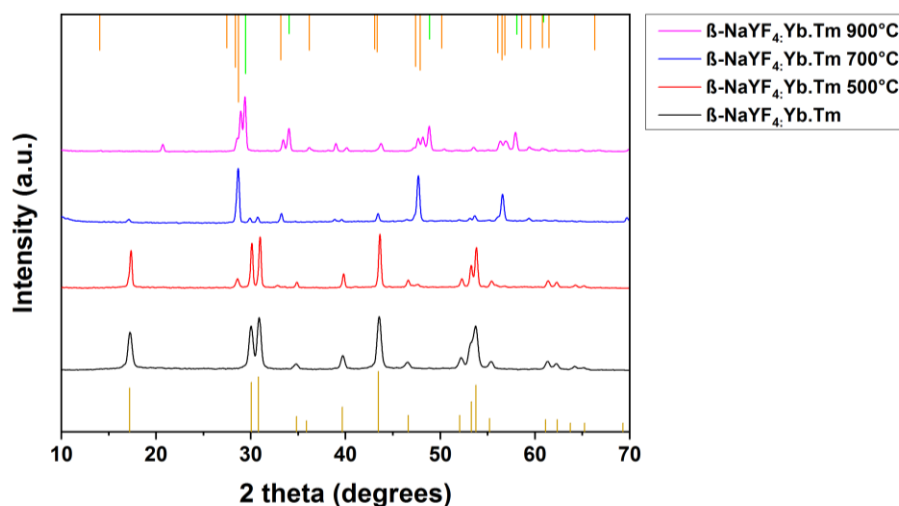


Figure 116. XRD patterns of non-annealed β -UCNPs and β -UCNPs annealed at 500 °C, 700 °C, and 900 °C. Measurements were acquired using a Cu K- α . Reference cards are indicated with a yellow-ochre line for β -UCNPs (PDF Card No.:00-016-0334), orange line for cubic YOF (PDF Card No.: 01-071-2100), and green line for trigonal Y_2O_3 (PDF Card No.: 00-043-0661).

The XRD patterns revealed that the crystal structure of the β -UCNPs remained stable up to 500 °C. Above this temperature, the diffraction peaks from the β -UCNPs were attenuated in intensity and above 700 °C the peaks disappeared in agreement to the XRD from **Figure 115**. A new set of diffraction peaks appeared at 700 °C indicating a structural deformation from the β -UCNPs. Although the intensity of the new set of peaks was not very intense, we attributed them to the appearance of a trigonal-YOF phase. Further increase in the temperature to 900 °C produced a new structural transition giving way to the cubic- Y_2O_3 . In order to determine more precisely these transition temperatures and obtain the pure structures of YOF and Y_2O_3 , it would be necessary to measure diffraction patterns in finer temperature steps. In all the cases, the samples were measured in ambient conditions by XRD after 24 hours of annealing, therefore we concluded that for both cases (β -UCNPs/ TiO_2 and β -UCNPs), the phase transitions imply irreversible processes.

Next, we studied the effect of the annealing temperature on the UC luminescence of β -UCNPs/ TiO_2 and β -UCNPs. The measurements were taken in ambient conditions, under a 980 nm laser (see laser set-up from **Figure 16**).

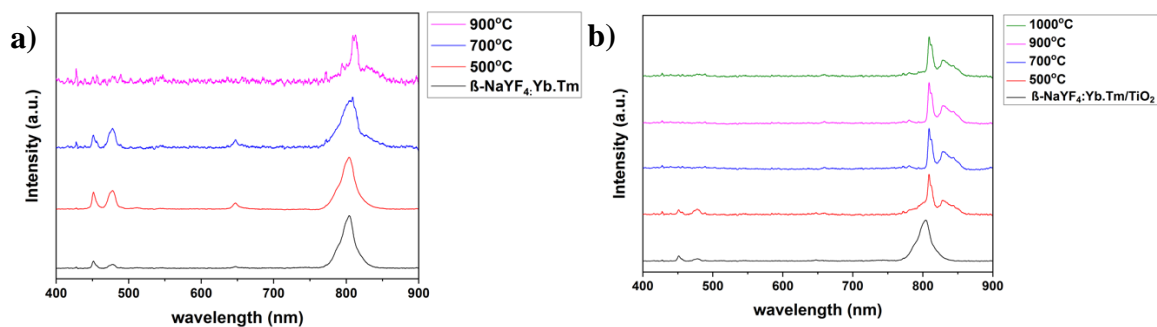


Figure 117. Emission spectra of β -UCNPs (a) before coating the TiO_2 and (b) after TiO_2 coating and annealing at different temperatures.

Figure 117a and **b** represent the normalized intensity of the β -UCNPs before and after titania coating, respectively, and annealed at different temperatures. Overall, it was observed that the UC intensity decreased with the annealing temperature. Results showed that after 700 °C, the samples produced no blue emission in any of the two peaks centred at 452 nm and 476 nm; associated to the $^1\text{D}_2 \rightarrow ^3\text{F}_4$ and $^1\text{G}_4 \rightarrow ^3\text{H}_6$ transitions of Tm^{3+} , respectively. Interestingly, it can be observed from **Figure 117b**, that the peak at 800 nm corresponding to the $^3\text{H}_4 \rightarrow ^3\text{H}_6$ transitions of Tm^{3+} split in two. This peak splitting has been already reported in the literature. Zhang group observed a similar splitting at 675 nm when studying

phase transitions in NaYF₄: Yb. Er.³⁷⁰ We attributed this sharp splitting to the new Y₂Ti₂O₇ phase.

To conclude this section, we investigated the effect of annealing temperature on the photocatalytic activity of Rz/glycerol, using β -UCNPs/TiO₂ as catalyst. Our experiments affirmed that the intensity in the absorbance of the samples decreased when increasing the annealing temperature.

Observing the absorbance spectra of the β -UCNPs/TiO₂ annealed at different temperatures (**Figure 118a**), we can see that the one with highest absorbance corresponded to the one annealed at 500 °C and coincides with the anatase phase of the TiO₂. It can be seen a sharp peak at 400 nm, corresponding to its theoretical bandgap absorption of ~ 3.2 eV (~ 380 nm). When β -UCNPs/TiO₂ were annealed at 700 °C, the formed nanocomposites showed significantly improved light absorption compared to the β -UCNPs/TiO₂ anatase, with the peak emerging at 600-700 nm. However, the intensity of the latter presented much lower intensity than the former. β -UCNPs/TiO₂ annealed at 900 °C and 1000 °C did not absorb in the UV-vis region coinciding with the absence of TiO₂ observed from the XRD analysis.

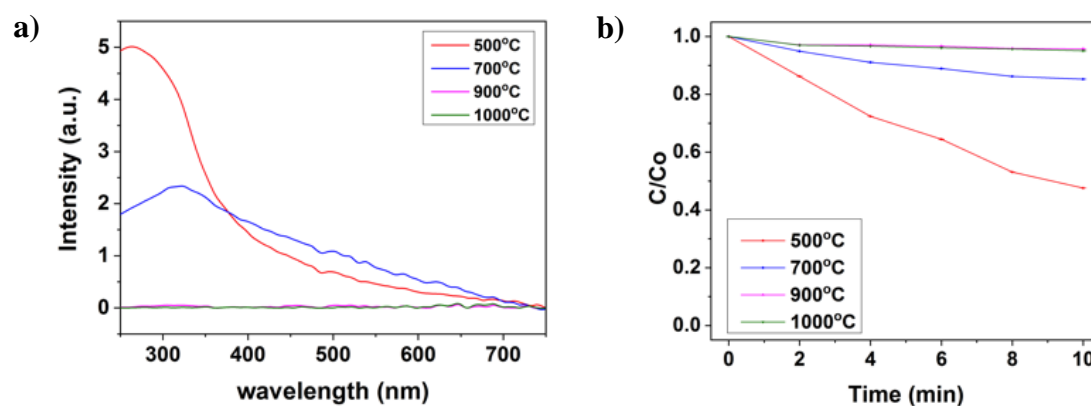


Figure 118. (a) UV-Vis spectra and (b) photodegradation of Rz using β -UCNPs/TiO₂ annealed at different temperatures under full irradiation of a Xenon lamp.

Figure 118b displays the effect of annealing temperature of β -UCNPs/TiO₂ on the photodegradation for Rz. Using the full irradiation of a Xenon lamp, the sample of β -UCNPs/TiO₂ annealed at 500 °C degraded effectively 50% of Rz within 10 min. It can be seen that the photocatalytic activity got reduced with further increase in the annealing temperature of the β -UCNPs/TiO₂, until was lost, due to the transition to the new Y₂Ti₂O₇ structure.

In summary, we have observed that the β -UCNPs/TiO₂ can transform into a Y₂Ti₂O₇ structure when annealing in the (700 °C-1000 °C) range. It has been found that although the photocatalytic activity was not very high, samples were able to absorb in the visible region when annealed at 700 °C. We predict, that the holes in the intermediate structure can be excited into the valence band (VB) under irradiation with visible light. However, it could be that in our experiments, the fast recombination of photogenerated electron-hole pairs seriously limited their efficiency.

Chapter 5 Result and discussion on Organic functionalization of upconversion nanoparticles

A strategy to increase the excitation efficiency of UCNPs involves sensitizing the particles with organic dyes. It has been reported that hybridization of UCNPs with molecules that absorb efficiently in the NIR (specifically IR-806 dyes) allows for an overall increase in the absorption cross section of the UCNPs.²²⁸ The concept involves organic IR-806 dyes acting like antennas that transfer the harvested photons to the Ln^{3+} ions of the UCNPs where the UC process is realized (see **Figure 119**).

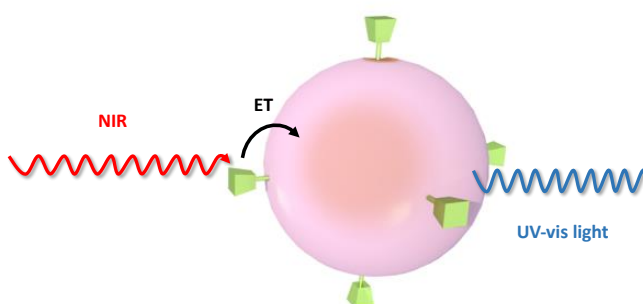


Figure 119. Schematic illustration of the dye-sensitized β -UCNPs energy transfer: antenna dyes (in green) absorb the NIR light (red wiggled arrows) and transfer it to the β -UCNP core (in pink) where the UC process is realized. The blue arrow represents the visible energy emitted by the β -UCNPs.

Recent investigations revealed a further increase in the UC luminescence utilizing simultaneously IR-dye sensitization and the advantages of core@shell β -UCNPs.³⁷¹ As we have seen in previous chapters, core@shell β -UCNPs with an inert shell of few nanometer thicknesses can enhance the UC properties because of minimization of surface quenching processes. Wu et al. reported that doping the shell with Yb^{3+} ions (so-called active shell) can result in an eightfold increase of the UC luminescence in comparison with dye-sensitized core-only β -UCNPs.³⁷¹ With the aim of achieving the perfect design of β -UCNPs sensitized by IR-dyes for efficient FRET, we fabricated different types of β - NaYF_4 UCNPs covered by IR-dyes and studied their efficiency of FRET.

Section 5.1 will discuss the synthesis and characterization of IR-806 dye. The effect of the dye-sensitized process was studied using three different types of β -UCNPs: core-only, core@active shell and core@inert shell, and their synthesis and optimal properties are

described in **Section 5.2**. The IR-806 dye-sensitized β -UCNPs and optimal surface coverage of the β -UCNPs by dye molecules is discussed in detailed in **Section 5.3**.

Section 5.4 discuss the results of our recent publication,²⁷⁵ which have been carried out thanks to a joint collaboration between us and the and the Skolkovo Institute of Science and Technology in Moscow. Here, we report an investigation of the UC luminescence in dye-sensitized β -UCNPs compared to that in non-sensitized β -UCNPs. We also use time-resolved measurements to characterize the overall non-radiative energy transfer from dyes to the β -UCNPs. It also includes an analysis of the UC kinetic, showing difference in the rise dynamics in dye-sensitized β -UCNPs compared to that in non-sensitized β -UCNPs. We believe that understanding the contribution of the radiative and non-radiative energy transfer in the dye-sensitized β -UCNPs is important for the future design strategy of dye-sensitized β -UCNPs for luminescence enhancement.

In addition to the UC luminescence, we also studied downshifting luminescence spectra for the dye-sensitized β -UCNPs. This part of the research is explained throughout **Section 5.5**. The work of this chapter concludes in **Section 5.6** with a preliminary study based on the use of a new IR dye (1076 IR-dye) to alleviate the luminescence concentration quenching effect of the β -UCNPs.

5.1 Synthesis and characterization of Near Infrared IR-806 Dyes

The general synthesis of IR-806 dye-sensitized β -UCNPs involves two major steps; preparation of the carboxylic acid-functionalized organic dyes molecules and their subsequent attachment to the OAm coated β -UCNPs.²²⁸ The chemical modification of the commercial IR-780 dye to obtain the carboxylic acid-functionalized organic dyes IR-806 involves a nucleophilic substitution through the central chlorine atom of the IR-780 using 4-mercaptobenzoic acid as the nucleophile and DMF as the solvent³⁷² (see **Figure 120**). When the reaction is performed in polar aprotic solvents, such as DMF, the $S_{RN}1$ pathway will be favoured.³⁷³ See the experimental procedure described in **Section 2.4.1** for a full description of the chemical functionalization to obtain the IR-806 dye.

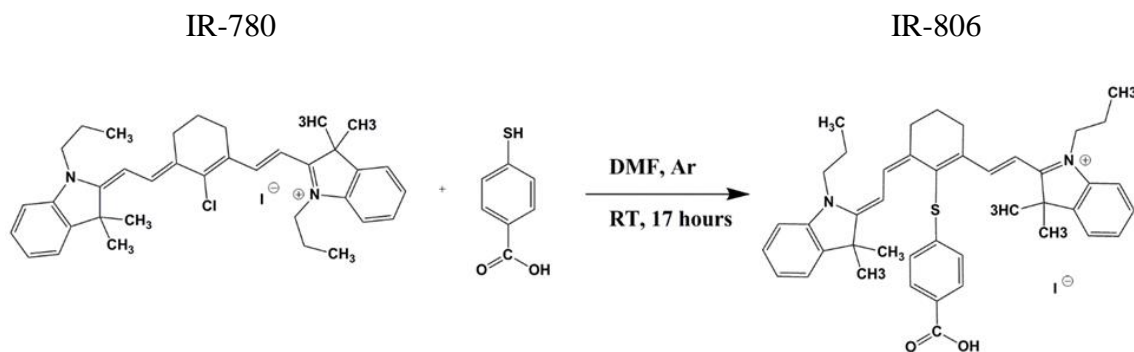


Figure 120. Synthesis of the organic dye IR-806 using the commercial dye IR-780. 4-mercaptobenzoic acid was used as the nucleophile and DMF as solvent.

The dyes before (IR-780) and after functionalization (IR-806) were characterized using UV-vis spectroscopy. The absorption spectra of the different samples of IR-dye sensitized UCNP were recorded on a Jasco FT-IR 620 spectrometer with a 1 nm resolution from 600 to 1000 nm. From **Figure 121** it was observed that after functionalization, the dye had a very strong absorption in the NIR region with a maximum absorbance at 806 nm. The overlap between the emission of the dye and the absorption of the β -UCNPs at 980 nm will allow the energy transfer from the dye to the Ln^{3+} ions of the β -UCNPs (see **Figure 122**).

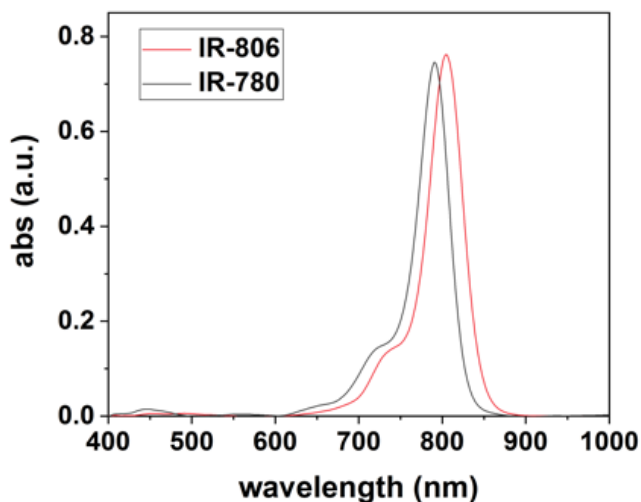


Figure 121. Red and black lines indicate the absorption spectra of IR-806 (2 $\mu\text{g/ml}$) and IR-780 (2.5 $\mu\text{g/ml}$), respectively. For the measurements, organic dyes were dissolved in CHCl_3 .

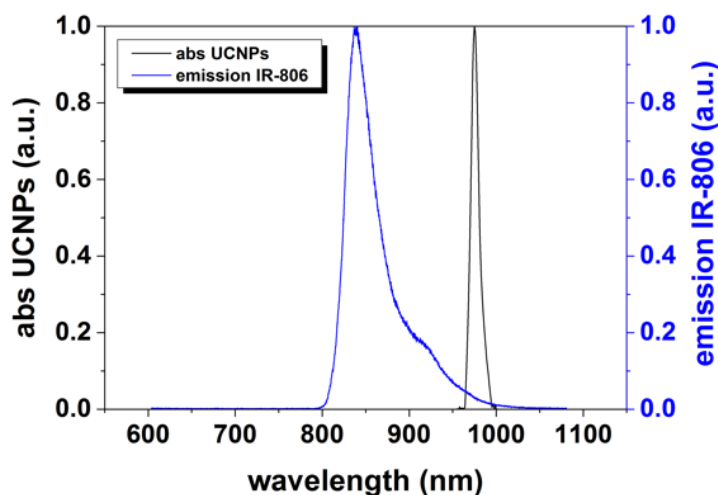


Figure 122. Normalized absorption of β -NaYF₄: Yb³⁺(20%), Er³⁺(2%) (black line) and emission of spectra of IR-806 dye (blue line) in CHCl₃.

HRMS, ¹H NMR and ¹³C NMR were performed to verify the elemental compositions and the structure of the organic IR-806 molecules. The mass spectrum was recorded by an ACQUITY UPLC H-Class System. ¹H and ¹³C NMR spectra were recorded on AVII400 (400 and 100.61 MHz, respectively) using CDCl₃ as a solvent.

According to the HRMS spectra from **Figure 123**, the found mass was [M]⁺ = 657.66, which agrees with the one calculated using ChemDraw software ([M]⁺ = 657.35). ¹H and ¹³C NMR spectra are shown in **Figure 124** and **Figure 125**, respectively. The interpretation of the spectrum is reported as follows: s = singlet, d = doublet, dd = double doublet, t = triplet, and m = multiplet

¹H NMR (400 MHz, CDCl₃): δ 8.57 (d, *J* = 14.1 Hz, 2H), 7.95 (d, *J* = 8.5 Hz, 2H), 7.34 (t, *J* = 7.6 Hz, 2H), 7.30 – 7.23 (m, 6H), 7.19 (t, *J* = 7.4 Hz, 2H), 7.12 (d, *J* = 8.0 Hz, 2H), 6.26 (d, *J* = 14.1 Hz, 2H), 4.14 (t, *J* = 7.2 Hz, 4H), 2.81 (t, *J* = 5.7 Hz, 4H), 2.11 – 2.01 (m, 2H), 1.87 (dd, *J* = 14.6 Hz, *J* = 7.3 Hz 4H), 1.43 (s, 12H), 1.04 (t, *J* = 7.4 Hz, 6H).

¹³C NMR (101 MHz, CDCl₃): δ 172.52 (s), 170.26(s), 148.79 (s), 145.52 (s), 144.65 (s), 142.26 (s), 141.12 (s), 134.13 (s), 131.11 (s), 128.73 (s), 125.50 (s), 125.32(s), 122.19 (s), 110.99 (s), 102.05 (s), 49.22 (s), 46.45 (s), 29.69 (s), 27.87 (s), 26.87 (s), 20.96 (s), 20.74 (s), 11.69 (s).

Peak 1, RT 2.615, Scan 746, NL 1.194E08, MS2 (150:1500) ES +

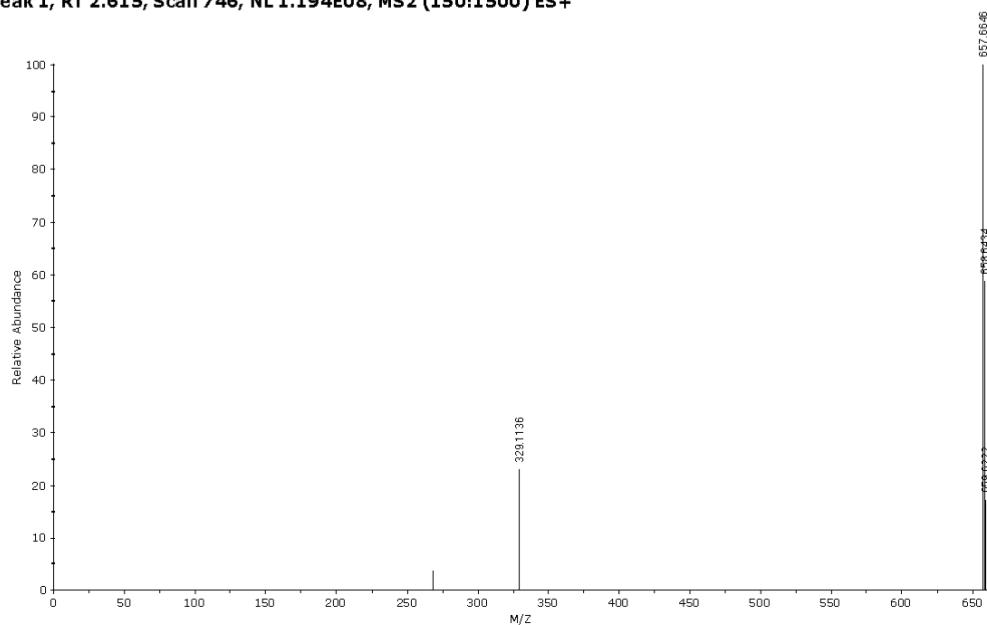


Figure 123. HRMS spectrum of IR-806. The analysis was done to a sample containing 50 $\mu\text{g/ml}$ of the dye dissolved in anhydrous methanol.

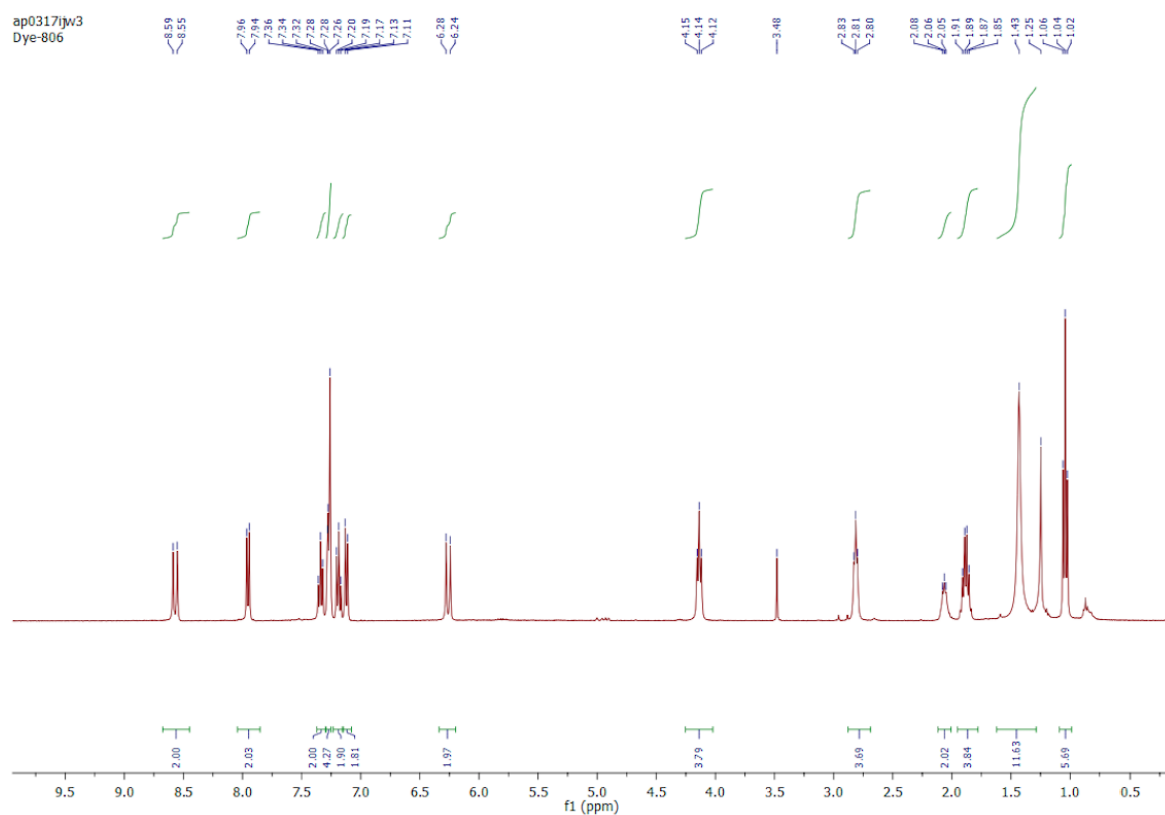


Figure 124. ^1H NMR (400 MHz, CDCl_3) spectrum of IR-806. (20 mg/ml). Diethyl ether $\text{D}(\text{CH}_3)$ at 3.472 ppm/ $\text{D}(\text{CH}_2)$ at 1.206/ $J(\text{CH}_3\text{-CH}_2) = 7.00$.

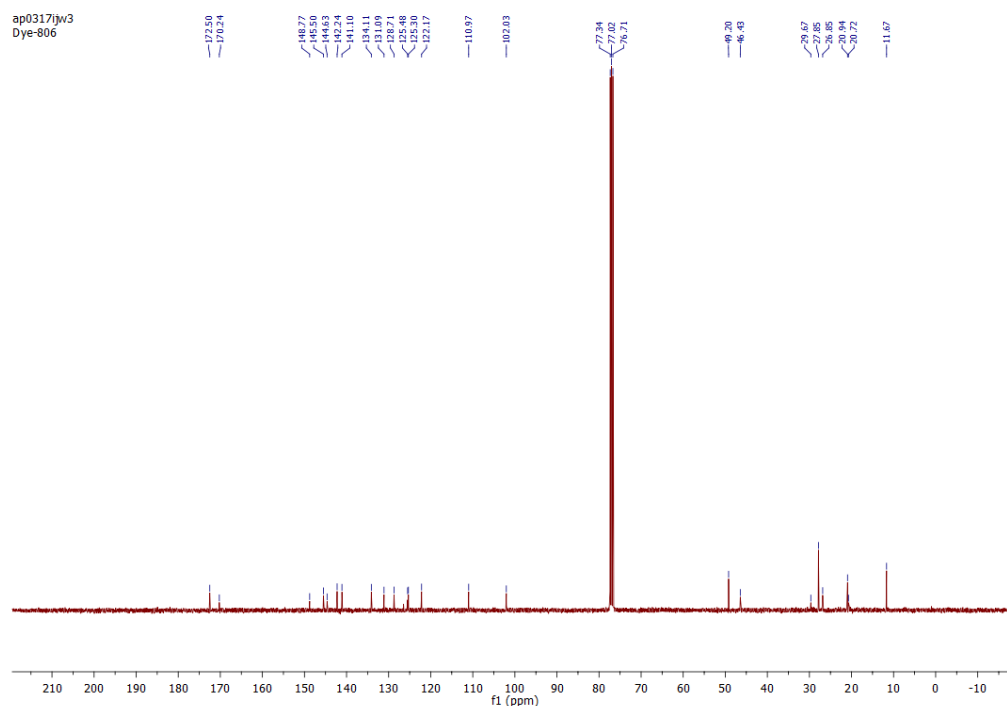


Figure 125. ^{13}C NMR (101 MHz, CDCl_3) spectrum of IR-806 dye. (20 mg/ml).

5.2 Synthesis of core-only, core@inert shell and core@active shell

To systematically study and compare the effect of the shell on dye-sensitized β -UCNPs, we synthesised three different types of β -UCNPs named conveniently core-only, core@inert shell and core@active shell.

Core-only β - NaYF_4 : Yb^{3+} (20%), Er^{3+} (2%) UCNPs were prepared following the experimental procedure detailed in **Section 2.1.1**. Core@inert shell β - NaYF_4 : Yb^{3+} (20%), Er^{3+} (2%)@ NaYF_4 and core@active shell β - NaYF_4 : Yb^{3+} (20%), Er^{3+} (2%)@ NaYF_4 : Yb (10%) UCNPs were both prepared following the procedure from **Section 2.1.2**. For the core@active shell, we have used a 10% concentration of Yb^{3+} ions that according to previous reports is optimal for the UC luminescence enhancement in dye-sensitized β -UCNPs.³⁷¹ The particle sizes and morphologies were first characterized by TEM and the micrographs and size distributions are shown in **Figure 126**. The size distribution was analysed considering over 100 UCNPs for each of the samples.

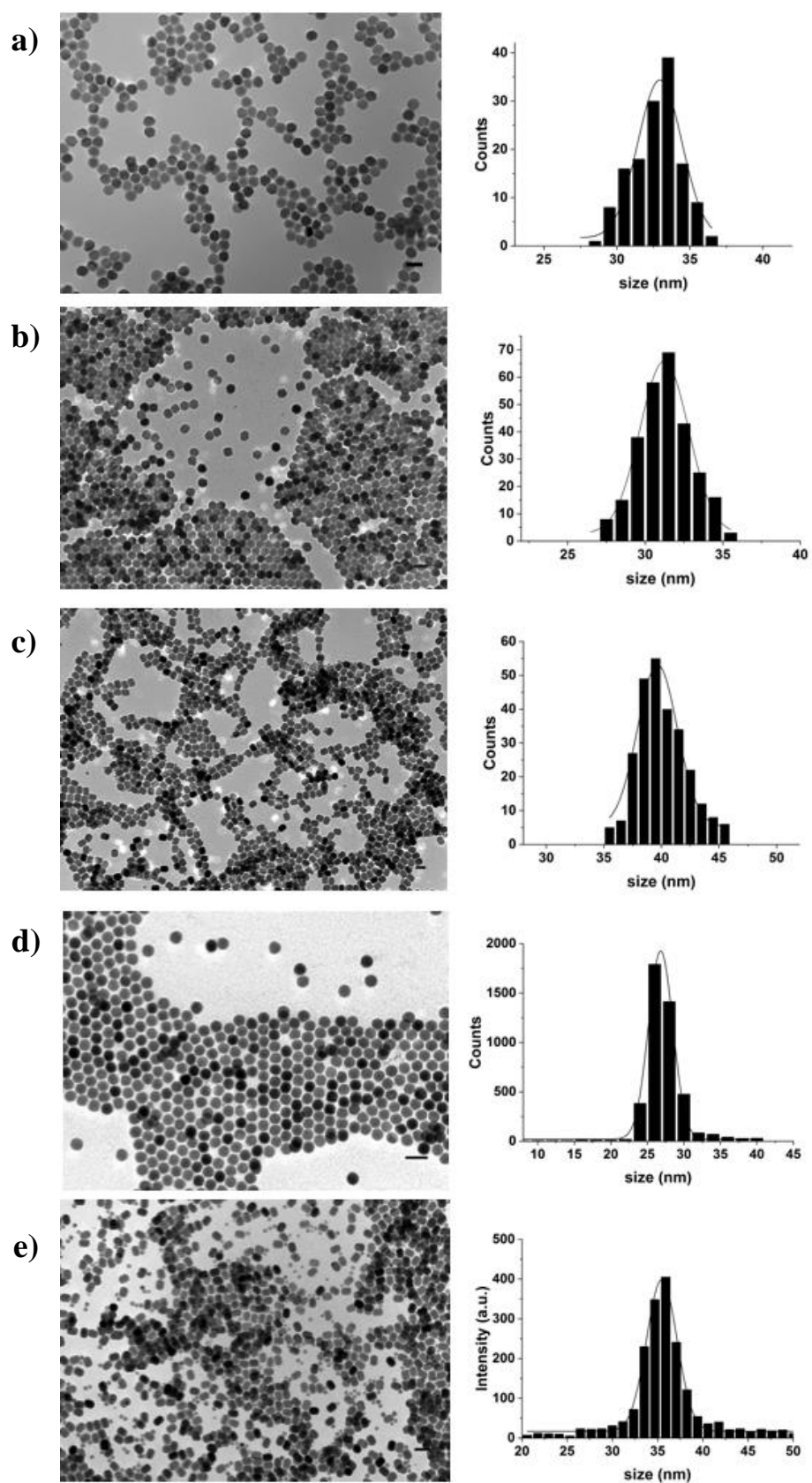


Figure 126. TEM images and size distributions of (a) core-only, (b) core used to create (c) core@active shell and (d) core to grow the (e) core@inert shell. Scale bars are 50 nm.

Figure 126 shows that particles were monodispersed in size. Core-only β -UCNPs had a mean size of 33 ± 2 nm. Core@active shell exhibited size uniformity with an average diameter of 40 ± 2 nm, synthesized from core with a mean size of 31 ± 2 nm. Core@inert shell exhibited size uniformity with an average diameter of 36 ± 2 , synthesized from core with a mean size of 27 ± 2 . From the difference of mean diameters, we estimated the thickness of the active shell, doped with Yb^{3+} ions and of the inert shell, to be approximately 4.5 nm in both of cases. The shell surrounding the β -UCNPs appeared very uniform in thickness and quite smooth in the surface with elliptical shape (more information about the growing mechanism using NaYF_4 shell can be found in **Section 3.3.1**).

The small nucleation particles (~ 10 nm) are excess of β - NaYF_4 and β - $\text{NaYF}_4\text{:Yb}^{3+}$ that are optically inactive (“inert” particles). This is an excess of shell precursor that did not react fully with the core particles but their concentration is significantly lower than concentration of desired core@shell β -UCNPs.

5.2.1 Surface modification of the OA coated UCNPs with BF_4^-

In 2011, Dong et al.⁷² reported a general strategy for ligand exchange using nitrosonium tetrafluoroborate (NOBF_4) to replace OA ligands attached to the UCNPs surface. This procedure enabled the phase transfer of initial hydrophobic UCNPs into polar, hydrophilic media such as N, N-dimethylformamide (DMF). Additionally, it was demonstrated that hydrophilic BF_4^- stabilized UCNPs could be covered with new ligands using a sequential coating step. See **Figure 127**.

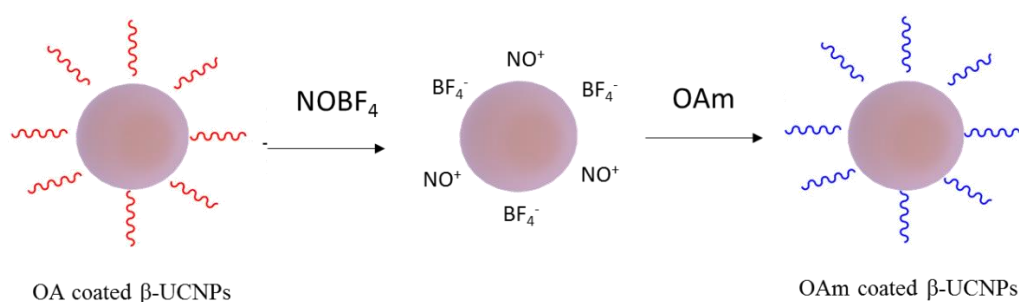


Figure 127. Ligand exchange strategy using nitrosonium tetrafluoroborate (NOBF_4) to replace OA ligands attached to the β -UCNPs surface. The red and blue arrow represent the OA and OAm ligand attached to the surface of β -UCNPs.

In our work, the surface modification of OA coated β -UCNPs with OAm as the new ligand was performed using this ligand exchange procedure employing NOBF_4 as a temporary surface ligand. The synthesis is described in detail in **Section 2.3.8**.

5.3 Synthesis of IR-806 dye-sensitized β -UCNPs

The IR-806 dye molecules were attached to the surface of the OAm coated β -UCNPs according to a reported procedure which is detailed in **Section 2.4.2**.

In order to control the possible alteration of the properties of the β -UCNPs when attaching the IR dyes, we measured the IR-806 dye sensitized β -UCNPs and the non-sensitized β -UCNPs in a range of different wavelengths, using in all cases a laser of 2 mW excitation. The ratio of β -UCNPs:IR-806 used for this experiment was 0.80 mg/ml: 0.004 mg/ml. The set-up used to characterize the UC luminescence for the following samples is described in **Section 2.6.3**.

Figure 128a shows the UC emission spectra from the IR-806 dye sensitized β -UCNPs for different excitation wavelength. It can be seen that although the emission intensities are quite different, there are always three bands centred at 525 nm, 540 nm, and 650 nm, which can be assigned to $^2H_{11/2} \rightarrow ^4I_{15/2}$, $^4S_{3/2} \rightarrow ^4I_{15/2}$ and $^4F_{9/2} \rightarrow ^4I_{15/2}$ transition of Er^{3+} ion.³⁴ **Figure 128b** shows that IR-806 dye-sensitized β -UCNPs (black line) emitted similarity to the no-sensitized β -UCNPs (blue line) when irradiated at 980 nm. Results showed the same emission pattern either they were coated with the dyes or not, when excited to 980 nm. This observation indicates that the attachment of IR-dyes on the β -UCNPs surface maintained intact their initial UC properties.

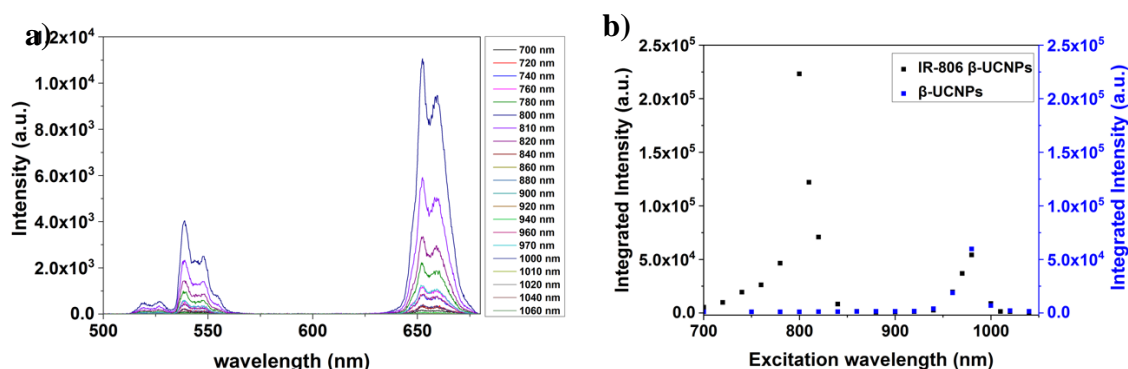


Figure 128. (a) UC emission intensities of IR-806 – sensitized core@active shell β -UCNPs in function of different excitation wavelengths and (b) UC excitation spectra integrated in the 500-680 nm range for the IR-806 – sensitized core@active shell β -UCNPs (black line) and no sensitized core@active shell β -UCNPs (blue line), dissolved in $CHCl_3$. The spectra were recorded using a 2 mW laser excitation.

5.3.1 Optimization of the surface coverage of the β -UCNPs by IR-806 molecules

We studied the optimal surface coverage on the as-prepared β -UCNPs by the IR-806 dye molecules, to obtain the most efficient dye-sensitized UC system in CHCl_3 solution under excitation at 800 nm. All samples were prepared in identical conditions in a quartz cuvette, with a final concentration of 0.8 mg/ml of β -UCNPs in CHCl_3 and the IR-806 dye concentration was varied as following: 0.000, 0.001, 0.003, 0.005, 0.007, 0.010, and 0.015 mg/ml. The samples were excited by a 800 nm laser (2 mW). The integrated emission intensity in the range 500-685 nm as a function of IR-806 content is shown in **Figure 129**, **Figure 130** and **Figure 131** for the core-only, core@active shell and core@inert shell, respectively.

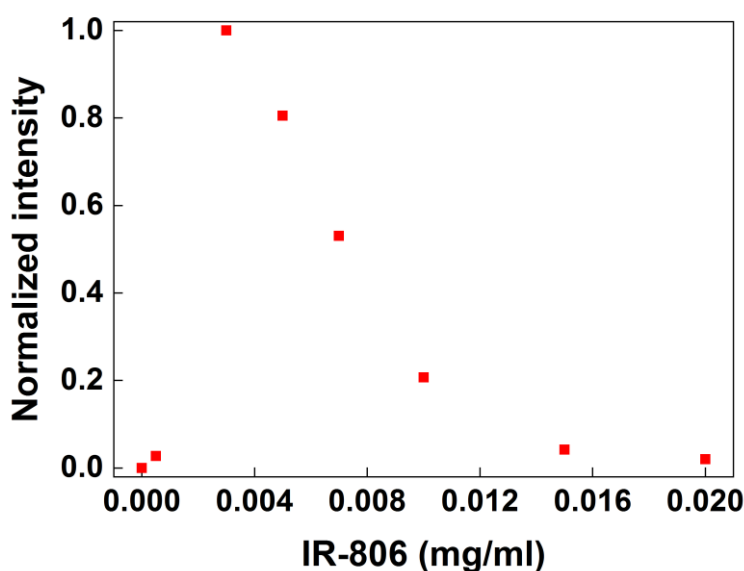


Figure 129. Normalized emission intensities integrated in the range 500-685 nm for IR-806-sensitized core-only β -UCNPs as a function of IR-806 content in CHCl_3 . Measured by a 2 mW, 800 nm laser excitation.

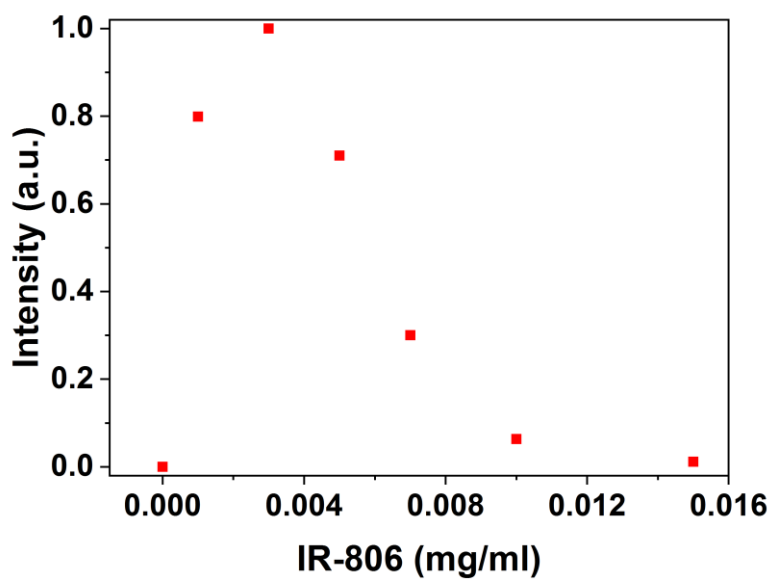


Figure 130. Normalized emission intensities integrated in the range 500–685 nm for IR-806–sensitized core@active shell β -UCNPs as a function of IR-806 content in CHCl_3 . Measured by a 2 mW, 800 nm laser excitation.

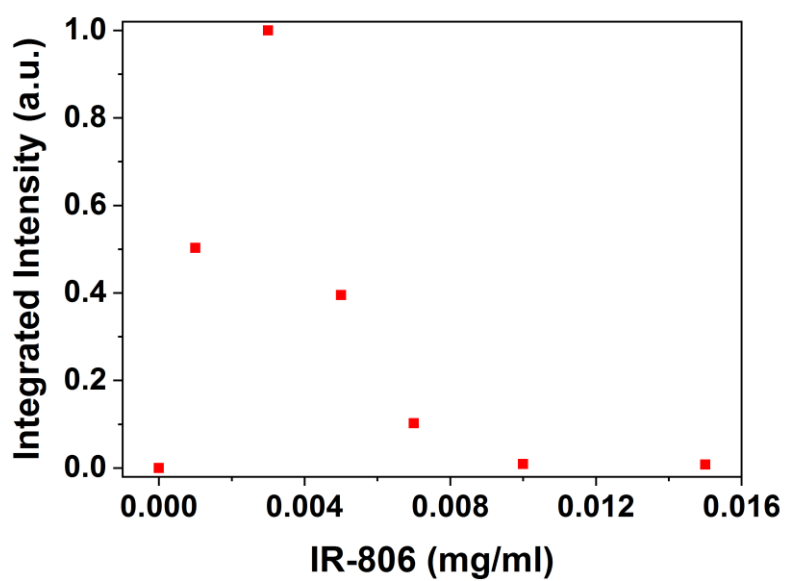


Figure 131. Normalized emission intensities integrated in the range 500–685 nm for IR-806–sensitized core@inert shell β -UCNPs as a function of IR-806 content in CHCl_3 . Measured by a 2 mW, 800 nm laser excitation.

In our three experiments, the optimum β -UCNPs:IR-806 concentration was determined to be 0.8 mg/ml: 0.003 mg/ml. By adding the IR-806 molecules to a fixed solution of the UCNP, the intensity of the UC emission increased first, but beyond a certain dye concentration, it resulted in a decrease in the UC emission. Our results are in agreement with those reported in the literature.^{228,371} The increase in UC intensity is explained by an increase in the absorption at 800 nm by an increasing number of dye molecules adhered to the surface of the β -UCNPs. The observed decrease can be explained by two factors: first, self-quenching due to mutual interactions between the antenna molecules on the surface of the β -UCNP and second, the undesired production of an excess of free antenna molecules (unbound) in solution that absorb excitation energy but do not transfer it to the β -UCNPs.²²⁸

In the following, we compare the UC emission spectra of the IR-806-sensitized β -UCNPs at the optimum β -UCNPs:IR-806 concentration of 0.8 mg/ml: 0.003 mg/ml with the non-sensitized β -UCNPs.

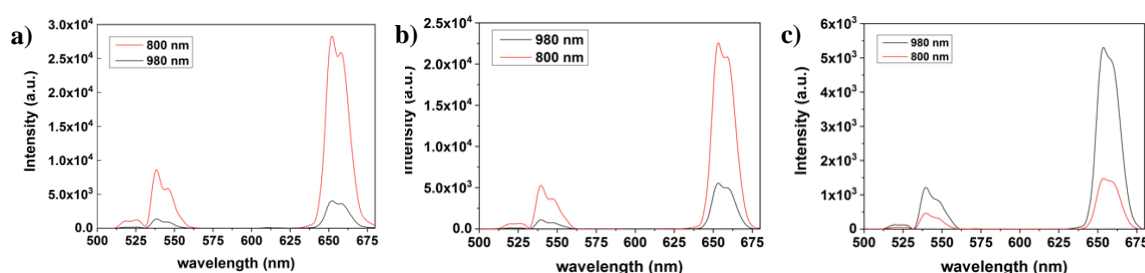


Figure 132. Comparison of the UC emission intensities of the non-sensitized (black line) and IR-806-sensitized (red line) (a) core-only, (b) core@active shell and (c) core@inert shell β -UCNPs in CHCl_3 . IR-sensitized β -UCNPs and non-sensitized β -UCNPs were excited under 800 nm and 980 nm laser, respectively. All the measurements were recorded using a 2 mW laser excitation.

Figure 132 (a-b) shows that when using core-only and core@active shell β -UCNPs, the UC luminescence obtained upon 800 nm excitation was higher than with 980 nm excitation laser. On the contrary, **Figure 132c** shows that when the inert shell was used, the emission intensity was higher using an excitation of 980 nm than using an excitation of 800 nm.

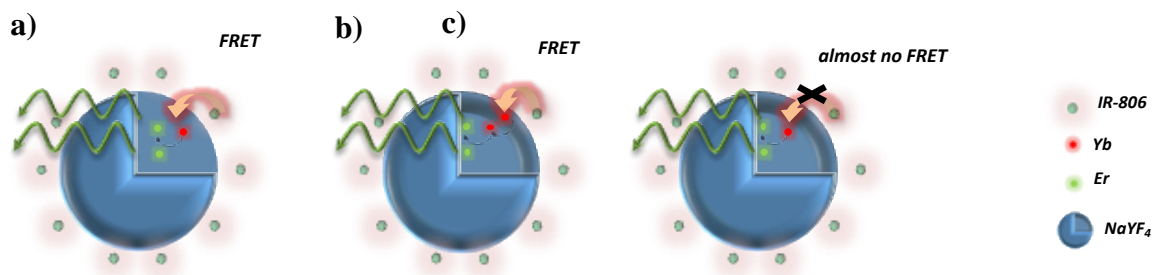


Figure 133. Illustration showing the basic principle of dye-sensitized UC applied to the cases of (a) core-only, (b) core@active shell and (c) core@inert shell structures. Excitation at 800 nm results in efficient absorption by the dye molecules and subsequent energy transfer to the Ln^{3+} ions in the core and in the active shell of the β -UCNPs. Core@inert shell results in an inefficient energy transfer from the dye molecules to the Ln^{3+} ions of the β -UCNPs.

The experimental results clearly suggest that an inert coating has an adverse effect on the UC emission sensitized by the IR-dye and that the transfer of energy from the IR-dye to these β -UCNPs was partially prohibited by the thickness of the inert shell. However, the active shell acted as a bridge and allowed for energy migration between Yb^{3+} ions across the shell, which resulted in the excitation of core Er^{3+} ions that ultimately emitted upconverted light. Our results are in agreement with other reports.³⁷¹

5.3.2 Estimation of dye molecules attached to the upconversion surface

We performed experimental measurements of the supernatants to determine quantitatively the concentration of bound dye to the surface of the particles. The measurements were performed using the samples at the optimum β -UCNPs:IR-806 concentration of 0.8 mg/ml: 3 $\mu\text{g/ml}$.

A calibration curve was created by UV-measurements of a series of IR-806 dye concentrations. The calibration curve is shown in **Figure 134b** and it was fitted with a line $y = 0.3262x - 0.06404$ and $R=0.99$.

Supernatants of different solutions (core and core@active shell) were obtained by centrifugation at the speed of 10000 rpm for 15 min. Solutions were illuminated under a 980 nm laser pointer before and after the centrifugation to visualize the full precipitation of the NPs. **Figure 135 (a- b)** shows how the green luminescence disappeared due the absence of the β -UCNPs in the collected supernatant.

Then, we measured the absorbance of the supernatants by UV-vis spectroscopy and used the calibration curve from **Figure 134b** to determine the dye concentration, and thus unbound dye molecules.

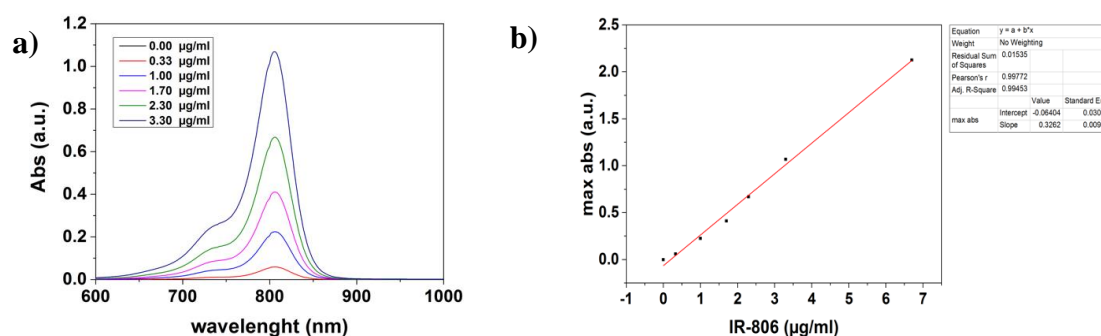


Figure 134. (a) UV-vis spectra of IR-806 at different concentrations. (b) Calibration curve, with the maxima absorption observed at 806 nm against the IR dye concentration.

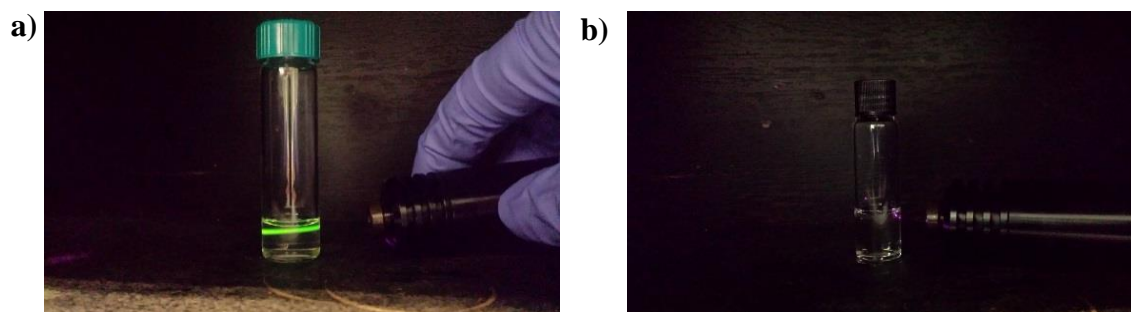


Figure 135. Digital images of IR-806 dye sensitized β -UCNPs dispersed in CHCl_3 under ambient light and under a 980 nm laser pointer (a) before and (b) after particles removal.

Results showed that the fraction of the dye bound to the core-only and to the core@active shell was $88.6\% \pm 1.9\%$, and $91.2\% \pm 1.9\%$, respectively. **Table 20** summarizes the experimental results obtained for the bound and unbound IR-dyes to the surface of the β -UCNPs, where C_0 indicates the concentration measured from supernatants using the calibration curve and C_1 is the concentration of the estimated dye attached to the β -UCNPs. See **Appendix H** for a complete analysis of the data.

Table 20. Experimentally obtained concentration of bound and unbound IR-dye to the surface of the core-only and core@active shell β -UCNPs, using in both cases 0.8 mg/ml: 3 μ g/ml of β -UCNPs: IR-806.

Solution	C_0 (μ g/ml)	C_1 (μ g/ml)	Fraction of bound dye	Fraction of dye free on solution
Core-only	0.34 ± 0.01	2.66 ± 0.03	$88.6\% \pm 1.9\%$	$11.3\% \pm 0.3\%$
Core@active shell	0.26 ± 0.01	2.74 ± 0.03	$91.2\% \pm 1.9\%$	$8.8\% \pm 0.3\%$

The β -UCNPs concentration was calculated following the procedure of Zou, Wenqiang.²²⁸ Assuming spherical morphology, the volume of one UCNP (v_{UCNPs}) can be described by the next equation:

$$v_{UCNPs} = \frac{4}{3}\pi r^3 \quad (19)$$

, where r is the radius of the β -UCNPs. From the TEM analysis we obtained an average particle diameter for the core-only of 33 nm. Therefore,

$$v_{UCNPs} = 18816.57 \text{ nm}^3$$

The average β -UCNP core weight can be calculated with the following equation:

$$UCNP_{weight} = \rho_{UCNP} v_{UCNP} \quad (20)$$

, where ρ_{UCNP} is the density of pure β -NaYF₄ and has a value of $4.21 \cdot 10^{-21} \text{ g/nm}^3$.³⁷⁴ Therefore,

$$UCNP_{weight} = 7.92 \cdot 10^{-17} \text{ g}$$

and this value can be recalculated as molecular weight, using the $6.023 \cdot 10^{23}$ Avogadro's number.

$$UCNP_{molecular\ weight} = 47.71 \cdot 10^6 \text{ g/mol}$$

We deduced that the average molecular weight for our OAm coated core-only β -UCNPs was $47.71 \cdot 10^6 \text{ g/mol}$.

In previous experiments, we have determined that 0.8 mg/ml: 2.66 µg/ml was the real concentration for the β-UCNPs:IR-806 when considering the bound IR-dyes. This value can be expressed in function of weight ratio as:

$$UCNP:IR - 806 \approx 301:1.$$

The number of IR-806 dyes attached per β-UCNP is calculated using the known molecular weight of the IR-806 dye which is 657 without the counter anion or 784 as the iodide.

$$47.71 \cdot 10^6 / 301:657/1 = 158.51 \cdot 10^3: 657$$

$$47.71 \cdot 10^6 / 301:784/1 = 158.51 \cdot 10^3: 784$$

, which can be further simplified to 241:1 and 202:1, when using the molecular weight of IR-806 as 657 g/mol or 784 g/mol, respectively. Therefore, we estimated that at the weight ratio of ~301:1, the number of IR-806 molecules per β-UCNP ranged between 241 and 202.

Doing the same calculation for the core@active shell β-UCNPs with a size of 40 nm, we obtained that at the weight ratio of 292:1 the number of IR-806 molecules per UCNPs ranged between 442 and 371, when using the molecular weight of IR-806 as 657 g/mol or 784 g/mol, respectively.

Table 21. Summary of: calculated molecular weight, experimental and real concentration between β-UCNPs and dyes, weigh ratio and number of IR-dye antennas per single β-UCNP for the core-only and core@active shell β-UCNPs.

Type of particles	Core-only	core@active shell
Molecular weight	47.10·10 ⁶ g/mol	84.97·10 ⁶ g/mol
Experimental concentration β-UCNPs: IR-806	0.8 mg/ml: 3 µg/ml	0.8 mg/ml: 3 µg/ml
Real concentration β-UCNPs: IR-806	0.8 mg/ml: 2.66 µg/ml	0.8 mg/ml: 2.74 µg/ml
Weight ratio	~301:1	~292:1
antennas per β-UCNP (MW IR-806: 657 g/mol)	~241:1	~442:1
antennas per β-UCNP (MW IR-806: 784 g/mol)	~202:1	~371:1

Table 21 summarizes the calculated molecular weight of the β -UCNPs. The Experimental β -UCNPs: IR-806 concentration is the results obtained from **Figure 129** and **Figure 130**, whilst the real β -UCNPs: IR-806 concentration takes into account only the bound IR-dye to the surface of the β -UCNPs. The last two rows indicate the number of IR-dye antennas per single β -UCNP when considering the molecular weight of IR-806 as 657 g/mol or 784 g/mol.

5.4 Analysis of excitation dynamics in dye-sensitized upconversion core and core@active shell nanoparticles.

The content of this section substantially covers the main topic presented in Ref. ²⁷⁵ The results have been carried out thanks to a joint collaboration between the department of Physics and Astronomy of the University of Southampton and the Skolkovo Institute of Science and Technology in Moscow, under the supervision of Prof. Antonios Kanaras and Prof. Pavlos Lagoudakis. The particles used in the next experiments were synthesised and characterized in Southampton by the author of this thesis according to the previous sections while a deep analysis of their excitation dynamics was performed in Moscow by Sergey Alyatkin and the study is presented below.

5.4.1 Non-radiative energy transfer in dye-sensitized β -UCNPs

In the following experiments, the core-only and core@active shell β -UCNPs prepared and characterized according to **Section 5.1**, **Section 5.2** and **Section 5.3** were used. At the optimum β -UCNPs: IR-806 concentration of 0.8 mg/ml: 0.003 mg/ml (see **Section 5.3.1**), for the dye-sensitized sets of core-only and core@active shell, spectrally resolved measurements were performed under photoexcitation at 800 nm (a pulse train with a frequency of 295 Hz, duty cycle 5%) and the UC emission was observed. The set-up used to measure UC luminescence in the present section is described in **Section 2.6.4**.

Figure 136a shows the UC spectra of the dye-sensitized core@active shell β -UCNPs as a function of the excitation power. The main emission bands of the β -UCNPs correspond to the following transitions of Er^{3+} ions: $^2\text{H}_{11/2} \rightarrow ^4\text{I}_{15/2}$ (~525 nm), $^4\text{S}_{3/2} \rightarrow ^4\text{I}_{15/2}$ (~540 nm), and $^4\text{F}_{9/2} \rightarrow ^4\text{I}_{15/2}$ (~657 nm). The integrated intensity in the spectral range of 510–690 nm of the Er^{3+} emission followed a quadratic dependence on the pump power, providing evidence of dye-sensitized UC. As shown in **Figure 136b** the results of the fitting clearly demonstrate the two-photon nature of the UC process.

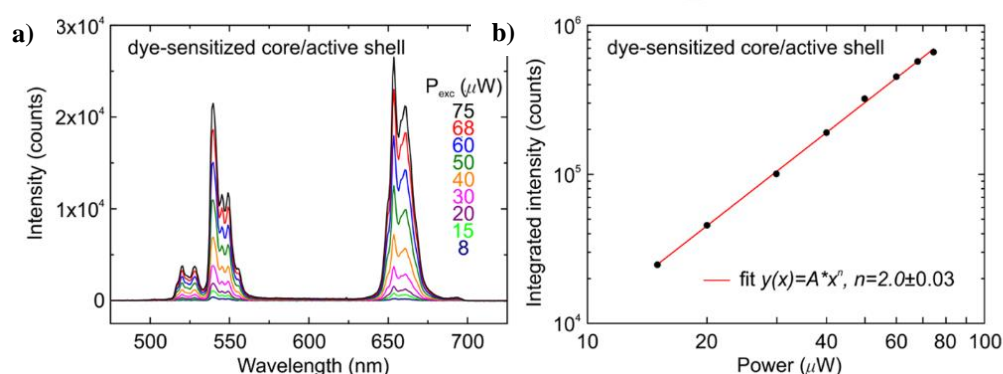


Figure 136. (a) UC spectra of dye-sensitized core@active β-UCNPs as a function of the excitation power at 800 nm. (b) Power dependence of UC luminescence intensity of dye-sensitized core@active shell β-UCNPs, spectrally integrated in the range of 510–690 nm pumped at 800 nm.

Although spectrally resolved measurements provide strong evidence of energy transfer from the dyes to the Ln^{3+} ions, they do not allow one to distinguish whether the nature of energy transfer is radiative or non-radiative. To reveal the nature of the energy transfer process, fluorescence lifetime measurements were performed where the excitation wavelength was 800 nm and the laser repetition rate was 20 MHz. **Figure 137** shows the fluorescence decay curves of the pure dye (black solid curve), the dye attached to the core-only β-UCNPs (red solid curve), and the dye attached to the core@active shell β-UCNPs (blue solid curve). It is shown that the fluorescence decay of the pure IR-806 dye is mono-exponential with a decay time of 1.29 ns (the best fit is shown with a straight black line). The fluorescence decay of the dye molecules bound to the β-UCNPs is however nearly bi-exponential. The fast decay component (the blue dashed line) was attributed to the fluorescence of the dye molecules attached to the surface of the β-UCNPs, and the slow component (the black dashed line) was attributed to the unbound organic molecules dispersed in the solvent. Indeed, the slow component of fluorescence decay is virtually identical to that of the solution of pure dye.

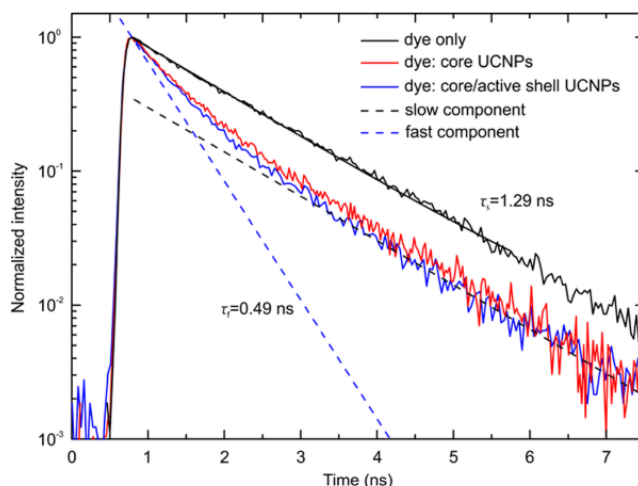


Figure 137. Fluorescence decay curves of the pure IR-806 dye molecules (black solid curve), the molecules bound to the core-only β -UCNPs (red solid curve), and the molecules bound to the core@active shell β -UCNPs (blue solid curve). Excitation wavelength was 800 nm and the laser repetition rate was 20 MHz. The non-radiative energy transfer from the IR-806 dye to the β -UCNPs is evidenced by the acceleration of the fluorescence decay from 1.29 to 0.49 ns.

To improve the accuracy of the estimation of the fast component, the decay time of the slow component was fixed to that of the pure dye, 1.29 ns here, and a biexponential function was used to fit the fluorescence decay dynamics of the hybridized systems. The fluorescence lifetime of the fast component resulted to be of 0.52 ns for the dye-sensitized core-only β -UCNPs and 0.49 ns for the dye-sensitized core@active shell β -UCNPs (see **Figure 138**).

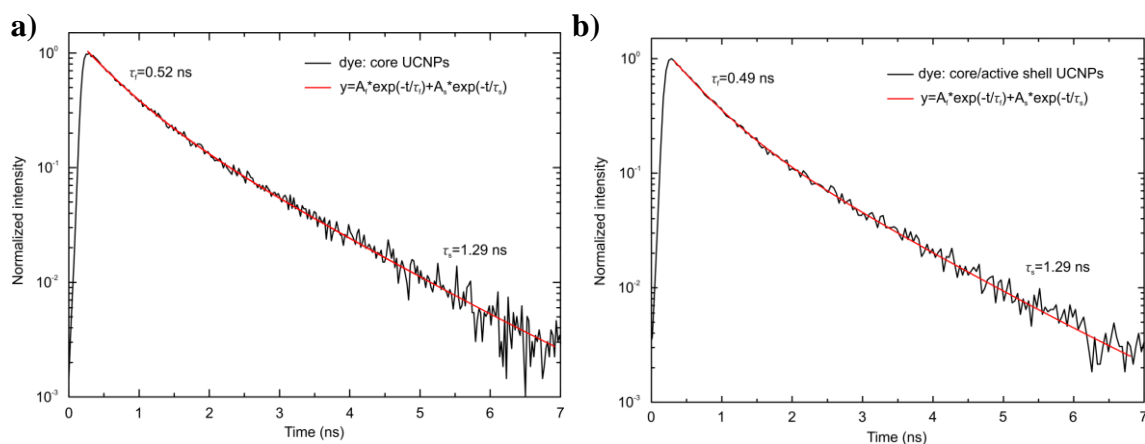


Figure 138. The fluorescence decay curves of the dye IR-806 molecules (black solid curves) attached to the surface of β -UCNPs pumped at 800 nm (1 μ W, 20 MHz) for (a) core-only and (b) core@active shell structure. Red solid curves are the results of bi-exponential fitting of the decay curves.

Therefore, the efficiency of the non-radiative energy transfer from the dye to the core@active shell β -UCNPs is $\sim 62\%$ and to the core-only β -UCNP is 59.7% .

Although we already estimated the fraction of bound dye molecules for the core-only and core@active shell β -UCNPs in a previous experiment (see **Section 5.3.2**), a theoretical evaluation was also obtained and is discussed below.

It was noted that although the fast decay lifetime of the molecules attached to the core@active shell β -UCNPs was similar to that of the molecules attached to the core-only β -UCNPs, the ratio of the amplitudes of the fast over the slow component was distinguishably higher for the molecules attached to the core@active shell β -UCNPs ($A_f/A_s = 2.76$) than for the molecules attached to the core-only β -UCNPs ($A_f/A_s = 1.99$). This leads to reasonable evaluation of free dye fraction in solutions as $100\% / (1+2.76) \approx 26.6\%$ for dye-sensitized core@active shell β -UCNPs solution, and $100\% / (1+1.99) \approx 33.3\%$ for dye-sensitized core-only β -UCNPs solution. Therefore, it was assumed that approximately 73.4% of all dye molecules were bound with the core@active shell β -UCNPs and 66.7% of dye were bound with core-only β -UCNPs. This difference could be explained by different surface area of core-only and core@active shell β -UCNPs.

In the dye-sensitized core-only β -UCNPs, the fast component was attributed to the non-radiative ET (Förster resonance energy transfer) between the dye and Yb^{3+} and Er^{3+} ions in the core of the β -UCNPs. In dye-sensitized core@active shell β -UCNPs, the fast component was however, attributed to the non-radiative ET between the dye and Yb^{3+} ions in the shell. In our case, for a shell thickness of 4.5 nm , non-radiative energy transfer between the dye and core Yb^{3+} and Er^{3+} ions is expectedly suppressed.³⁷¹ Also, because of the large difference of the optical dipole moments of Yb^{3+} and Er^{3+} ions, we could safely assume that non-radiative energy transfer occurred predominantly from the dye to Yb^{3+} ions. Our assumption was corroborated by the experimental measurement of similar fast decay lifetimes in the case of the hybridized core-only and core@active shell β -UCNPs. Evidence of radiative energy transfer in dye-sensitized β -UCNPs is discussed in the **Section 5.4.3**.

5.4.2 Upconversion luminescence enhancement

Figure 139 shows the UC luminescence spectra of the sensitized and the non-sensitized β -UCNPs. Non-sensitized β -UCNPs were pumped at 980 nm and the dye-sensitized β -UCNPs were pumped at 800 nm under the same excitation power (50 μ W).

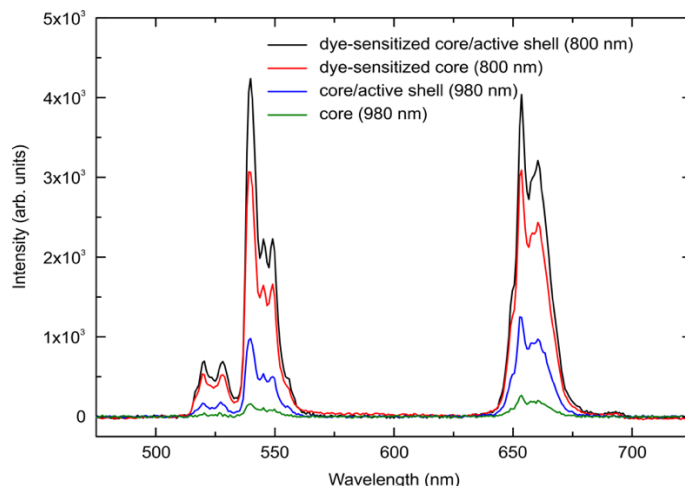


Figure 139. Comparison of the UC luminescence intensities of the non-sensitized and dye-sensitized β -UCNPs pumped with 50 μ W at 980 nm and 800 nm.

From **Figure 139**, it can be observed that the non-sensitized core-only β -UCNPs (green curve) were the least luminescent under 980 nm excitation because of the low absorption cross section inherent to the Ln^{3+} ions. It can be seen that the UC luminescence intensity of the non-sensitized core-only β -UCNPs (green curve) is ~ 5.5 times lower than UC luminescence intensity of non-sensitized core@active shell β -UCNPs (blue curve) because of the reduced surface quenching and increased number of Yb^{3+} ion sensitizers of the latter.¹³⁸ Dye-sensitized core-only β -UCNPs (red curve) demonstrate an increase in intensity in comparison with non-sensitized β -UCNPs. The UC luminescence of dye-sensitized core@active shell β -UCNPs (black curve) is ~ 20 times stronger than the UC luminescence of conventional non-sensitized core-only β -UCNPs. The observed improvement of UC luminescence intensity is due to the active shell, as described above, and the non-radiative energy transfer from the epilayer of organic dyes to Yb^{3+} ions in the shell. Our observations are within the typical range of the reported enhancement factors of the UC luminescence.

371,375

However, as we already mentioned, a comparison based only on spectrally resolved measurements does not suffice to distinguish between radiative and non-radiative energy transfer. Such a comparison can easily lead to a large variation of the recorded intensity because of fluctuations in the number of β -UCNPs during the measurement, for example,

improper functionalization of the β -UCNPs' surface may lead to aggregation and precipitation of the dye-sensitized β -UCNPs. Another challenge for the dye-sensitized β -UCNPs is related to their photostability. In this study, we ensure that the excitation configuration leads to highly reproducible results both for spectrally and time-resolved measurements. From **Figure 140**, it can be seen the photostability of dye-sensitized β -UCNPs.

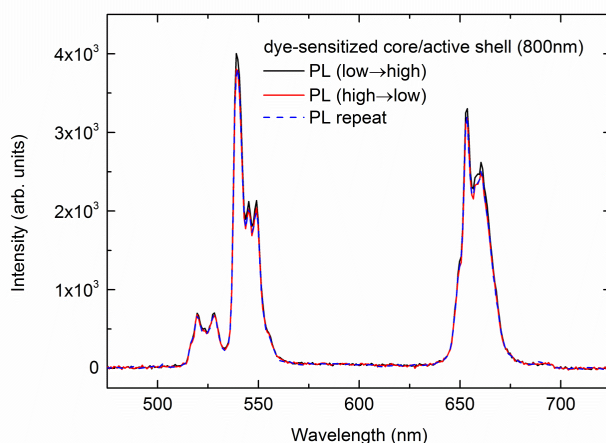


Figure 140. Reproducibility of UC luminescence signal (at 800 nm photoexcitation) to demonstrate short-term photostability of dye-sensitized β -UCNPs. Black solid curve shows PL of β -UCNPs when excitation power (here 50 μ W) was increased step by step from low value (8 μ W) to higher (75 μ W). Red curve shows PL of β -UCNPs when excitation power was decreased from 75 μ W to 50 μ W. Blue dashed curve shows results of repeated one more time PL measurement at 50 μ W excitation.

A broad range of enhancement factors has been reported in the literature for UCNPs of different sizes, compounds, and dye sensitizers.³⁷⁶ Expectedly, there is a correlation between the UC enhancement and the diameter of the UCNPs. The number of Ln^{3+} ion sensitizers for non-sensitized β -UCNPs scales with the third power of the particle's diameter, whereas for the dye-sensitized β -UCNPs, the number of dye sensitizers scales with the second power of the particle's diameter. Thus, the UC luminescence enhancement due to dye sensitization is defined by the ratio of absorbers at the excitation wavelengths resonant to the absorption of the dye and the Ln^{3+} ion. This results in a monotonic dependence of the enhancement factor on the particle's diameter, when considered solely from a geometric perspective. Additionally, the smaller the diameter of the UCNPs, the higher the proportion of the Ln^{3+} ions that can interact non-radiatively with the dye sensitizers. We note a further correlation between the initial UC efficiency of the UCNPs and the obtained enhancement factor. As ultrasmall UCNPs suffer from very low UC efficiency because of the negative influence of

non-radiative surface states, they allow for a significant UC luminescence enhancement. In view of the aforementioned discussion, the comparison of enhancement factors in different systems is not obvious.

5.4.3 Excitation dynamics in non-sensitized and dye-sensitized β -UCNPs

In this section, it is investigated the excitation dynamics in the dye-sensitized and non-sensitized β -UCNPs.

5.4.3.1 Non-sensitized Core-Only and Core@Active Shell β -UCNPs.

The luminescence kinetics of the involved Er^{3+} transitions are different for green and red lines of emission and strongly dependent on the experimental conditions. However, the luminescence intensity of these lines quadratically depends on the excitation intensity that was confirmed experimentally in **Figure 136**.

The study of kinetics of dye-sensitized and non-sensitized UCNPs at different excitation intensities even for a particular wavelength is a non-trivial task because of the complicated internal dynamics within the UCNPs. Here, we spectrally integrated the UC luminescence in the range of 510–690 nm and time-resolved the UC kinetics of the non-sensitized core-only, shown in **Figure 141a** (red curve), and non-sensitized core@active shell β -UCNPs shown in **Figure 141b** (red curve), under 980 nm excitation.

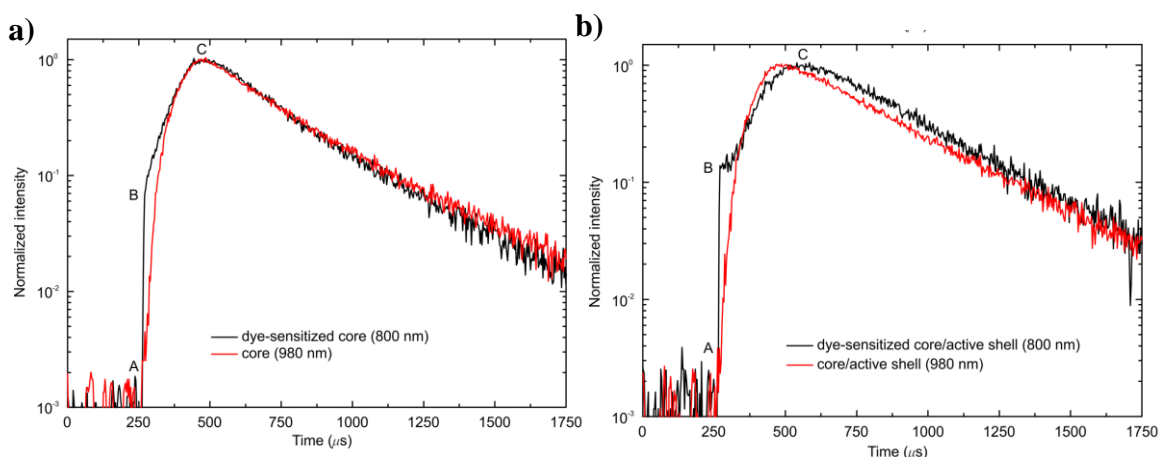


Figure 141. The UC kinetics of non-sensitized and dye-sensitized β -UCNPs pumped with 50 μW at 980 nm and 800 nm, respectively for (a) core-only and (b) core@active shell β -UCNPs. The UC luminescence rise dynamics between non-sensitized (red curves) and dye-sensitized (black curves) β -UCNPs differ substantially. The rise dynamics of the UC luminescence of dye-sensitized β -UCNPs is characterised by two-components: the fast component (AB) is driven by direct radiative pumping of Er^{3+} ions from the dyes, while the

slow component (BC) is due to non-radiative energy transfer from the dyes predominantly to Yb^{3+} ions, followed by non-radiative energy transfer from Yb^{3+} to Er^{3+} ions.

In both cases, the rise dynamics during the excitation pulse ($\sim 170 \mu\text{s}$) are virtually the same.

For convenience, the two curves are shown on the same panel in **Figure 142**.

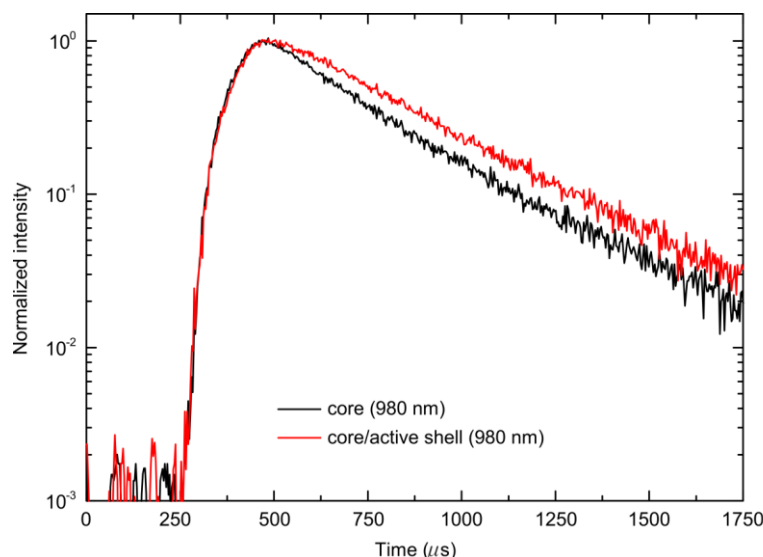


Figure 142. UC kinetics of non-sensitized core-only (black solid curve) and core@active shell (red solid curve) β -UCNPs pumped at 980 nm with frequency of 295 Hz, duty cycle 5%.

According to **Figure 142** and following the excitation pulse, the UC luminescence of the core@active shell β -UCNPs exhibits a longer lifetime in comparison with the UC luminescence of the core-only β -UCNPs, which confirms better surface passivation in the core@active shell β -UCNPs. In both the cases, the rise time ($\sim 220 \mu\text{s}$) of the kinetics is associated with non-radiative energy transfer from Yb^{3+} to Er^{3+} ions rather than the radiative energy transfer, as the rise time is much shorter than the luminescence lifetime of Yb^{3+} ions in the host matrix (2.3 ms).³⁷⁷

5.4.3.2 Non-sensitized Core-Only and Dye-Sensitized Core-Only β -UCNPs

From **Figure 141a**, it is easy to compare the UC kinetics of the non-sensitized core-only β -UCNPs and dye-sensitized core-only β -UCNPs pumped at 980 and 800 nm, respectively. The main difference lies in the rise time of the dye-sensitized UC luminescence that consists of two components; annotated in **Figure 141a** with letters A–C. The first component (AB) was extremely fast (sub-microsecond) (black curve) in comparison with the rise time of the

non-sensitized UC luminescence ($\sim 220 \mu\text{s}$) (red curve). The second component (BC) initially showed slower dynamics than that in the non-sensitized β -UCNPs, until finally both kinetics coincided.

In the following, it is discussed the various processes that could contribute to the observed ultrafast UC in the dye-sensitized core-only β -UCNPs. Among the possible excitation routes of Er^{3+} ions are both the radiative and non-radiative energy transfer from the IR-806 dye.

The lifetime measurements of the dye emission revealed that the non-radiative energy transfer from the dye molecules to Er^{3+} is less effective than that to Yb^{3+} ions, although this path's contribution to the ultrafast rise time cannot be excluded. This issue is addressed in the next paragraph, with a discussion in the kinetics of the dye-sensitized core@active shell β -UCNPs.

Another possible excitation route of Er^{3+} ions in the dye-sensitized β -UCNPs is *via* Yb^{3+} ions, excited by the dye. However, following from the previous experiments, the energy transfer from the excited Yb^{3+} led to a slower rise time of the UC luminescence. The addition of the dye sensitizer in the chain of energy transfer would make the rise time even slower in comparison with the non-sensitized β -UCNPs. Therefore, although this excitation path describes well the slow component (BC) of the rise time of the dye-sensitized UC luminescence, it cannot describe the fast one (AB). Thus, it is conceivable that the fast component of the UC luminescence is due to the radiative pumping of Er^{3+} ions by the dye sensitizer that has a fluorescence lifetime of $\sim 1.29 \text{ ns}$.

5.4.3.3 Non-sensitized Core@active shell and Dye-Sensitized Core@Active Shell β -UCNPs.

Figure 141b compares the UC kinetics of the dye-sensitized core@active shell β -UCNPs pumped at 800 nm and the non-sensitized core@active shell β -UCNPs pumped at 980 nm. Similar to the dye-sensitized core-only β -UCNPs, in the dye-sensitized core@active shell β -UCNPs we observed a very abrupt (sub-microsecond) increase of the UC luminescence, followed by a slow component ($\sim 310 \mu\text{s}$).

First, we can eventually clarify the contribution of the radiative energy transfer from the IR-806 dye to Er^{3+} ions. Considering the UC kinetics of the dye-sensitized core-only and the dye-sensitized core@active shell β -UCNPs (**Figure 143**), the fast components of the rise time look very similar in amplitude and overlap in time.

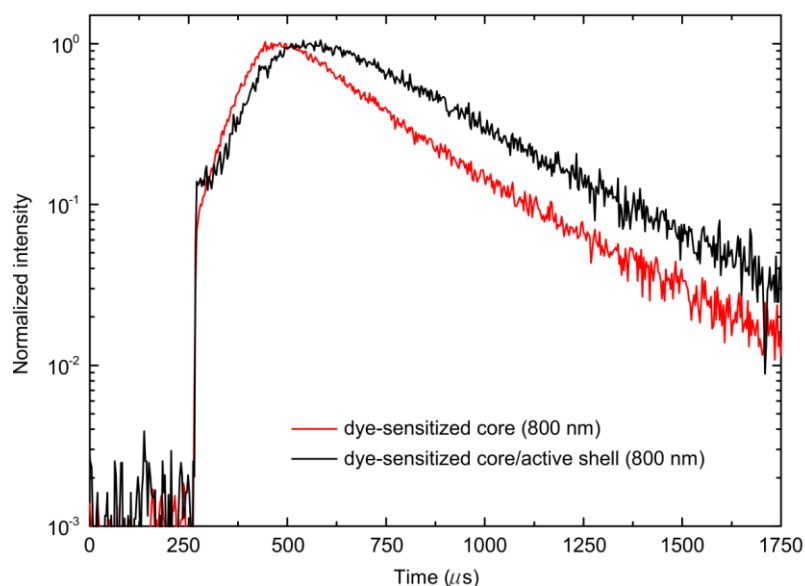


Figure 143. UC kinetics of dye-sensitized core@active shell (black solid curve) and dye-sensitized core-only (red solid curve) β -UCNPs pumped at 800 nm with frequency of 295 Hz, duty cycle 5%.

As the shell significantly suppresses the non-radiative energy transfer from the dye molecules to Er^{3+} ions, we concluded that the fast component of the rise time was due to the direct radiative pumping of Er^{3+} ions by the fluorescent dye (see cartoon illustrating the process in **Figure 144**).

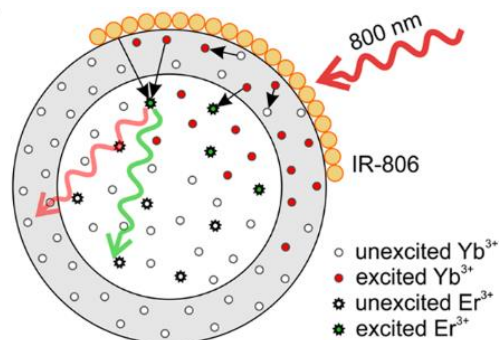


Figure 144. Principle of dye-sensitized UC for core@active shell β -UCNPs. Black arrows indicate possible radiative and non-radiative channels of the energy transfer in dye-sensitized β -UCNPs. Adapted from Ref. ²⁷⁵

The observed minor difference in the intensities of the fast components was due to the larger number of molecules attached to the surface of the core@active shell β -UCNPs with respect to the core-only β -UCNPs that have a smaller surface. We estimated the relative contribution of the radiative energy transfer to $\sim 2\%$ of the total UC luminescence and $10 \pm 1\%$ of the rise dynamics.

The rise time to the maximum of the UC luminescence in the kinetics of the dye-sensitized core@active shell β -UCNPs was significantly longer in comparison with that of the dye-sensitized core-only β -UCNPs. This difference could be attributed to the process of energy migration between Yb^{3+} ions in the shell.^{3,260,273} Yb^{3+} ions excited by the dye sensitizers would bring the energy across the shell and would transfer it non-radiatively to the core Yb^{3+} and Er^{3+} ions. Therefore, the thickness of the active shell plays an important role in optimizing the UC luminescence enhancement.

It should be chosen so that the time necessary for the energy migration through the shell for the subsequent sensitization of the core Er^{3+} ions is shorter than the lifetime of Yb^{3+} ions in the host matrix. The fine-tuning of the energy migration time can be achieved *via* design of the spatial separation of the dopant ions.³⁷⁸

5.5 Downconversion luminescence properties

UCNPs exhibit efficient downconversion (DC) NIR emissions in addition to their UC emissions. DC luminescence is described as the conversion of higher energy photons into lower energy photons.^{379,380} Contrary to UC, DC is a linear process and therefore the efficiency is independent of the incident power. To date, there are several reports in the literature about UC and DC luminescence in β - NaYF_4 UCNPs.^{116,235,381} To the best of our knowledge, among the reported UC materials, there are no investigation in the NIR-DC of UCNPs with NIR-dyes attached on their surfaces. Herein, in this section, we investigate the downshifted NIR emission (1550 nm) behaviour for the dye-sensitized core-only, core@inert shell, and core@active shell, upon 800 nm excitation.

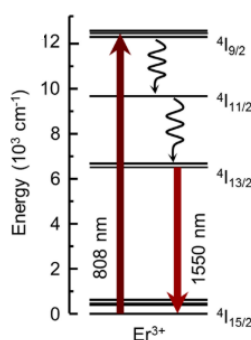


Figure 145. Energy level diagram of Er^{3+} showing the excitation (808 nm) and the downshifted emission (1550 nm) levels. Picture adapted by Ref.³⁸¹

The 806-dye-sensitized and no sensitized β -UCNPs were freshly prepared from the same batch of core-only and core@active shell (see **Section 5.3**). In order to obtain the most efficient dye-sensitized UC system, we studied the optimal surface coverage on the as-prepared β -UCNPs by the dye molecules. All samples were prepared in identical conditions in a quartz cuvette, with a final concentration of 0.8 mg/ml of β -UCNPs in CHCl_3 and the IR-806 dye concentration was varied as following: 0.000, 0.001, 0.003, 0.005, 0.007, and 0.010 mg/ml. The samples were excited by 800 nm laser (50 mW). The set-up used to measure DC luminescence in the present section is similar to the one described in the previous section but using an IR spectrometer to collect the emission (see **Figure 21**).

The DC emission spectra and integrated emission intensity in the range 1450-1650 nm as a function of IR-806 content are shown in **Figure 146** and **Figure 147** for the core-only, and core@active shell, respectively. The optimum β -UCNPs:IR-806 concentration was determined to be 0.8 mg/ml: 0.003 mg/ml in agreement to the UC experiments carried out days before in **Section 5.3.2**. Due to the low signal, it was not possible to record DC data for the core@inert shell β -UCNPs.

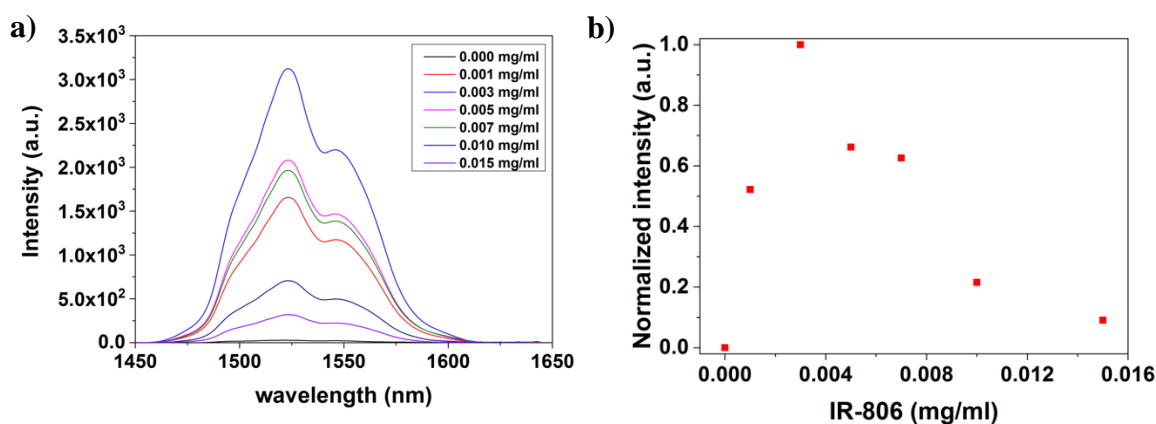


Figure 146. (a) DC emission spectra of IR-806 – sensitized core-only in function of IR-806 dye and (b) normalized DC emission intensities integrated in the range 1450-1650 nm of β - $\text{NaYF}_4\text{:Yb}^{3+}(20\%), \text{Er}^{3+}(2\%)$ (0.8 mg/ml) as a function of IR-806 content in CHCl_3 excited by 50 mW 800 nm laser and 10 seconds of exposure time.

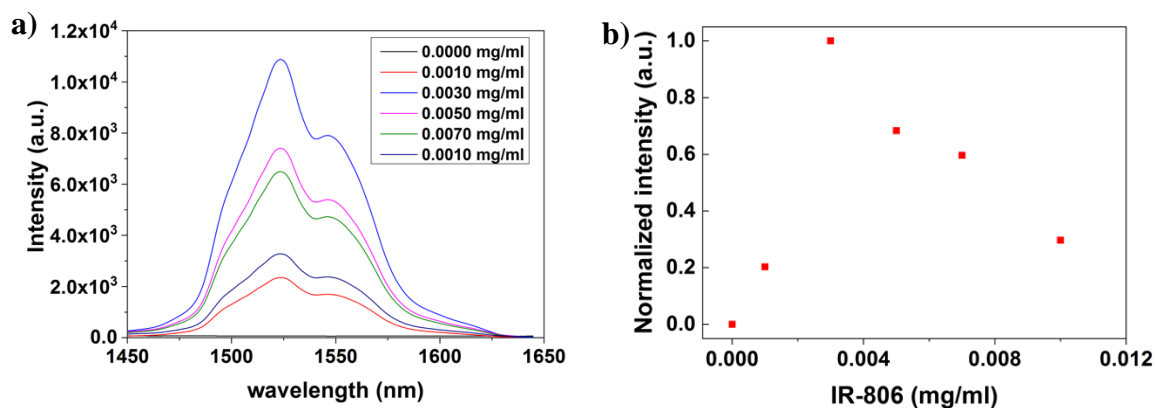


Figure 147. (a) DC emission spectra of IR-806 – sensitized core@active shell in function of IR-806 dye and (b) normalized DC emission intensities integrated in the range 1450-1650 nm of β -NaYF₄:Yb³⁺(20%), Er³⁺(2%)@ NaYF₄:Yb³⁺(10%) (0.8 mg/ml) as a function of IR-806 content in CHCl₃ excited by 50 mW 800 nm laser and 10 seconds of exposure time.

The DC emission spectra and excitation spectra of the optimized dye sensitized UCNP (β-UCNP: IR-806 - 0.8 mg/ml: 0.003 mg/ml) were measured to investigate whether energy transfer from the IR-806 dye molecules to Yb³⁺ and Er³⁺ ions of the core UCNP could occur.

The NIR emission spectra of dye-sensitized core-only under the 800 nm and non-sensitized core-only at 980 nm excitation is shown in **Figure 148a**. As can be seen, in both cases, the emission intensity includes a strong emission peak around ~1550 nm, which could be assigned to the $^4F_{13/2} \rightarrow ^4I_{15/2}$ transition of Er³⁺ ion. It was observed that the NIR-sensitized core-only β-UCNPs excited at 800 nm (red line) exhibited a ~1.3 stronger enhancement than the non-sensitized core-only β-UCNPs excited at 980 nm (black line).

Figure 148b shows the integrated intensity in a range of 1450-1650 nm of the emission when plotted against different excitation wavelengths and showed that the dye-sensitized core-only β-UCNPs can be activated separately at the excitation wavelength of 800 nm and 980 nm. It was noted that NIR emission first increased, approached a maximum at 800 nm and decreased quickly. A further increment in the excitation wavelength monotonically increased the NIR emission to a maximum at 980 nm and finally decreased recurrently.

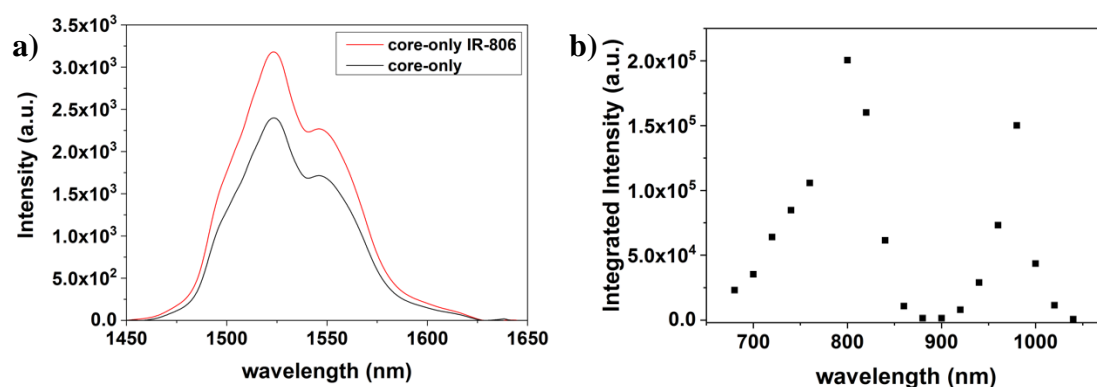


Figure 148. (a) DC emission intensities of IR-806-sensitized core-only β -UCNPs in CHCl_3 (0.003 mg/ml: 0.8 mg/ml) under 800nm laser excitation (red line) and emission of the same particles with no dye under 980 nm laser excitation (black line). (b) Integrated intensity in the range of 1450-1650 nm of the DC emission for the core-only β -UCNPs (0.003 mg/ml: 0.8 mg/ml) dissolved in CHCl_3 at different excitation wavelengths. All measurements were taken under a 57 mW laser excitation, and 10 seconds of exposure time.

To investigate the DC mechanism we have also studied the pump power dependence of IR-sensitized core-only for the excitation wavelengths at 800 nm and of non-sensitized core-only excited at 980 nm. The results are displayed in **Figure 149** on a double logarithmic plot. **Figure 149** shows the power dependence of DC luminescence intensity of dye-sensitized core-only, spectrally integrated in the range of 1450–1650 nm pumped at 800 nm (red line). The non-sensitized core-only pumped at 980 nm is represented in a black line.

We used the relation between the DC emission intensity and laser power expressed as:

$$I_{DC} \sim P^n \quad (21)$$

where I and P denote the DC emission intensity and pump power, respectively, and (n) refers to the number of photons absorbed per photon emitted, and its value can be derived from the slope of the fitted line of the plot $\log(I_{DC})$ vs $\log(P)$. We extracted the values of the exponent n of the β -UCNPs from a linear fitted of the experimental data. The values of the parameter n (photons absorbed per photon emitted) for DC emissions were found to be 0.93 for IR-sensitized core-only excited at 800 nm and 0.96 for non-sensitized core-only excited at 980 nm. In both cases, the results of the fitting clearly demonstrate the one-photon nature of the DC process.

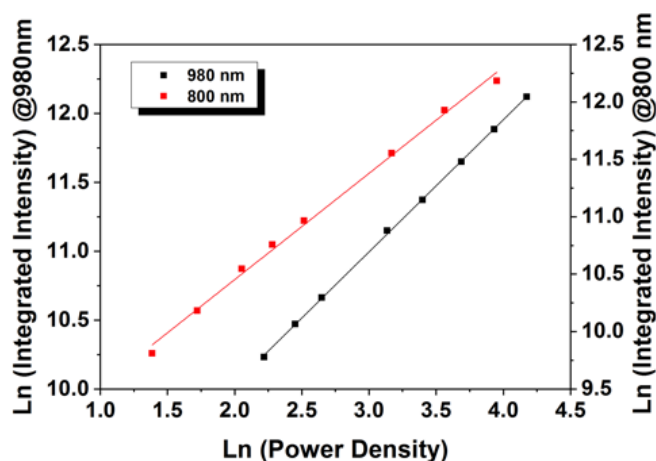


Figure 149. Power dependence of DC luminescence intensity of IR-806-sensitized core-only β -UCNPs, spectrally integrated in the range of 1450–1650 nm pumped at 800 nm (red line) and non-sensitized core-only excited at 980 nm (black line).

Similar behaviour was observed for the dye-sensitized core@active shell. The comparison of PL spectra for dye-sensitized core@active shell excited at 800 nm and non-sensitized core@active shell at 980 nm is shown in **Figure 150a**. It can be seen that the NIR-sensitized core@active shell β -UCNPs excited at 800 nm (red line) exhibited a ~ 2.6 stronger enhancement than the non-sensitized core@active shell excited at 980 nm (black line). **Figure 150b** displays the integrated intensity over 1450–1650 nm range of the emission when plotted against different excitation wavelengths and demonstrated that the dye-sensitized core@active shell β -UCNPs can be also activated separately at the excitation wavelength of 800 nm and 980 nm.

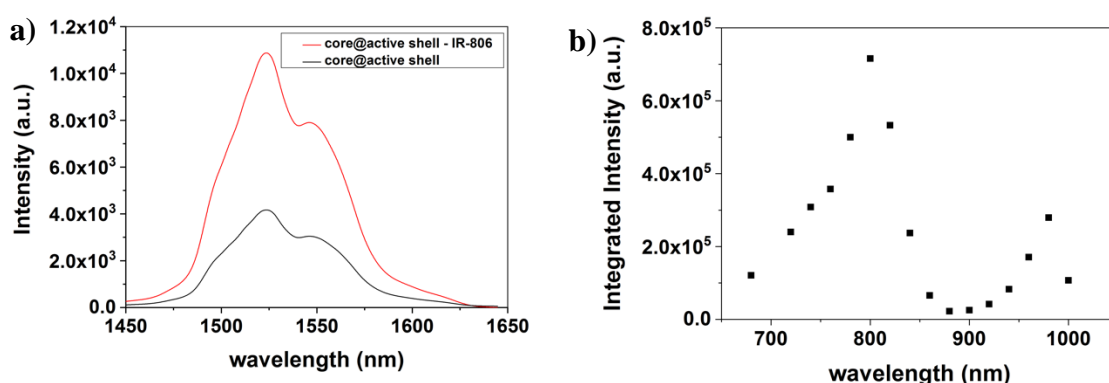


Figure 150. (a) DC emission intensities of IR-806-sensitized core@active shell β -UCNPs in CHCl_3 (0.003 mg/ml: 0.8 mg/ml) under 800 nm laser excitation (red line) and DC emission of the same particles with no dye under 980 nm laser excitation (black line). (b) Integrated intensity in the range of 1450–1650 nm of the DC emission for the core@active shell β -

UCNPs (0.003 mg/ml: 0.8 mg/ml) dissolved in CHCl_3 at different excitation wavelengths. All measurements were taken under a 50 mW laser excitation.

The pump power dependence of IR-sensitized core@active shell for the excitation wavelengths at 800 nm and of non-sensitized core@active shell excited at 980 nm have been also investigated. The results are displayed in **Figure 151** on a double logarithmic plot.

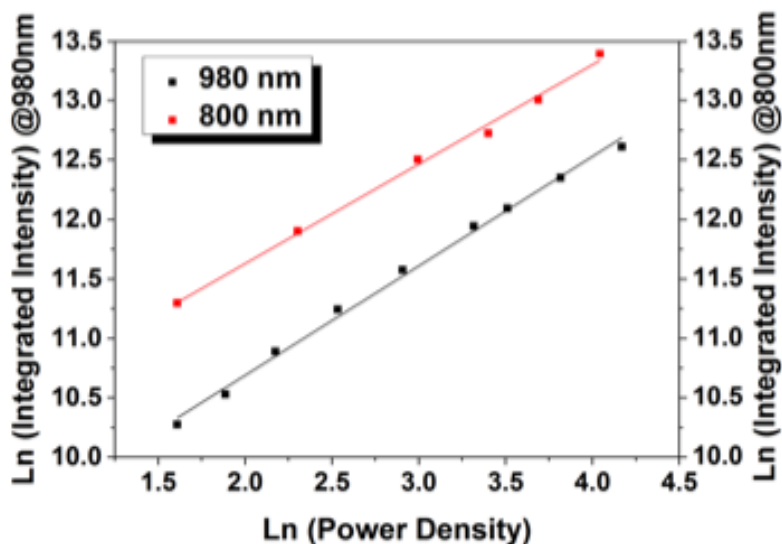


Figure 151. Power dependence of DC luminescence intensity of IR-806-sensitized core@active shell β -UCNPs, spectrally integrated in the range of 1450–1650 nm pumped at 800 nm (red line) and non-sensitized core@active shell excited at 980 nm (black line).

Figure 151 shows the power dependence of DC luminescence intensity of dye-sensitized core@active shell and non-sensitized core@active shell, pumped at 800 nm (red line) and at 980 (black line), respectively, spectrally integrated in the range of 1450–1650 nm. The values of the parameter n (photons absorbed per photon emitted) for DC emissions were found to be 0.98 for IR-sensitized core@active shell excited at 800 nm and 0.92 for non-sensitized core@active shell excited at 980 nm. Again, in both cases, the results of the fitting clearly demonstrate the one-photon nature of the DC process.

In addition, we measured the PL spectra for the core@inert shell. **Figure 152a** shows the NIR emission spectra of dye-sensitized core@inert shell under the 800 nm (red line) and non-sensitized core@inert shell under a 980 nm excitation (black line). **Figure 152b** displays the integrated intensity of IR-sensitized core@inert shell over the 1450-1650 nm range of the emission when plotted versus different excitation wavelengths. It can be seen

that, as expected from previous UC experiments, DC emissions at 1550 nm only existed when exciting at 980 nm. The result of the fitting from **Figure 153** clearly demonstrate the one-photon nature of the DC process indicative from the parameter $n=0.74$ obtained from the slope.

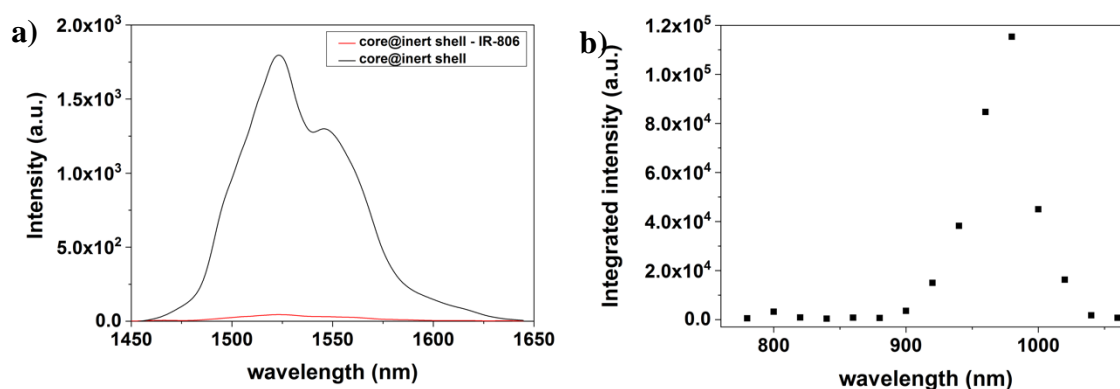


Figure 152. (a) DC emission intensities of IR-806-sensitized core@inert shell β -UCNPs in CHCl_3 (0.003 mg/ml: 0.8 mg/ml) under 800 nm laser excitation (red line) and DC emission of the same particles with no dye under 980 nm laser excitation (black line). (b) Integrated intensity in the range of 1450-1650 nm of the DC emission for the core@inert shell β -UCNPs (0.003 mg/ml: 0.8 mg/ml) dissolved in CHCl_3 at different excitation wavelengths. All measurements were taken under a 50 mW laser excitation.

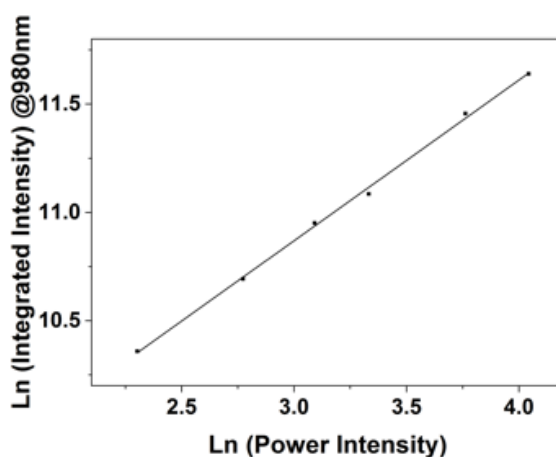


Figure 153. Power dependence of DC luminescence intensity of β - $\text{NaYF}_4:\text{Yb}^{3+}(20\%), \text{Er}^{3+}(2\%)$ @ NaYF_4 spectrally integrated in the range of 1450 – 1650 nm pumped at 980 nm.

In the following, we present the results contrasted in a single diagram to facilitate the comparison. **Figure 154** shows the DC emission spectra for the IR-sensitized core-only and IR-sensitized core@active shell when excited at 800 nm (red and green lines) and the DC emission spectra for the core-only and core@active shell when excited at 980 nm (black and blue lines).

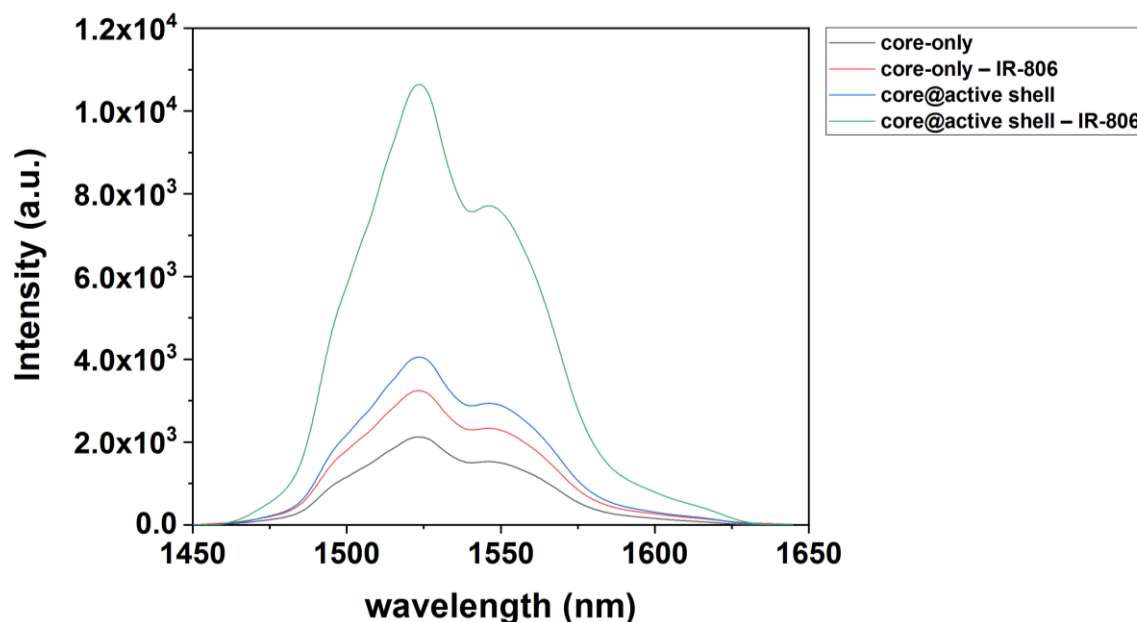


Figure 154. DC emission spectra of the different types of β -UCNPs. Measured by a 50 mW, 980 nm and 800 nm laser excitation (10 s).

We found the IR-sensitized core@active shell pumped at 800 nm to be the brightest. The emission is ~ 5.02 times higher than that of the non-sensitized core-only pumped at 980 nm and ~ 2.62 times higher than that of IR-sensitized core-only pumped at 800 nm. Results provide direct evidence of achieving enhance DC luminescence from a structure with active dopant established in the epitaxial shell.

5.6 Alleviating concentration quenching through IR-1076 nm.

One of the most important reason of the low efficiency UC luminescence as mentioned in previous chapters, is the concentration quenching effect when using high levels of the activator (Er^{3+} ions) concentration. Wei et al. reported a strategy based on the use of a IR-dye in $\text{NaYF}_4:\text{Nd}^{3+}$ UCNPs to alleviate the quenching concentration. They boosted the UC luminescence ~ 10 times by increasing the concentration of Nd^{3+} from 2% to 20% through sensitization at 800 nm of an ICG dye on the surface of the particles.³⁸²

We envisioned that this strategy might also work for a different IR dye absorbing a different IR part of the solar spectrum. In the previous sections we have shown that by using the organic IR-806 dye as sensitizer, photons with energies across a broader wavelength range were absorbed by the dye, and then the energy transfer from the dye to the β -UCNPs resulted in a dramatic 20-fold enhancement of the overall UC emission of β -UCNPs. We assume that this strategy might also work for a different band of the IR spectrum. The desired working principle is that the new organic dye sensitizers, bound to the β -UCNPs and absorbing a different IR part of the solar spectrum, transfer the absorbed energy to the β -UCNPs breaking the concentration quenching of the ion activator producing an enhancement of the UC emission.

We considered that the commercially available IR-1048 dye would be a good candidate as starting material in this investigation, because it has structural similarities with the IR-806 dye, already studied.

The chemical modification of the commercial IR-1048 dye to obtain the carboxylic acid-functionalized organic dye was carried out following the identical experimental procedure described for the preparation of the IR-806; using the IR-1048 dye instead of the IR-780 dye (see **Figure 155**).

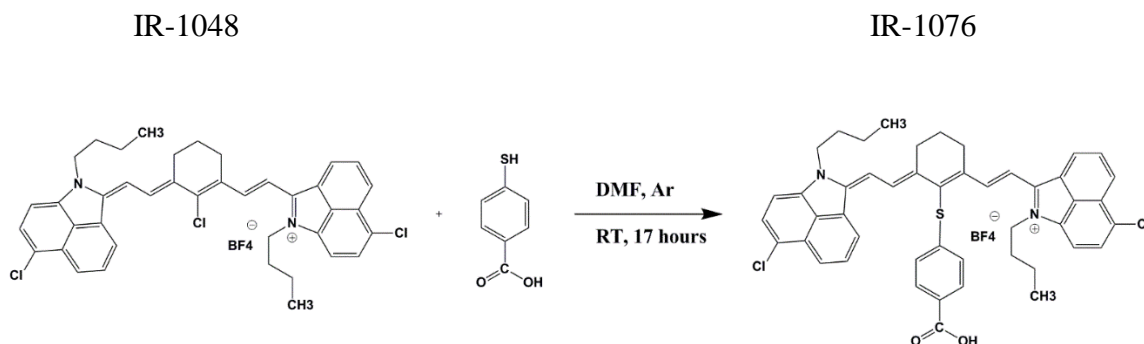
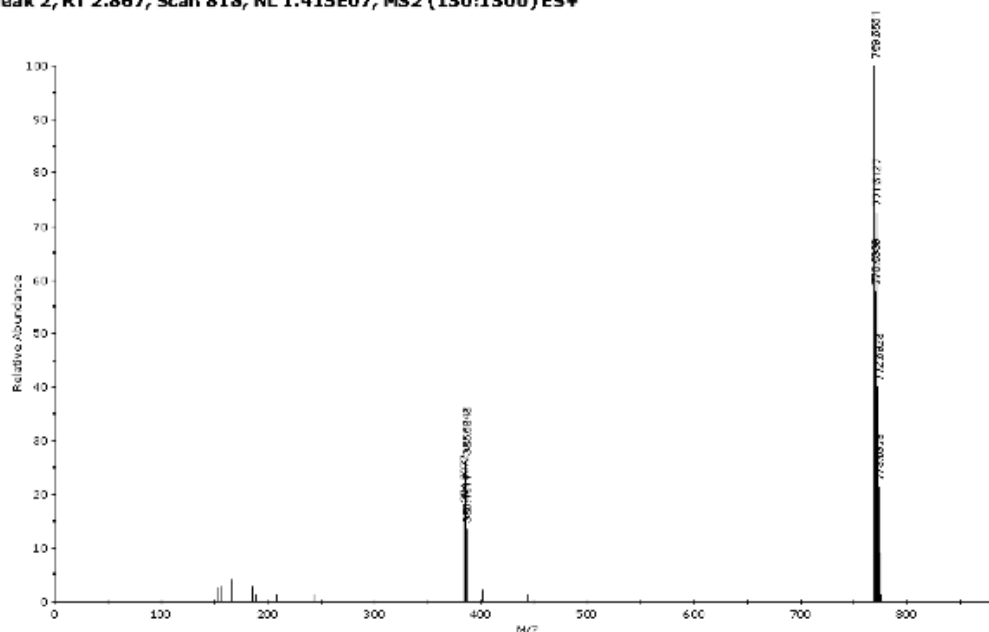


Figure 155. Proposed synthesis to obtain the IR-1076 nm through the IR-1048 nm.

According to the HRMS spectra from **Figure 156** the found mass was $[M]^+ = 769.56$, which agrees with the one calculated using ChemDraw software which resulted to be $[M]^+ = 769.24$. However, the nucleophilic substitution reaction allows for three possible isomers (**Figure 157**), depending on the attacking chlorine atom. Therefore, verification and separation of isomers need to be achieved before further experiments.

Peak 2, RT 2.867, Scan 818, NL 1.415E07, MS2 (150:1500) ES+



the IR-1076 shown in **Figure 159** revealed that in order to overlap the emission of the dye with the absorption of the β -UCNPs, we need to use β -UCNPs that absorb in the 1100-1250 nm region.

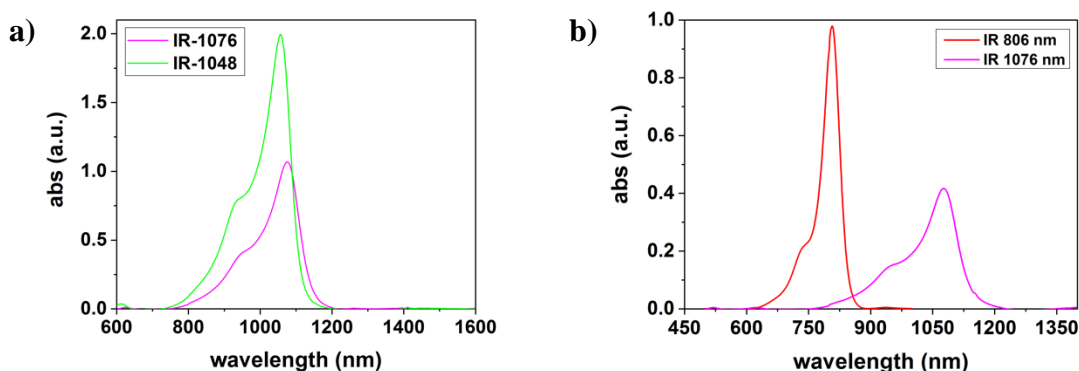


Figure 158. (a) Absorption spectra of IR-1048 nm (0.4 μ g/ml) and IR-1076 nm (5 μ g/ml) dispersed in CHCl₃. (b) Absorption spectra of IR-806 vs IR-1076 (0.25 μ g/ml) in CHCl₃.

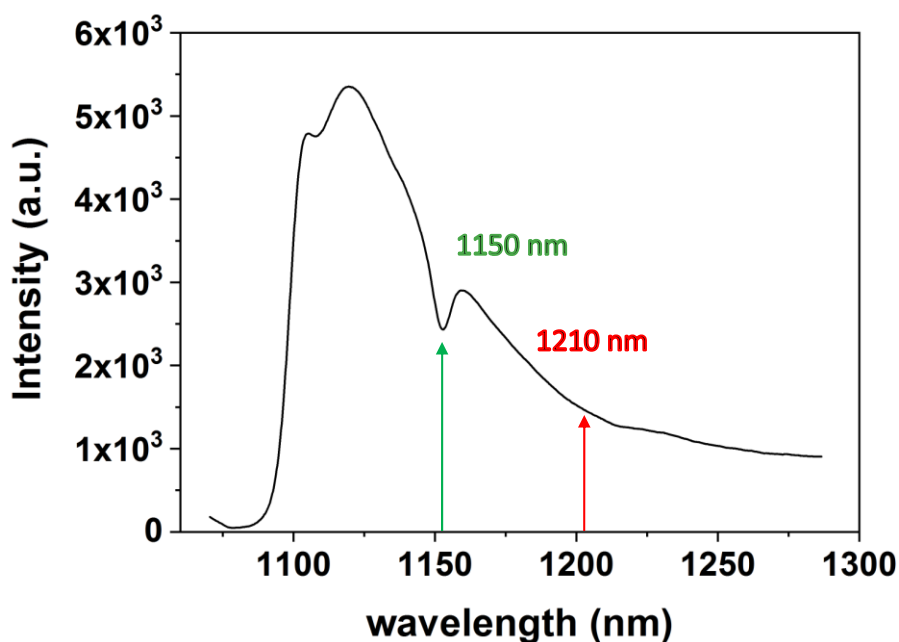


Figure 159. Emission intensities of IR-1076 dye in CHCl₃ under 77 mW, 1070 nm laser excitation (5s).

After a literature search we reasoned that NaYF₄: Ho³⁺ and NaYF₄: Tm³⁺ are the most appropriate candidates for the IR-1076 dye sensitizing. Two samples of NaYF₄: Ho³⁺ (1%) and NaYF₄: Tm³⁺ (5%) were prepared following the experimental procedure detailed in **Section 2.1.1**.

β -NaYF₄: Ho³⁺ (1%) UCNP were synthesised by adding the corresponding YCl₃·6H₂O (0.795 mmol, 241.17 mg), and HoCl₃·6H₂O (0.005 mmol, 1.92 mg); while β -NaYF₄: Tm³⁺ (5%) UCNP were synthesised by adding the corresponding YCl₃·6H₂O (0.795 mmol, 241.17 mg), and TmCl₃·6H₂O (0.005 mmol, 1.92 mg) at the initial step of the reaction. The particles sizes and their morphologies were first characterized by TEM. A representative TEM image of the resulting particles and the corresponding size histogram are illustrated in **Figure 160** and **Figure 161**, indicating a narrow size distribution of 21 nm \pm 1 nm and 28 nm \pm 3 nm for the β -NaYF₄: Tm³⁺ (5%) and β -NaYF₄: Ho³⁺ (1%), respectively. The size distribution was analysed considering over 100 UCNP for both of the samples.

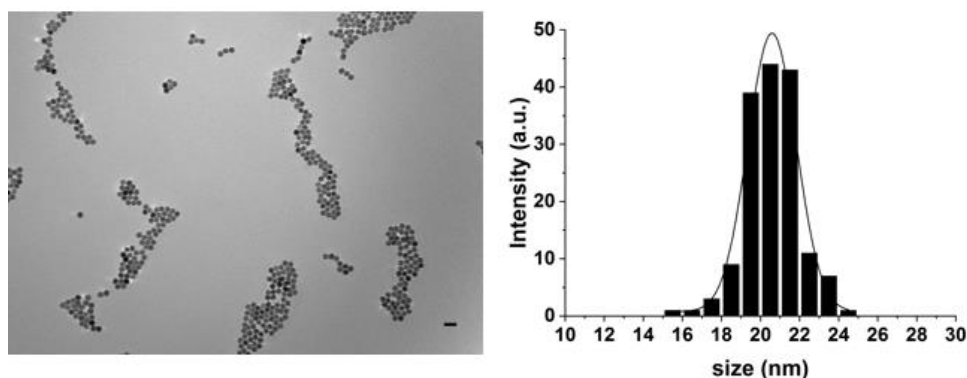


Figure 160. TEM images and size distribution of the β -NaYF₄: Tm³⁺ (5%) UCNP. Scale bars are 50 nm.

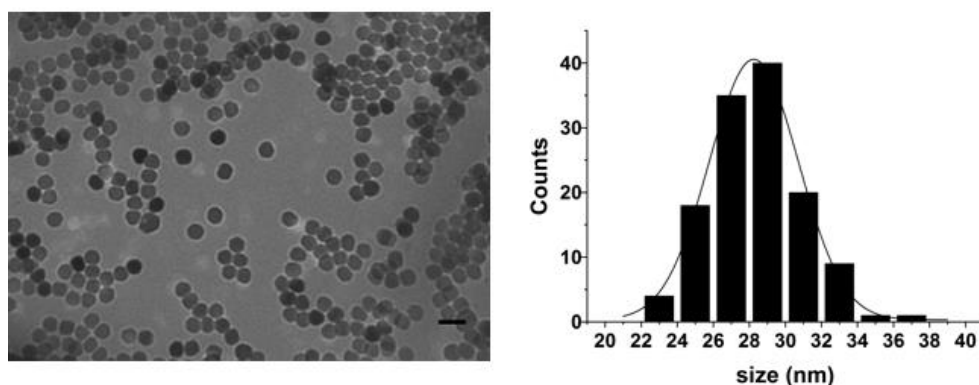


Figure 161. TEM images and size distribution of the β -NaYF₄: Ho³⁺ (1%) UCNP. Scale bars are 50 nm.

Figure 162 and **Figure 163** show the experimental UC luminescence of β -NaYF₄: Ho³⁺ (1%) and β -NaYF₄: Tm³⁺ (5%), respectively in function of different excitation wavelengths. The results revealed that the former emitted higher luminescence when excited at 1150 nm, while the latter obtained maximum luminescence when excited at 1210 nm.

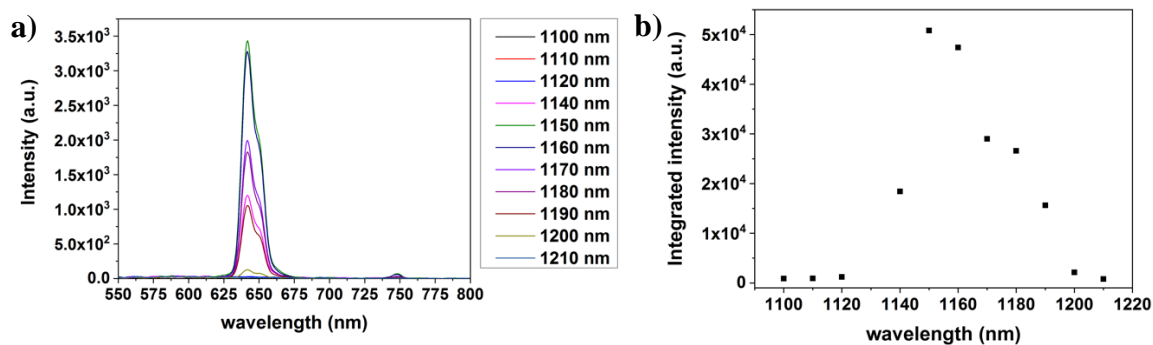


Figure 162. (a) UC emission intensities of $\beta\text{-NaYF}_4\text{: Ho}^{3+}$ (1%) in CHCl_3 in function of the laser excitation and (b) Integrated intensity in the range of 600-700 nm of the UC emission for the $\beta\text{-NaYF}_4\text{: Ho}^{3+}$ (1%) dissolved in CHCl_3 at different excitation wavelengths. All measurements were taken with 77 mW and 70 ms.

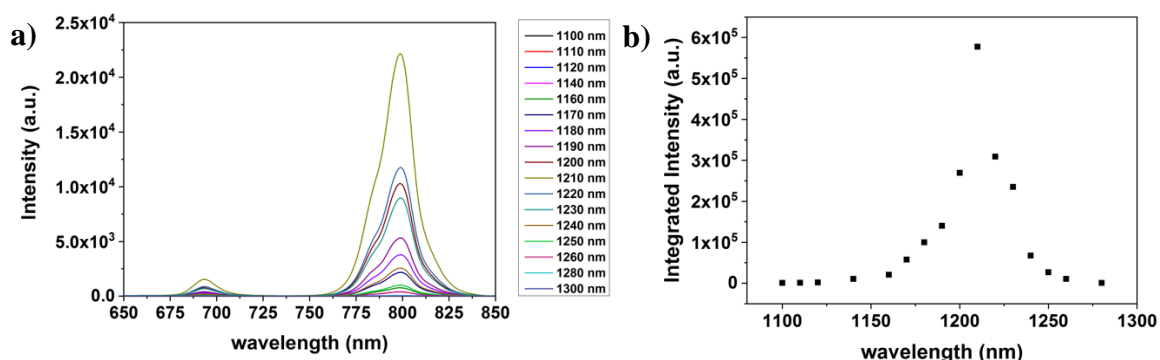


Figure 163. (a) UC emission intensities of $\beta\text{-NaYF}_4\text{: Tm}^{3+}$ (5%) in CHCl_3 in function of the laser excitation and (b) integrated intensity in the range of 650-850 nm of the UC emission for the $\beta\text{-NaYF}_4\text{: Tm}^{3+}$ (5%) dissolved in CHCl_3 at different excitation wavelengths. All measurements were taken with 77 mW and 70 ms.

The proposed underlying UC mechanism is that upon 1076 nm excitation, the IR-dye can absorb the light and transfer it to the Ln^{3+} ions of the $\beta\text{-UCNPs}$ (Ho^{3+} and Tm^{3+}). The overlap between the emission of the dye and the absorption of the $\beta\text{-UCNPs}$ will allow Förster energy transfer. Although our experiments are still ongoing, we expect that our results could open new opportunities to obtain higher UC and DC luminescence intensity using higher activator doping concentration.

Chapter 6 Summary and outlook

6.1 Summary of Results

The goal in nanomaterial engineering is based on controlling the synthesis with high precision at the atomic scale in order to obtain a precise control in the properties of the NPs. In **Chapter 3**, we have shown that variations of the OA played a crucial role in defining the morphologies of the resulting particles. β -NaYF₄: Yb³⁺(20%), Er³⁺(2%) UCNPs with different ARs were synthesised using a co-precipitation method by only varying the amount of OA in the reaction mixture, and using NH₄F as fluoride source. We have observed that OA can be used to inhibit or promote different crystallographic facets of the β -UCNPs. Our results showed that high concentration of COO⁻ favoured the growth of the particles along the longitudinal [001] direction due to a high level of passivating COO⁻ ions on the (10-10) prismatic facets of the β -UCNPs. Hence, the presence of high content of OA is believed to have a greater effect on the formation of nanorods.

In terms of optical properties, the UC luminescence and absorbance of the β -UCNPs were studied. We observed that under the same experimental conditions, larger β -UCNPs with hexagonal shape showed brighter UC emission, compared to those with small nanorod shape. The outcome was attributed to the surface quenching effect of larger UCNPs. To gain insights into the UC efficiency, we took power dependence UC luminescence measurements. The results confirmed that the presence of nanorod shape produced the highest UC efficiencies. We proposed that this phenomenon could be associated to the pathways of the UC in different geometries of the UCNPs. We hypothesised that the effective energy transfer between Yb³⁺ and Er³⁺ ions is lower in UCNPs with hexagonal shape due to the energy migration occurring in 3 directions inside the crystal. On the other hand, in a rod-shape UCNP, the spatial position of the activator's molecules (Er³⁺) are supposedly more accessible to sensitizers molecules (Yb³⁺), and the effective energy migration is higher compared with those where the migration occurs equally well in all 3 directions.

In the following section, we synthesized Na_xScF_{3+x} UCNPs using the same experimental protocol but with Sc³⁺ as doping ion in the host matrix. We found that by substituting different Ln³⁺ in the same matrix Na_xLnF_{3+x} (Ln³⁺ = Sc³⁺, Y³⁺) and keeping the other experimental parameters fixed during the synthesis, it was possible to obtain a transition from a brighter hexagonal NaYF₄ phase to a mixture of hexagonal NaScF₄ and monoclinic

Na₃ScF₆ phases. It was found that this host material resulted in multicolour emissions ranging from red-orange to yellow and green.

Then, we synthesized Na_xScF_{3+x} UCNPs with NaF as fluoride source and we studied the dependence on different experimental factors such as the reaction time and temperature, and the molar ratio of NaF: Ln³⁺.

The results revealed that although the theoretical molar ratio of NaF: Ln³⁺ = 2 is generally imposed in the growth of Na₃ScF₆ nanorods,²¹⁶ as long as temperature and time are appropriately adjusted, nanorods could be also synthesized at different NaF: Ln³⁺ molar ratio. Our work revealed that the synthetic temperature and time have prominent effects on the growth of the Na_xScF_{3+x} UCNPs. Overall, we believe that the phase and morphology of the samples could be tailored through a systematic adjustment of temperature and time conditions, independently of the NaF: Ln³⁺ molar ratio.

We concluded **Chapter 3** with a discussion on the synthesis and characterization of different core@shell UCNPs. We prepared successfully various core@shell structures where different shells materials (β-NaYF₄, β-NaLuF₄, and β-NaGdF₄) were grown on the surface of the core. We observed how compressive and tensile strains affected the final geometry, and we studied their structural properties using XRD.

Core@shell structure is an obvious concept to suppress surface-related deactivation in UCNPs.²¹⁹ All core@shell structures exhibited enhanced UC emission intensity, compared to the unshelled core UCNPs. The results showed that the UC emission intensity from more isotropic core@shell (β-NaYF₄@NaLuF₄) was brighter than those generated from more anisotropic structures such as β-NaYF₄@NaGdF₄ and β-NaYF₄@NaYF₄. In general, all the results from **Chapter 3** further complement the exploration of shape evolution in RE based nanomaterials.

In the first section of **Chapter 4** we introduced an approach to create uniform silica coating of the β-UCNPs using a reverse microemulsion technique and a wet annealing process prior to the coating. The reported approach produces silica coating UCNPs with a single core and with different shell thicknesses, and consider different sizes and morphologies of β-UCNPs. Additionally, the silica coating mechanism on the β-UCNPs was discussed.

It is well-known that the fabrication of uniform silica coating β-UCNPs is crucial for biological and environmental applications. In order to use the particles in biological environments we prepared two types of water-dispersible β-UCNPs, which were obtained directly from the same core material: OA free β-UCNPs and β-UCNPs@SiO₂-NH₂.

We performed optical measurements to understand how the luminescence properties of the β -UCNPs were affected by the silica and water dispersibility. The changes in both, the UC emission intensity and the RGR were observed when dispersing the particles in Milli-Q water. The UC quenching effect was attributed to the scattering of the excitation light and emission light by silica. The results showed that although a significant reduction in the UC luminescence appeared in both of the samples compared to the original hydrophobic β -UCNPs, the as-prepared samples showed excellent colloidal stability, suitable for subsequent functionalization.

In order to covalently couple the water dispersible UCNPs with biomolecules, and more specifically synthetic oligonucleotides, -COOH functional groups were introduced to the surface of UCNPs and used for binding to oligonucleotides through a s-NHS/EDC coupling strategy.^{225,307} The β -UCNPs@SiO₂-ssDNA nanohybrid showed UC luminescence imaging after being incubated with A549 cells and therefore signs of good biocompatibility. Although the work is still ongoing, we expect that the nanohybrid could be used in other biological applications and further extend the current knowledge of UCNP biocompatibility.

In the following section of **Chapter 4**, we have fabricated an Au shell around the β -UCNPs and studied the tunability of the SPR peak. We observed that when the Au shell was very thin, the SPR peak moved to longer wavelengths. In our experiments, the peak gradually moved in the following manner: 525 nm, 590 nm and 670 nm. Unfortunately, the obtained nanostructures had a considerable thickness and featured broad plasmon bands. We hypothesize that the decrease of Au precursor would lead to a shift of the SPR to higher wavelengths, precisely to the region where UCNPs absorb (980 nm).

Additionally, we have prepared AuNRs with different AR. AuNRs were prepared by one-step seed mediated growth method reported by El Sayed,²¹⁷ while more elongated AuNRs were synthesised via a three-step protocol, developed by Murphy et al.²¹⁸ In the first method, the AR was controlled by the amount of AgNO₃ used, and it increased from 2.12 to 4.38, whilst the longitudinal SPR peak maxima varied from 600 nm to 800 nm. The presence of high AR structures in colloidal solution resulted in even greater red-shift of the SPR to 800-1200 nm. Although the work is still ongoing, we expect that the presence of high AR AuNRs bound or in close proximity to the UCNPs can influence both its absorption in the NIR and emission in the Vis, thus enhancing the UC luminescence.

In the last section of **Chapter 4** we described the synthesis and characterization of β -NaYF₄: Yb³⁺(20%), Tm³⁺(0.5%) UCNPs coated with TiO₂. The resulting particles were designed

and employed as the photocatalyst for the DCPIP and Rz degradation under different irradiation bands of a Xe lamp. It was shown that the β -UCNPs/TiO₂ produced photocatalytic activity under UV and NIR irradiation. Results revealed that under the same conditions, Rz exhibited a higher degradation compared to DCPIP. Still further investigations are necessary to find out the causes that provoked differences in the behaviour for both of dyes. Different effects including the β -UCNPs/TiO₂ dosage, recyclability and kinetics were investigated.

It is known that the kinetics of photoreduction for the DCPIP and Rz inks are very sensitive to the amount of glycerol added. This phenomenon may be associated with a solvatochromic effect, where the environment in which the dye finds itself affects its reactivity and can be altered significantly by small changes in the glycerol content.³⁵³ Therefore, since the glycerol is a main parameter in the degradation progress, future work will focus on comparative experiments performed at different glycerol contents

It is well known that the pH influences the characteristics of the photocatalyst surface charge,³⁸³ and is another significant parameter which we did not contemplate in our experiments. Since the pH of dye solution is one of the main parameters in the degradation progress, future work could focus also on comparative experiments performed at different pH values.

Cobalt doped β -UCNPs/TiO₂ photocatalysts were prepared by an impregnation method and studied. Although the UCNPs/TiO₂-Co did not exhibit a good photocatalytic activity, a dedicated research will be carried out in the future.

The work concluded with a study on the structural effects caused by annealing the β -UCNPs/TiO₂ nanostructures at different temperature. XRD results revealed that heating above 900 °C leads to conversion of β -UCNPS/TiO₂ into a Y₂Ti₂O₇ structure, whereas β -UCNPs undergo transformation to Y₂O₃ above 900 °C. The luminescent properties showed differences between the annealed and non-annealed structures possibly due to the rearrangement of atoms at high temperature. It was found that although the photocatalytic activity was not very high, β -UCNPS/TiO₂ were able to absorb in the visible region when annealed at 700 °C.

In **Chapter 5**, we discussed the effect of the IR-806 dye-sensitized using three different types of β -UCNPs: core-only, core@active shell and core@inert shell. The surface coverage of IR-dye molecules around the β -UCNPs was optimized and the resulting particles were used for a collaboration with the Skolkovo Institute of Science and Technology in Moscow. There, we reported an investigation of the UC luminescence in dye-sensitized β -UCNPs

compared to that in non-sensitized β -UCNPs. We also use time-resolved measurements to characterize the overall non-radiative energy transfer from dyes to the β -UCNPs.

Overall, it was observed a 20-fold enhancement of the UC emission in the dye-sensitized core@active shell β -UCNPs in comparison with the non-sensitized core-only β -UCNPs. The fluorescence decay measurements of the dye-sensitized core-only and core@active shell β -UCNPs revealed a non-radiative energy transfer from the dye molecules to Yb^{3+} ions rather than to Er^{3+} ions with an efficiency of 62%. Also, the analysis of the UC kinetics of the dye-sensitized and non-sensitized β -UCNPs showed a dramatic difference in the rise dynamics. The dye-sensitized β -UCNPs, unlike the non-sensitized β -UCNPs, produced an extremely fast rise time, which was attributed to a radiative energy transfer from the dye directly to the core Er^{3+} ions.

In addition to the UC luminescence, we also studied DC luminescence spectra for the dye-sensitized of core-only, core@active shell and core@inert shell. The results revealed that when excited at 800 nm, the IR-dye sensitized core-only and IR-dye sensitized core@active shell manifested ~ 1.3 and ~ 2.6 stronger enhancement in the NIR-DC luminescence peak at ~ 1550 than the non-sensitized β -UCNPs excited at 980 nm. These results provided new insights on the energy migration and surface effects in $\beta\text{-NaYF}_4$ UCNPs. Futures efforts could be directed to resolve the details of the DC mechanism for the β -UCNPs with IR-dyes attached to their surface.

Chapter 5 concluded with a preliminary study based on the use of a new IR dye (1076 IR-dye) to alleviate the luminescence concentration quenching of the β -UCNPs. The proposed underlying UC mechanism is such that upon 1076 nm excitation, the IR-dye can absorb the light and transfer it to the Ln^{3+} ions of the β -UCNPs (doped with Ho^{3+} and Tm^{3+}). The overlap between the emission of the dye and the absorption of the β -UCNPs will allow Förster energy transfer. Although our experiments are still ongoing, we expect that our results may open new opportunities to achieve higher UC and DC luminescence intensity by means of higher activator doping concentrations.

6.2 Outlook of future work

Lanthanides doped UCNPs present low cytotoxicity, long excitation wavelength, and low autofluorescence back-ground.³⁸⁴ Therefore, UCNPs are promising nanomaterials for biological applications such as biosensor, bioimaging, siRNA delivery, and cancer treatment.

Recently UCNPs have been utilised in cells due to their unique properties.³¹⁷ In **Section 4.2**, we have demonstrated a good understanding in the manipulation of the UCNPs with ssDNA and subsequent cell incubation. Having showed promising signs of good biocompatibility, future work will focus on monitoring the intracellular fate of the UCNPs in real time in conjunction with mRNA detection.

Firstly, this study will focus on investigating the intracellular fate of UCNPs following their uptake by cells. To achieve this, we will perform colocalization studies by monitoring multiple emissions outputs by staining endocellular compartments such as the nucleus, endosomes, extracellular membrane, and mitochondria.³⁸⁵

Secondly, we will combine the UCNPs with sensing of mRNA. We will monitor where the UCNPs are at the same time as monitoring mRNA detection in order to determine at what timepoint and where does mRNA detection take place.

A common approach for live cell mRNA detection uses a probe based on the development of small nucleoid acid (SNAs) named as nanoflares.^{385,386} Since their initial development, nanoflares have been used extensively for the detection of mRNA targets by monitoring the fluorescence output of the flare strand. There are several reports about mRNA sensing using AuNPs and it is believed that mRNA sensing happens in the cytoplasm. In our experiments we will alter the nanoflare technology in order to incorporate an UCNP core instead of a Au core.

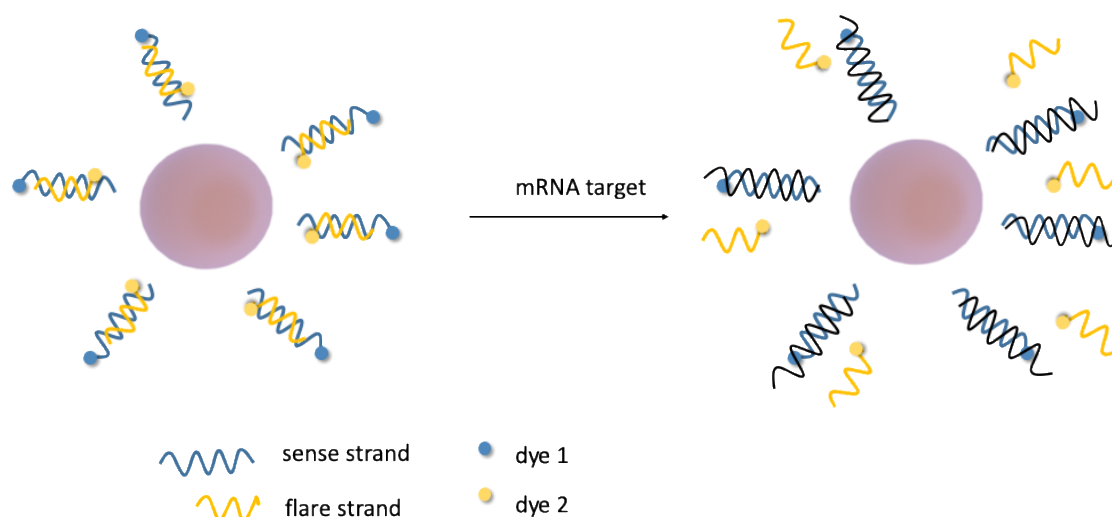


Figure 164. Schematic illustration of nanoflares used for live cell mRNA detection. Fluorophore tagged oligonucleotides (flare strand) are used which are initially quenched. When the target mRNA binds to the sense strand the release of the flare can be detected as an increase in its fluorescence signature. Blue and yellow arrows indicate sense strand and flare strand, respectively.

We will design a system with SNAs to be conjugated to the UCNP surface. To this, a shorter fluorophore modified oligonucleotide (flare strand) will be attached. The sense sequence can be designed to detect a specific mRNA target thus when the target mRNA binds, the fluorophore flare strand will be released due to competitive hybridization and a fluorescence signal will be detected.^{385,386}

Appendix A Schlenk line set-up

A Schlenk line was used to protect the atmosphere of our reaction from moisture and oxygen traces by running the synthesis under an Argon (Ar) gas and also for solvent removal. From **Figure 165** it can be seen that the line consists of a double manifold for introduction of both inert gas and vacuum. Located before the pump at the end of the line there is a cold trap which condenses evacuated organic vapours as methanol, preventing their entry into the pump. There is an oil bubbler filled with silica oil which apart of helping in maintaining an inert atmosphere, also provides for a means for pressure relief.

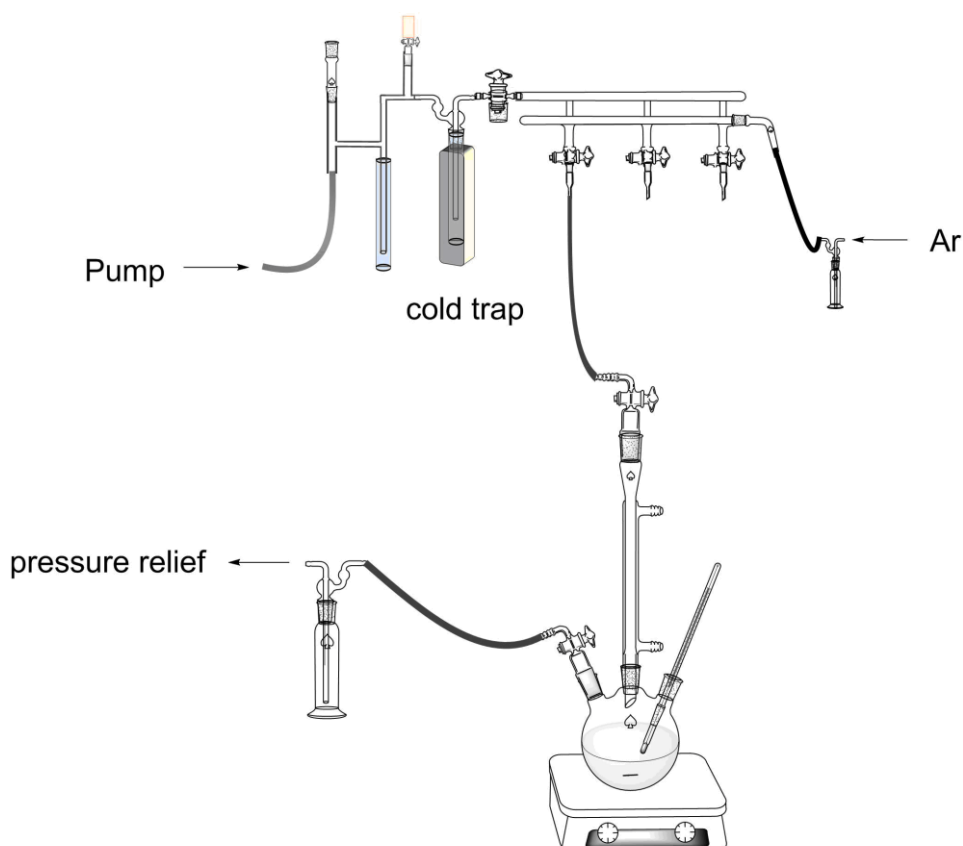


Figure 165. Diagram showing a scheme of the Schlenk – line used to synthesise lanthanides doped UCNPs.

Appendix B Equations for the surface area calculation in a hexagonal prism.

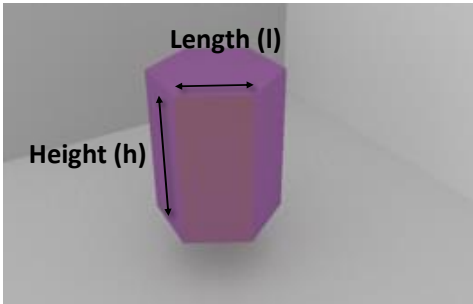
$$\begin{aligned} \text{Cubic volume (V)} \quad V &= A \times h = \\ &1.5 \times \sqrt{3} \times l^2 \times h \end{aligned} \quad (22)$$

$$\text{Total surface area of a prism (SA}_T\text{)} \quad SA_T = 2A + M \quad (7)$$

$$\text{Surface area of the base (A)} \quad A = 1.5\sqrt{3} l^2 \quad (8)$$

$$\begin{aligned} \text{Surface area of the lateral prism} \\ \text{(M)} \quad M &= 6hl \end{aligned} \quad (9)$$

$$\text{Surface to volume ratio (SV)} \quad SV = \frac{SA_T}{V} \quad (23)$$



Appendix C Lattice constant calculation.

In **Section 3.1.2**, the lattice constant (a, b, c) of the unit cell were calculated in order to visualize the 3D structure of the β -NaYF₄ UCNPs. (See **Figure 30b**) For this purpose, the interplanar spacing (d_{hkl}) was calculated experimentally from the first three peaks, using the Bragg's law:

$$d_{hkl} = \frac{\lambda}{2\sin(\theta)} \quad (24)$$

, where hkl are the Miller indices which determine a family of lattice planes. The summary of the experimental XRD diffractions peaks and the calculated values of d_{hkl} are summarized in **Table 22** and **Table 23**, respectively.

Table 22. Data of the XRD diffraction peaks of the Sample (1-4) made of NaYF₄, with 0.2 s/degree scan rate and 0.02° step size from 10° to 80°. Values were obtained by fitting the peaks individually with a Lorentzian function.

	2 θ (degrees)		
	(100)	(110)	(101)
Sample 1	17.17	29.96	30.82
Sample 2	17.23	30.00	30.90
Sample 3	17.28	30.06	30.94
Sample 4	17.22	30.02	30.91

Table 23. Experimental values of d_{hkl} obtained for Samples (1-4) using the first three peaks from the XRD patterns.

	d_{100}	d_{110}	d_{101}
Sample 1	5.16 Å	2.98 Å	2.90 Å
Sample 2	5.14 Å	2.98 Å	2.89 Å
Sample 3	5.13 Å	2.97 Å	2.89 Å
Sample 4	5.14 Å	2.97 Å	2.89 Å

The lattice constants were obtained using the standard formula for the hexagonal crystal system from eq (25) and the results are summarized in **Table 24**.

Results indicated similar lattice parameters for the different samples, which are also in agreements to others publications. Several studies have reported the crystal lattice parameters associated with α -NaYF₄ and β -NaYF₄ UCNPs: these are summarized in **Table 25**.

$$\frac{1}{d_{hkl}} = \frac{4}{3} \left(\frac{h^2 + hk + k^2}{a^2} \right) + \frac{l^2}{c^2} \quad (25)$$

Table 24. Experimental values of the lattice constants obtained for Samples (1-4)

	Calculated lattice parameters	
Sample 1	$\alpha=\beta=90^\circ, \gamma=120^\circ$	$a=b=5.96 \text{ \AA}, c=3.58 \text{ \AA}$
Sample 2	$\alpha=\beta=90^\circ, \gamma=120^\circ$	$a=b=5.95 \text{ \AA}, c=3.58 \text{ \AA}$
Sample 3	$\alpha=\beta=90^\circ, \gamma=120^\circ$	$a=b=5.93 \text{ \AA}, c=3.57 \text{ \AA}$
Sample 4	$\alpha=\beta=90^\circ, \gamma=120^\circ$	$a=b=5.94 \text{ \AA}, c=3.57 \text{ \AA}$

Table 25. Crystal lattice reported in the literature. Table adapted from Ref. ³⁸⁷

Study	Dopant composition	Lattice structure	a	c
Sikora et al. ³⁸⁸	30% Yb ³⁺ , 2% Er ³⁺	α -NaYF ₄	5.51 Å	-
Cao et al. ¹⁰⁰	20% Yb ³⁺ , 2% Er ³⁺	β -NaYF ₄	5.960 Å	3.510 Å
Wang et al. ¹⁰¹	18% Yb ³⁺ , 2% Er ³⁺	β -NaYF ₄	5.96 Å	3.53 Å
Want et al. ¹⁰¹	18% Yb ³⁺ , 2% Er ³⁺ ,60% Gd ³⁺	β -NaYF ₄	6.02 Å	3.60 Å

Appendix D Propagation of uncertainties equations list

Function, $f(A, B)$	Uncertainty	
$Z = A \pm B$	$\alpha_Z = \sqrt{\alpha_A^2 + \alpha_B^2}$	(26)
$Z = A \times B$ or, $Z = \frac{A}{B}$	$\frac{\alpha_Z}{Z} = \sqrt{\left(\frac{\alpha_A}{A}\right)^2 + \left(\frac{\alpha_B}{B}\right)^2}$	(27)
$Z = k \frac{A}{B}$	$\frac{\alpha_Z}{Z} = \sqrt{\left(\frac{\alpha_A}{A}\right)^2 + \left(\frac{\alpha_B}{B}\right)^2}$	(28)
$Z = k \frac{A^n}{B^m}$	$\frac{\alpha_Z}{Z} = \sqrt{\left(n \frac{\alpha_A}{A}\right)^2 + \left(m \frac{\alpha_B}{B}\right)^2}$	(29)
$Z = A + B - C + D$	$\alpha_Z = \sqrt{\alpha_A^2 + \alpha_B^2 + \alpha_C^2 + \alpha_D^2}$	(30)
$Z = \frac{A \times B}{C \times D}$	$\frac{\alpha_Z}{Z} = \sqrt{\left(\frac{\alpha_A}{A}\right)^2 + \left(\frac{\alpha_B}{B}\right)^2 + \left(\frac{\alpha_C}{C}\right)^2 + \left(\frac{\alpha_D}{D}\right)^2}$	(31)
$Z = \frac{A^n \times B^m}{C^p \times D^q}$	$\frac{\alpha_Z}{Z} = \sqrt{\left(n \frac{\alpha_A}{A}\right)^2 + \left(m \frac{\alpha_B}{B}\right)^2 + \left(p \frac{\alpha_C}{C}\right)^2 + \left(q \frac{\alpha_D}{D}\right)^2}$	(32)
$Z = \ln A$	$\alpha_Z = \frac{\alpha_A}{A}$	(33)

Appendix E Error analysis in TEM measurements

The values of standard deviation (σ) were automatically calculated by the Software Origin after fitting the data with a Gaussian function and these σ values were used as the uncertainty in the UCNPs sizes. The Gaussian equation used for the fitting is expressed in eq.(34) and the (σ) values in eq.(35) :

$$y = y_0 + \frac{A}{w\sqrt{\pi/2}} e^{-2\frac{(x-x_c)^2}{w^2}} \quad (34)$$

$$\sigma = w/2 \quad (35)$$

$$FWHM \text{ (full width at half maximum)} = \sqrt{2 \times \ln(2)} \times w \quad (36)$$

Meanings: y_0 = offset, x_c = centre, w = width, A = area

Appendix F Error analysis for calibration curve

Data from calibration curve seen in **Figure 58** were fitted with a straight-line using Origin. Error bars in mg/ml ($\alpha_{mg/ml}$) were calculated using the equations from **Appendix D** and assuming an initial uncertainty in the measurement of the weight and the volume of ± 100 ug and ± 0.1 ml, respectively.

$$\frac{\alpha_{mg/ml}}{mg/ml} = \sqrt{\left(\frac{\alpha_{mg}}{mg}\right)^2 + \left(\frac{\alpha_{ml}}{ml}\right)^2} \quad (37)$$

$$\alpha_{mg/ml} = \left(\sqrt{\left(\frac{\alpha_{mg}}{mg}\right)^2 + \left(\frac{\alpha_{ml}}{ml}\right)^2} \right) \times mg/ml \quad (38)$$

Error bars α_{SAT} were calculated using the equations from **Appendix D** applied to the formula for the total surface area of a prism:

$$SA_T = 2A + M = 3\sqrt{3} l^2 + 6hl \quad (7)$$

Where the errors were calculated as follow:

$$\alpha_{SAT} = \sqrt{(\alpha_{(3\sqrt{3} l^2)})^2 + (\alpha_{(6hl)})^2} \quad (39)$$

$$\frac{\alpha_{3\sqrt{3} l^2}}{3\sqrt{3} l^2} = \sqrt{\left(2 \frac{\alpha_l}{l}\right)^2} \quad (40)$$

$$\frac{\alpha_{(6hl)}}{6hl} = \sqrt{\left(\frac{\alpha_h}{h}\right)^2 + \left(\frac{\alpha_l}{l}\right)^2} \quad (41)$$

$$\alpha_{(3\sqrt{3} l^2)} = 6\sqrt{3} \alpha_l l \quad (42)$$

$$\alpha_{(6hl)} = 6hl \sqrt{\left(\frac{\alpha_h}{h}\right)^2 + \left(\frac{\alpha_l}{l}\right)^2} \quad (43)$$

$$\alpha_{SAT} = \sqrt{108l^2 \alpha_l^2 + 36l^2 \alpha_h^2 + 36h^2 \alpha_l^2} \quad (44)$$

Table 4 collects the information about the uncertainties of the side length (α_l) and the height (α_h).

Error bars α_V and α_{SV} were calculated using the equations from **Appendix D** applied to the formula for the volume (V) and surface volume ratio (SV) of a prism, and the errors were calculated as:

$$\alpha_V = \left(\sqrt{\left(\frac{2\alpha_l}{l}\right)^2 + \left(\frac{\alpha_h}{h}\right)^2} \right) \times V \quad (45)$$

$$\alpha_{SV} = \left(\sqrt{\left(\frac{\alpha_{SA_T}}{SA_T}\right)^2 + \left(\frac{\alpha_V}{V}\right)^2} \right) \times SV \quad (46)$$

Appendix G Error analysis in photocatalysis

The measurements of absorbance were repeated for 3 times for each sample at each time interval and the errors associated to each measurement were expressed as follows:

At each time t we performed three measurements of absorbance to subsequent determine the concentration C_i with $i=1,2,3$. Then, for each time we considered the average value of the C_i s as C and its maximal deviation to the measurements as errors α_C .

The photodegradation was evaluated according to the C/C_o value for the different dyes, where C is the concentration of dye in solution after photoirradiation and C_o is the initial concentration of the dye. The error (α_{C/C_o}) of C/C_o for each measurement were calculated as follow.

$$\frac{\alpha_{C/C_o}}{C/C_o} = \sqrt{\left(\frac{\alpha_{C_o}}{C_o}\right)^2 + \left(\frac{\alpha_C}{C}\right)^2} \quad (47)$$

$$\alpha_{C/C_o} = \left(\sqrt{\left(\frac{\alpha_{C_o}}{C_o}\right)^2 + \left(\frac{\alpha_C}{C}\right)^2} \right) \times C/C_o \quad (48)$$

The error ($\alpha_{\ln(C/C_o)}$) of C/C_o for each measurement were calculated as follow.

$$\alpha_{\ln(C/C_o)} = \frac{\alpha_{C/C_o}}{C/C_o} \quad (49)$$

Appendix H Calculation of errors in IR-806 dye molecules attached to UCNPs

Our studies revealed that 3 µg/ml was the optimal concentration of IR dye for 0.8 mg/ml of UCNPs. In order to estimate the uncertainty in the dye concentration, we used the equations from **Appendix D** to calculate the dilution errors associated to the sample preparation. For the error propagation, we assumed that the uncertainty in the measurement of the weight and the volume was ± 0.1 mg and ± 0.1 ml, respectively. Thus, we report the optimal and initial concentration of IR-dye as:

$$dye_{initial} = 3 \text{ µg/ml} \pm 0.03 \text{ µg/ml}$$

The analysis from supernatants revealed that part of these dye concentration was free on solution. In detail, it was found that 0.34 µg/ml and 0.26 µg/ml of the total IR-dyes molecules were unbound from the core and from the core@active shell UCNPs, respectively. Errors were calculated assuming the linear relation from the calibration curve from **Figure 134b**, and the instrumental uncertainty (± 0.002) of the apparatus at the maximum wavelength. Therefore:

$$dye_{supernatant} = 0.34 \text{ µg/ml} \pm 0.01 \text{ µg/ml for the core}$$

$$dye_{supernatant} = 0.26 \text{ µg/ml} \pm 0.01 \text{ µg /ml for the core@active shell}$$

The real concentration of dye bound to surface of the UCNPs was calculated in based to the next equation:

$$dye_{bound} = dye_{initial} - dye_{supernatant} \quad (50)$$

$$dye_{bound} = 2.66 \text{ µg/ml} \pm 0.03 \text{ µg/ml for the core}$$

$$dye_{bound} = 2.74 \text{ µg/ml} \pm 0.03 \text{ µg /ml for the core@active shell}$$

Where the error associated to the dye attached to the core and core@shell was calculated as follows:

$$\alpha_{dye_{bound}} = \sqrt{(\alpha_{dye_{initial}})^2 + (\alpha_{dye_{supernatant}})^2} \quad (51)$$

The percentage of dye bound to the UCNPs was expressed as:

$$\% dye_{bound} = \frac{dye_{bound}}{dye_{initial}} \times 100 \quad (52)$$

$$\% dye_{bound} = 88.6\% \pm 1.9\% \text{ for the core}$$

$$\% dye_{bound} = 91.2\% \pm 1.9\% \text{ for the core@active shell}$$

where error associated to the % of dye attached to the core and core@shell was calculated as follows:

$$\frac{\alpha_{\%dye_{bound}}}{\%dye_{bound}} = \sqrt{\left(\frac{\alpha_{dye_{bound}}}{dye_{bound}}\right)^2 + \left(\frac{\alpha_{dye_{initial}}}{dye_{initial}}\right)^2} \quad (53)$$

$$\alpha_{\%dye_{bound}} = \left(\sqrt{\left(\frac{\alpha_{dye_{bound}}}{dye_{bound}}\right)^2 + \left(\frac{\alpha_{dye_{initial}}}{dye_{initial}}\right)^2} \right) \times \% dye_{bound} \quad (54)$$

The percentage of dye free on solution was expressed as:

$$\% dye_{free} = \frac{dye_{supernatant}}{dye_{initial}} \times 100 \quad (55)$$

$$\% dye_{free} = 11.3\% \pm 0.3\% \text{ for the core}$$

$$\% dye_{free} = 8.8\% \pm 0.3\% \text{ for the core@active shell}$$

, where error associated to the % of free dye was calculated as follows:

$$\frac{\alpha_{\%dye_{free}}}{\% dye_{free}} = \sqrt{\left(\frac{\alpha_{dye_{free}}}{dye_{free}}\right)^2 + \left(\frac{\alpha_{dye_{initial}}}{dye_{initial}}\right)^2} \quad (56)$$

$$\alpha_{\%dye_{free}} = \left(\sqrt{\left(\frac{\alpha_{dye_{free}}}{dye_{free}}\right)^2 + \left(\frac{\alpha_{dye_{initial}}}{dye_{initial}}\right)^2} \right) \times \% dye_{free} \quad (57)$$

Appendix I Additional images of silica coating before and after annealing treatment

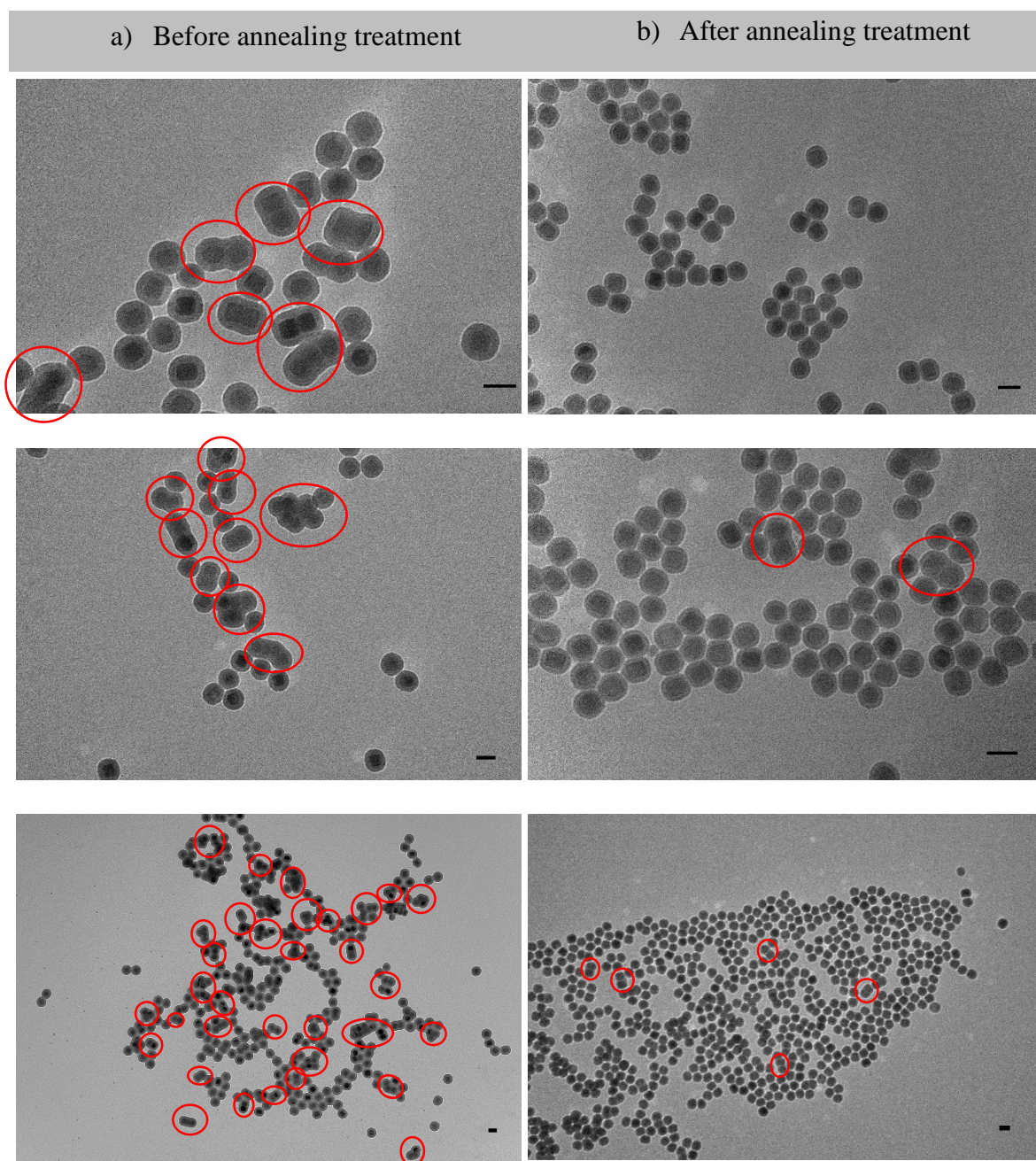


Figure 166. Additional TEM images of β -UCNPs@SiO₂ (a) before and (b) after the annealing treatment showing the visual NPs distribution. Scales bars are 50 nm. Red circles have been drawn around multiple NP cores coated by the same silica shell to facilitate the comparison.

Bibliography

1. Duan, C., Liang, L., Li, L., Zhang, R. & Xu, Z. P. Recent progress in upconversion luminescence nanomaterials for biomedical applications. *J. Mater. Chem. B* **6**, 192–209 (2018).
2. Haase, M. & Schäfer, H. Upconverting nanoparticles. *Angew. Chemie - Int. Ed.* **50**, 5808–5829 (2011).
3. Feng, W., Han, C. & Li, F. Upconversion-nanophosphor-based functional nanocomposites. *Adv. Mater.* **25**, 5287–5303 (2013).
4. Bharat Bhushan (Ed.). *Springer Handbook of Nanotechnology*. (2010). doi:10.1007/978-3-642-02525-9
5. Quirk, T. There's plenty of room at the bottom. *Australasian Biotechnology* **16**, 36 (2006).
6. Bankinter, F. de la I. *The Industrial Revolution of the 21st Century*. (2006).
7. Chen, G., Roy, I., Yang, C. & Prasad, P. N. Nanochemistry and Nanomedicine for Nanoparticle-based Diagnostics and Therapy. *Chem. Rev.* **116**, 2826–2885 (2016).
8. El-Sayed, M. A. Small is different: Shape-, size-, and composition-dependent properties of some colloidal semiconductor nanocrystals. *Acc. Chem. Res.* **37**, 326–333 (2004).
9. Prasad, Paras, N. *Nanophotonics*. (Wiley-Interscience, 2004).
10. Alivisatos, A. Semiconductor Clusters, Nanocrystals, and Quantum Dots. *Science* (80-.). **271**, 933–937 (1996).
11. Zhang, B. Chapter 8 - Optical Properties of Nanomaterials. in *Micro and Nano Technologies* (ed. Zhang, B. B. T.-P. F. of N.) 291–335 (William Andrew Publishing, 2018). doi:https://doi.org/10.1016/B978-0-12-410417-4.00008-3
12. Mittal, A. K. & Banerjee, U. C. Chapter 5 - Current status and future prospects of nanobiomaterials in drug delivery. in *Nanobiomaterials in Drug Delivery Applications of Nanobiomaterials Volume 9* (ed. Grumezescu, A. M. B. T.-N. in D. D.) 147–170 (William Andrew Publishing, 2016). doi:https://doi.org/10.1016/B978-0-323-42866-8.00005-8

Bibliography

13. Zhang, F. *Photon Upconversion Nanomaterials*. (2015).
14. Xue, X. *et al.* Size-dependent upconversion luminescence and quenching mechanism of LiYF₄: Er³⁺/Yb³⁺ nanocrystals with oleate ligand adsorbed. *Opt. Mater. Express* **3**, 989 (2013).
15. Schietinger, S., Menezes, L. de S., Lauritzen, B. & Benson, O. Observation of Size Dependence in Multicolor Upconversion in Single Yb³⁺, Er³⁺ Codoped NaYF₄ Nanocrystals. *Nano Lett.* **9**, 2477–2481 (2009).
16. Shan, J., Uddi, M., Yao, N. & Ju, Y. Anomalous raman scattering of colloidal Yb³⁺,Er³⁺ codoped NaYF₄ nanophosphors and dynamic probing of the upconversion luminescence. *Adv. Funct. Mater.* **20**, 3530–3537 (2010).
17. Yin, Y. & Alivisatos, A. P. Colloidal nanocrystal synthesis and the organic-inorganic interface. *Nature* **437**, 664–670 (2005).
18. Kanelidis, I. & Kraus, T. The role of ligands in coinage-metal nanoparticles for electronics. *Beilstein J. Nanotechnol.* **8**, 2625–2639 (2017).
19. Jorgensen, K. Lanthanides since 1839: From Crowded Elements to Quantum-chemical Rosetta Stone. *Inorganica Chim. Acta* **139**, 1–5 (1987).
20. Eliseeva, S. V. & Bünzli, J. C. G. Rare earths: Jewels for functional materials of the future. *New J. Chem.* **35**, 1165–1176 (2011).
21. Hedrick, J. B. The global rare-earth cycle. *J. Alloys Compd.* **225**, 609–618 (1995).
22. Ripa, R. S. *et al.* *Encyclopedia of Metalloproteins*. (2013). doi:10.1007/978-1-4614-1533-6
23. Cotton, S. *Lanthanide and Actinide Chemistry and Spectroscopy*. (John Wiley & Sons, Ltd, 2006). doi:10.1002/0470010088
24. Boatner, L. A. & Abraham, M. M. Electron paramagnetic resonance from actinide elements. *Reports Prog. Phys.* **41**, 87–155 (1978).
25. Wang, F., Banerjee, D., Liu, Y., Chen, X. & Liu, X. Upconversion nanoparticles in biological labeling, imaging, and therapy. *Analyst* **135**, 1839–1854 (2010).
26. Chen, J. & Zhao, J. X. Upconversion nanomaterials: Synthesis, mechanism, and applications in sensing. *Sensors* **12**, 2414–2435 (2012).

Bibliography

27. Reisfeld, R. Optical properties of lanthanides in condensed phase, theory and applications. *AIMS Mater. Sci.* **2**, 37–60 (2015).
28. Wisser, M. D. *et al.* Strain-induced modification of optical selection rules in lanthanide-based upconverting nanoparticles. *Nano Lett.* **15**, 1891–1897 (2015).
29. Antoniak, C. Extended X-ray absorption fine structure of bimetallic nanoparticles. *Beilstein J. Nanotechnol.* **2**, 237–251 (2011).
30. Liu, G. Advances in the theoretical understanding of photon upconversion in rare-earth activated nanophosphors. *Chem. Soc. Rev.* **44**, 1635–1652 (2015).
31. *Spectroscopic Properties of Rare Earths in Optical Materials.* (Springer Berlin Heidelberg, 2005).
32. Werts, M. H. V. Making sense of lanthanide luminescence. *Sci. Prog.* **88**, 101–31 (2005).
33. M.F.joubert. Photon Avalanche Upconversion in Laser Rare-Earth Laser Materials. *Opt.Mat.* **11**, 181–203 (1999).
34. DaCosta, M. V., Doughan, S., Han, Y. & Krull, U. J. Lanthanide upconversion nanoparticles and applications in bioassays and bioimaging: A review. *Anal. Chim. Acta* **832**, 1–33 (2014).
35. Shalav, A., Richards, B. S., Kramer, K. & Gudel, G. Improvements of an up-conversion NaYF₄:Er³⁺ phosphor/silicon solar cell system for an enhanced response in the near-infrared. in *Conference Paper in Conference Record of the IEEE Photovoltaic Specialists Conference* 114–117 (2005). doi:10.1109/pvsc.2005.1488082
36. Suyver, J. F. *et al.* Upconversion spectroscopy and properties of NaYF₄ doped with Er³⁺, Tm³⁺ and/or Yb³⁺. *J. Lumin.* **117**, 1–12 (2006).
37. Strohhöfer, C. & Polman, A. Absorption and emission spectroscopy in Er³⁺ - Yb³⁺ doped aluminum oxide waveguides. *Opt. Mater. (Amst).* **21**, 705–712 (2003).
38. Wang, F. & Liu, X. Recent advances in the chemistry of lanthanide-doped upconversion nanocrystals. *Chem. Soc. Rev.* **38**, 976–989 (2009).
39. Tikhomirov, V. K. *et al.* Preparation and up-conversion luminescence of 8 nm rare-

Bibliography

- earth doped fluoride nanoparticles. *Opt. Express* **16**, 14544–14549 (2008).
40. Auzel, F. Upconversion and Anti-Stokes Processes with f and d Ions in Solids. *Chem. Rev.* **104**, 139–174 (2004).
 41. Wang, F. & Liu, X. Upconversion Multicolor Fine-Tuning: Visible to Near-Infrared Emission from Lanthanide-Doped NaYF₄ Nanoparticles. *J. Am. Chem. Soc.* **130**, 5642–5643 (2008).
 42. Geitenbeek, R. G. *et al.* NaYF₄:Er³⁺,Yb³⁺/SiO₂ Core/Shell Upconverting Nanocrystals for Luminescence Thermometry up to 900 K. *J. Phys. Chem. C* **121**, 3503–3510 (2017).
 43. Achatz, D. E., Ali, R. & Wolfbeis, O. S. Luminescent Chemical Sensing, Biosensing, and Screening Using Upconverting Nanoparticles BT - Luminescence Applied in Sensor Science. *Lumin. Appl. Sens. Sci.* **300**, 29–50 (2011).
 44. Bogdan, N., Vetrone, F., Ozin, G. A. & Capobianco, J. A. Synthesis of Ligand-Free Colloidally Stable Water Dispersible Brightly Luminescent Lanthanide-Doped Upconverting Nanoparticles. *Nano Lett.* **11**, 835–840 (2011).
 45. Boyer, J.-C., Cuccia, L. A. & Capobianco, J. A. Synthesis of colloidal upconverting NaYF₄: Er³⁺/Yb³⁺ and Tm³⁺/Yb³⁺ monodisperse nanocrystals. *Nano Lett.* **7**, 847–852 (2007).
 46. Wei, Y., Lu, F., Zhang, X. & Chen, D. Synthesis and characterization of efficient near-infrared upconversion Yb and Tm codoped NaYF₄ nanocrystal reporter. *J. Alloys Compd.* **427**, 333–340 (2007).
 47. Yang, L. W., Han, H. L., Zhang, Y. Y. & Zhong, J. X. White Emission by Frequency Up-Conversion in Yb³⁺-Ho³⁺-Tm³⁺ Triply Doped Hexagonal NaYF₄ Nanorods. *J. Phys. Chem. C* **113**, 18995–18999 (2009).
 48. Annemarie Nadorta, J. Z. and E. M. G. Lanthanide upconversion luminescence at a nanoscale: fundamentals and optical properties. *Nanoscale* **8**, 13099–13130 (2016).
 49. Pin, M. W. *et al.* Atomistic evolution during the phase transition on a metastable single NaYF₄:Yb,Er upconversion nanoparticle. *Sci. Rep.* **8**, 1–10 (2018).
 50. Stouwdam, J. W. & Van Veggel, F. C. J. M. Near-infrared Emission of Redispersible Er³⁺, Nd³⁺, and Ho³⁺ Doped LaF₃ Nanoparticles. *Nano Lett.* **2**, 733–737 (2002).

Bibliography

51. Yi, G. & Chow, G.-M. Colloidal LaF₃:Yb,Er, LaF₃:Yb,Ho and LaF₃:Yb,Tm nanocrystals with multicolor upconversion fluorescence. *J. Mater. Chem.* **15**, (2005).
52. Heer, S., Kömpe, K., Güdel, H.-U. & Haase, M. Highly Efficient Multicolor Upconversion Emission in Transparent Colloids of Lanthanide-Doped NaYF₄ Nanocrystals. *Adv. Mater.* **16**, 2102–2105 (2004).
53. Yi, G. *et al.* Synthesis, characterization, and biological application of size-controlled nanocrystalline NaYF₄:Yb,Er infrared-to-visible up-conversion phosphors. *Nano Lett.* **4**, 2191–2196 (2004).
54. Li, Z. & Zhang, Y. An efficient and user-friendly method for the synthesis of hexagonal-phase NaYF₄:Yb, Er/Tm nanocrystals with controllable shape and upconversion fluorescence. *Nanotechnology* **19**, 1–5 (2008).
55. Li, Z., Zhang, Y. & Jiang, S. Multicolor core/shell-structured upconversion fluorescent nanoparticles. *Adv. Mater.* **20**, 4765–4769 (2008).
56. Mai, H.-X. *et al.* High-Quality Sodium Rare-Earth Fluoride Nanocrystals: Controlled Synthesis and Optical Properties. *J. Am. Chem. Soc.* **128**, 6426–6436 (2006).
57. Mai, H.-X., Zhang, Y.-W., Sun, L.-D. & Yan, C.-H. Size- and Phase-Controlled Synthesis of Monodisperse NaYF₄:Yb,Er Nanocrystals from a Unique Delayed Nucleation Pathway Monitored with Upconversion Spectroscopy. *J. Phys. Chem. C* **111**, 13730–13739 (2007).
58. Yi, G. & Moog Chow, G. Synthesis of Hexagonal-Phase NaYF₄:Yb,Er and NaYF₄:Yb,Tm Nanocrystals with Efficient Up-Conversion Fluorescence. *Adv. Funct. Mater.* **16**, 2324–2329 (2006).
59. Zhang, Y.-W., Sun, X., Si, R., You, L.-P. & Yan, C.-H. Single-Crystalline and Monodisperse LaF₃ Triangular Nanoplates from a Single-Source Precursor. *J. Am. Chem. Soc.* **127**, 3260–3261 (2005).
60. Das, G. K. & Tan, T. T. Y. Rare-Earth-Doped and Codoped Y₂O₃ Nanomaterials as Potential Bioimaging Probes. *J. Phys. Chem. C* **112**, 11211–11217 (2008).
61. Zeng, J.-H., Su, J., Li, Z.-H., Yan, R.-X. & Li, Y.-D. Synthesis and Upconversion Luminescence of Hexagonal-Phase NaYF₄:Yb, Er³⁺ Phosphors of Controlled Size and Morphology. *Adv. Mater.* **17**, 2119–2123 (2005).

Bibliography

62. Wang, X., Zhuang, J., Peng, Q. & Li, Y. A general strategy for nanocrystal synthesis. *Nature* **437**, 121–124 (2005).
63. Li, C. *et al.* Shape controllable synthesis and upconversion properties of NaYbF₄/NaYbF₄:Er³⁺ and YbF₃/YbF₃:Er³⁺ microstructures. *J. Mater. Chem.* **18**, 1353–1361 (2008).
64. Wang, F., Fan, X., Wang, M. & Zhang, Y. Multicolour PEI/NaGdF₄:Ce³⁺,Ln³⁺ nanocrystals by single-wavelength excitation. *Nanotechnology* **18**, 25701 (2006).
65. Liu, C. & Chen, D. Controlled synthesis of hexagon shaped lanthanide-doped LaF₃ nanoplates with multicolor upconversion fluorescence. *J. Mater. Chem.* **17**, 3875–3880 (2007).
66. Boyer, J. C., Vetrone, F., Cuccia, L. A. & Capobianco, J. A. Synthesis of colloidal upconverting NaYF₄ nanocrystals doped with Er³⁺, Yb³⁺ and Tm³⁺, Yb³⁺ via thermal decomposition of lanthanide trifluoroacetate precursors. *J. Am. Chem. Soc.* **128**, 7444–7445 (2006).
67. Lin, M. *et al.* Recent advances in synthesis and surface modification of lanthanide-doped upconversion nanoparticles for biomedical applications. *Biotechnol. Adv.* **30**, 1551–1561 (2012).
68. Algar, W. R. *et al.* The controlled display of biomolecules on nanoparticles: A challenge suited to bioorthogonal chemistry. *Bioconjug. Chem.* **22**, 825–858 (2011).
69. Sperling, R. A. & Parak, W. J. Surface modification, functionalization and bioconjugation of colloidal Inorganic nanoparticles. *Philos. Trans. R. Soc. A Math. Phys. Eng. Sci.* **368**, 1333–1383 (2010).
70. Zhang, T., Ge, J., Hu, Y. & Yin, Y. A general approach for transferring hydrophobic nanocrystals into water. *Nano Lett.* **7**, 3203–3207 (2007).
71. Boyer, J.-C., Manseau, M.-P., Murray, J. I. & van Veggel, F. C. J. M. Surface Modification of Upconverting NaYF₄ Nanoparticles with PEG–Phosphate Ligands for NIR (800 nm) Biolabeling within the Biological Window. *Langmuir* **26**, 1157–1164 (2010).
72. Dong, A. *et al.* A generalized ligand-exchange strategy enabling sequential surface functionalization of colloidal nanocrystals. *J. Am. Chem. Soc.* **133**, 998–1006 (2011).

Bibliography

73. Chen, Z. *et al.* Versatile synthesis strategy for carboxylic acid-functionalized upconverting nanophosphors as biological labels. *J. Am. Chem. Soc.* **130**, 3023–3029 (2008).
74. Zhou, H., Xu, C., Sun, W. & Yan, C.-H. Clean and Flexible Modification Strategy for Carboxyl/Aldehyde-Functionalized Upconversion Nanoparticles and Their Optical Applications. *Adv. Funct. Mater.* **19**, 3892–3900 (2009).
75. Wang, M. *et al.* Two-phase solvothermal synthesis of rare-earth doped NaYF₄ upconversion fluorescent nanocrystals. *Mater. Lett.* **63**, 325–327 (2009).
76. Sedlmeier, A. & Gorris, H. H. Surface modification and characterization of photon-upconverting nanoparticles for bioanalytical applications. *Chem. Soc. Rev.* **44**, 1526–1560 (2015).
77. Jiang, G., Pichaandi, J., Johnson, N. J. J., Burke, R. D. & Van Veggel, F. C. J. M. An effective polymer cross-linking strategy to obtain stable dispersions of upconverting NaYF₄ nanoparticles in buffers and biological growth media for biolabeling applications. *Langmuir* **28**, 3239–3247 (2012).
78. Cheng, L., Yang, K., Shao, M., Lee, S. T. & Liu, Z. Multicolor in vivo imaging of upconversion nanoparticles with emissions tuned by luminescence resonance energy transfer. *J. Phys. Chem. C* **115**, 2686–2692 (2011).
79. Cheng, L. *et al.* Highly-sensitive multiplexed in vivo imaging using pegylated upconversion nanoparticles. *Nano Res.* **3**, 722–732 (2010).
80. Budijono, S. J. *et al.* Synthesis of stable block-copolymer-protected NaYF₄:Yb³⁺, Er³⁺ up-converting phosphor nanoparticles. *Chem. Mater.* **22**, 311–318 (2010).
81. Liang, S. *et al.* Decoration of up-converting NaYF₄:Yb,Er(Tm) nanoparticles with surfactant bilayer. A versatile strategy to perform oil-to-water phase transfer and subsequently surface silication. *CrystEngComm* **14**, 3484–3489 (2012).
82. Li, L.-L. *et al.* Biomimetic Surface Engineering of Lanthanide-Doped Upconversion Nanoparticles as Versatile Bioprobes. *Angew. Chem. Int. Ed. Engl.* **51**, 6121–6125 (2013).
83. Wang, L. *et al.* Fluorescence Resonant Energy Transfer Biosensor Based on Upconversion-Luminescent Nanoparticles. *Angew. Chem. Int. Ed. Engl.* **44**, 6054–

Bibliography

- 6057 (2005).
84. Liu, Z. *et al.* Monodisperse silica nanoparticles encapsulating upconversion fluorescent and superparamagnetic nanocrystals. *Chem. Commun.* 694–696 (2008). doi:10.1039/b715402j
 85. Li, Z., Zhang, Y., Shuter, B. & Idris, N. M. Hybrid lanthanide nanoparticles with paramagnetic shell coated on upconversion fluorescent nanocrystals. *Langmuir* **25**, 12015–12018 (2009).
 86. Shan, J. & Ju, Y. Controlled synthesis of lanthanide-doped NaYF₄ upconversion nanocrystals via ligand induced crystal phase transition and silica coating. *Appl. Phys. Lett.* **91**, 123103 (2007).
 87. Darbandi, M. & Nann, T. One-pot synthesis of YF₃@silica core/shell nanoparticles. *Chem. Commun.* 776–778 (2006). doi:10.1039/b516171a
 88. Li, Z. & Zhang, Y. Monodisperse silica-coated polyvinyl-pyrrolidone/NaYF₄ nanocrystals with multicolor upconversion fluorescence emission. *Angew. Chemie - Int. Ed.* **45**, 7732–7735 (2006).
 89. WERNER STÖBER, A. F. A. & BOHN, D. E. Controlled Growth of Monodisperse Silica Spheres in the Micron Size Range. *J. Colloid Interface Sci.* **26**, 62–69 (1968).
 90. Xing, H. *et al.* Multifunctional nanoprobe for upconversion fluorescence, MR and CT trimodal imaging. *Biomaterials* **33**, 1079–1089 (2012).
 91. Liu, J. N., Bu, W. B. & Shi, J. L. Silica Coated Upconversion Nanoparticles: A Versatile Platform for the Development of Efficient Theranostics. *Acc. Chem. Res.* **48**, 1797–1805 (2015).
 92. Qian, H., Guo, H. C., Ho, P. C., Mahendran, R. & Zhang, Y. Mesoporous-silica-coated up-conversion fluorescent nanoparticles for photodynamic therapy. *Small* **5**, 2285–2290 (2009).
 93. Gai, S. *et al.* Synthesis of Magnetic, Up-Conversion Luminescent, and Mesoporous Core-Shell-Structured Nanocomposites as Drug Carriers. *Adv. Funct. Mater.* **20**, 1166–1172 (2010).
 94. Liu, J. *et al.* Real-Time In Vivo Quantitative Monitoring of Drug Release by Dual-Mode Magnetic Resonance and Upconverted Luminescence Imaging. *Angew. Chem.*

Bibliography

- Int. Ed. Engl.* **53**, 4551–4555 (2014).
95. Yang, D. *et al.* Current Advances of Lanthanide Ion (Ln³⁺)-Based Upconversion Nanomaterials for Drug Delivery. *Chem. Soc. Rev.* **53**, 4551–4555 (2014).
 96. Kamimura, M., Miyamoto, D., Saito, Y., Soga, K. & Nagasaki, Y. Design of poly(ethylene glycol)/streptavidin coimmobilized upconversion nanophosphors and their application to fluorescence biolabeling. *Langmuir* **24**, 8864–8870 (2008).
 97. Liu, Q. *et al.* ¹⁸F-labeled magnetic-upconversion nanophosphors via rare-earth cation-assisted ligand assembly. *ACS Nano* **5**, 3146–3157 (2011).
 98. Li, F. *et al.* High Contrast Upconversion Luminescence Targeted Imaging in Vivo Using Peptide-Labeled Nanophosphors. *Anal. Chem.* **81**, 8687–8694 (2009).
 99. Zhou, J. *et al.* Dual-modality in vivo imaging using rare-earth nanocrystals with near-infrared to near-infrared (NIR-to-NIR) upconversion luminescence and magnetic resonance properties. *Biomaterials* **31**, 3287–3295 (2010).
 100. Cao, T. *et al.* Water-soluble NaYF₄:Yb/Er upconversion nanophosphors: Synthesis, characteristics and application in bioimaging. *Inorg. Chem. Commun.* **13**, 392–394 (2010).
 101. Wang, F. *et al.* Simultaneous phase and size control of upconversion nanocrystals through lanthanide doping. *Nature* **463**, 1061–1065 (2010).
 102. Dong, B. *et al.* Multifunctional NaYF₄:Yb³⁺, Er³⁺ @Ag core/shell nanocomposites: Integration of upconversion imaging and photothermal therapy. *J. Mater. Chem.* **21**, 6193–6200 (2011).
 103. Wang, Z. L. *et al.* Simultaneous synthesis and functionalization of water-soluble up-conversion nanoparticles for in-vitro cell and nude mouse imaging. *Nanoscale* **3**, 2175–2181 (2011).
 104. Nyk, M., Kumar, R., Ohulchanskyy, T. Y., Bergey, E. J. & Prasad, P. N. High Contrast in Vitro and in Vivo Photoluminescence Bioimaging Using Near Infrared to Near Infrared Up-Conversion in Tm³⁺ and Yb³⁺ Doped Fluoride Nanophosphors. *Nano Lett.* **8**, 3834–3838 (2008).
 105. Zhan, Q. *et al.* Using 915 nm laser excited Tm³⁺/Er³⁺/Ho³⁺-doped NaYbF₄ upconversion nanoparticles for in vitro and deeper in vivo bioimaging without

Bibliography

- overheating irradiation. *ACS Nano* **5**, 3744–3757 (2011).
106. Chen, Q. *et al.* Functionalization of upconverted luminescent NaYF₄:Yb/Er nanocrystals by folic acid-chitosan conjugates for targeted lung cancer cell imaging. *J. Mater. Chem.* **21**, 7661–7667 (2011).
 107. Shen, J., Sun, L. D., Zhang, Y. W. & Yan, C. H. Superparamagnetic and upconversion emitting Fe₃O₄/NaYF₄:Yb,Er hetero-nanoparticles via a crosslinker anchoring strategy. *Chem. Commun.* **46**, 5731–5733 (2010).
 108. Zhou, J., Yao, L., Li, C. & Li, F. A versatile fabrication of upconversion nanophosphors with functional-surface tunable ligands. *J. Mater. Chem.* **20**, 8078–8085 (2010).
 109. Rantanen, T., Järvenpää, M.-L., Vuojola, J., Kuningas, K. & Soukka, T. Fluorescence-Quenching-Based Enzyme-Activity Assay by Using Photon Upconversion. *Angew. Chemie Int. Ed.* **47**, 3811–3813 (2008).
 110. Chen, G., Ohulchanskyy, T. Y., Law, W. C., Ågren, H. & Prasad, P. N. Monodisperse NaYbF₄:Tm³⁺/NaGdF₄ core/shell nanocrystals with near-infrared to near-infrared upconversion photoluminescence and magnetic resonance properties. *Nanoscale* **3**, 2003–2008 (2011).
 111. Chatterjee, D. K. & Yong, Z. Upconverting nanoparticles as nanotransducers for photodynamic therapy in cancer cells. *Nanomedicine* **3**, 73–82 (2008).
 112. Wang, F. *et al.* Synthesis of polyethylenimine/NaYF₄ nanoparticles with upconversion fluorescence. *Nanotechnology* **17**, 5786–5791 (2006).
 113. Wang, M. *et al.* Immunolabeling and NIR-Excited Fluorescent Imaging of HeLa Cells by Using NaYF₄:Yb,Er Upconversion Nanoparticles. *ACS Nano* **3**, 1580–1586 (2009).
 114. Wang, C., Cheng, L. & Liu, Z. Drug delivery with upconversion nanoparticles for multi-functional targeted cancer cell imaging and therapy. *Biomaterials* **32**, 1110–1120 (2011).
 115. Cheng, L. *et al.* Facile Preparation of Multifunctional Upconversion Nanoprobes for Multimodal Imaging and Dual-Targeted Photothermal Therapy. *Angew. Chemie Int. Ed.* **50**, 7385–7390 (2011).

Bibliography

116. Wang, L. & Li, Y. Green upconversion nanocrystals for DNA detection. *Chem. Commun.* 2557–2559 (2006). doi:10.1039/B604871D
117. Bogdan, N., Vetrone, F., Roy, R. & Capobianco, J. A. Carbohydrate-coated lanthanide-doped upconverting nanoparticles for lectin recognition. *J. Mater. Chem.* **20**, 7543–7550 (2010).
118. Liu, K. *et al.* Covalently assembled NIR nanoplatform for simultaneous fluorescence imaging and photodynamic therapy of cancer cells. *ACS Nano* **6**, 4054–4062 (2012).
119. Li, Z., Wang, L., Wang, Z., Liu, X. & Xiong, Y. Modification of NaYF₄:Yb,Er@SiO₂ nanoparticles with gold nanocrystals for tunable green-to-red upconversion emissions. *J. Phys. Chem. C* **115**, 3291–3296 (2011).
120. Xiong, L. Q. *et al.* Synthesis, characterization, and in vivo targeted imaging of amine-functionalized rare-earth up-converting nanophosphors. *Biomaterials* **30**, 5592–5600 (2009).
121. Lezhnina, M. M., Jüstel, T., Kätker, H., Wiechert, D. U. & Kynast, U. H. Efficient Luminescence from Rare-Earth Fluoride Nanoparticles with Optically Functional Shells. *Adv. Funct. Mater.* **16**, 935–942 (2006).
122. Yi, G. S. & Chow, G. M. Water-soluble NaYF₄:Yb,Er(Tm)/NaYF₄/polymer core/shell/shell nanoparticles with significant enhancement of upconversion fluorescence. *Chem. Mater.* **19**, 341–343 (2007).
123. Zhang, F. *et al.* Direct Imaging the Upconversion Nanocrystal Core/Shell Structure at the Subnanometer Level: Shell Thickness Dependence in Upconverting Optical Properties. *Nano Lett.* **12**, 2852–2858 (2012).
124. Guo, H., Li, Z., Qian, H., Hu, Y. & Muhammad, I. N. Seed-mediated synthesis of NaYF₄:Yb,Er/NaGdF₄ nanocrystals with improved upconversion fluorescence and MR relaxivity. *Nanotechnology* **21**, 1–6 (2010).
125. Dong, C., Korinek, A., Blasiak, B., Tomanek, B. & Van Veggel, F. C. J. M. Cation exchange: A facile method to make NaYF₄:Yb,Tm-NaGdF₄ core-shell nanoparticles with a thin, tunable, and uniform shell. *Chem. Mater.* **24**, 1297–1305 (2012).
126. Mai, H.-X., Zhang, Y.-W., Sun, L.-D. & Yan, C.-H. Highly Efficient Multicolor Up-Conversion Emissions and Their Mechanisms of Monodisperse NaYF₄:Yb,Er Core

Bibliography

- and Core/Shell-Structured Nanocrystals. *J. Phys. Chem. C* **111**, 13721–13729 (2007).
127. Wang, Y. *et al.* Upconversion Luminescence of NaYF₄:Yb³⁺,Er³⁺@NaYF₄ Core/Shell Nanoparticles: Excitation Power Density and Surface Dependence. *J. Mater. Chem. C* **113**, 7164–7169 (2009).
128. Wang, F., Wang, J. & Liu, X. Direct evidence of a surface quenching effect on size-dependent luminescence of upconversion nanoparticles. *Angew. Chemie - Int. Ed.* **49**, 7456–7460 (2010).
129. Park, Y. Il *et al.* Nonblinking and Nonbleaching Upconverting Nanoparticles as an Optical Imaging Nanoprobe and T1 Magnetic Resonance Imaging Contrast Agent. *Adv. Mater.* **21**, 4467–4471 (2009).
130. Chen, G. *et al.* Core/Shell NaGdF₄:Nd³⁺/NaGdF₄ Nanocrystals with Efficient Near-Infrared to Near-Infrared Downconversion Photoluminescence for Bioimaging Applications. *ACS Nano* **6**, 2969–2977 (2012).
131. Boyer, J. C., Gagnon, J., Cuccia, L. A. & Capobianco, J. A. Synthesis, characterization, and spectroscopy of NaGdF₄: Ce³⁺, Tb³⁺/NaYF₄ core/shell nanoparticles. *Chem. Mater.* **19**, 3358–3360 (2007).
132. Li, C. *et al.* LaF₃, CeF₃, CeF₃:Tb³⁺, and CeF₃:Tb³⁺@LaF₃ (core-shell) nanoplates: Hydrothermal synthesis and luminescence properties. *J. Phys. Chem. C* **112**, 2904–2910 (2008).
133. Wang, Z. L. *et al.* A facile synthesis and photoluminescent properties of redispersible CeF₃, CeF₃:Tb³⁺, and CeF₃:Tb³⁺/LaF₃ (core/shell) nanoparticles. *Chem. Mater.* **18**, 2030–2037 (2006).
134. Gai, S. *et al.* Monodisperse CeF₃, CeF₃:Tb³⁺, and CeF₃:Tb³⁺@LaF₃ core/shell nanocrystals: synthesis and luminescent properties. *J. Mater. Chem.* **21**, 14610–14615 (2011).
135. Schäfer, H., Ptacek, P., Zerzouf, O. & Haase, M. Synthesis and Optical Properties of KYF₄/Yb, Er Nanocrystals, and their Surface Modification with Undoped KYF₄. *Adv. Funct. Mater.* **18**, 2913–2918 (2008).
136. Yi, G., Peng, Y. & Gao, Z. Strong red-emitting near-infrared-to-visible upconversion fluorescent nanoparticles. *Chem. Mater.* **23**, 2729–2734 (2011).

Bibliography

137. Chen, G., Qiu, H., Prasad, P. N. & Chen, X. Upconversion Nanoparticles: Design, Nanochemistry, and Applications in Theranostics. *Chem. Rev.* **114**, 5161–5214 (2014).
138. Vetrone, F., Naccache, R., Mahalingam, V., Morgan, C. G. & Capobianco, J. A. The Active-Core/Active-Shell Approach: A Strategy to Enhance the Upconversion Luminescence in Lanthanide-Doped Nanoparticles. *Adv. Funct. Mater.* **19**, 2924–2929 (2009).
139. Liu, J. *et al.* Recent advances of plasmonic nanoparticles and their applications. *Materials (Basel)*. **11**, 1–21 (2018).
140. Zhang, F. *et al.* Fabrication of Ag@SiO₂@Y₂O₃:Er nanostructures for bioimaging: tuning of the upconversion fluorescence with silver nanoparticles. *J. Am. Chem. Soc.* **132**, 2850–1 (2010).
141. Zhang, H. *et al.* Plasmonic Modulation of the Upconversion Fluorescence in NaYF₄:Yb/Tm Hexaplate Nanocrystals Using Gold Nanoparticles or Nanoshells. *Angew. Chemie Int. Ed.* **49**, 2865–2868 (2010).
142. Priyam, A., Idris, N. M. & Zhang, Y. Gold nanoshell coated NaYF₄nanoparticles for simultaneously enhanced upconversion fluorescence and darkfield imaging. *J. Mater. Chem.* **22**, 960–965 (2012).
143. Liu, X. & Lei, D. Y. Simultaneous excitation and emission enhancements in upconversion luminescence using plasmonic double-resonant gold nanorods. *Sci. Rep.* **5**, 1–13 (2015).
144. Luoshan, M. *et al.* Surface plasmon resonance enhanced multi-shell-modified upconversion NaYF₄:Yb³⁺, Er³⁺@SiO₂@Au@TiO₂ crystallites for dye-sensitized solar cells. *J. Power Sources* **307**, 468–473 (2016).
145. Chen, C.-W., Chan, Y.-C., Hsiao, M. & Liu, R.-S. Plasmon-Enhanced Photodynamic Cancer Therapy by Upconversion Nanoparticles Conjugated with Au Nanorods. *ACS Appl. Mater. Interfaces* **8**, 32108–32119 (2016).
146. Aigouy, L. *et al.* AC thermal imaging of a microwire with a fluorescent nanocrystal: Influence of the near field on the thermal contrast. *J. Appl. Phys.* **106**, 074301 (2009).
147. Saïdi, E. *et al.* Scanning thermal imaging by near-field fluorescence spectroscopy.

Bibliography

- Nanotechnology* **20**, 115703 (2009).
148. Wang, X., Kong, X., Yu, Y., Sun, Y. & Zhang, H. Effect of annealing on upconversion luminescence of ZnO:Er³⁺ nanocrystals and high thermal sensitivity. *J. Phys. Chem. C* **111**, 15119–15124 (2007).
149. Tikhomirov, V. K., Driesen, K., Rodriguez, V. D., Gredin, P. & Mortier, M. Optical nanoheater based on the Yb³⁺-Er³⁺ co-doped nanoparticles. *Opt. Express* **17**, 11794–11798 (2009).
150. Singh, S., Kumar, K. & B. Rai, S. Multifunctional Er³⁺-Yb³⁺ Codoped Gd₂O₃ Nanocrystalline Phosphor Synthesized Through Optimized Combustion Route. *Appl. Phys. B* **94**, 165–173 (2009).
151. Vetrone, F. *et al.* Intracellular imaging of HeLa cells by non-functionalized NaYF₄: Er³⁺, Yb³⁺ upconverting nanoparticles. *Nanoscale* **2**, 495–498 (2010).
152. Corstjens, P. *et al.* Use of up-converting phosphor reporters in lateral-flow assays to detect specific nucleic acid sequences: A rapid, sensitive DNA test to identify human papillomavirus type 16 infection. *Clin. Chem.* **47**, 1885–1893 (2001).
153. Van De Rijke, F. *et al.* Up-converting phosphor reporters for nucleic acid microarrays. *Nat. Biotechnol.* **19**, 273–276 (2001).
154. Zijlmans, H. J. M. A. A. *et al.* Detection of cell and tissue surface antigens using up-converting phosphors: A new reporter technology. *Anal. Biochem.* **267**, 30–36 (1999).
155. Hampl, J. *et al.* Upconverting phosphor reporters in immunochromatographic assays. *Anal. Biochem.* **288**, 176–187 (2001).
156. Lim, S. F. *et al.* In vivo and scanning electron microscopy imaging of upconverting nanophosphors in *Caenorhabditis elegans*. *Nano Lett.* **6**, 169–174 (2006).
157. Chatterjee, D. K., Rufaihah, A. J. & Zhang, Y. Upconversion fluorescence imaging of cells and small animals using lanthanide doped nanocrystals. *Biomaterials* **29**, 937–943 (2008).
158. Xing, H. *et al.* Computed tomography imaging-guided radiotherapy by targeting upconversion nanocubes with significant imaging and radiosensitization enhancements. *Sci. Rep.* **3**, 9–11 (2013).

Bibliography

159. Nomoto, T. & Nishiyama, N. Photodynamic therapy. *J. Natl. Cancer Inst.* **90**, 889–905 (1998).
160. Zhang, P., Steelant, W., Kumar, M. & Scholfield, M. Versatile photosensitizers for photodynamic therapy at infrared excitation. *J. Am. Chem. Soc.* **129**, 4526–4527 (2007).
161. Hackbarth, S., Schlothauer, J., Preuß, A. & Röder, B. New insights to primary photodynamic effects - Singlet oxygen kinetics in living cells. *J. Photochem. Photobiol. B Biol.* **98**, 173–179 (2010).
162. Ethirajan, M., Chen, Y., Joshi, P. & Pandey, R. K. The role of porphyrin chemistry in tumor imaging and photodynamic therapy. *Chem. Soc. Rev.* **40**, 340–362 (2011).
163. Maiya, B. G. Photodynamic Therapy (PDT). *Resonance* **5**, 6–18 (2000).
164. Park, Y. Il *et al.* Theranostic Probe Based on Lanthanide-Doped Nanoparticles for Simultaneous In Vivo Dual-Modal Imaging and Photodynamic Therapy. *Adv. Mater.* **24**, 5755–5761 (2012).
165. Shan, J. *et al.* Pegylated Composite Nanoparticles Containing Upconverting Phosphors and meso- Tetraphenyl porphine (TPP) for Photodynamic Therapy. *Adv. Funct. Mater.* **21**, 2488–2495 (2011).
166. Celli, J. P. *et al.* Imaging and Photodynamic Therapy: Mechanisms, Monitoring, and Optimization. *Chem. Rev.* **110**, 2795–2838 (2010).
167. Liu, X. *et al.* Separately doped upconversion-C60 nanoplatfrom for NIR imaging-guided photodynamic therapy of cancer cells. *Chem. Commun.* **49**, 3224–3226 (2013).
168. Fukuzumi, S. *et al.* Selective one-electron and two-electron reduction of C60 with NADH and NAD dimer analogues via photoinduced electron transfer. *J. Am. Chem. Soc.* **120**, 8060–8068 (1998).
169. Arbogast, J. W. & Foote, C. S. Photophysical properties of C70. *Am. Chem. Soc.* **113**, 8886–8889 (1991).
170. Hamano, T. *et al.* Singlet oxygen production from fullerene derivatives: effect of sequential functionalization of the fullerene core. *Chem. Commun.* 21–22 (1997). doi:10.1039/A606335G

Bibliography

171. Shen, J., Zhao, L. & Han, G. Lanthanide-doped upconverting luminescent nanoparticle platforms for optical imaging-guided drug delivery and therapy. *Adv. Drug Deliv. Rev.* **65**, 744–755 (2013).
172. Kang, X. *et al.* Core-shell structured up-conversion luminescent and mesoporous NaYF₄:Yb³⁺/Er³⁺@ nSiO₂@ mSiO₂ nanospheres as carriers for drug delivery. *J. Phys. Chem. C* **115**, 15801–15811 (2011).
173. Hou, Z. *et al.* Electrospinning Preparation and Drug-Delivery Properties of an Up-conversion Luminescent Porous NaYF₄:Yb³⁺, Er³⁺@Silica Fiber Nanocomposite. *Adv. Funct. Mater.* **21**, 2356–2365 (2011).
174. Xu, Z. *et al.* Monodisperse core-shell structured up-conversion Yb(OH)CO₃@YbPO₄:Er³⁺ hollow spheres as drug carriers. *Biomaterials* **32**, 4161–4173 (2011).
175. Dong, L. *et al.* PEGylated Upconverting Luminescent Hollow Nanospheres for Drug Delivery and In Vivo Imaging. *Small* **9**, 3235–3241 (2013).
176. Ren, W. *et al.* TWEEN coated NaYF₄:Yb,Er/NaYF₄ core/shell upconversion nanoparticles for bioimaging and drug delivery. *RSC Adv.* **2**, 7037–7041 (2012).
177. Liu, J. N. *et al.* Simultaneous nuclear imaging and intranuclear drug delivery by nuclear-targeted multifunctional upconversion nanoprobe. *Biomaterials* **33**, 7282–7290 (2012).
178. Méndez-Ramos, J. *et al.* Turning into the blue: materials for enhancing TiO₂ photocatalysis by up-conversion photonics. *RSC Adv.* **3**, 23028–23034 (2013).
179. Vaiano, V. *et al.* Enhanced visible light photocatalytic activity by up-conversion phosphors modified N-doped TiO₂. *Appl. Catal. B Environ.* **176–177**, 594–600 (2015).
180. Chen, Z. & Fu, M. L. Recyclable magnetic Fe₃O₄@SiO₂/ β-NaYF₄: Yb³⁺, Tm³⁺/TiO₂ composites with NIR enhanced photocatalytic activity. *Mater. Res. Bull.* **107**, 194–203 (2018).
181. Di, W., Yang, R., Qin, W., Tang, Y. & Zhai, X. NIR-Responsive Photocatalytic Activity and Mechanism of NaYF₄:Yb,Tm@TiO₂ Core-Shell Nanoparticles. *ACS Catal.* **3**, 405–412 (2013).

Bibliography

182. Wang, W., Huang, W., Ni, Y., Lu, C. & Xu, Z. Different upconversion properties of β -NaYF₄:Yb³⁺,Tm³⁺/Er³⁺ in affecting the near-infrared-driven photocatalytic activity of high-reactive TiO₂. *ACS Appl. Mater. Interfaces* **6**, 340–348 (2014).
183. Xu, Z. *et al.* Harvesting Lost Photons: Plasmon and Upconversion Enhanced Broadband Photocatalytic Activity in Core@Shell Microspheres Based on Lanthanide-Doped NaYF₄, TiO₂, and Au. *Adv. Funct. Mater.* **25**, 2950–2960 (2015).
184. Zhang, Y. & Hong, Z. Synthesis of lanthanide-doped NaYF₄@TiO₂ core–shell composites with highly crystalline and tunable TiO₂ shells under mild conditions and their upconversion-based photocatalysis. *Nanoscale* **5**, 8930–8933 (2013).
185. Wang, W., Li, Y., Kang, Z., Wang, F. & Yu, J. C. A NIR-driven photocatalyst based on α -NaYF₄:Yb,Tm@TiO₂ core-shell structure supported on reduced graphene oxide. *Appl. Catal. B Environ.* **182**, 184–192 (2016).
186. Zhang, F., Zhang, C.-L., Peng, H.-Y., Cong, H.-P. & Qian, H.-S. Near-Infrared Photocatalytic Upconversion Nanoparticles/TiO₂ Nanofibers Assembled in Large Scale by Electrospinning. *Part. Part. Syst. Character.* **33**, 248–253 (2016).
187. Wang, K. *et al.* Coating a N-doped TiO₂ shell on dually sensitized upconversion nanocrystals to provide NIR-enhanced photocatalysts for efficient utilization of upconverted emissions. *Inorg. Chem. Front.* **3**, 1190–1197 (2016).
188. Hou, Z. *et al.* UV-emitting upconversion-based TiO₂ photosensitizing nanoplatform: Near-infrared light mediated in vivo photodynamic therapy via mitochondria-involved apoptosis pathway. *ACS Nano* **9**, 2584–2599 (2015).
189. Wu, S. *et al.* Photocatalytic degradation of microcystin-LR with a nanostructured photocatalyst based on upconversion nanoparticles@TiO₂ composite under simulated solar lights. *Sci. Rep.* **7**, 1–11 (2017).
190. Challagulla, S., Payra, S., Bajaj, M. & Roy, S. Role of synthesis of upconversion nanoparticles towards surface modification and photocatalysis. *Bull. Mater. Sci.* **42**, 102 (2019).
191. Sarkar, D., Ganguli, S., Samanta, T. & Mahalingam, V. Design of Lanthanide-Doped Colloidal Nanocrystals: Applications as Phosphors, Sensors, and Photocatalysts. *Langmuir* **35**, 6211–6230 (2019).

Bibliography

192. Chen, Y., Zou, L., Zhang, X., Huang, Q. & Yu, H. Sublattice Energy Cluster Construction for The Enhancement of NIR Photocatalytic Performance of LiYF₄:Tm@TiO₂. *ChemistrySelect* **4**, 4262–4270 (2019).
193. Liang, S. *et al.* Fabrication and characterization of BiOBr:Yb³⁺,Er³⁺/g-C₃N₄ p-n junction photocatalysts with enhanced visible-NIR-light-driven photoactivities. *Sep. Purif. Technol.* **206**, 69–79 (2018).
194. Ciamician, G. THE PHOTOCHEMISTRY OF THE FUTURE. *Science (80-.)*. **36**, 385–394 (1912).
195. FUJISHIMA, A. & HONDA, K. Electrochemical Photolysis of Water at a Semiconductor Electrode. *Nature* **238**, 37–38 (1972).
196. Pascual, J., Camassel, J. & Mathieu, H. Fine structure in the intrinsic absorption edge of TiO₂. *Phys. Rev. B* **18**, 5606–5614 (1978).
197. Turner, J. A. Sustainable Hydrogen Production. *Science (80-.)*. **305**, 972–974 (2004).
198. Wang, J. *et al.* Origin of photocatalytic activity of Nitrogen-doped TiO₂ nanobelts. *J. Am. Chem. Soc.* **131**, 12290–12297 (2009).
199. Wu, N. *et al.* Shape-enhanced photocatalytic activity of single-crystalline anatase TiO₂ (101) nanobelts. *J. Am. Chem. Soc.* **132**, 6679–6685 (2010).
200. Thimsen, E., Le Formal, F., Grätzel, M. & Warren, S. C. Influence of plasmonic Au nanoparticles on the photoactivity of Fe₂O₃ electrodes for water splitting. *Nano Lett.* **11**, 35–43 (2011).
201. Yang, T. T. *et al.* Interfacial charge carrier dynamics in core-shell au-CdS nanocrystals. *J. Phys. Chem. C* **114**, 11414–11420 (2010).
202. Tian, J. *et al.* A Bi₂WO₆-Based Hybrid Photocatalyst with Broad Spectrum Photocatalytic Properties under UV, Visible, and Near-Infrared Irradiation. *Adv. Mater.* **25**, 5075–5080 (2013).
203. Wang, J. *et al.* Investigation on degradation of dyestuff wastewater using visible light in the presence of a novel nano TiO₂ catalyst doped with upconversion luminescence agent. *J. Photochem. Photobiol. A Chem.* **180**, 189–195 (2006).
204. Zhang, F., Zhang, C.-L., Wang, W.-N., Cong, H.-P. & Qian, H.-S. Titanium

Bibliography

- Dioxide/Upconversion Nanoparticles/Cadmium Sulfide Nanofibers Enable Enhanced Full-Spectrum Absorption for Superior Solar Light Driven Photocatalysis. *ChemSusChem* **9**, 1449–1454 (2016).
205. Zhang, J. *et al.* Efficient Upconverting Multiferroic Core@Shell Photocatalysts: Visible-to-Near-Infrared Photon Harvesting. *ACS Appl. Mater. Interfaces* **9**, 8142–8150 (2017).
206. Li, S. *et al.* Remarkably enhanced photocatalytic activity of laser ablated Au nanoparticle decorated BiFeO₃ nanowires under visible-light. *Chem. Commun.* **49**, 5856–5858 (2013).
207. Sun, S., Wang, W., Zhang, L. & Shang, M. Visible Light-Induced Photocatalytic Oxidation of Phenol and Aqueous Ammonia in Flowerlike Bi₂Fe₄O₉ Suspensions. *J. Phys. Chem. C* **113**, 12826–12831 (2009).
208. Yang, W., Li, X., Chi, D., Zhang, H. & Liu, X. Lanthanide-doped upconversion materials: Emerging applications for photovoltaics and photocatalysis. *Nanotechnology* **25**, 1–16 (2014).
209. Ren, L. *et al.* Upconversion-P25-graphene composite as an advanced sunlight driven photocatalytic hybrid material. *J. Mater. Chem.* **22**, 11765–11771 (2012).
210. Chen, C. K., Chen, H. M., Chen, C.-J. & Liu, R.-S. Plasmon-enhanced near-infrared-active materials in photoelectrochemical water splitting. *Chem. Commun.* **49**, 7917–7919 (2013).
211. Wu, X. *et al.* Dye-Sensitized Core/Active Shell Upconversion Nanoparticles for Optogenetics and Bioimaging Applications. *ACS Nano* **10**, 1060–1066 (2016).
212. Liu, C. *et al.* Magnetic/upconversion fluorescent NaGdF₄:Yb,Er nanoparticle-based dual-modal molecular probes for imaging tiny tumors in vivo. *ACS Nano* **7**, 7227–7240 (2013).
213. Johnson, N. J. J., Oakden, W., Stanis, G. J., Scott Prosser, R. & Van Veggel, F. C. J. M. Size-tunable, ultrasmall NaGdF₄ nanoparticles: Insights into their T₁ MRI contrast enhancement. *Chem. Mater.* **23**, 3714–3722 (2011).
214. Huang, K., Jayakumar, M. K. G. & Zhang, Y. Lutetium doping for making big core and core-shell upconversion nanoparticles. *J. Mater. Chem. C* **20**, 25–33 (2013).

Bibliography

215. Pei, W. B. *et al.* Controlled synthesis of uniform $\text{Na}_x\text{ScF}_{3+x}$ nanopolyhedrons, nanoplates, nanorods, and nanospheres using solvents. *Cryst. Growth Des.* **15**, 2988–2993 (2015).
216. Pei, W. B. *et al.* NaF-mediated controlled-synthesis of multicolor $\text{Na}_x\text{ScF}_{3+x}:\text{Yb/Er}$ upconversion nanocrystals. *Nanoscale* **7**, 4048–4054 (2015).
217. Babak Nikoobakht and Mostafa A. El-Sayed. Preparation and Growth Mechanism of Gold Nanorods (NRs) Using Seed-Mediated Growth Method. *Chem. Mater* **15**, 1957–1962 (2003).
218. Murphy, C. J. *et al.* Anisotropic metal nanoparticles: Synthesis, assembly, and optical applications. *J. Phys. Chem. B* **109**, 13857–13870 (2005).
219. Bian, W. *et al.* Direct Identification of Surface Defects and Their Influence on the Optical Characteristics of Upconversion Nanoparticles. *ACS Nano* **12**, 3623–3628 (2018).
220. Xu, J. M. *et al.* $\text{Fe}_3\text{O}_4@\text{SiO}_2$ Core/Shell Nanoparticles: The Silica Coating Regulations with a Single Core for Different Core Sizes and Shell Thicknesses. *Chem. Mater.* **24**, 4572–4580 (2012).
221. Vaz, A. M. *et al.* Synthesis and characterization of biocatalytic $\gamma\text{-Fe}_2\text{O}_3@\text{SiO}_2$ particles as recoverable bioreactors. *Colloids Surfaces B Biointerfaces* **114**, 11–19 (2014).
222. Han, S. *et al.* Gold and Hairpin DNA Functionalization of Upconversion Nanocrystals for Imaging and In Vivo Drug Delivery. *Adv. Mater.* **29**, 1–7 (2017).
223. Duff, D. G., Baiker, A. & Edwards, P. P. A New Hydrosol of Gold Clusters. 1. Formation and Particle Size Variation. *Langmuir* **9**, 2301–2309 (1993).
224. Westcott, S. L., Oldenburg, S. J., Lee, T. R. & Halas, N. J. Formation and Adsorption of Clusters of Gold Nanoparticles onto Functionalized Silica Nanoparticle Surfaces. *Langmuir* **14**, 5396–5401 (1998).
225. Alonso-Cristobal, P. *et al.* Highly Sensitive DNA Sensor Based on Upconversion Nanoparticles and Graphene Oxide. *ACS Appl. Mater. Interfaces* **7**, 12422–12429 (2015).
226. Maeda, K. *et al.* Cobalt Oxide Nanoclusters on Rutile Titania as Bifunctional Units

Bibliography

- for Water Oxidation Catalysis and Visible Light Absorption: Understanding the Structure-Activity Relationship. *ACS Appl. Mater. Interfaces* **9**, 6114–6122 (2017).
227. Mills, A., Wells, N. & O'Rourke, C. Correlation between Δabs , ΔrGB (red) and stearic acid destruction rates using commercial self-cleaning glass as the photocatalyst. *Catal. Today* **230**, 245–249 (2014).
228. Zou, W., Visser, C., Maduro, J. A., Pshenichnikov, M. S. & Hummelen, J. C. Broadband dye-sensitized upconversion of near-infrared light. *Nat. Photonics* **6**, 560–564 (2012).
229. Krämer, K. W. *et al.* Hexagonal Sodium Yttrium Fluoride Based Green and Blue Emitting Upconversion Phosphors. *Chem. Mater.* **16**, 1244–1251 (2004).
230. Xu, C. T. *et al.* Upconverting nanoparticles for pre-clinical diffuse optical imaging, microscopy and sensing: Current trends and future challenges. *Laser Photonics Rev.* **7**, 663–697 (2013).
231. Wang, F. & Liu, X. Supporting Information Upconversion Multicolor Fine-Tuning : Visible to Near-Infrared Emission from Lanthanide-Doped NaYF₄ nanoparticles. *Synthesis (Stuttg.)* **3**, 1–7 (2008).
232. Wang, X., Zhuang, J., Peng, Q. & Li, Y. Hydrothermal synthesis of rare-earth fluoride nanocrystals. *Inorg. Chem.* **45**, 6661–6665 (2006).
233. Zhang, F., Li, J., Shan, J., Xu, L. & Zhao, D. Shape, size, and phase-controlled rare-earth fluoride nanocrystals with optical up-conversion properties. *Chem. - A Eur. J.* **15**, 11010–11019 (2009).
234. Cao, C. *et al.* Hydrothermal synthesis and white luminescence of Dy³⁺-Doped NaYF₄ microcrystals. *J. Am. Ceram. Soc.* **94**, 3405–3411 (2011).
235. Wang, L. & Li, Y. Controlled synthesis and luminescence of lanthanide doped NaYF₄ nanocrystals. *Chem. Mater.* **19**, 727–734 (2007).
236. Liu, J., Chen, G., Hao, S. & Yang, C. Sub-6 nm monodisperse hexagonal core/shell NaGdF₄ nanocrystals with enhanced upconversion photoluminescence. *Nanoscale* **9**, 91–98 (2017).
237. Dongdong, L. I., Qiyue, S., Yan, D. & Jianqing, J. Phase-, shape- and size-controlled synthesis of NaYF₄:Yb³⁺,Er³⁺ nanoparticles using rare-earth acetate precursors. *J.*

Bibliography

- Rare Earths* **32**, 1032–1036 (2014).
238. Gao, D. *et al.* Codopant ion-induced tunable upconversion emission in β -NaYF₄: Yb³⁺/Tm³⁺ nanorods. *Dalt. Trans.* **42**, 1834–1841 (2013).
239. Huang, K., Jayakumar, M. K. G. & Zhang, Y. Lutetium doping for making big core and core-shell upconversion nanoparticles. *J. Mater. Chem. C* **3**, 10267–10272 (2015).
240. Liang, X., Wang, X., Zhuang, J., Peng, Q. & Li, Y. Synthesis of NaYF₄ nanocrystals with predictable phase and shape. *Adv. Funct. Mater.* **17**, 2757–2765 (2007).
241. Ding, M. *et al.* Simultaneous morphology manipulation and upconversion luminescence enhancement of β -NaYF₄:Yb³⁺/Er³⁺ microcrystals by simply tuning the KF dosage. *Sci. Rep.* **5**, 1–14 (2015).
242. Li, C. *et al.* Different microstructures of β -NaYF₄ fabricated by hydrothermal process: Effects of pH values and fluoride sources. *Chem. Mater.* **19**, 4933–4942 (2007).
243. Grzechnik, A. *et al.* Hexagonal Na_{1.5}Y_{1.5}F₆ at high pressures. *J. Solid State Chem.* **165**, 159–164 (2002).
244. Wang, C. & Cheng, X. Controlled hydrothermal growth and tunable luminescence properties of β -NaYF₄:Yb³⁺/Er³⁺ microcrystals. *J. Alloys Compd.* **617**, 807–815 (2014).
245. Li, C., Quan, Z., Yang, J., Yang, P. & Lin, J. Highly uniform and monodisperse β -NaYF₄:Ln³⁺ (Ln = Eu, Tb, Yb/Er, and Yb/Tm) hexagonal micropillar crystals: Hydrothermal synthesis and luminescent properties. *Inorg. Chem.* **46**, 6329–6337 (2007).
246. Yang, K., Peng, H., Wen, Y. & Li, N. Re-examination of characteristic FTIR spectrum of secondary layer in bilayer oleic acid-coated Fe₃O₄ nanoparticles. *Appl. Surf. Sci.* **256**, 3093–3097 (2010).
247. Laudise, R. A. Kinetics of Hydrothermal Quartz Crystallization. *J. Am. Chem. Soc.* **81**, 562–566 (1959).
248. Chunxia, L. *et al.* β -NaYF₄ and β -NaYF₄:Eu³⁺ microstructures: Morphology control and tunable luminescence properties. *J. Phys. Chem. C* **113**, 2332–2339 (2009).

Bibliography

249. Rinkel, T., Nordmann, J., Raj, A. N. & Haase, M. Ostwald-ripening and particle size focussing of sub-10 nm NaYF₄ upconversion nanocrystals. *Nanoscale* **6**, 14523–14530 (2014).
250. Xue, X., Penn, R. L., Leite, E., Huang, F. & Lin, Z. Crystal Growth by Oriented Attachment: Kinetic Models and Control Factors. *CrystEngComm* **16**, 1419–1429 (2014).
251. Haase, M. & Schäfer, H. Upconverting nanoparticles. *Angew. Chemie - Int. Ed.* **50**, 5808–5829 (2011).
252. Lai, S. *et al.* Preparation and Upconversion Emission Modification of Crystalline Colloidal Arrays and Rare Earth Fluoride Microcrystal Composites. *Sci. Rep.* **5**, 1–8 (2015).
253. Chen, G., Yang, C. & Prasad, P. N. Nanophotonics and nanochemistry: Controlling the excitation dynamics for frequency up- and down-conversion in lanthanide-doped nanoparticles. *Acc. Chem. Res.* **46**, 1474–1486 (2013).
254. van Veggel, F. C. J. M., Dong, C., Johnson, N. J. J. & Pichaandi, J. Ln³⁺-doped nanoparticles for upconversion and magnetic resonance imaging: some critical notes on recent progress and some aspects to be considered. *Nanoscale* **4**, 7309 (2012).
255. Zhao, J. *et al.* Upconversion luminescence with tunable lifetime in NaYF₄:Yb,Er nanocrystals: role of nanocrystal size. *Nanoscale* **5**, 944–952 (2013).
256. Wang, C. & Cheng, X. Controlled hydrothermal growth and tunable luminescence properties of β -NaYF₄:Yb³⁺/Er³⁺ microcrystals. *J. Alloys Compd.* **617**, 807–815 (2014).
257. Lim, S. F., Ryu, W. S. & Austin, R. H. Particle size dependence of the dynamic photophysical properties of NaYF₄:Yb, Er nanocrystals. *Opt. Express* **18**, 2309 (2010).
258. Liao, J. *et al.* Upconversion Emission Enhancement of NaYF₄:Yb,Er Nanoparticles by Coupling Silver Nanoparticle Plasmons and Photonic Crystal Effects. *J. Phys. Chem. C* **118**, 17992–17999 (2014).
259. Ye, X. *et al.* Morphologically controlled synthesis of colloidal upconversion nanophosphors and their shape-directed self-assembly. *Proc. Natl. Acad. Sci.* **107**,

Bibliography

- 22430–22435 (2010).
260. Alyatkin, S. *et al.* The influence of energy migration on luminescence kinetics parameters in upconversion nanoparticles. *Nanotechnology* **28**, 1–10 (2017).
261. Wang, Y. *et al.* Insights into Li⁺-induced morphology evolution and upconversion luminescence enhancement of KSc₂F₇:Yb/Er nanocrystals. *J. Mater. Chem. C* **5**, 3503–3508 (2017).
262. Zhang, H., Song, S., Feng, J., Pang, M. & Wang, Z. Phase-tunable synthesis and upconversion photoluminescence of rare-earth-doped sodium scandium fluoride nanocrystals. *CrystEngComm* **15**, 6901 (2013).
263. Cao, J. *et al.* Tuning the phase, morphology and size of monodisperse ScF₃ and NaScF₄ crystals through lanthanide doping. *CrystEngComm* **18**, 5940–5951 (2016).
264. Zhang, L. *et al.* The colour tuning of upconversion emission from green to red in NaScF₄:Yb³⁺/Er³⁺ nanocrystals by adjusting the reaction time. *J. Alloys Compd.* **699**, 1–6 (2017).
265. Liang, Z. *et al.* Controllable synthesis of tetragonal LiScF₄:Yb³⁺, Er³⁺ nanocrystals and its upconversion photoluminescence properties: Lithium scandium fluoride nanocrystals. *Opt. Mater. (Amst)*. **62**, 255–260 (2016).
266. Ai, Y. *et al.* Lanthanide-doped NaScF₄ nanoprobles: Crystal structure, optical spectroscopy and biodetection. *Nanoscale* **5**, 6430–6438 (2013).
267. Wang, M., Huang, Q. L., Hong, J. M., Chen, X. T. & Xue, Z. L. Controlled synthesis and characterization of nanostructured EuF₃ with different crystalline phases and morphologies. *Cryst. Growth Des.* **6**, 2169–2173 (2006).
268. Gulzar, A., Xu, J., Yang, P., He, F. & Xu, L. Upconversion processes: Versatile biological applications and biosafety. *Nanoscale* **9**, 12248–12282 (2017).
269. P.W.Voorhees. The Theory of Ostwald Ripening. *J. Stat. Phys.* **38**, 231–252 (1985).
270. Shan, J. & Ju, Y. A single-step synthesis and the kinetic mechanism for monodisperse and hexagonal-phase NaYF₄:Yb, Er upconversion nanophosphors. *Nanotechnology* **20**, (2009).
271. Liu, S. *et al.* Size, phase-controlled synthesis, the nucleation and growth mechanisms

Bibliography

- of NaYF₄:Yb/Er nanocrystals. *J. Rare Earths* **36**, 1060–1066 (2018).
272. Lay, A. *et al.* Bright, Mechanosensitive Upconversion with Cubic-Phase Heteroepitaxial Core-Shell Nanoparticles. *Nano Lett.* **18**, 4454–4459 (2018).
273. Wang, F. *et al.* Tuning upconversion through energy migration in core-shell nanoparticles. *Nat. Mater.* **10**, 968–973 (2011).
274. Boyer, J.-C., Carling, C.-J., Gates, B. D. & Branda, N. R. Two-Way Photoswitching Using One Type of Near-Infrared Light, Upconverting Nanoparticles, and Changing Only the Light Intensity. *J. Am. Chem. Soc.* **132**, 15766–15772 (2010).
275. Alyatkin, S. *et al.* In-Depth Analysis of Excitation Dynamics in Dye-Sensitized Upconversion Core and Core/Active Shell Nanoparticles. *J. Phys. Chem. C* **122**, 18177–18184 (2018).
276. Haase, M. & Schäfer, H. Upconverting Nanoparticles. *Angew. Chemie - Int. Ed.* **50**, 5808–5829 (2011).
277. Chen, X., Peng, D., Jia, Q. & Wang, F. Photon Upconversion in Core-Shell Nanoparticles. *Chem. Soc. Rev.* **44**, 1318–1330 (2015).
278. Wen, H. Q. *et al.* Sequential Growth of NaYF₄:Yb/Er@NaGdF₄ Nanodumbbells for Dual-Modality Fluorescence and Magnetic Resonance Imaging. *ACS Appl. Mater. Interfaces* **9**, 9226–9232 (2017).
279. Johnson, N. J. J. & Van Veggel, F. C. J. M. Lanthanide-based heteroepitaxial core-shell nanostructures: Compressive versus tensile strain asymmetry. *ACS Nano* **8**, 10517–10527 (2014).
280. Zhang, C. & Lee, J. Y. Prevalence of anisotropic shell growth in rare earth core-shell upconversion nanocrystals. *ACS Nano* **7**, 4393–4402 (2013).
281. Liu, D. *et al.* Three-dimensional controlled growth of monodisperse sub-50 nm heterogeneous nanocrystals. *Nat. Commun.* **7**, 1–8 (2016).
282. Wang, Y. *et al.* Critical shell thickness of core/shell upconversion luminescence nanoplatform for fret application. *J. Phys. Chem. Lett.* **2**, 2083–2088 (2011).
283. Abdul Jalil, R. & Zhang, Y. Biocompatibility of silica coated NaYF₄ upconversion fluorescent nanocrystals. *Biomaterials* **29**, 4122–4128 (2008).

Bibliography

284. Arriagada, F. J. & Osseo-Asare, K. Synthesis of Nanosize Silica in a Nonionic Water-in-Oil Microemulsion: Effects of the Water/Surfactant Molar Ratio and Ammonia Concentration. *J. Colloid Interface Sci.* **211**, 210–220 (1999).
285. Kostiv, U. *et al.* Silica-coated upconversion lanthanide nanoparticles: The effect of crystal design on morphology, structure and optical properties. *Beilstein J. Nanotechnol.* **6**, 2290–2299 (2015).
286. Mondal, M., Rai, V. K. & Srivastava, C. Influence of silica surface coating on optical properties of Er^{3+} - Yb^{3+} : YMoO_4 upconverting nanoparticles. *Chem. Eng. J.* **327**, 838–848 (2017).
287. Lee, D. C., Mikulec, F. V., Pelaez, J. M., Koo, B. & Korgel, B. A. Synthesis and Magnetic Properties of Silica-Coated FePt Nanocrystals. *J. Phys. Chem. B* **110**, 11160–11166 (2006).
288. Zhang, M., Cushing, B. L. & O'Connor, C. J. Synthesis and characterization of monodisperse ultra-thin silica-coated magnetic nanoparticles. *Nanotechnology* **19**, (2008).
289. Yi, D. K., Lee, S. S., Papaefthymiou, G. C. & Ying, J. Y. Nanoparticle Architectures Templated by $\text{SiO}_2/\text{Fe}_2\text{O}_3$ Nanocomposites. *Chem. Mater.* **18**, 614–619 (2006).
290. Chen, S. L., Dong, P., Yang, G. H. & Yang, J. J. Kinetics of Formation of Monodisperse Colloidal Silica Particles through the Hydrolysis and Condensation of Tetraethylorthosilicate. *Ind. Eng. Chem. Res.* **35**, 4487–4493 (1996).
291. Artaki, I., Bradley, M., Zerda, T. W. & Jonas, J. NMR and Raman study of the hydrolysis reaction in sol-gel processes. *J. Phys. Chem.* **89**, 4399–4404 (1985).
292. Greenberg, S. A. The depolymerization of silica in sodium hydroxide solutions. *J. Phys. Chem.* **61**, 960–965 (1957).
293. Ajithkumar, G. *et al.* Multimodal bioimaging using a rare earth doped $\text{Gd}_2\text{O}_3\text{S}:\text{Yb}/\text{Er}$ phosphor with upconversion luminescence and magnetic resonance properties. *J. Mater. Chem. B* **1**, 1561–1572 (2013).
294. Vanblaaderen, A. & P. M. Kentgens, A. Particle Morphology and Chemical Microstructure of Colloidal Silica Sphere Made from Alkoxysilanes. *J. Non. Cryst. Solids* **149**, 161–178 (1992).

Bibliography

295. Zhang, L. *et al.* Tuning the mechanical properties of silica microcapsules. *Phys. Chem. Chem. Phys.* **12**, 15392–15398 (2010).
296. Cong, T. *et al.* Solvent-Induced Luminescence Variation of Upconversion Nanoparticles. *Langmuir* **32**, 13200–13206 (2016).
297. Arppe, R. *et al.* Quenching of the upconversion luminescence of NaYF₄:Yb³⁺,Er³⁺ and NaYF₄:Yb³⁺,Tm³⁺ nanophosphors by water: The role of the sensitizer Yb³⁺ in non-radiative relaxation. *Nanoscale* **7**, 11746–11757 (2015).
298. Bünzli, J.-C. G. & Piguet, C. Taking advantage of luminescent lanthanide ions. *Chem. Soc. Rev.* **34**, 1048–1077 (2005).
299. Bischof, C., Wahsner, J., Scholten, J., Trosien, S. & Seitz, M. Quantification of C–H Quenching in Near-IR Luminescent Ytterbium and Neodymium Cryptates. *J. Am. Chem. Soc.* **132**, 14334–14335 (2010).
300. Wilhelm, S. *et al.* Water dispersible upconverting nanoparticles: Effects of surface modification on their luminescence and colloidal stability. *Nanoscale* **7**, 1403–1410 (2015).
301. Strelow, C. *et al.* Ultrathin and Highly Passivating Silica Shells for Luminescent and Water-Soluble CdSe/CdS Nanorods. *Langmuir* **33**, 5253–5260 (2017).
302. Brinker, C. J. & Scherer, G. W. The physics and chemistry of sol gel processing. (1990).
303. Yamauchi, H., Ishikawa, T. & Kondo, S. Surface Characterization of Ultramicro Spherical Particles of Silica Prepared by W/O Microemulsion Method. *Colloids and Surfaces* **37**, 71–80 (1989).
304. Osseo-Asare, K. & Arriagada, F. J. Preparation of SiO₂ Nanoparticles in a Non-Ionic Reverse Micellar System. *Colloids and Surfaces* **50**, 321–339 (1990).
305. Guerrero-Martínez, A., Pérez-Juste, J. & Liz-Marzán, L. M. Recent progress on silica coating of nanoparticles and related nanomaterials. *Adv. Mater.* **22**, 1182–1195 (2010).
306. Vogt, C. *et al.* High quality and tuneable silica shell-magnetic core nanoparticles. *J. Nanoparticle Res.* **12**, 1137–1147 (2010).

Bibliography

307. Bartczak, D. & Kanaras, A. G. Preparation of peptide-functionalized gold nanoparticles using one pot EDC/Sulfo-NHS coupling. *Langmuir* **27**, 10119–10123 (2011).
308. Patil, M. M. & Rajput, S. S. SUCCINIMIDES : SYNTHESIS , REACTION AND BIOLOGICAL ACTIVITY. *Int. J. Pharm. Pharm. Sci.* **6**, 8–14 (2014).
309. Hülsemann, M. *et al.* Biofunctionalized Silica Nanoparticles: Standards in Amyloid- β Oligomer-Based Diagnosis of Alzheimer's Disease. *J. Alzheimer's Dis.* **54**, 1–10 (2016).
310. Olariu, C. I. *et al.* Multifunctional Fe₃O₄ nanoparticles for targeted bi-modal imaging of pancreatic cancer. *J. Mater. Chem.* **21**, 12650–12659 (2011).
311. Yüce, M. & Kurt, H. How to make nanobiosensors: Surface modification and characterisation of nanomaterials for biosensing applications. *RSC Adv.* **7**, 49386–49403 (2017).
312. Quarta, A. *et al.* Bioconjugation of rod-shaped fluorescent nanocrystals for efficient targeted cell labeling. *Langmuir* **25**, 12614–12622 (2009).
313. Giard, D. J. *et al.* In Vitro Cultivation of Human Tumors: Establishment of Cell Lines Derived From a Series of Solid Tumors2. *JNCI J. Natl. Cancer Inst.* **51**, 1417–1423 (1973).
314. Lieber, M., Todaro, G., Smith, B., Szakal, A. & Nelson-Rees, W. A continuous tumor cell line from a human lung carcinoma with properties of Type II alveolar epithelial cells. *Int. J. Cancer* **17**, 62–70 (1976).
315. Thavarajah, R., Mudimbaimannar, V., Rao, U., Ranganathan, K. & Elizabeth, J. Chemical and physical basics of routine formaldehyde fixation. *J. Oral Maxillofac. Pathol.* **16**, 400 (2012).
316. Kiernan, J. A. Formaldehyde, Formalin, Paraformaldehyde And Glutaraldehyde: What They Are And What They Do. *Micros. Today* **8**, 8–13 (2000).
317. Jin, J. *et al.* Polymer-coated NaYF₄:Yb³⁺, Er³⁺ upconversion nanoparticles for charge-dependent cellular imaging. *ACS Nano* **5**, 7838–7847 (2011).
318. Shukla, R. *et al.* Biocompatibility of Gold Nanoparticles and Their Endocytotic Fate Inside the Cellular Compartment: A Microscopic Overview. *Langmuir* **21**, 10644–

Bibliography

- 10654 (2005).
319. Kim, F., Song, J. H. & Yang, P. Photochemical Synthesis of Gold Nanorods. *J. Am. Chem. Soc.* **124**, 14316–14317 (2002).
320. Jana, N. R., Gearheart, L. & Murphy, C. J. Wet chemical synthesis of silver nanorods and nanowires of controllable aspect ratio. *Chem. Commun.* 617–618 (2001). doi:10.1039/B100521I
321. Westcott, S. L., Oldenburg, S. J., Lee, T. R. & Halas, N. J. Formation and Adsorption of Clusters of Gold Nanoparticles onto Functionalized Silica Nanoparticle Surfaces. *Langmuir* **14**, 5396–5401 (1998).
322. Kreibig, U. & Genzel, L. Optical absorption of small metallic particles. *Surf. Sci.* **156**, 678–700 (1985).
323. Mie, G. Beiträge zur Optik trüber Medien, speziell kolloidaler Metallösungen. *Ann. Phys.* **330**, 377–445 (1908).
324. Kelly, K. L., Coronado, E., Zhao, L. L. & Schatz, G. C. The Optical Properties of Metal Nanoparticles: The Influence of Size, Shape, and Dielectric Environment. *J. Phys. Chem. B* **107**, 668–677 (2003).
325. Noginov, M. A., Zhu, G. & Gavrilenko, V. I. Sensitized nonlinear emission of gold nanoparticles. *Opt. Express* **15**, 15648 (2007).
326. Ward, C. J., Tronndorf, R., Eustes, A. S., Auad, M. L. & Davis, E. W. Seed-mediated growth of gold nanorods: Limits of length to diameter ratio control. *J. Nanomater.* **2014**, (2014).
327. Johnson, C. J., Dujardin, E., Davis, S. A., Murphy, C. J. & Mann, S. Growth and form of gold nanorods prepared by seed-mediated, surfactant-directed synthesis. *J. Mater. Chem.* **12**, 1765–1770 (2002).
328. Chhatre, A., Thaokar, R. & Mehra, A. Formation of Gold Nanorods by Seeded Growth: Mechanisms and Modeling. *Cryst. Growth Des.* **18**, 3269–3282 (2018).
329. Jana, N. R., Gearheart, L. & Murphy, C. J. Wet chemical synthesis of high aspect ratio cylindrical gold nanorods. *J. Phys. Chem. B* **105**, 4065–4067 (2001).
330. Hoffmann, M. R., Martin, S. T., Choi, W. & Bahnemann, D. W. Environmental

Bibliography

- Applications of Semiconductor Photocatalysis. *Chem. Rev.* **95**, 69–96 (1995).
331. Linsebigler, A. L., Lu, G. & Yates, J. T. Photocatalysis on TiO₂ Surfaces: Principles, Mechanisms, and Selected Results. *Chem. Rev.* **95**, 735–758 (1995).
332. Fox, M. A. & Dulay, M. T. Heterogeneous photocatalysis. *Chem. Rev.* **93**, 341–357 (1993).
333. Chen, X. & Mao, S. S. Titanium Dioxide Nanomaterials: Synthesis, Properties, Modifications, and Applications. *Chem. Rev.* **107**, 2891–2959 (2007).
334. Asahi, R., Taga, Y., Mannstadt, W. & Freeman, A. J. Electronic and Optical Properties of Anatase TiO₂. *Phys. Rev. B* **61**, 7459–7465 (2000).
335. Amtout, A. & Leonelli, R. Optical properties of rutile near its fundamental band gap. *Phys. Rev. B* **51**, 6842–6851 (1995).
336. Wang, K. *et al.* Coating N-doped TiO₂ shell on Dually Sensitized Upconversion Nanocrystals as NIR-enhanced Photocatalysts for Efficient Utilization of the Upconverted Emissions. *Inorg. Chem. Front.* **3**, 1190–1197 (2016).
337. Zhao, J. *et al.* Direct coating of mesoporous titania on CTAB-capped gold nanorods. *Nanoscale* **8**, 5417–5421 (2015).
338. Sanchez, C., Livage, J., Henry, M. & Babonneau, F. Chemical Modification of Alkoxide Precursors. *J. Non. Cryst. Solids* **100**, 65–76 (1988).
339. Caulton, K. G. & Hubert-Pfalzgraf, L. G. Synthesis, structural principles and reactivity of heterometallic alkoxides. *Chem. Rev.* **90**, 969–995 (1990).
340. Jin, L. M., Chen, X., Siu, C. K., Wang, F. & Yu, S. F. Enhancing Multiphoton Upconversion from NaYF₄:Yb/Tm@NaYF₄ Core–Shell Nanoparticles via the Use of Laser Cavity. *ACS Nano* **11**, 843–849 (2017).
341. Hussain, S. A. An Introduction to Fluorescence Resonance Energy Transfer (FRET). (2009). Available at: <http://arxiv.org/abs/0908.1815>.
342. Salehi, M., Hashemipour, H. & Mirzaee, M. Experimental Study of Influencing Factors and Kinetics in Catalytic Removal of Methylene Blue with TiO₂ Nanopowder. *Am. J. Environ. Eng.* **2**, 1–7 (2012).
343. Hamad, H. A., Sadik, W. A., Abd El-latif, M. M., Kashyout, A. B. & Feteha, M. Y.

Bibliography

- Photocatalytic parameters and kinetic study for degradation of dichlorophenol-indophenol (DCPIP) dye using highly active mesoporous TiO₂ nanoparticles. *J. Environ. Sci.* **43**, 26–39 (2016).
344. Hernández-Gordillo, A. *et al.* Good practices for reporting the photocatalytic evaluation of a visible-light active semiconductor: Bi₂O₃, a case study. *Catal. Sci. Technol.* **9**, 1476–1496 (2019).
 345. Houas, A. *et al.* Photocatalytic degradation pathway of methylene blue in water. *Appl. Catal. B Environ.* **31**, 145–157 (2001).
 346. Lachheb, H. *et al.* Photocatalytic degradation of various types of dyes (Alizarin S) in water by UV-irradiated titania. *Appl. Catal. B Environ.* **Volume 39**, 75–90 (2002).
 347. Xu, C., Rangaiah, G. P. & Zhao, X. S. Photocatalytic Degradation of Methylene Blue by Titanium Dioxide: Experimental and Modeling Study. *Ind. Eng. Chem. Res.* **53**, 14641–14649 (2014).
 348. Sarkar, D., Chakrabarti, S. & Dutta, B. K. Diffusion of methylene blue in glass fibers - Application of the shrinking core model. *Appl. Math. Model.* **33**, 2874–2881 (2009).
 349. Al-Kadhemy, M. F., Alsharuee, I. F. & Al-Zuky, A. A. D. Analysis of the effect of the concentration of rhodamine B in ethanol on the fluorescence spectrum using the ‘Gauss Mod’ function. *J. Phys. Sci.* **22**, 77–86 (2011).
 350. Ferrer, M. L., Del Monte, F. & Levy, D. Rhodamine 19 fluorescent dimers resulting from dye aggregation on the porous surface of sol-gel silica glasses. *Langmuir* **19**, 2782–2786 (2003).
 351. Mills, A., Wang, J., Lee, S. K. & Simonsen, M. An intelligence ink for photocatalytic films. *Chem. Commun.* 2721–2723 (2005). doi:10.1039/b501131k
 352. Mills, A. & McGrady, M. A study of new photocatalyst indicator inks. *J. Photochem. Photobiol. A Chem.* **193**, 228–236 (2008).
 353. Mills, A., McGrady, M., Wang, J. & Hepburn, J. A Rapid Method of Assessing the Photocatalytic Activity of Thin TiO₂ Films Using an Ink Based on the Redox Dye 2,6-Dichloroindophenol. *Int. J. Photoenergy* **2008**, 1–6 (2008).
 354. Brezová, V., Čeppan, M., Veselý, M. & Lapčík, L. Photocatalytic oxidation of 2, 6-dichloroindophenol in the titanium dioxide aqueous suspension. **45**, 233–246 (1991).

Bibliography

355. Mills, A., Wang, J. & McGrady, M. Method of rapid assessment of photocatalytic activities of self-cleaning films. *J. Phys. Chem. B* **110**, 18324–18331 (2006).
356. Sadik, W. A., Nashed, A. W. & El-Demerdash, A. G. M. Photodecolourization of ponceau 4R by heterogeneous photocatalysis. *J. Photochem. Photobiol. A Chem.* **189**, 135–140 (2007).
357. San, N., Kiliç, M., Tuiebakhova, Z. & Çinar, Z. Enhancement and modeling of the photocatalytic degradation of benzoic acid. *J. Adv. Oxid. Technol.* **10**, 43–50 (2007).
358. Gao, C. *et al.* A Photoresponsive Rutile TiO₂ Heterojunction with Enhanced Electron–Hole Separation for High-Performance Hydrogen Evolution. *Adv. Mater.* **31**, 1–6 (2019).
359. Zhang, A. Y. *et al.* Epitaxial facet junctions on TiO₂ single crystals for efficient photocatalytic water splitting. *Energy Environ. Sci.* **11**, 1444–1448 (2018).
360. Ramakrishnan, V., Kim, H., Park, J. & Yang, B. Cobalt oxide nanoparticles on TiO₂ nanorod/FTO as a photoanode with enhanced visible light sensitization. *RSC Adv.* **6**, 9789–9795 (2016).
361. Kamat, P. V. Photophysical, photochemical and photocatalytic aspects of metal nanoparticles. *J. Phys. Chem. B* **106**, 7729–7744 (2002).
362. Guo, Z.-C., Xie, Y., Hong, I. & Kim, J. Catalytic oxidation of NO to NO₂ on activated carbon. *Energy Conversion and Management* **42**, (2001).
363. Sadanandam, G., Lalitha, K., Kumari, V. D., Shankar, M. V. & Subrahmanyam, M. Cobalt doped TiO₂: A stable and efficient photocatalyst for continuous hydrogen production from glycerol: Water mixtures under solar light irradiation. *Int. J. Hydrogen Energy* **38**, 9655–9664 (2013).
364. Chandra Sekhar, P. S. *et al.* Preparation and characterization of Co-doped TiO₂ materials for solar light induced current and photocatalytic applications. *Mater. Chem. Phys.* **135**, 220–234 (2012).
365. Hamadanian, M., Reisi-Vanani, A. & Majedi, A. Sol-gel preparation and characterization of Co/TiO₂ nanoparticles: Application to the degradation of methyl orange. *J. Iran. Chem. Soc.* **7**, S52–S58 (2012).
366. Barakat, M. A., Schaeffer, H., Hayes, G. & Ismat-Shah, S. Photocatalytic degradation

Bibliography

- of 2-chlorophenol by Co-doped TiO₂ nanoparticles. *Appl. Catal. B Environ.* **57**, 23–30 (2005).
367. Amadelli, R. *et al.* Preparation, characterisation, and photocatalytic behaviour of Co-TiO₂ with visible light response. *Int. J. Photoenergy* **2008**, (2008).
368. Sakthivel, S. *et al.* Enhancement of photocatalytic activity by metal deposition: Characterisation and photonic efficiency of Pt, Au and Pd deposited on TiO₂ catalyst. *Water Res.* **38**, 3001–3008 (2004).
369. Chen, Z. S., Gong, W. P., Chen, T. F. & Li, S. L. Synthesis and characterization of pyrochlore-type yttrium titanate nanoparticles by modified sol-gel method. *Bull. Mater. Sci.* **34**, 429–434 (2011).
370. Janjua, R. A. *et al.* Na⁺-Driven Nucleation of NaYF₄:Yb,Er Nanocrystals and Effect of Temperature on Their Structural Transformations and Luminescent Properties. *J. Phys. Chem. C* **122**, 23242–23250 (2018).
371. Wu, X. *et al.* Dye-sensitized core/active shell upconversion nanoparticles for optogenetics and bioimaging applications. *ACS Nano* **10**, 1060–1066 (2016).
372. Zou, W. *Molecular upconversion for photovoltaics*. (2015).
373. Streckowski, L., Lipowska, M. & Patonay, G. Substitution reactions of a nucleofugal group in heptamethine cyanine dyes. Synthesis of an isothiocyanato derivative for labeling of proteins with a near-infrared chromophore. *J. Org. Chem.* **57**, 4578–4580 (1992).
374. Pyatenko, Y. A. & Voronkov, A. A. The formula of gagarinite. *J. Struct. Chem.* **3**, 696–697 (1962).
375. Shao, Q. *et al.* Enhancing the upconversion luminescence and photothermal conversion properties of ~800 nm excitable core/shell nanoparticles by dye molecule sensitization. *J. Colloid Interface Sci.* **486**, 121–127 (2017).
376. Wang, X. *et al.* Dye-sensitized lanthanide-doped upconversion nanoparticles. *Chem. Soc. Rev.* **46**, 4150–4167 (2017).
377. Villanueva-Delgado, P., Krämer, K. W. & Valiente, R. Simulating Energy Transfer and Upconversion in β -NaYF₄: Yb³⁺, Tm³⁺. *J. Phys. Chem. C* **119**, 23648–23657 (2015).

Bibliography

378. Zuo, J. *et al.* Precisely Tailoring Upconversion Dynamics via Energy Migration in Core–Shell Nanostructures. *Angew. Chemie - Int. Ed.* **57**, 3054–3058 (2018).
379. Zheng, B. *et al.* Plasmon enhanced near-infrared downconversion luminescence of β -NaYF₄:Pr³⁺ nanoparticles by high-ordered Ag nanopillar arrays with tunable nanogaps. *Opt. Mater. Express* **8**, 3401 (2018).
380. Li, L. *et al.* Near-infrared downconversion luminescence of SrMoO₄:Tm³⁺,Yb³⁺ phosphors. **93**, 144–149 (2017).
381. Johnson, N. J. J. *et al.* Direct Evidence for Coupled Surface and Concentration Quenching Dynamics in Lanthanide-Doped Nanocrystals. *J. Am. Chem. Soc.* **139**, 3275–3282 (2017).
382. Wei, W. *et al.* Alleviating Luminescence Concentration Quenching in Upconversion Nanoparticles through Organic Dye Sensitization. *J. Am. Chem. Soc.* **138**, 15130–15133 (2016).
383. Tsega, M. & Dejene, F. B. Influence of acidic pH on the formulation of TiO₂ nanocrystalline powders with enhanced photoluminescence property. *Heliyon* **3**, e00246 (2017).
384. Wang, S., Bi, A., Zeng, W. & Cheng, Z. Upconversion nanocomposites for photo-based cancer theranostics. *J. Mater. Chem. B* **4**, 5331–5348 (2016).
385. Moser, B., Hochreiter, B., Herbst, R. & Schmid, J. A. Fluorescence colocalization microscopy analysis can be improved by combining object-recognition with pixel-intensity-correlation. *Biotechnol. J.* **12**, (2017).
386. Seferos, D. S., Giljohann, D. A., Hill, H. D., Prigodich, A. E. & Mirkin, C. A. Nanoflares: Probes for transfection and mRNA detection in living cells. *J. Am. Chem. Soc.* **129**, 15477–15479 (2007).
387. Mackenzie, L. E. *et al.* The theoretical molecular weight of NaYF₄:RE upconversion nanoparticles. *Sci. Rep.* **8**, 1–11 (2018).
388. Sikora, B. *et al.* Transport of NaYF₄:Er³⁺, Yb³⁺ up-converting nanoparticles into HeLa cells. *Nanotechnology* **24**, (2013).